Mathematical Problems in Engineering

Fractional Nonlinear Partial Differential Equations for Physical Models: Analytical and Numerical Methods

Lead Guest Editor: Mustafa Inc
Guest Editors: Younes Menni and José Francisco Gómez Aguilar

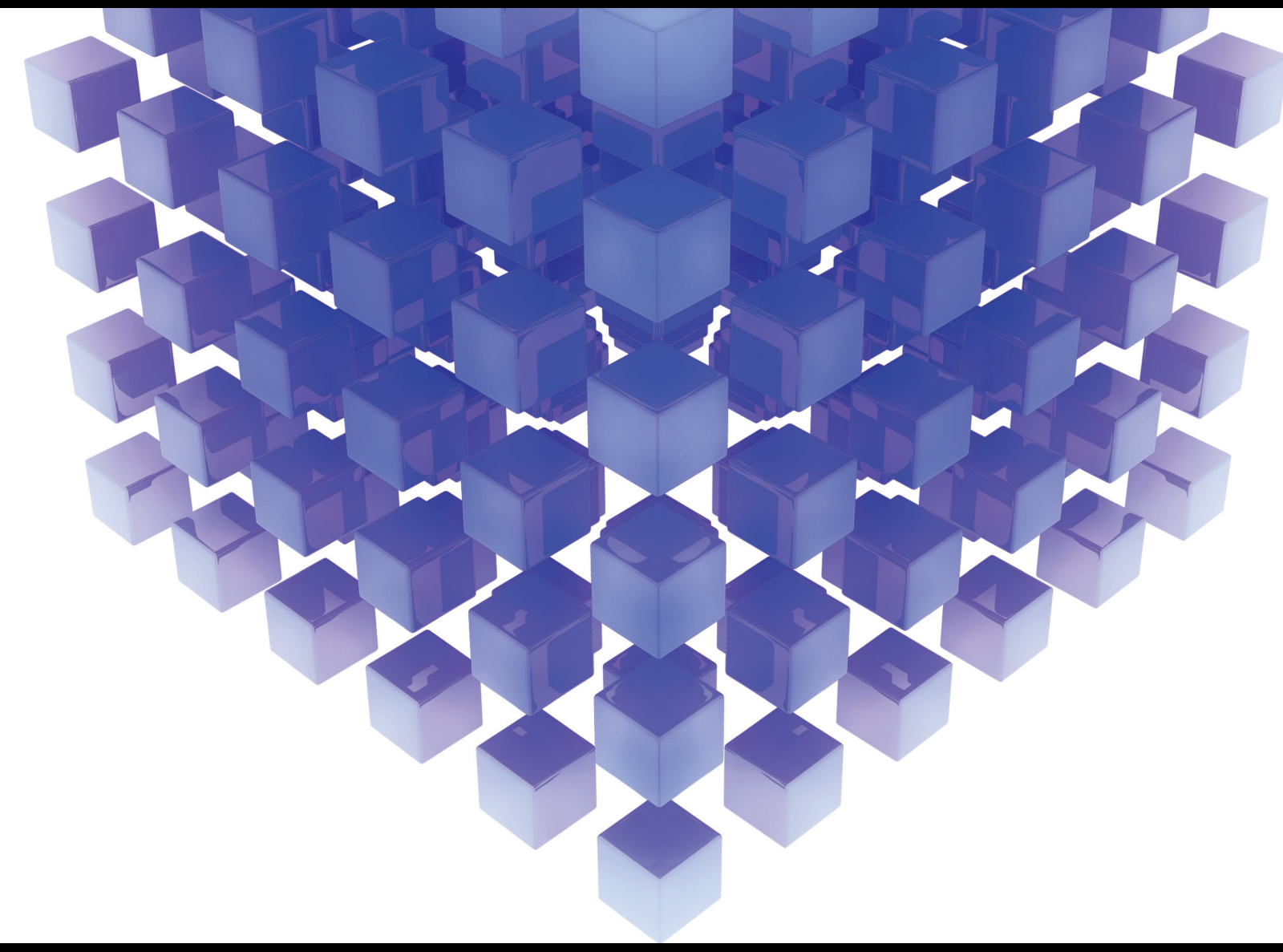

Fractional Nonlinear Partial Differential Equations for Physical Models: Analytical and Numerical Methods

Mathematical Problems in Engineering

Fractional Nonlinear Partial Differential Equations for Physical Models: Analytical and Numerical Methods

Lead Guest Editor: Mustafa Inc
Guest Editors: Younes Menni and José Francisco Gómez Aguilar

Chief Editor

Academic Editors

Contents

Hindawi
Mathematical Problems in Engineering
Volume 2021, Article ID 5529443, 16 pages
https://doi.org/10.1155/2021/5529443

Research Article

Abundant Explicit Solutions to Fractional Order Nonlinear Evolution Equations

M. Ayesha Khatun,[1] Mohammad Asif Arefin,[1] M. Hafiz Uddin,[1] and Mustafa Inc[2,3,4]

[1]*Department of Mathematics, Jashore University of Science and Technology, Jashore 7408, Bangladesh*
[2]*Department of Computer Engineering, Biruni University, Istanbul, Turkey*
[3]*Department of Mathematics, Science Faculty, Firat University, Elazig 23119, Turkey*
[4]*Department of Medical Research, China Medical University Hospital, China Medical University, Taichung, Taiwan*

Correspondence should be addressed to Mustafa Inc; minc@firat.edu.tr

Received 7 January 2021; Revised 9 May 2021; Accepted 23 June 2021; Published 3 July 2021

Academic Editor: Luigi Rodino

We utilize the modified Riemann–Liouville derivative sense to develop careful arrangements of time-fractional simplified modified Camassa–Holm (MCH) equations and generalized $(3+1)$-dimensional time-fractional Camassa–Holm–Kadomtsev–Petviashvili (gCH-KP) through the potential double $(G'/G, 1/G)$-expansion method (DEM). The mentioned equations describe the role of dispersion in the formation of patterns in liquid drops ensued in plasma physics, optical fibers, fluid flow, fission and fusion phenomena, acoustics, control theory, viscoelasticity, and so on. A generalized fractional complex transformation is appropriately used to change this equation to an ordinary differential equation; thus, many precise logical arrangements are acquired with all the freer parameters. At the point when these free parameters are taken as specific values, the traveling wave solutions are transformed into solitary wave solutions expressed by the hyperbolic, the trigonometric, and the rational functions. The physical significance of the obtained solutions for the definite values of the associated parameters is analyzed graphically with 2D, 3D, and contour format. Scores of solitary wave solutions are obtained such as kink type, periodic wave, singular kink, dark solitons, bright-dark solitons, and some other solitary wave solutions. It is clear to scrutinize that the suggested scheme is a reliable, competent, and straightforward mathematical tool to discover closed form traveling wave solutions.

1. Introduction

In recent years, fractional calculus (FC) assumed a basic part of a capable, catalyst, and rudimentary hypothetical structure for more sufficient displaying of multifaceted powerful cycles. FC and nonlinear fractional differential equations (NLFDEs) have recently been used to solve problems in plasma physics, protein chemistry, cell biology, mechanical engineering, signal processing and systems recognition, electrical transmission, control theory, economics, and fractional dynamics. FDE has a wide range of applications in fields such as magnetism, sound waves propagation in rigid porous materials, cardiac tissue electrode interface, principle of viscoelasticity, fluid dynamics, lateral and longitudinal regulation of autonomous vehicles, ultrasonic wave propagation in human cancerous bone, wave propagation in viscoelastic horn, heat transfer, RLC electric circuit, modeling of earthquake, and some other areas [1–5]. The highly prepared polylayer portion of the human body is a particularly capable model system for using fractional calculus. As a result, researchers are increasingly interested in seeking exact solutions to NLFDEs, which play a significant role in nonlinear science. Wave shape has an effect on sediment transport and beach morphodynamics, while wave skewness has an impact on radar altimetry signals and asymmetry has an impact on ship responses to wave impacts. Traveling wave solutions is a special class of analytical solutions for nonlinear evolution equations (NLEEs). Solitary waves are transmitted traveling waves with constant speeds and shapes that achieve asymptotically zero at distant locations. In order

to know the inner mechanism of the mentioned complex tangible phenomena, investigation of exact solutions of NLFDEs are very much important. In this way, numerous authors have been interested in studying the FC and finding precise and productive techniques for comprehending nonlinear fractional partial differential equations (NFPDEs). In the previous few decades, numerous strategies have been produced for illuminating NFPDEs, for example, nearby variational iteration method [6], the F-expansion method [7], homotopy perturbation method [8], Kudryashov method [9], improved (G'/G)-expansion method [10], and the DEM [11–13].

As of late, a clear and succinct method called the DEM, which is presented in [14], and is exhibited as a mighty method for looking at analytical solutions of NLDEs. The DEM is a reliable technique, which provides different types of solitary wave solutions (SWS), namely, the hyperbolic, the trigonometric, and the rational functions. The proposed MCH equation has been researched for its precise diagnostic arrangements through the (G'/G)-expansion method [15], exp-function method [16], modified simple equation method [17], and so on. Also, the proposed (gCH-KP) equation has been investigated for its exact analytic solutions through Agrawal's method [18] and the bifurcation method [19]. To the best of our knowledge, the recommended condition has not been concentrated through the DEM [12]. So, the point of this investigation is to build up some fresh and further broad precise solutions for the previously mentioned condition utilizing the DEM.

The rest of of the article is planned as follows. In Section 2, we have presented the definition and primers. In Section 3, the DEM has been depicted. In Section 4, we have built up the specific answer for the proposed equation by the previously mentioned method. In Section 5, we have uncovered the graphical portrayal and conversation, and in Section 6, comparison of results has been drawn. In Section 7, the conclusion is given.

2. Definition and Primers

Jumarie offered a mRL. With such a fractional derivative and some accommodating ways, we can change over fractional differential equations (FDEs) into integer-order differential equations applying variable transformation [20]. In this section, we first provide a couple of features and definitions of the mRL subsidiary which is used further in this study. Acknowledge that $f: R \longrightarrow R, x \longrightarrow f(x)$ implies a continuous, however, not really differentiable function. Jumarie's mRL having order a is defined by the articulation

$$D_x^{\alpha} f(x) = \begin{cases} \dfrac{1}{\Gamma(-\alpha)} \displaystyle\int_0^x (x-\xi)^{-\alpha-1} [f(\xi) - f(0)] \mathrm{d}\xi, & \alpha < 0, \\ \dfrac{1}{\Gamma(1-\alpha)} \dfrac{\mathrm{d}}{\mathrm{d}x} \displaystyle\int_0^x (x-\xi)^{-\alpha} [f(\xi) - f(0)] \mathrm{d}\xi, & 0 < \alpha < 1, \\ \left(f^{(n)}(x)\right)^{(a-n)}, & n \le \alpha \le n+1, n > 1. \end{cases} \tag{1}$$

Two or three features of the mRL were concise and four acclaimed conditions of them are as follows:

$$D_t^{\alpha} t^{\gamma} = \frac{\Gamma(1+\gamma)}{\Gamma(1+\gamma-\alpha)} t^{(\gamma-\alpha)}, \quad \gamma > 0, \tag{2}$$

$$D_t^{\alpha} (a f(t) + b g(t)) = a D_t^{\alpha} f(t) + b D_t^{\alpha} g(t), \tag{3}$$

wherever a and b stand for constants and

$$D_x^{\alpha} f[u(x)] = f_u^{\alpha}(u) D_x^{\alpha} u(x), \tag{4}$$

$$D_x^{\alpha} f[u(x)] = D_u^{\alpha} f(u) \left(u'(x)\right)^{\alpha}, \tag{5}$$

which are the immediate results of

$$d^{\alpha} x(t) = \Gamma(1+\alpha) \mathrm{d}x(t). \tag{6}$$

This holds for nondifferentiable function. Among equations (3)–(5), $u(x)$ is nondifferentiable in equations (3) and (4) but differentiable in equation (5). The function $u(x)$ is nondifferentiable, and $f(u)$ is differentiable in equation (4) and no differentiable in equation (5). So, the explanation equations (3)–(5) should be used mindfully.

3. The Double-Expansion Method

In this part, the center aspect of the DEM to assess the specific traveling wave solution of the NFPDEs has been represented. Let us guess the standard differential equation of order two:

$$G''(\xi) + \lambda G(\xi) = \mu. \tag{7}$$

Also, the accompanying relations

$$\phi = \frac{G'}{G}, \qquad \psi = \frac{1}{G}. \tag{8}$$

Subsequently, it gives

$$\phi' = -\phi^2 + \mu\psi - \lambda, \quad \psi' = -\phi\psi, \tag{9}$$

The solution for equation (7) relies upon λ as $\lambda < 0, \lambda > 0$, and $\lambda = 0$.

For $\lambda < 0$, the complete solution of equation (7) will be

$$G(\xi) = C_1 \sinh(\sqrt{-\lambda}\,\xi) + C_2 \cosh(\sqrt{-\lambda}\,\xi) + \frac{\mu}{\lambda}. \tag{10}$$

Take into account that we obtain

$$\psi^2 = \frac{-\lambda}{\lambda^2\sigma + \mu^2}\left(\phi^2 - 2\mu\psi + \lambda\right), \tag{11}$$

where $\sigma = C_1^2 - C_2^2$.

On the off chance that $\lambda > 0$, the solution for equation (7) is as follows:

$$G(\xi) = C_1 \sin(\sqrt{\lambda}\,\xi) + C_2 \cos(\sqrt{\lambda}\,\xi) + \frac{\mu}{\lambda}. \tag{12}$$

Considering that we acquire

$$\psi^2 = \frac{\lambda}{\lambda^2\sigma - \mu^2}\left(\phi^2 - 2\mu\psi + \lambda\right), \tag{13}$$

where $\sigma = C_1^2 + C_2^2$, when $\lambda = 0$, the overall solution for condition (7) is as follows:

$$G(\xi) = \frac{\mu}{2}\xi^2 + C_1\xi + C_2. \tag{14}$$

Taking into account that we acquire

$$\psi^2 = \frac{1}{C_1^2 - 2\mu C_2}\left(\phi^2 - 2\mu\psi\right), \tag{15}$$

where C_1 and C_2 stand for constants and those are arbitrary, in this section, we talk about the principle part of proposed methods to take exact traveling wave solutions to the NLFDE is as the form

$$p\left(u, D_t^\alpha u, D_x^\beta u, D_t^\alpha D_t^\alpha u, D_t^\alpha D_x^\beta u, D_x^\beta D_{x'}^\beta, \ldots,\right) = 0, \quad 0 < \alpha \le 1, 0 < \beta \le 1, \tag{16}$$

where u speaks to an unidentified function of spatial subordinate x and transient subsidiary t and speaks to a polynomial of $u(x,t)$ and its derivatives wherein the most maximal order of derivatives and nonlinear terms of the maximal order are related.

Step 1 : take into account the traveling wave transformation:

$$\xi = Lx + V\frac{t^\alpha}{\Gamma(1+\alpha)}, \tag{17}$$

where c and k are nonzero abstract constant.

Applying this wave transformation in (16), it is reworked as

$$Q\left(u, u', u'', u''', \ldots,\right) = 0, \tag{18}$$

where the prime speaks to the ordinary derivative of u regarding ξ.

Step 2 : take the arrangement of equation (9) which have been uncovered as polynomial in ϕ and ψ of the endorse type:

$$u(\xi) = \sum_{i=0}^{N} a_i \phi^i + \sum_{i=1}^{N} b_i \phi^{i-1}\psi, \tag{19}$$

where a_i and b_i stand for constants which will be calculated later.

Step 3 : in equation (18), "N" will be calculated using homogeneous balance principal which determines equation (19).

Step 4 : put (19) in (18) along with (9) and (11), and it decreases to a polynomial in ϕ, where the degree is one. Contrasting the polynomial of similar terms with zero, a game plan of logarithmic conditions that are examined by using computational programming produces the estimations of a_i, b_i, μ, C_1, C_2, and λ where $\lambda < 0$, which give hyperbolic function arrangements.

Step 5 : in a similar fashion, we explore the estimations of a_i, b_i, μ, C_1, C_2, and λ, where $\lambda > 0$ and $\lambda = 0$ which are giving trigonometric and rational function results correspondingly.

4. Formulation of Exact Solution

4.1. The Exact Solutions to the Space-Time Fractional MCH Equation. This equation was presented by Camassa and Holm [21] in 1993 which describes shallow water waves with peakon solutions. The peakon solution is a special solitary wave solution which is peaked in the limiting case, and the first derivatives are discontinuous in the peaks [22] and pseudospherical surfaces, and therefore, its integrability properties can be studied by geometrical means [23].

First, take the space-time fractional MCH equation [15] in the form

$$D_t^\alpha + 2\delta u_x - u_{xxt} + \gamma u^2 u_x = 0, \tag{20}$$

where $u(x,t)$ is the velocity of the fluid, δ is the coefficient related to the critical shallow water wave speed, and γ is a nonzero constant. Employing transformation (17), equation (20) reduced an ODE as follows:

$$Vu' + 2L\delta u' - L^2 Vu''' + \gamma L u^2 u' = 0, \tag{21}$$

where V, L, and γ are nonzero constants and δ is the coefficient related to the critical shallow water wave speed.

Integrating (21) once and taking the constant of the integration as zero, it becomes

$$u(v + 2L\delta) - L^2 Vu'' + \gamma L \frac{u^3}{3} = 0. \tag{22}$$

Balancing the maximal order derivative term u'' with the most order nonlinear term u^3, the adjusting number is resolved to be $N = 1$. At that point, expect the specific arrangement of equation (22) as

$$u(\xi) = a_0 + a_1\phi + b_1\psi, \tag{23}$$

wherever a_0, a_1, and b_1 are constants to be resolved.

Case 1 : for $\lambda < 0$, setting equation (23) in (22) and by using (9) and (11), we get the following solution:

$$\begin{aligned} a_0 &= 0, \\ a_1 &= b_1\sqrt{-\frac{\lambda}{\lambda^2\sigma + \mu^2}}, \\ b_1 &= b_1, \\ L &= b_1\sqrt{\frac{2\gamma\lambda}{6\mu^2\delta + \gamma b_1^2\lambda^2 + 6\delta\lambda^2\sigma}}, \\ V &= -\frac{2\gamma b_1\lambda}{3\left(\lambda^2\sigma + \mu^2\right)}\sqrt{\frac{6\mu^2\delta + \gamma b_1^2\lambda^2 + 6\delta\lambda^2\sigma}{2\gamma\lambda}}. \end{aligned} \tag{24}$$

Substituting these values in (23), we find to the solution for the MCH equation (20) as the structure:

$$\begin{aligned} u_{1_1}(x,t) = b_1\sqrt{-\frac{\lambda}{\lambda^2\sigma + \mu^2}} &\times \frac{C_1\sqrt{-\lambda}\cosh\left(\sqrt{-\lambda}\,\xi\right) + C_2\sqrt{-\lambda}\sinh\left(\sqrt{-\lambda}\,\xi\right)}{C_1\sinh\left(\sqrt{-\lambda}\,\xi\right) + C_2\cosh\left(\sqrt{-\lambda}\,\xi\right) + (\mu/\lambda)} \\ &+ \frac{b_1}{C_1\sinh\left(\sqrt{-\lambda}\,\xi\right) + C_2\cosh\left(\sqrt{-\lambda}\,\xi\right) + (\mu/\lambda)}, \end{aligned} \tag{25}$$

wherever

$$\begin{aligned} \xi &= b_1\sqrt{\frac{2\gamma\lambda}{6\mu^2\delta + \gamma b_1^2\lambda^2 + 6\delta\lambda^2\sigma}}x \\ &\quad - \frac{2\gamma b_1\lambda}{3\left(\lambda^2\sigma + \mu^2\right)}\sqrt{\frac{6\mu^2\delta + \gamma b_1^2\lambda^2 + 6\delta\lambda^2\sigma}{2\gamma\lambda}}\,\frac{t^\alpha}{\Gamma(1+\alpha)}, \\ \sigma &= C_1^2 - C_2^2. \end{aligned} \tag{26}$$

Since C_1 and C_2 are arbitrary constants, it may be self-assertively picked. In the event that we pick $C_1 = \mu = 0$ and $C_2 \neq 0$ in equation (25), we get the solitary wave solution:

$$u_{1_2}(x,t) = b_1\sqrt{-\frac{\lambda}{\lambda^2\sigma}} \times \sqrt{-\lambda}\tanh\left(\sqrt{-\lambda}\,\xi\right) + b_1 sech\left(\sqrt{-\lambda}\,\xi\right). \tag{27}$$

Again, if we choose $C_1 \neq 0$ and $C_2 = \mu = 0$ in equation (25), we will find the solitary wave solution:

$$u_{1_3}(x,t) = b_1\sqrt{-\frac{\lambda}{\lambda^2\sigma}} \times \sqrt{-\lambda}\coth\left(\sqrt{-\lambda}\,\xi\right) + b_1\cos ech\left(\sqrt{-\lambda}\,\xi\right), \tag{28}$$

wherever

$$\begin{aligned} \xi &= b_1\sqrt{\frac{2\gamma\lambda}{6\mu^2\delta + \gamma b_1^2\lambda^2 + 6\delta\lambda^2\sigma}}x \\ &\quad - \frac{2\gamma b_1\lambda}{3\left(\lambda^2\sigma + \mu^2\right)}\sqrt{\frac{6\mu^2\delta + \gamma b_1^2\lambda^2 + 6\delta\lambda^2\sigma}{2\gamma\lambda}}\,\frac{t^\alpha}{\Gamma(1+\alpha)}, \end{aligned} \tag{29}$$

Case 2 : for $\lambda > 0$, setting equation (23) in (22) by using (9) and (13), we get the resulting result:

$$\begin{aligned} a_0 &= 0, \\ a_1 &= b_1\sqrt{-\frac{\lambda}{\left(-\lambda^2\sigma + \mu^2\right)}}, \\ b_1 &= b_1, \\ L &= b_1\sqrt{\frac{2\gamma\lambda}{6\mu^2\delta + \gamma b_1^2\lambda^2 - 6\delta\lambda^2\sigma}}, \\ V &= -\frac{2\gamma b_1\lambda}{3\left(-\lambda^2\sigma + \mu^2\right)}\sqrt{\frac{6\mu^2\delta + \gamma b_1^2\lambda^2 - 6\delta\lambda^2\sigma}{2\gamma\lambda}}. \end{aligned} \tag{30}$$

Substituting these values in (23), we find the solution for the MCH equation (20) as the structure:

$$\begin{aligned} u_{1_4}(x,t) = b_1\sqrt{-\frac{\lambda}{\left(-\lambda^2\sigma + \mu^2\right)}} &\times \frac{C_1\sqrt{\lambda}\cos\left(\sqrt{-\lambda}\,\xi\right) - C_2\sqrt{\lambda}\sin\left(\sqrt{-\lambda}\,\xi\right)}{C_1\sin\left(\sqrt{\lambda}\,\xi\right) + C_2\cos\left(\sqrt{\lambda}\,\xi\right) + (\mu/\lambda)} \\ &+ \frac{b_1}{C_1\sinh\left(\sqrt{\lambda}\,\xi\right) + C_2\cosh\left(\sqrt{\lambda}\,\xi\right) + (\mu/\lambda)}, \end{aligned} \tag{31}$$

wherever

$$\xi = b_1\sqrt{\frac{2\gamma\lambda}{6\mu^2\delta + \gamma b_1^2\lambda^2 - 6\delta\lambda^2\sigma}}x - \frac{2\gamma b_1\lambda}{3\left(-\lambda^2\sigma + \mu^2\right)}\sqrt{\frac{6\mu^2\delta + \gamma b_1^2\lambda^2 - 6\delta\lambda^2\sigma}{2\gamma\lambda}}\frac{t^\alpha}{\Gamma(1+\alpha)},$$

$$\sigma = C_1^2 + C_2^2. \tag{32}$$

It can be chosen arbitrarily, since C_1 and C_2 are arbitrary constants. We get the solitary wave solution by choosing $C_1 = \mu = 0$ and $C_2 \neq 0$ in equation (31):

$$u_{1_5}(x,t) = b_1\sqrt{-\frac{\lambda}{\left(-\lambda^2\sigma\right)}} \times \sqrt{\lambda}\tan\left(\sqrt{\lambda}\,\xi\right) + b_1\sec\left(\sqrt{\lambda}\,\xi\right). \tag{33}$$

Again, if we choose $C_1 \neq 0$ and $C_2 = \mu = 0$ in equation (31), we will get the solitary wave solution:

$$u_{1_6}(x,t) = \sqrt{-\frac{\lambda}{\left(-\lambda^2\sigma\right)}} \times \sqrt{\lambda}\tan\left(\sqrt{\lambda}\,\xi\right) + b_1\sec\left(\sqrt{\lambda}\,\xi\right), \tag{34}$$

wherever

$$\xi = b_1\sqrt{\frac{2\gamma\lambda}{6\mu^2\delta + \gamma b_1^2\lambda^2 - 6\delta\lambda^2\sigma}}x - \frac{2\gamma b_1\lambda}{3\left(-\lambda^2\sigma + \mu^2\right)}\sqrt{\frac{6\mu^2\delta + \gamma b_1^2\lambda^2 - 6\delta\lambda^2\sigma}{2\gamma\lambda}}\frac{t^\alpha}{\Gamma(1+\alpha)}. \tag{35}$$

Case 3 : in a similar arrangement, when $\lambda = 0$, setting equation (23) in (22) by using (9) and (15), we acquire

$$\begin{aligned} a_0 &= \frac{\lambda C_2 + \sqrt{\lambda^2 C_2^2 + C_1^2\lambda}}{C_1^2}b_1, \\ a_1 &= 0, \\ b_1 &= b_1, \\ L &= \frac{2\gamma b_1}{48C_2\left(\lambda C_2 + \sqrt{\lambda^2 C_2^2 + C_1^2\lambda}\right) - 24C_1^2\lambda - 96C_1^2\lambda\delta}, \\ V &= \frac{2\gamma b_1}{576C_1^2C_2\left(\lambda C_2 + \sqrt{\lambda^2 C_2^2 + C_1^2\lambda}\right) - 24C_1^2\lambda - 96C_1^2\lambda\delta}\left(2\gamma b_1^2\lambda C_2\frac{\lambda C_2 + \sqrt{\lambda^2 C_2^2 + C_1^2\lambda}}{C_1^2}24\delta C_1^2 + b_1^2\gamma\lambda\right). \end{aligned} \tag{36}$$

Substituting these values in (23), we achieve to the rational function solution for the MCH equation (20) as the structure:

$$u_{1_7}(x,t) = \frac{\lambda C_2 + \sqrt{\lambda^2 C_2^2 + C_1^2\lambda}}{C_1^2}b_1 + \frac{b_1}{(\mu/2)\xi^2 + C_1\xi + C_2}, \tag{37}$$

wherever

$$\xi = \frac{2\gamma b_1}{48C_2\left(\lambda C_2 + \sqrt{\lambda^2 C_1^2 + C_1^2\lambda}\right) - 24C_1^2\lambda - 96C_1^2\lambda\delta}x$$
$$- \frac{2\gamma b_1}{576C_1^2C_2\left(\lambda C_2 + \sqrt{\lambda^2 C_2^2 + C_1^2\lambda}\right) - 24C_1^2\lambda - 96C_1^2\lambda\delta} \tag{38}$$
$$\left(2\gamma b_1^2\lambda C_2\frac{\lambda C_2 + \sqrt{\lambda^2 C_2^2 + C_1^2\lambda}}{C_1^2} + 24\delta C_1^2 + b_1^2\gamma\lambda\right)\frac{t^\alpha}{\Gamma(1+\alpha)}.$$

It is observable to see that the traveling wave arrangements u_{1_1}–u_{1_7} of our proposed MCH equation are broadly new and general. These picked up arrangements have not been checked in the previous investigation. These arrangements are advantageous to assign the above expressed wonders.

4.2. Generalized (3 + 1)-Dimensional gCH-KP Equation.

$$\left(D_t^\alpha u + au_x + buu_x + cD_t^\alpha u_{xx}\right)_x + c_1u_{yy} + c_2u_{zz} = 0, \tag{39}$$

describes the role of dispersion in the formation of patterns in liquid drops, where a, b, c, c_1, and c_2 are nonzero constants and D_t^α is the Riemann–Liouville fractional derivative of $u(t, x, y, z)$, $0 < \alpha < 1$ [20].

Introduce the following fractional transformation:

$$\xi = kx + ly + mz - \frac{nt^\alpha}{\Gamma(1+\alpha)}. \tag{40}$$

Applying equation (40) in (39), we have

$$k\left(-nu' + aku' + bkuu' - cnk^2u'''\right)' + c_1l^2u'' + c_2m^2u'' = 0. \tag{41}$$

Integrating equation (41) two times and taking integrating constant as zero, we obtain

$$cnk^3 + nku - ak^2u - \frac{bk^2}{2}u^2 - c_1l^2u - c_2m^2u = 0. \tag{42}$$

Balancing linear and nonlinear higher-order term, we get $N = 2$, which implies using (19) that

$$u(\xi) = a_0 + a_1\phi + a_2\phi^2 + b_1\psi + b_2\phi\psi, \tag{43}$$

where a_0, a_1, a_2, b_1, and b_2 are constants to be resolved.

Case 1 : for $\lambda < 0$, setting equation (43) in (42), close to (9) and (11), generates an arrangement of mathematical equations by utilizing computer-based math such as maple, and we get the subsequent result.

Set 1:

$$a_0 = \frac{4k\lambda nc}{b},$$
$$a_1 = 0,$$
$$a_2 = \frac{6knc}{b},$$
$$b_1 = -\frac{6knc\mu}{b},$$
$$b_2 = \frac{knc}{b}\sqrt{\frac{-36\left(\mu^2 + \lambda^2\sigma\right)}{\lambda}}, \quad k = k,$$
$$l = \sqrt{\frac{-ak^2 + nk - c_2m^2 + k^3\lambda nc}{c_1}}, \quad m = m \text{ and } n = n. \tag{44}$$

Set 2:

$$a_0 = \frac{6k\lambda nc}{b},$$
$$a_1 = 0,$$
$$a_2 = \frac{6knc}{b},$$
$$b_1 = -\frac{6knc\mu}{b},$$
$$b_2 = \frac{knc}{b}\sqrt{\frac{-36\left(\mu^2 + \lambda^2\sigma\right)}{\lambda}},$$
$$k = k,$$
$$l = \sqrt{\frac{-ak^2 + nk - c_2m^2 + k^3\lambda nc}{c_1}}, \quad m = m \text{ and } n = n. \tag{45}$$

For Set 1, substituting these values in (43), we get the solution for the gCH–KP equation (39) as the structure

$$u_{2_1}(x,t) = \frac{4k\lambda nc}{b} + \frac{6knc}{b} \times \left(\frac{C_1\sqrt{-\lambda}\cosh(\sqrt{-\lambda}\,\xi) + C_2\sqrt{-\lambda}\sinh(\sqrt{-\lambda}\,\xi)}{C_1\sinh(\sqrt{-\lambda}\,\xi) + C_2\cosh(\sqrt{-\lambda}\,\xi) + (\mu/\lambda)} \right)^2 - \frac{6knc\mu}{b} \times \frac{1}{C_1\sinh(\sqrt{-\lambda}\,\xi) + C_2\cosh(\sqrt{-\lambda}\,\xi) + (\mu/\lambda)} + \frac{knc}{b} \times \left(\sqrt{\frac{-36\left(\mu^2 + \lambda^2\sigma\right)}{\lambda}} \right) \times \frac{C_1\sqrt{-\lambda}\cosh(\sqrt{-\lambda}\,\xi) + C_2\sqrt{-\lambda}\sinh(\sqrt{-\lambda}\,\xi)}{\left(C_1\sinh(\sqrt{-\lambda}\,\xi) + C_2\cosh(\sqrt{-\lambda}\,\xi) + (\mu/\lambda)\right)^2}, \tag{46}$$

where $\xi = kx + \sqrt{((-ak^2 + nk - c_2m^2 + k^3\lambda nc)/c_1)}\,y + mz - (nt^\alpha/(\Gamma(1+\alpha)))$ and $\sigma = C_1^2 - C_2^2$.

Since C_1 and C_2 are arbitrary constants, it may be self-assertively picked. We get the following solitary wave solution by choosing $C_1 = \mu = 0$ and $C_2 \neq 0$ in equation (46):

$$u_{2_2}(x,t) = \frac{4k\lambda nc}{b} + \frac{6knc}{b}(\sqrt{-\lambda})^2\tanh^2(\sqrt{-\lambda}\,\xi) + \frac{knc}{b}\left(\sqrt{\frac{-36\left(\lambda^2\sigma\right)}{\lambda}} \right)\sqrt{-\lambda}\tanh(\sqrt{-\lambda}\,\xi)\mathrm{sech}(\sqrt{-\lambda}\,\xi). \tag{47}$$

Again, we get the following solitary wave solution by choosing $C_1 \neq 0$ and $C_2 = \mu = 0$ in equation (46):

$$u_{2_3}(x,t) = \frac{4k\lambda nc}{b} + \frac{6knc}{b}(\sqrt{-\lambda})^2\coth^2(\sqrt{-\lambda}\,\xi) + \frac{knc}{b} \times \left(\sqrt{\frac{-36\left(\lambda^2\sigma\right)}{\lambda}} \right)\sqrt{-\lambda}\coth(\sqrt{-\lambda}\,\xi)\cos ech(\sqrt{-\lambda}\,\xi), \tag{48}$$

where $\xi = kx + \sqrt{((-ak^2 + nk - c_2m^2 + k^3\lambda nc)/c_1)}\,y + mz - (nt^\alpha/(\Gamma(1+\alpha)))$ and $\sigma = C_1^2 - C_2^2$.

Similarly, for Set 2, substituting these values in (43), we get the solution for the gCH–KP equation (39) as the structure:

$$u_{2_4}(x,t) = \frac{6k\lambda nc}{b} + \frac{6knc}{b} \times \left(\frac{C_1\sqrt{-\lambda}\cosh(\sqrt{-\lambda}\,\xi) + C_2\sqrt{-\lambda}\sinh(\sqrt{-\lambda}\,\xi)}{C_1\sinh(\sqrt{-\lambda}\,\xi) + C_2\cosh(\sqrt{-\lambda}\,\xi) + (\mu/\lambda)} \right)^2 - \frac{6knc\mu}{b} \times \frac{1}{C_1\sinh(\sqrt{-\lambda}\,\xi) + C_2\cosh(\sqrt{-\lambda}\,\xi) + (\mu/\lambda)} + \frac{knc}{b} \times \left(\sqrt{\frac{-36\left(\mu^2 + \lambda^2\sigma\right)}{\lambda}} \right) \times \frac{\left(C_1\sqrt{-\lambda}\cosh(\sqrt{-\lambda}\,\xi) + C_2\sqrt{-\lambda}\sinh(\sqrt{-\lambda}\,\xi)\right)}{\left(C_1\sinh(\sqrt{-\lambda}\,\xi) + C_2\cosh(\sqrt{-\lambda}\,\xi) + (\mu/\lambda)\right)^2}, \tag{49}$$

where $\xi = kx + \sqrt{((-ak^2 + nk - c_2m^2 + k^3\lambda nc)/c_1)}\,y + mz - (nt^\alpha/(\Gamma(1+\alpha)))$ and $\sigma = C_1^2 - C_2^2$.

Since C_1 and C_2 are arbitrary constants, it may be self-assertively picked. We get the following

solitary wave solution by choosing $C_1 = \mu = 0$, and $C_2 \neq 0$ in equation (49):

$$u_{2_5}(x,t) = \frac{6k\lambda nc}{b} + \frac{6knc}{b}(\sqrt{-\lambda})^2\tanh^2(\sqrt{-\lambda}\,\xi) + \frac{knc}{b}\left(\sqrt{\frac{-36(\lambda^2\sigma)}{\lambda}}\right)\sqrt{-\lambda}\tanh(\sqrt{-\lambda}\,\xi)\mathrm{sec}h(\sqrt{-\lambda}\,\xi). \tag{50}$$

Again, we get the following solitary wave solution by choosing $C_1 \neq 0$ and $C_2 = \mu = 0$ in equation (49):

$$u_{2_6}(x,t) = \frac{6k\lambda nc}{b} + \frac{6knc}{b}(\sqrt{-\lambda})^2\coth^2(\sqrt{-\lambda}\,\xi) + \frac{knc}{b}\times\left(\sqrt{\frac{-36(\lambda^2\sigma)}{\lambda}}\right)\sqrt{-\lambda}\coth(\sqrt{-\lambda}\,\xi)\cos ech(\sqrt{-\lambda}\,\xi), \tag{51}$$

where $\xi = kx + \sqrt{((-ak^2 + nk - c_2m^2 + k^3\lambda nc)/c_1)}\,y + mz - (nt^\alpha/(\Gamma(1+\alpha)))$ and $\sigma = C_1^2 - C_2^2$.

Case 2 : with the same system, when $\lambda > 0$, putting equation (43) in (42) close by (9) and (13) generates an arrangement of mathematical equations by utilizing computer-based math such as maple, we get the result as follows.

Set 1:

$$\begin{aligned}
a_0 &= \frac{4k\lambda nc}{b},\\
a_1 &= 0,\\
a_2 &= \frac{6knc}{b},\\
b_1 &= -\frac{6knc\mu}{b},\\
b_2 &= \frac{knc}{b}\sqrt{\frac{36(\lambda^2\sigma - \mu^2)}{\lambda}}, \quad k = k,\\
l &= \sqrt{\frac{-ak^2 + nk - c_2m^2 + k^3\lambda nc}{c_1}}, \quad m = m \text{ and } n = n.
\end{aligned} \tag{52}$$

Set 2:

$$\begin{aligned}
a_0 &= \frac{6k\lambda nc}{b},\\
a_1 &= 0,\\
a_2 &= \frac{6knc}{b},\\
b_1 &= -\frac{6knc\mu}{b},\\
b_2 &= \frac{knc}{b}\sqrt{\frac{36(\lambda^2\sigma - \mu^2)}{\lambda}}, \quad k = k,\\
l &= \sqrt{\frac{-ak^2 + nk - c_2m^2 + k^3\lambda nc}{c_1}}, \quad m = m \text{ and } n = n.
\end{aligned} \tag{53}$$

For Set 1, substituting these values in (43), we get the solution for the gCH–KP equation (39) as the structure:

$$u_{2_7} = \frac{4k\lambda nc}{b} + \frac{6knc}{b} \times \left(\frac{C_1\sqrt{\lambda}\,\cos(\sqrt{\lambda}\,\xi) - C_2\sqrt{\lambda}\,\sin(\sqrt{\lambda}\,\xi)}{C_1\sinh(\sqrt{-\lambda}\,\xi) + C_2\cosh(\sqrt{-\lambda}\,\xi) + (\mu/\lambda)} \right)^2 - \frac{6knc\mu}{b} \times \frac{1}{C_1\sin(\sqrt{\lambda}\,\xi) + C_2\cos(\sqrt{\lambda}\,\xi) + (\mu/\lambda)} + \frac{knc}{b} \times \left(\sqrt{\frac{36\left(\lambda^2\sigma - \mu^2\right)}{\lambda}} \right) \times \frac{C_1\sqrt{\lambda}\cos(\sqrt{\lambda}\,\xi) - C_2\sqrt{\lambda}\sin(\sqrt{\lambda}\,\xi)}{\left(C_1\sin(\sqrt{\lambda}\,\xi) + C_2\cos(\sqrt{\lambda}\,\xi) + (\mu/\lambda)\right)^2}, \tag{54}$$

where $\xi = kx + \sqrt{((-ak^2 + nk - c_2m^2 + k^3\lambda nc)/c_1)}\,y + mz - (nt^\alpha/(\Gamma(1+\alpha)))$ and $\sigma = C_1^2 + C_2^2$.

Since C_1 and C_2 are arbitrary constants, it might be self-assertively picked. The following solitary wave solution can be found by choosing $C_1 = \mu = 0$ and $C_2 \neq 0$ in equation (54):

$$u_{2_8}(x,t) = \frac{4k\lambda nc}{b} + \frac{6k\lambda nc}{b}\tan^2(\sqrt{\lambda}\,\xi) - \frac{knc}{b}\left(\sqrt{\frac{36\left(\lambda^2\sigma\right)}{\lambda}}\right)\sqrt{\lambda}\tan(\sqrt{\lambda}\,\xi)\sec(\sqrt{\lambda}\,\xi). \tag{55}$$

Again, by choosing $C_1 \neq 0$ and $C_2 = \mu = 0$ in equation (54), the following solitary wave solution can be obtained:

$$u_{2_9}(x,t) = \frac{4k\lambda nc}{b} + \frac{6k\lambda nc}{b}\cot^2(\sqrt{\lambda}\,\xi) + \frac{knc}{b}\left(\sqrt{\frac{36\left(\lambda^2\sigma\right)}{\lambda}}\right)\sqrt{\lambda}\cot(\sqrt{\lambda}\,\xi)\cos ec(\sqrt{\lambda}\,\xi), \tag{56}$$

where $\xi = kx + \sqrt{((-ak^2 + nk - c_2m^2 + k^3\lambda nc)/c_1)}\,y + mz - (nt^\alpha/(\Gamma(1+\alpha)))$ and $\sigma = C_1^2 + C_2^2$.

Case 3 : at last, when $\lambda = 0$, putting equation (43) in (42) along with equations (9) and (15), we will reach a set of mathematical equations having the solutions.

Set 1:

$$
\begin{aligned}
a_0 &= -\frac{1}{bk^2}\left(ak^2 - nk + c_2m^2 - 11cn\lambda k^3 + \sqrt{-c_1\left(\sqrt{73}\,cnk^3\lambda + c_2m^2 - nk + ak^2\right)}\right),\\
a_1 &= 0,\\
a_2 &= \frac{12knc}{b},\\
b_1 &= -\frac{12knc}{b}\left(\lambda C_2 + \sqrt{\lambda^2 C_2^2 - \lambda C_1^2}\right),\\
b_2 &= 0,\\
k &= k,\\
l &= \frac{\sqrt{c_1\left(\sqrt{73}\,cnk^3\lambda - c_2m^2 \mp nk - ak^2\right)}}{c_1}, \quad m = m \text{ and } n = n.
\end{aligned}
\tag{57}
$$

For set 1, substituting these values into (43), we get the solution for the gCH–KP equation (39) as the structure:

Set 2:

$$
\begin{aligned}
a_0 &= a_0,\\
a_1 &= a_1,\\
a_2 &= \frac{b_1C_2\left(bb_1C_2 + cnkC_1^2\right)}{kC_1^4cn},\\
b_1 &= b_1,\\
b_2 &= 0.
\end{aligned}
\tag{58}
$$

$$
\begin{aligned}
u_{2_{10}} = {} & -\frac{1}{bk^{2\times}}\left(ak^2 - nk + c_2m^2 - 11cn\lambda k^3 + \sqrt{-c_1\left(\sqrt{73}\,cnk^3\lambda + c_2m^2 - nk + ak^2\right)}\right)\\
& + \frac{12knc}{b}\times\left(\frac{\mu\xi + C_1}{(\mu/2)\xi^2 + C_1\xi + C_2}\right)^2 - \frac{12knc}{b}\times\left(\lambda C_2 + \sqrt{\lambda^2C_2^2 - \lambda C_1^2}\right)\times\left(\frac{1}{(\mu/2)\xi^2 + C_1\xi + C_2}\right),
\end{aligned}
\tag{59}
$$

where
$\xi = kx + ((\sqrt{c_1(\sqrt{73}\,cnk^3\lambda - c_2m^2 \mp nk - ak^2)})/c_1)y + mz - (nt^\alpha/(\Gamma(1+\alpha)))$.

It is essential to see that, for the aftereffect of the constants given in set 2 for both in (case 2, and case 3), we achieve new and simpler solitary wave solutions whose are additionally valuable to examine the above-stated matter. For plainness, the solutions have been excluded from this section.

5. Brief Discussion and Graphical Representation Discussion

The specific arrangements accomplished from the current method are novel and not quite the same as the existing procedure which is built by different authors. We utilized proposed DEM to get general arrangements. In this study, a group of traveling wave arrangements as obscure boundaries are acquired. Achieved traveling wave solutions show various types of solitary waves when particular values are given

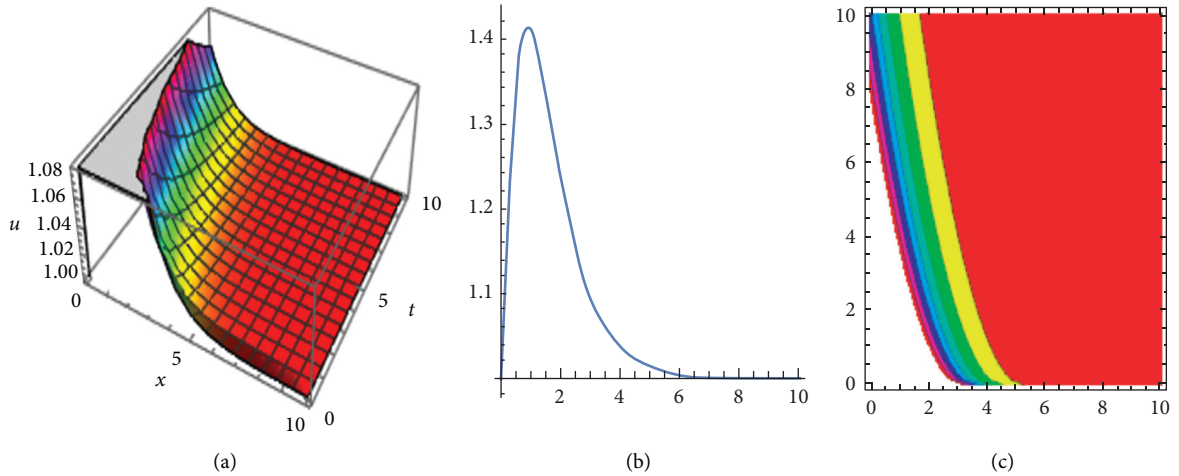

(a) (b) (c)

FIGURE 1: 3D (left section), 2D (middle section), and contour (right section) for $u_{1_2}(x,t)$ when $C_1 = 0, C_2 = 1, \mu = 0, \lambda = -1, b_1 = 1, \sigma = 1, L = 1, V = 1, \alpha = (1/2), 0 \le t \le 10$, and $0 \le x \le 10$. (a) Three-dimensional plotline. (b) Two-dimensional plotline. (c) Plot of contour.

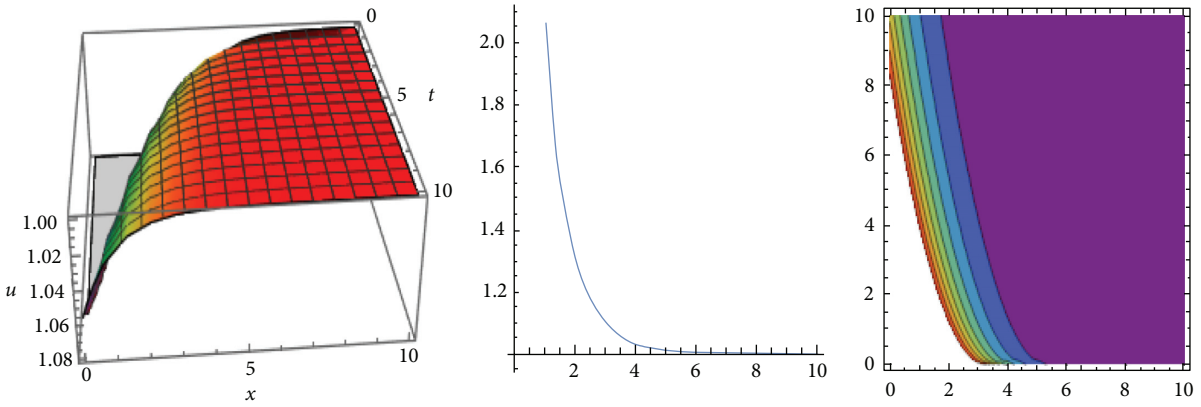

(a) (b) (c)

FIGURE 2: 3D (left section), 2D (middle section), and contour (right section) plots represent to the kink wave solution of $u_{1_3}(x,t)$ when $C_1 = 1, C_2 = 0, \mu = 0, \lambda = -1, b_1 = 1, \sigma = 1, L = 1, V = 1, \alpha = (1/2), 0 \le t \le 10$, and $0 \le x \le 10$. (a) Three-dimensional plotline. (b) Two-dimensional plotline. (c) Plot of contour.

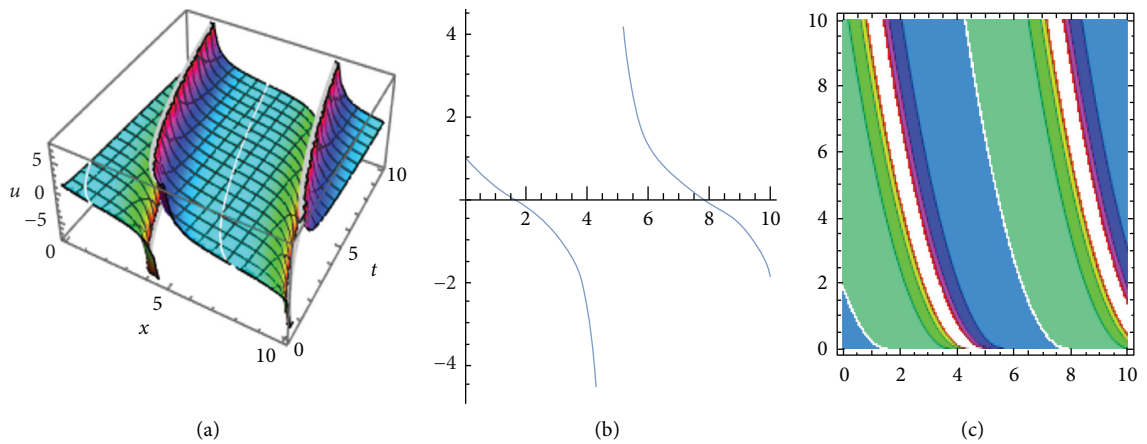

(a) (b) (c)

FIGURE 3: 3D (left section), 2D (middle section), and contour (right section) plots represent to the periodic wave solution of $u_{1_5}(x,t)$ when $C_1 = 0, C_2 = 1, \mu = 0, \lambda = 1, b_1 = 1, \sigma = 1, L = 1, V = 1, \alpha = (1/2), 0 \le t \le 10$, and $0 \le x \le 10$. (a) Three-dimensional plotline. (b) Two-dimensional plotline. (c) Plot of contour.

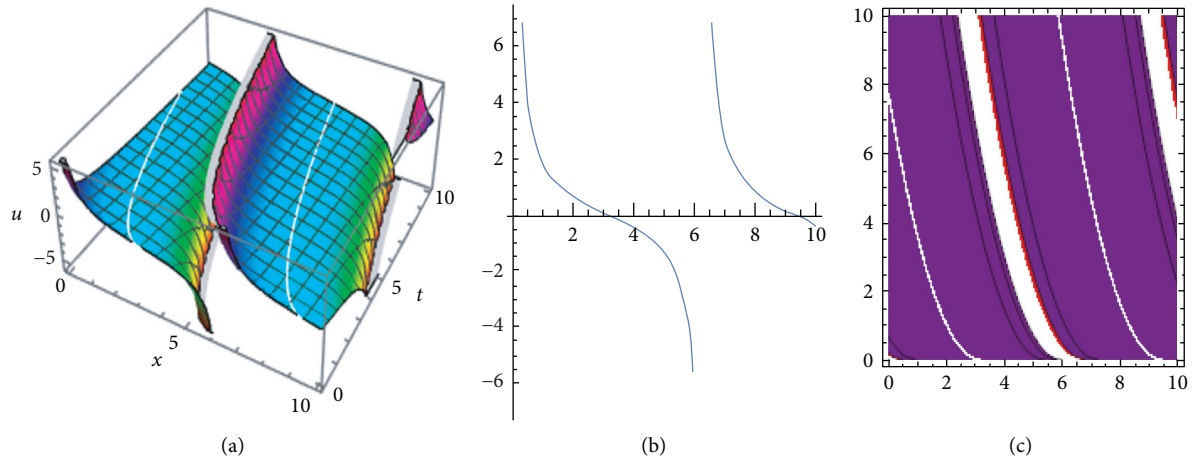

FIGURE 4: 3D (left section), 2D (middle section), and contour (right section) plots represent solitary wave solution of $u_{1_6}(x,t)$ when $C_1 = 1, C_2 = 0, \mu = 0, \lambda = 1,\ b_1 = 1, \sigma = 1, L = 1, V = 1, \alpha = (1/2), 0 \le t \le 10$, and $0 \le x \le 10$. (a) Three-dimensional plotline. (b) Two-dimensional plotline. (c) Plot of contour.

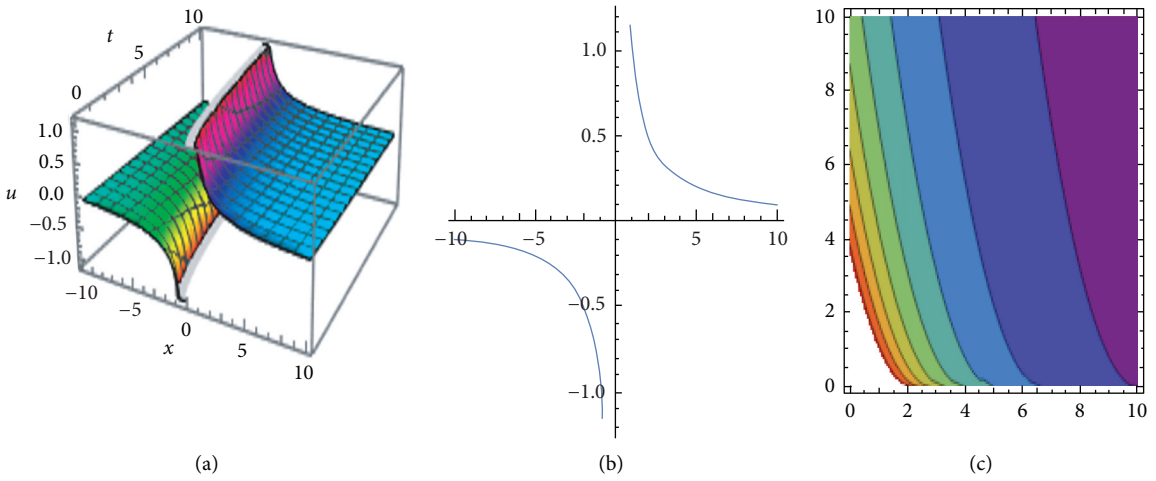

FIGURE 5: 3D (left section), 2D (middle section), and contour (right section) plots represent bright-dark wave solution of $u_{1_7}(x,t)$ when $C_1 = 1, C_2 = 0, \mu = 0, \lambda = 0, a_1 = 0, a_2 = 0, b_2 = 0,\ b_1 = 1, L = 1, V = 1, \alpha = (1/2), 0 \le t \le 10$, and $0 \le x \le 10$. (a) Three-dimensional plotline. (b) Two-dimensional plotline. (c) Plot of contour.

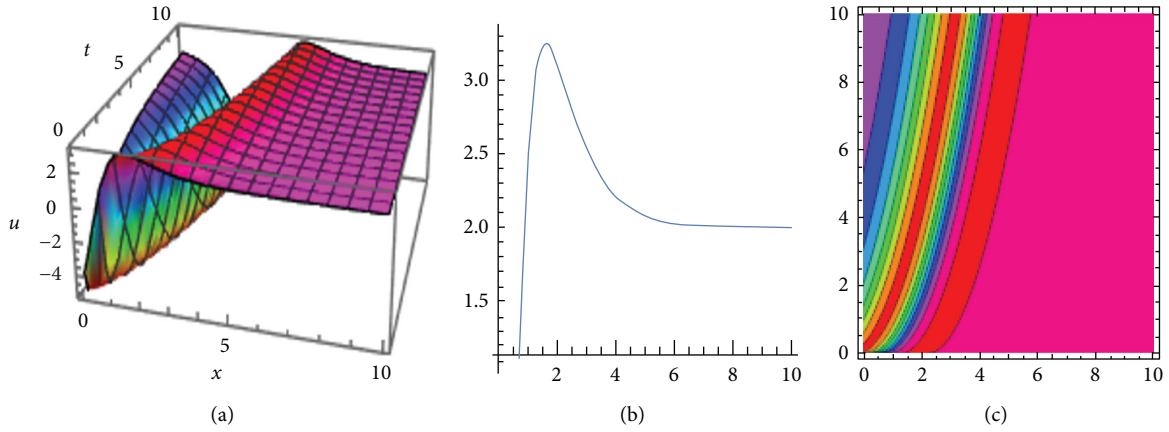

FIGURE 6: 3D (left section), 2D (middle section), and contour (right section) plots represent dark soliton solution of $u_{2_2}(x,t)$ when $C_1 = 0, C_2 = 1, \mu = 0, c = 1, k = 1, n = 1, \lambda = -1, b = 1, \sigma = 1,\ l = 1, m = 1, \alpha = (1/2), y = z = 0, 0 \le t \le 10$, and $0 \le x \le 10$. (a) Three-dimensional plotline. (b) Two-dimensional plotline. (c) Plot of contour.

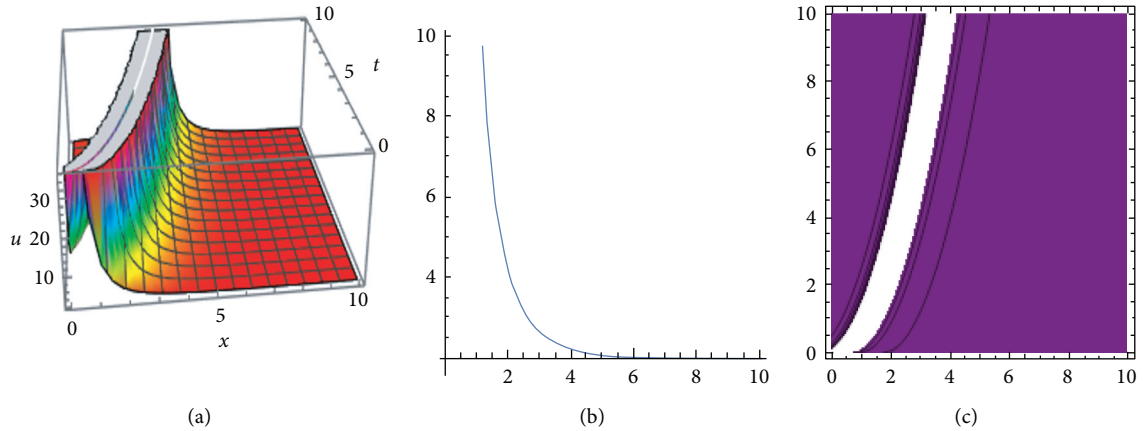

(a) (b) (c)

FIGURE 7: 3D (left section), 2D (middle section), and contour (right section) plots represent bright soliton solution of $u_{2_3}(x,t)$ when $C_1 = 1, C_2 = 0, \mu = 0, c = 1, k = 1,\ n = 1, \lambda = -1, b = 1, \sigma = 1,\ l = 1, m = 1, \alpha = (1/2), y = z = 0, 0 \le t \le 10,$ and $0 \le x \le 10$. (a) Three-dimensional plotline. (b) Two-dimensional plotline. (c) Plot of contour.

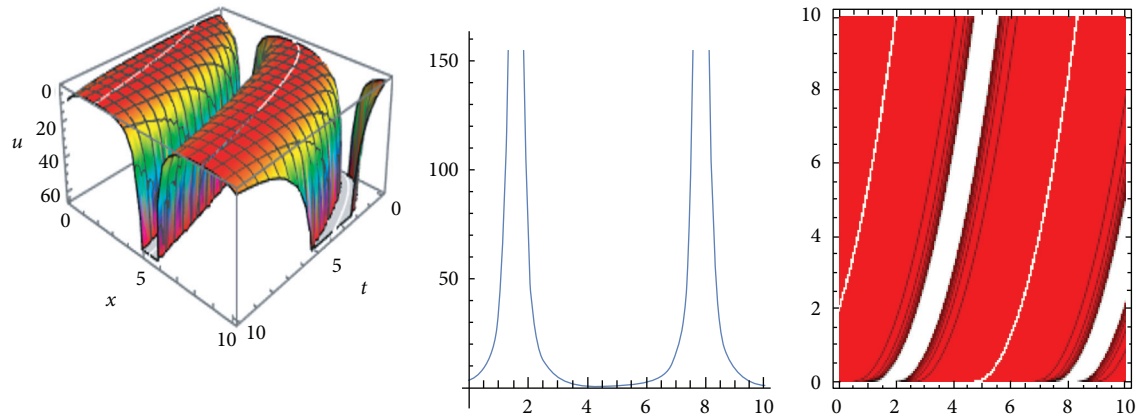

(a) (b) (c)

FIGURE 8: 3D (left section), 2D (middle section), and contour (right section) plots represent periodic wave solution of $u_{2_5}(x,t)$ when $C_1 = 0, C_2 = 1, \mu = 0, c = 1, k = 1,\ n = 1, \lambda = 1, b = 1, \sigma = 1,\ l = 1, m = 1, \alpha = (1/2), y = z = 0, 0 \le t \le 10,$ and $0 \le x \le 10$. (a) Three-dimensional plotline. (b) Two-dimensional plotline. (c) Plot of contour.

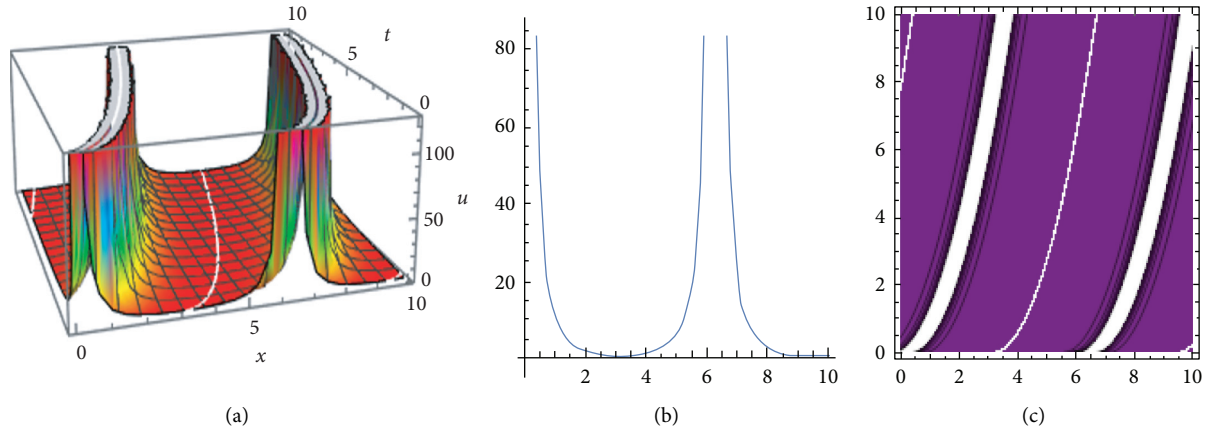

(a) (b) (c)

FIGURE 9: 3D (left section), 2D (middle section), and contour (right section) plots represent periodic solitary wave solution of $u_{2_6}(x,t)$ when $C_1 = 1, C_2 = 0, \mu = 0, c = 1, k = 1, n = 1, \lambda = 1,\ b = 1, \sigma = 1, l = 1, m = 1, \alpha = (1/2),\ y = z = 0, 0 \le t \le 10$ and $0 \le x \le 10$. (a) Three-dimensional plotline. (b) Two-dimensional plotline. (c) Plot of contour.

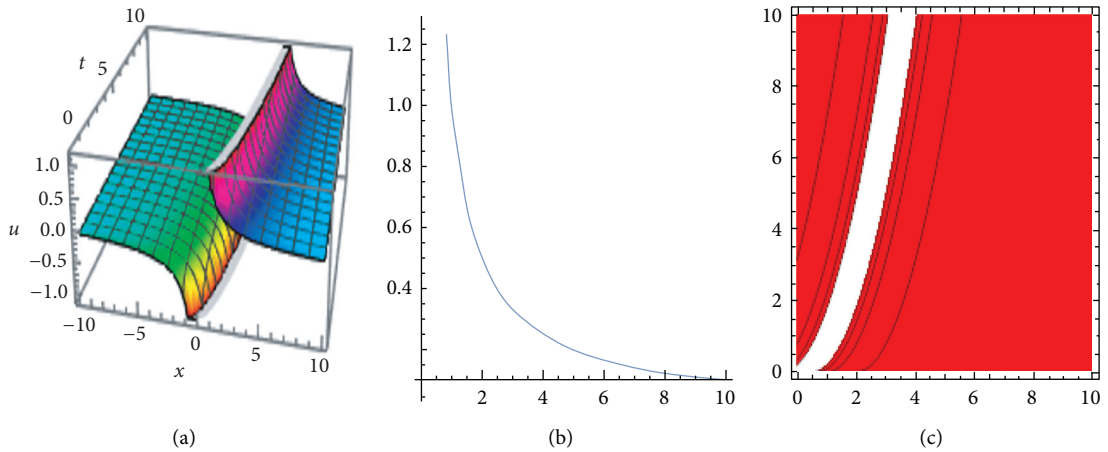

(a) (b) (c)

Figure 10: 3D (left section), 2D (middle section), and contour (right section) plots represent singular kink type wave solution of $u_{2_7}(x,t)$ when $C_1 = -1, C_2 = 0, \mu = 0, c = 1, k = 1, \quad n = 1, \lambda = 0, b = 1, \sigma = 1, l = 1, m = 1, a = 1, \quad \alpha = (1/2), y = z = 0, 0 \le t \le 10, \quad \text{and} \quad 0 \le x \le 10.$ (a) Three-dimensional plotline. (b) Two-dimensional plotline. (c) Plot of contour.

Table 1: Comparison between Liu et al. [23] solutions and our solutions to the gCH-KP equation.

Liu et al. [23]	Obtained solutions
If $A = 3$ and $B = 2$, then equation (16) becomes $u(t,x,y,z) = 1 - \tanh^2((1/\sqrt{2})\lvert kx + ly + mz - (nt^\alpha/(\Gamma(1+\alpha)))\rvert)$.	If $C_1 = \mu = \sigma = 0, \lambda = -1, c = 1, b = 1,$ and $C_2 = 1$, then the obtained solution $u_{2_2}(x,t)$ becomes $u_{2_2}(x,t) = -4k + 6kn\tanh^2(kx + ly + mz - (nt^\alpha/(\Gamma(1+\alpha))))$
If $A = 1$ and $B = -2$, then equation (23) becomes $u(t,x,y,z) = 1 - 3\tanh^2((1/\sqrt{2})\lvert kx + ly + mz - (nt^\alpha/(\Gamma(1+\alpha)))\rvert)$	If $C_1 = \mu = \sigma = 0, \lambda = -1, c = 1, b = 1,$ and $C_2 = 1$, then the obtained solution $u_{2_5}(x,t)$ becomes $u_{2_2}(x,t) = -6k + 6kn\tanh^2(kx + ly + mz - (nt^\alpha/(\Gamma(1+\alpha))))$
If $A = 6$ and $B = 0$, then equation (25) becomes $u(t,x,y,z) = (1/(kx + ly + mz - (nt^\alpha/(\Gamma(1+\alpha)))))^2)$	If $b = 1, a = 0, C_1 = -1, c = 1, \lambda = 0, C_2 = 0,$ and $\mu = 0$, then the obtained solution $u_{2_7}(x,t)$ becomes $u_{2_{10}}(x,t) = (kn/(kx + ly + mz - (nt^\alpha/(\Gamma(1+\alpha)))))^2)$

to its unknown parameters such as Kink wave and singular kink wave, single soliton, periodic wave, bright soliton, dark soliton, and combined dark-bright solitary wave solutions in Figures 1–10. From attained solutions, some solutions cannot be created by other methods such as the exp $(-\psi(\xi))$-expansion method [24] and modified simple equation method [25]. Therefore, some solutions are novel from earlier constructed solutions in the literature. We also demonstrate all the figures in this study which have been represented in three arrangements such as 3D plot, 2D plot, and contour plot within the specified domain $0 \le t \le 10$ and $-10 \le x \le 10$ (see Figures 1–10). Mathematica, a computation package application, was used to construct all of the figures. In order to observe the physical appearance of these models, the structure of figures is depicted via giving suitable values of parameters.

6. Results' Comparison

It is amazing to observe that some of the achieved solutions demonstrate good similarity with earlier established solutions. A comparison of the solutions of Liu et al. [23] and obtained solutions is presented in Table 1.

The hyperbolic and rational function solutions alluded to in the above table are comparative, and for setting the definite values of the arbitrary constants, they are indistinguishable. In a nutshell, it is substantial to realize that the TWS $u_{2_1}(x,t), u_{2_3}(x,t), u_{2_4}(x,t), u_{2_6}(x,t), \quad u_{2_7}(x,t), u_{2_8}(x,t),$ and SWS $u_{2_9}(x,t)$ of the fractional gCH-KP equation all are recent and very much significant, which were not originally in the previous works. The time-fractional gCH-KP equation is also solved by the bilinear and RBF method [19]. It can be seen from here that the RBF method gives a high-precision numerical solution of the fractional differential equation. Applying our proposed DEM on the mentioned equation, we acquire hyperbolic, trigonometric, and rational function solution containing parameters which are fresh and further general. The obtained solutions are capable to examine the role of dispersion in the formation of patterns in liquid drops and shallow water waves with peakon solutions ensued in plasma physics, optical fibers, fluid flow, fission and fusion phenomena, control theory, and some other areas.

7. Conclusion

In this study, we have successfully established the more and further general stable solitary wave solitary wave solutions with assorted physical structures which appeal wide attention to physicist, engineers, and mathematicians to the new solutions of space-time fractional MCH and space-time fractional gCH-KP equation in the light of

Riemann–Liouville fractional derivative by implementing the novel approach DEM. The depiction of the solutions are in the form of hyperbolic, trigonometric, and rational functions including kink wave, antikink wave, dark, bright, singular, combined, optical solitons, periodic wave, and traveling wave, and some new types of solitary wave solutions are discovered which expose the phenomena relating to plasma physics, optical fibers, fluid flow, fission and fusion phenomena, acoustics, control theory, viscoelasticity, geophysics, nonlinear mechanics, protein chemistry, and chemical kinematics. The physical significance of the obtained solutions for the definite values of the associated parameters is analyzed graphically with 2D, 3D, and contour shape. The solutions achieved in this study have been observed with maple by placing them back into NLFDEs and found precise. It is possible to conclude that the adopted method is direct, reliable, effective, and conformable and provides many new physical model solutions to NLPFEEs that arise in mathematical physics, applied mathematics, and engineering.

Data Availability

The data used to support the findings of the study are included within the article.

Conflicts of Interest

The authors author declare that they have no conflicts of interest.

Authors' Contributions

M. Ayesha Khatun helped with software, curated the data, and wrote the manuscript. Mohammad Asif Arefin helped with software, curated the data, and carried out formal analysis. M. Hafiz Uddin conceptualized and supervised the study, reviewed and edited the manuscript, and validated the study. Mustafa Inc reviewed and edited and investigated the study.

References

[1] D. Baleanu, J. A. Tenreiro Machado, and W. Chen, "Fractional differentiation and its applications I," *Computers & Mathematics with Applications*, vol. 66, no. 5, p. 575, 2013.

[2] W. S. Chung, S. Zarrinkamar, S. Zare, and H. Hassanabadi, "Scattering study of a modified cusp potential in conformable fractional formalism," *Journal of the Korean Physical Society*, vol. 70, no. 4, pp. 348–352, 2017.

[3] D. T. Spasic, N. I. Kovincic, and D. V. Dankuc, "A new material identification pattern for the fractional Kelvin-Zener model describing biomaterials and human tissues," *Communications in Nonlinear Science and Numerical Simulation*, vol. 37, pp. 193–199, 2016.

[4] F. S. Mozaffari, H. Hassanabadi, H. Sobhani, and W. S. Chung, "Investigation of the Dirac equation by using the conformable fractional derivative," *Journal of the Korean Physical Society*, vol. 72, no. 9, pp. 987–990, 2018.

[5] I. Podlubny, I. Petráš, B. M. Vinagre, P. O'Leary, and Ľ. Dorčák, "Analogue realizations of fractional-order controllers," *Nonlinear Dynamics*, vol. 29, no. 1, pp. 281–296, 2002.

[6] H. Anaç, M. Merdan, and T. Kesemen, "Solving for the random component time-fractional partial differential equations with the new Sumudu transform iterative method," *SN Applied Sciences*, vol. 2, pp. 1–11, 2020.

[7] A. R. Seadawy and K. El-Rashidy, "Dispersive solitary wave solutions of Kadomtsev-Petviashvili and modified Kadomtsev-Petviashvili dynamical equations in unmagnetized dust plasma," *Results in Physics*, vol. 8, pp. 1216–1222, 2018.

[8] R. I. Nuruddeen and A. M. Nass, "Exact solitary wave solution for the fractional and classical GEW-Burgers equations: an application of Kudryashov method," *Journal of Taibah University for Science*, vol. 12, no. 3, pp. 309–314, 2018.

[9] H. Jafari, C. M. Khalique, and M. Nazari, "Application of the Laplace decomposition method for solving linear and nonlinear fractional diffusion-wave equations," *Applied Mathematics Letters*, vol. 24, no. 11, pp. 1799–1805, 2011.

[10] H. Ahmad, A. Akgül, T. A. Khan, P. S. Stanimirović, and Y. M. Chu, "New perspective on the conventional solutions of the nonlinear time-fractional partial differential equations," *Complexity*, vol. 2020, Article ID 8829017, 2020.

[11] A. Zafar, M. Raheel, K. K. Ali, and W. Razzaq, "On optical soliton solutions of new Hamiltonian amplitude equation via Jacobi elliptic functions," *The European Physical Journal Plus*, vol. 135, no. 8, pp. 1–17, 2020.

[12] M. Hafiz Uddin, M. A. Akbar, M. Ali Akbar, M. Ashrafuzzaman Khan, and M. Abdul Haque, "New exact solitary wave solutions to the space-time fractional differential equations with conformable derivative," *AIMS Mathematics*, vol. 4, no. 2, pp. 199–214, 2019.

[13] M. H. Uddin, M. A. Khan, M. A. Akbar, and M. A. Haque, "Multi-solitary wave solutions to the general time fractional Sharma-Tasso-Olver equation and the time fractional Cahn-Allen equation," *Arab Journal of Basic and Applied Sciences*, vol. 26, no. 1, pp. 193–201, 2019.

[14] M. H. Uddin, M. A. Khan, M. A. Akbar, and M. A. Haque, "Analytical wave solutions of the space time fractional modified regularized long wave equation involving the conformable fractional derivative," *Kerbala International Journal of Modern Science*, vol. 5, no. 1, p. 7, 2019.

[15] L.-X. Li, E.-Q. Li, and M.-L. Wang, "The $(G'/G, 1/G)$-expansion method and its application to travelling wave solutions of the Zakharov equations," *Applied Mathematics-A Journal of Chinese Universities*, vol. 25, no. 4, pp. 454–462, 2010.

[16] M. Shakeel, Q. M. Ul-Hassan, and J. Ahmad, "Applications of the novel (G'/G)-Expansion method for a time fractional simplified modified camassa-holm (MCH) equation," *Abstract and Applied Analysis*, vol. 2014, Article ID 601961, 2014.

[17] Z. Aniqa and J. Ahmad, "Exact solitary wave solutions of fractional modified Camassa-Holm equation using an efficient method," *Alexandria Engineering Journal*, vol. 59, no. 5, pp. 3565–3574, 2020.

[18] M. N. Islam, M. Asaduzzaman, and M. S. Ali, "Exact wave solutions to the simplified modified Camassa–Holm equation in mathematical physics," *Aims Mathematics*, vol. 5, no. 1, pp. 26–41, 2019.

[19] C. Lu, L. Xie, and H. Yang, "Analysis of Lie symmetries with conservation laws and solutions for the generalized (3+1)-dimensional time fractional Camassa-Holm-Kadomtsev-Petviashvili equation," *Computers & Mathematics with Applications*, vol. 77, no. 12, pp. 3154–3171, 2019.

[20] M. Yue and R. Schlueter, "Bifurcation subsystem method based classification for power system stability problems," *Electric Power Components and Systems*, vol. 33, no. 2, pp. 213–231, 2005.

[21] G. Jumarie, "Modified Riemann-Liouville derivative and fractional Taylor series of nondifferentiable functions further results," *Computers & Mathematics with Applications*, vol. 51, no. 9-10, pp. 1367–1376, 2006.

[22] E. G. Reyes, "Geometric integrability of the camassa–holm equation," *Letters in Mathematical Physics*, vol. 59, no. 2, pp. 117–131, 2002.

[23] Z. Liu, Z. Kelei, and M. Li, "Exact traveling wave solutions and bifurcation of a generalized (3+1)-dimensional time-fractional camassa-holm-kadomtsev-petviashvili equation," *Journal of Function Spaces*, vol. 2020, Article ID 4532824, 2020.

[24] A. Ali, A. R. Seadawy, and D. Lu, "Computational methods and traveling wave solutions for the fourth-order nonlinear Ablowitz-Kaup-Newell-Segur water wave dynamical equation via two methods and its applications," *Open Physics*, vol. 16, no. 1, pp. 219–226, 2018.

[25] K. Khan, M. A. Akbar, and N. H. Ali, "The modified simple equation method for exact and solitary wave solutions of nonlinear evolution equation: the GZK-BBM equation and right-handed non-commutative Burgers equations," *International Scholarly Research Notices*, vol. 2013, Article ID 146704, 2013.

Hindawi
Mathematical Problems in Engineering
Volume 2021, Article ID 6698028, 11 pages
https://doi.org/10.1155/2021/6698028

Research Article

New Explicit Solutions to the Fractional-Order Burgers' Equation

M. Hafiz Uddin,[1] **Mohammad Asif Arefin**,[1] **M. Ali Akbar**,[2] **and Mustafa Inc**[3,4,5]

[1]*Department of Mathematics, Jashore University of Science and Technology, Jashore 7408, Bangladesh*
[2]*Department of Applied Mathematics, University of Rajshahi, Rajshahi 6205, Bangladesh*
[3]*Department of Computer Engineering, Biruni University, Istanbul, Turkey*
[4]*Department of Mathematics, Firat University, Elazig, Turkey*
[5]*Department of Medical Research, China Medical University Hospital, China Medical University, Taichung, Taiwan*

Correspondence should be addressed to Mustafa Inc; minc@firat.edu.tr

Received 7 November 2020; Revised 9 May 2021; Accepted 4 June 2021; Published 12 June 2021

Academic Editor: Maria Patrizia Pera

The closed-form wave solutions to the time-fractional Burgers' equation have been investigated by the use of the two variables $((G'/G), (1/G))$-expansion, the extended tanh function, and the exp-function methods translating the nonlinear fractional differential equations (NLFDEs) into ordinary differential equations. In this article, we ascertain the solutions in terms of tanh, sech, sinh, rational function, hyperbolic rational function, exponential function, and their integration with parameters. Advanced and standard solutions can be found by setting definite values of the parameters in the general solutions. Mathematical analysis of the solutions confirms the existence of different soliton forms, namely, kink, single soliton, periodic soliton, singular kink soliton, and some other types of solitons which are shown in three-dimensional plots. The attained solutions may be functional to examine unidirectional propagation of weakly nonlinear acoustic waves, the memory effect of the wall friction through the boundary layer, bubbly liquids, etc. The methods suggested are direct, compatible, and speedy to simulate using algebraic computation schemes, such as Maple, and can be used to verify the accuracy of results.

1. Introduction

The nonlinear fractional evolution equations (NLFEEs) emerge frequently in diverse research field of science and applications of engineering. The fractional derivative has been happening in numerous physical problems, for example, recurrence subordinate damping conduct of materials, motion of an enormous meager plate in a Newtonian fluid, creep and relaxation functions for viscoelastic materials, and $PI^{\lambda}D^{\mu}$ controller for the control of the dynamical system. Fractional-order differential equations describe the phenomena. The fractional-order differential equations are broadly used as generalizations of conventional differential equations with the integral order to explain different intricate phenomena in numerous fields including the diffusion of biological populations, electric circuit, fluid flow, chemical kinematics, control theory, signal processing, optical fiber, plasma physics, solid-state physics, and other areas [1–5]. The concepts of dissipation, dispersion, diffusion, convection, and reaction are closely related to the abovestated phenomena, and nonlinear fractional partial differential equations (NLFPDEs) can be used to evaluate them exactly. Wave shape has an effect on sediment transport and beach morpho dynamics, while wave skewness has an impact on radar altimetry signals, and asymmetry has an impact on ship responses to wave impacts. Traveling wave solutions are a special class of analytical solutions for NLFEEs. Solitary waves are transmitted traveling waves with constant speeds and shapes that achieve asymptotically zero at distant locations. The appearance of solitary waves in nature is rather frequent in plasmas, fluids dynamics, solid-state physics, condensed matter physics, chemical kinematics, optical fibers, electrical circuits, bio-genetics, elastic media, etc. Consequently, it is important to search for the exact traveling wave solutions of NLFPDEs to understand the facts. Therefore, many researchers have been motivated

on finding the exact solutions to nonlinear fractional-order differential equations, and significant progress has been made in analyzing the exact solutions of these types of equations. The major challenges, however, are that there is no unified numerical or analytical approach that can investigate all sorts of nonlinear fractional-order differential equations. Thus, several numerical and theoretical methods for finding solutions for NLFDEs have been established, for example, the differential transformation method [6, 7], the variational iteration method [8–10], the fractional subequation method [11], the Kudryashov [12] method, the homotopy perturbation method [13, 14], the homotopy analysis method [15], the exp-function method [16, 17], the (G'/G)-expansion method and its various modification [18–22], the Chelyshkov polynomial method [23, 24], the multiple exp-function method [25], the finite difference method [26], the finite element method [27], the first integral method [28, 29], the modified simple equation method [30], the reproducing kernel method [31], the two variables $((G'/G), (1/G))$-expansion method [32, 33], and the Picard technique [34].

The time-fractional Burgers' equation is crucial for modeling shallow water waves, weakly nonlinear acoustic waves propagating unidirectionally in gas-filled tubes, and bubbly liquids. Inc [9] studied the approximate and exact solutions to the time-fractional Burgers' equation by the variational iteration method. Bekir and Guner [35] established the exact solution to the mentioned equation by using the (G'/G)-expansion method. Bulut et al. [36] examined the analytical approximate solution to the suggested equation through the modified trial equation method. Recently, Saad and Al-Sharif [37] studied the exact and analytical solutions to this equation. As far as is known, the stated equation has not been investigated through the two variables $(((G'/G), (1/G)))$-expansion technique, exp-function strategy, and expanded tanh function method. Therefore, the aim of this study is to establish further general and some fresh solutions of the abovementioned equation using the suggested methods.

The residual segments of the article is schematized as follows: in Section 2, definition and preliminaries have been introduced; in Section 3, the two variables $((G'/G), (1/G))$-expansion method, the exp-function method, and the extended tanh function method have been described. In Section 4, the exact solutions to the suggested equation have established. In Section 5, physical interpretation and explanation of the extracted solutions are provided. In the lattermost part, the conclusions are given.

2. Definition and Preliminaries

Suppose $f\colon [0,\infty) \longrightarrow \mathbb{R}$ be a function. The α-order conformable derivative of f is interpreted as [38]

$$T_\alpha(f)(t) = \lim_{\varepsilon \longrightarrow 0} \frac{f\left(t + \varepsilon t^{1-\alpha}\right) - f(t)}{\varepsilon}, \tag{1}$$

for every $t > 0$ and $\alpha \in (0,1)$. If f is α-differentiable in some $(0,a)$, $a > 0$, and $\lim_{t \longrightarrow 0^+} f^{(\alpha)}(t)$ exists; then, $f^{(\alpha)}(0) = \lim_{t \longrightarrow 0^+} f^{(\alpha)}(t)$. The following theorems point out few axioms that are satisfied conformable derivatives.

Theorem 1. *Consider $\alpha \in (0,1]$ and let us suppose f and g be α-differentiable at a point $t > 0$. Therefore,*

(i) $T_\alpha(cf + dg) = cT_\alpha(f) + dT_\alpha(g)$, *for all c and $d \in \mathbb{R}$*

(ii) $T_\alpha(t^p) = pt^{p-\alpha}$, *for all $p \in \mathbb{R}$*

(iii) $T_\alpha(c) = 0$, *for all constant function $f(t) = c$*

(iv) $T_\alpha(fg) = fT_\alpha(g) + gT_\alpha(f)$

(v) $T_\alpha(f/g) = ((gT_\alpha(f) - fT_\alpha(g))/g^2)$

(vi) In addition, if f is differentiable, then $T_\alpha(f)(t) = t^{1-\alpha}(df/dt)$

Some more properties including the chain rule, Gronwall's inequality, some integration techniques, Laplace transform, Tailor series expansion, and exponential function with respect to the conformable fractional derivative are explained in [38].

Theorem 2. *Let f be an α-differentiable function in conformable differentiable, and suppose that g is also differentiable and defined in the range of f. Then,*

$$T_\alpha(f \circ g)(t) = t^{1-\alpha} g'(t) f_g(t). \tag{2}$$

The Caputo derivative is another important fractional derivative concept developed by Michele Caputo [39]. This definition is particularly useful for finding numerical solutions. The definition of Riesz [40, 41] in relation to the fractional derivative, on the contrary, is also important for extracting numerical solutions. The two concepts are not discussed in depth here since the aim of this article is to establish exact solutions.

3. Outline of the Methods

In this part, we summarize the principal parts of the suggested methods to analyze exact traveling wave solutions to the NLFEEs. Assume the general NLFEE is of the form

$$P\left(u, D_t^\alpha u, D_x^\beta u, D_t^\alpha D_t^\alpha u, D_t^\alpha D_x^\beta u, D_x^\beta D_x^\beta, \ \ldots\right) = 0, \quad 0 < \alpha \le 1 \text{ and } 0 < \beta \le 1, \tag{3}$$

where u represents an unknown function, consisting the spatial derivative x and temporal derivative t, and P represents a polynomial of $u(x,t)$ and its derivatives where the highest order of derivatives and nonlinear terms of the highest order are associated. Take into account the wave transformation

$$\xi = k\frac{x^\beta}{\beta} + c\frac{t^\alpha}{\alpha}, \qquad u(x,t) = u(\xi), \tag{4}$$

where c and k are nonzero arbitrary constants.

By means of wave transformation (4), equation (3) can be rewritten as

$$R(u, u', u'', u''', \ldots) = 0, \tag{5}$$

where the superscripts specify the ordinary derivative of u relating to ξ.

3.1. The Two Variables $((G'/G), (1/G))$-Expansion Method.

Step 1: In this subsection, we apply the two variables $((G'/G), (1/G))$-expansion method to acquire the wave solutions of the NLFEEs. Take into account the second order ODEs

$$G''(\xi) + \lambda G(\xi) = \mu, \tag{6}$$

along with the following relations

$$\phi = \frac{G'}{G}, \qquad \psi = \frac{1}{G}. \tag{7}$$

In this manner, it gives

$$\phi' = -\phi^2 + \mu\psi - \lambda, \qquad \psi' = -\phi\psi. \tag{8}$$

The solutions to equation (6) depend on λ as $\lambda < 0, \lambda > 0$, and $\lambda = 0$.

Case 1: when $\lambda < 0$, the general solution to equation (6) is

$$G(\xi) = A_1 \sinh(\sqrt{-\lambda}\,\xi) + A_2 \cosh(\sqrt{-\lambda}\,\xi) + \frac{\mu}{\lambda}. \tag{9}$$

In view of that, we obtain

$$\psi^2 = \frac{-\lambda}{\lambda^2\sigma + \mu^2}\left(\phi^2 - 2\mu\psi + \lambda\right), \tag{10}$$

where $\sigma = A_1^2 - A_2^2$.

Case 2: if $\lambda > 0$, the solution to (6) is given as follows:

$$G(\xi) = A_1 \sin(\sqrt{\lambda}\,\xi) + A_2 \cos(\sqrt{\lambda}\,\xi) + \frac{\mu}{\lambda}. \tag{11}$$

Therefore, we obtain

$$\psi^2 = \frac{\lambda}{\lambda^2\sigma - \mu^2}\left(\phi^2 - 2\mu\psi + \lambda\right), \tag{12}$$

where $\sigma = A_1^2 + A_2^2$.

Case 3: when $\lambda = 0$, the solution of equation (6) is

$$G(\xi) = \frac{\mu}{2}\xi^2 + A_1\xi + A_2. \tag{13}$$

Therefore, we find

$$\psi^2 = \frac{1}{A_1^2 - 2\mu A_2}\left(\phi^2 - 2\mu\psi\right). \tag{14}$$

where A_1 and A_2 are arbitrary constants.

Step 2: in agreement with two variables $((G'/G), (1/G))$-expansion scheme, the solution of (5) is presented as a polynomial of ϕ and ψ of the form

$$u(\xi) = \sum_{i=0}^{N} a_i \phi^i + \sum_{i=1}^{N} b_i \phi^{i-1}\psi, \tag{15}$$

where a_i and b_i are arbitrary constants to be determined later.

Step 3: after balancing the maximum order of derivatives and nonlinear terms, which appear in equation (5), it can be fixed the positive integer N.

Step 4: setting (15) into (5) along with (8) and (10), this modifies to a polynomial in ϕ and ψ having the degree of ψ as one or less than one. If we compare the polynomial of similar terms to zero, then it will give a set of mathematical equations which can be unraveled by computational software and finally yield the values of a_i, b_i, μ, A_1, A_2, and λ, where $\lambda < 0$; this condition provides solutions of the hyperbolic function.

Step 5: in a similar manner, we can examine the values of a_i, b_i, μ, A_1, A_2, and λ, and trigonometric and rational solutions can be established separately for the case of $\lambda > 0$ and $\lambda = 0$.

3.2. The Exp-Function Method.

Within this section, the key components of the exp-function method are described for searching the traveling wave solution to the NLFDEs.

Step 1: the arrangement is to be communicated in the shape as indicated by the exp-function method:

$$u(\xi) = \frac{\sum_{n=-c}^{d} p_n \exp(n\xi)}{\sum_{m=-p}^{q} q_m \exp(m\xi)}, \tag{16}$$

where c, d, p, and q are unknown positive integers, which can be evaluated later, and p_n and q_m are unidentified constants.

Step 2: the balancing principle between the highest-order linear and nonlinear terms presented in (5) and substituting (16) into (5) yield c and p, and the balance of lowest-order linear and nonlinear terms yields the values of d and q.

Step 3: introducing (16) into (5) and setting the coefficient of $\exp(n\xi)$ to zero provides an arrangement of set of mathematical equations for p_n, q_m, c, and k. Then, unraveling the set with the aid of computer software, such as Maple, we attain the constants.

Step 4: substituting the values that showed up in step 3 into (16), we ascertain exact solutions to the NLFEEs in (3).

3.3. The Extended Tanh Function Method.

In this section, the suggested extended tanh function method has been interpreted to obtain ample exact solutions to NLFEEs which was

summarized by Wazwaz [42]. The basic concept of this method is to present the solution as a polynomial of hyperbolic functions, and then, solving the coefficient of $\tanh(\mu\xi)$ implies solving a system of algebraic equations. The core steps of the extended tanh function method for finding exact analytic solutions of nonlinear PDEs of the fractional order are as follows:

Step 1: we consider the wave solution as follows:

$$u(\xi) = \sum_{i=0}^{N} a_i Y^i + \sum_{i=1}^{n} b_i Y^{-i}, \tag{17}$$

wherein

$$Y = \tanh(\mu\xi), \tag{18}$$

where μ is any arbitrary constant.

Step 2: taking uniform balance between the maximum order nonlinear term and the derivative of the maximum order appearing in equation (5) to determine the positive constant N.

Step 3: substitute solution (17) together with (18) into equation (5) with the value of n acquired in step 2, which yields the polynomials in Y. A set of algebraic equations for a_i's and b_i's are found by setting each the coefficient of the resulted polynomials to zero. With the help of symbolic computational software, namely, Maple, this set of equations for a_i and b_i can be solved.

Step 4: inserting the values that appeared in step 3 into equation (17) along with equation (18), we construct closed-form traveling wave solutions of nonlinear evolution equation (3).

4. Analysis of the Solutions

Here, we search further comprehensive exact analytic wave solutions for the stated time-fractional Burgers' equation by means of the suggested methods. Let us consider the time-fractional Burgers' equation as follows:

$$D_t^{\alpha} + puu_x - vu_{xx} = 0; \quad t > 0 \text{ and } 0 < \alpha \le 1, \tag{19}$$

where p and v are arbitrary constants. The physical processes of unidirectional propagation of weakly nonlinear acoustic waves through a gas-filled pipe are described by the time-fractional Burgers' equation. The fractional derivative results are obtained from the memory effect of the wall friction through the boundary layer. The similar formation can be found in several systems, namely, waves in bubbly liquids and shallow water waves. For equation (19), we recommend the subsequent wave transformation:

$$\xi = k\frac{x^{\alpha}}{\alpha} - c\frac{t^{\alpha}}{\alpha}, \qquad u(x,t) = u(\xi), \tag{20}$$

where c be the velocity of the traveling wave. For wave transformation (20), time-fractional Burgers' equation (19) reduced to the ensuing integral order differential equation:

$$-cu' + kpuu' - k^2 vu'' = 0. \tag{21}$$

Integrating equation (21) with zero constant, we obtain

$$-cu + \frac{kpu^2}{2} - k^2 vu' = 0. \tag{22}$$

4.1. Solutions through Two Variables $((G'/G), (1/G))$*-Expansion Method.* Considering the homogeneous balance of the highest-order nonlinear term and highest-order derivative showing up in equation (22), the arrangements of equation (15) accept the shape

$$u(\xi) = a_0 + a_1\phi(\xi) + b_1\psi(\xi), \tag{23}$$

where a_0, a_1, and b_1 are constants to be determined.

Case 1: for $\lambda < 0$, embedding solution (23) into (22) along with equations (8) and (10) yields a set of algebraic equations, and by explaining these equations by computer algebra such as Maple, we achieve the following results:

$$\begin{aligned} a_0 &= \pm \lambda b_1 \sqrt{\frac{1}{\lambda^2\sigma + \mu^2}}, \\ a_1 &= \pm b_1 \sqrt{\frac{\lambda}{-\lambda^2\sigma - \mu^2}}, \\ c &= \pm \frac{p^2\lambda b_1^2\sqrt{-\lambda}}{v\left(\lambda^2\sigma + \mu^2\right)}, \\ k &= \pm \frac{b_1 p\sqrt{-\lambda}}{v\sqrt{\left(\lambda^2\sigma + \mu^2\right)}}. \end{aligned} \tag{24}$$

Inserting the top values into solution (23), we find the solution to equation (19) in the form

$$\begin{aligned} u_{1_1}(x,t) = {} & \pm \lambda b_1 \sqrt{\frac{1}{\lambda^2\sigma + \mu^2}} \pm b_1 \sqrt{\frac{\lambda}{-\lambda^2\sigma - \mu^2}} \times \frac{\sqrt{-\lambda}\left(A_1\cosh\left(\sqrt{-\lambda}\,\xi\right) + A_2\sinh\left(\sqrt{-\lambda}\,\xi\right)\right)}{A_1\sinh\left(\sqrt{-\lambda}\,\xi\right) + A_2\cosh\left(\sqrt{-\lambda}\,\xi\right) + (\mu/\lambda)} \\ & \pm b_1 \times \frac{1}{A_1\sinh\left(\sqrt{-\lambda}\,\xi\right) + A_2\cosh\left(\sqrt{-\lambda}\,\xi\right) + (\mu/\lambda)}, \end{aligned} \tag{25}$$

where $\sigma = A_1^2 - A_2^2$ and $\xi = \pm\left((b_1 p\sqrt{-\lambda})/(\nu\sqrt{(\lambda^2\sigma+\mu^2)})\right)(x^\alpha/\alpha) \mp \left((p^2\lambda b_1^2\sqrt{-\lambda})/(\nu(\lambda^2\sigma+\mu^2))\right)(t^\alpha/\alpha)$.

Since A_1 and A_2 are basic constants, one might have picked self-assertively their values. If we take $\mu = 0$ and $(A_1 = 0, A_2 \neq 0)$ or $(A_1 \neq 0, A_2 = 0)$ in (25), we have

$$u_{1_2}(x,t) = \pm\frac{b_1}{\sqrt{\sigma}} \pm \frac{b_1}{\sqrt{-\lambda\sigma}}\tanh(\sqrt{-\lambda}\,\xi) + b_1\,\mathrm{sech}(\sqrt{-\lambda}\,\xi), \tag{26}$$

$$u_{1_3}(x,t) = \pm\frac{b_1}{\sqrt{\sigma}} \pm \frac{b_1}{\sqrt{-\lambda\sigma}}\coth(\sqrt{-\lambda}\,\xi) + b_1\,\mathrm{cosech}(\sqrt{-\lambda}\,\xi), \tag{27}$$

where $\xi = \pm\left((b_1 p\sqrt{-\lambda})/(\nu\sqrt{(\lambda^2\sigma+\mu^2)})\right)(x^\alpha/\alpha) \mp \left((p^2\lambda b_1^2\sqrt{-\lambda})/(\nu(\lambda^2\sigma+\mu^2))\right)(t^\alpha/\alpha)$.

Case 2: in a comparative way, when $\lambda > 0$, substituting (23) into (22) together with (8) and (12) yields an arrangement of algebraic equations for a_0, a_1, b_1, and ω, and we acquire the following results by working out these equations:

$$\begin{aligned} a_0 &= \pm\lambda b_1\sqrt{\frac{1}{-\lambda^2\sigma+\mu^2}},\\ a_1 &= \pm b_1\sqrt{\frac{\lambda}{\lambda^2\sigma-\mu^2}},\\ c &= \pm\frac{p^2\lambda b_1^2\sqrt{-\lambda}}{\nu\left(-\lambda^2\sigma+\mu^2\right)},\\ k &= \pm\frac{b_1 p\sqrt{-\lambda}}{\nu\sqrt{\left(-\lambda^2\sigma+\mu^2\right)}}. \end{aligned} \tag{28}$$

The substitution of these results into solution (23) possesses the following expression for the general solution of equation (19):

$$u_{1_4}(x,t) = \pm\lambda b_1\sqrt{\frac{1}{-\lambda^2\sigma+\mu^2}} \pm b_1\sqrt{\frac{\lambda}{\lambda^2\sigma-\mu^2}} \times \frac{\sqrt{\lambda}\left(A_1\cos(\sqrt{\lambda}\,\xi) + A_2\sin(\sqrt{\lambda}\,\xi)\right)}{A_1\sin(\sqrt{\lambda}\,\xi) + A_2\cos(\sqrt{\lambda}\,\xi) + (\mu/\lambda)} \pm b_1 \times \frac{1}{A_1\sin(\sqrt{\lambda}\,\xi) + A_2\cos(\sqrt{\lambda}\,\xi) + (\mu/\lambda)}, \tag{29}$$

where $\sigma = A_1^2 + A_2^2$ and $\xi = \pm\left((b_1 p\sqrt{-\lambda})/(\nu\sqrt{(-\lambda^2\sigma+\mu^2)})\right)(x^\alpha/\alpha) \mp \left((p^2\lambda b_1^2\sqrt{-\lambda})/(\nu(-\lambda^2\sigma+\mu^2))\right)(t^\alpha/\alpha)$.

If the unknown parameters are assigned as $\mu = 0$ and $A_1 = 0$ and $A_2 \neq 0$ or $A_1 \neq 0$ and $A_2 = 0$ in solution (29), it provides the next solitary wave solution:

$$u_{1_5}(x,t) = \pm\frac{b_1}{\sqrt{-\sigma}} \pm \frac{b_1}{\sqrt{\lambda\sigma}} \times \tan(\sqrt{\lambda}\,\xi) + b_1 \times \sec(\sqrt{\lambda}\,\xi), \tag{30}$$

$$u_{1_6}(x,t) = \pm\frac{b_1}{\sqrt{-\sigma}} \pm \frac{b_1}{\sqrt{\lambda\sigma}} \times \cot(\sqrt{\lambda}\,\xi) + b_1 \times \mathrm{cosec}(\sqrt{\lambda}\,\xi), \tag{31}$$

where $\xi = \pm\left((b_1 p\sqrt{-\lambda})/(\nu\sqrt{(-\lambda^2\sigma+\mu^2)})\right)(x^\alpha/\alpha) \mp \left((p^2\lambda b_1^2\sqrt{-\lambda})/(\nu(-\lambda^2\sigma+\mu^2))\right)(t^\alpha/\alpha)$.

Case 3: in the parallel algorithm when $\lambda = 0$, using equations (22) and (21) along with (8) and (14), we achieve a set of mathematical equations whose solutions are

$$\begin{aligned} a_0 &= 0,\\ a_1 &= \pm\frac{b_1}{\sqrt{A_1^2 - 2\mu A_2}},\\ b_1 &= b_1,\\ c &= c,\\ k &= \pm\frac{pb_1}{\nu}\sqrt{\frac{1}{A_1^2 - 2\mu A_2}}. \end{aligned} \tag{32}$$

Making use of these values into solution (23) produces the solution to equation (19) as

$$u_{1_7}(x,t) = \pm\frac{b_1}{\sqrt{A_1^2 - 2\mu A_2}} \times \frac{\mu\xi + A_1}{(\mu/2)\xi^2 + A_1\xi + A_2} + \frac{b_1}{(\mu/2)\xi^2 + A_1\xi + A_2}, \tag{33}$$

where $\xi = \pm\,(pb_1/\nu)\sqrt{(1/(A_1^2 - 2\mu A_2))}\,(x^\alpha/\alpha) - c\,(t^\alpha/\alpha)$.

It is substantial to observe that the traveling wave solutions u_{1_1}–u_{1_7} of the studied equation are inclusive and standard. The attained solutions have not been noted in the earlier study. These solutions are convenient to designate the physical processes of unidirectional propagation of weakly nonlinear acoustic waves via a gas-filled tube, shallow-water waves, and waves in bubbly liquids.

4.2. Solution by the Exp-Function Method. Considering the homogeneous balance, the solution of equation (16) takes the form

$$u(\xi) = \frac{p_1 \exp(\xi) + p_0 + p_{-1}\exp(-\xi)}{q_1 \exp(\xi) + q_0 + q_{-1}\exp(-\xi)}. \tag{34}$$

Substituting equation (34) into (22) leads a equation in $\exp(n\xi)$; here, n represents any whole number. Inserting each coefficient of this equation to zero yields a cluster of mathematical equations (for straightforwardness, here, we have discarded) for $p_i's$, $q_i's$, and ω. These mathematical equations are solved by computer algebra, namely, Maple, which gives the following outcomes:

$$\begin{aligned}
&\text{Set 1: } c = -\frac{1}{4}\frac{p^2p_1^2}{q_1^2\nu}, k = -\frac{1}{2}\frac{pp_1}{q_1\nu}, p_{-1} = 0, p_0 = 0, p_1 = p_1, q_{-1} = 0, q_0 = q_0, \quad \text{and } q_1 = q_1,\\
&\text{Set 2: } c = \frac{1}{4}\frac{p^2p_0^2}{q_0^2\nu}, k = \frac{1}{2}\frac{pp_0}{q_0\nu}, p_{-1} = 0, p_0 = p_0, p_1 = 0, q_{-1} = 0, q_0 = q_0, \quad \text{and } q_1 = q_1,\\
&\text{Set 3: } c = c, k = \frac{2cq_1}{pp_1}, p_{-1} = 0, p_0 = p_0, p_1 = p_1, q_{-1} = 0, q_0 = \frac{p_0q_1}{p_1}, \quad \text{and } q_1 = q_1,\\
&\text{Set 4: } c = -\frac{1}{4}\frac{p^2p_1^2}{q_1^2\nu}, k = -\frac{1}{2}\frac{pp_1}{q_1\nu}, p_{-1} = 0, p_0 = p_0, p_1 = p_1, q_{-1} = q_{-1}, q_0 = \frac{p_1^2q_{-1} + q_1p_0^2}{p_0p_1}, \quad \text{and } q_1 = q_1,\\
&\text{Set 5: } c = \frac{1}{8}\frac{p^2p_{-1}^2}{q_{-1}^2\nu}, k = \frac{1}{4}\frac{pp_{-1}}{q_{-1}\nu}, p_{-1} = p_{-1}, p_0 = 0, p_1 = 0, q_{-1} = q_{-1}, q_0 = 0, \quad \text{and } q_1 = q_1,\\
&\text{Set 6: } c = c, k = \frac{2cq_{-1}}{pp_{-1}}, p_{-1} = p_{-1}, p_0 = p_0, p_1 = 0, q_{-1} = q_{-1}, q_0 = \frac{p_0q_{-1}}{p_{-1}}, \quad \text{and } q_1 = 0,\\
&\text{Set 7: } c = -\frac{1}{4}\frac{p^2p_{-1}^2}{q_{-1}^2\nu}, k = \frac{1}{2}\frac{pp_{-1}}{q_{-1}\nu}, p_{-1} = p_{-1}, p_0 = p_0, p_1 = 0, q_{-1} = q_{-1}, q_0 = \frac{p_{-1}^2q_1 + q_{-1}p_0^2}{p_0p_{-1}}, \quad \text{and } q_1 = q_1,\\
&\text{Set 8: } c = c, k = \frac{2cq_0}{pp_0}, p_{-1} = p_{-1}, p_0 = p_0, p_1 = p_1, q_{-1} = \frac{p_{-1}q_0}{p_0}, q_0 = q_0, \quad \text{and } q_1 = \frac{p_1q_0}{p_0},\\
&\text{Set 9: } c = c, k = \frac{2cq_1}{pp_{-1}}, p_{-1} = p_{-1}, p_0 = 0, p_1 = p_1, q_{-1} = q_{-1}, q_0 = 0, \quad \text{and } q_1 = \frac{p_1q_{-1}}{p_{-1}}.
\end{aligned} \tag{35}$$

From the point of view of the above results, we achieve the following generalized solitary wave solutions:

$$u_{2_1}(x,t) = \frac{p_1 \exp\left[(-(1/2)((pp_1)/(q_1\nu))(x^\alpha/\alpha) + (1/4)\left(\left(p^2p_1^2\right)/\left(q_1^2\nu\right)\right)(t^\alpha/\alpha))\right]}{q_0 + q_1 \exp\left[(-(1/2)((pp_1)/(q_1\nu))(x^\alpha/\alpha) + (1/4)\left(\left(p^2p_1^2\right)/\left(q_1^2\nu\right)\right)(t^\alpha/\alpha))\right]}, \tag{36}$$

$$u_{2_2}(x.t) = \frac{p_0}{q_0 + q_1 \exp\left[((1/2)((pp_0)/(q_0\nu))(x^\alpha/\alpha) + (1/4)\left(\left(p^2p_0^2\right)/\left(q_0^2\nu\right)\right)(t^\alpha/\alpha))\right]}, \tag{37}$$

$$u_{2_3}(x,t) = \frac{p_0 + p_1 \exp\left[((2cq_1/pp_1)(x^\alpha/\alpha) - c(t^\alpha/\alpha))\right]}{((p_0q_1)/p_1) + q_1 \exp\left[((2cq_1/pp_1)(x^\alpha/\alpha) - c(t^\alpha/\alpha))\right]}, \tag{38}$$

$$u_{2_4}(x,t)=\frac{p_0+p_1\exp\left[(-1/2)\left((pp_1)/(q_1\nu)\right)(x^\alpha/\alpha)+(1/4)\left(\left(p^2p_1^2\right)/\left(q_1^2\nu\right)\right)(t^\alpha/\alpha)\right)\right]}{q_1\exp\left[(-1/2)\left((pp_1)/(q_1\nu)\right)(x^\alpha/\alpha)+(1/4)\left(\left(p^2p_1^2\right)/\left(q_1^2\nu\right)\right)(t^\alpha/\alpha)\right)\right]+\left(\left(p_1^2q_{-1}+q_1p_0^2\right)/(p_0p_1)\right)+q_{-1}\exp\left[-\left(-(1/2)\left((pp_1)/(q_1\nu)\right)(x^\alpha/\alpha)+(1/4)\left(\left(p^2p_1^2\right)/\left(q_1^2\nu\right)\right)(t^\alpha/\alpha)\right)\right]},\tag{39}$$

$$u_{2_5}(x,t)=\frac{p_{-1}\exp\left[(-1/4)\left((pp_{-1})/(q_{-1}\nu)\right)(x^\alpha/\alpha)-(1/8)\left(\left(p^2p_{-1}^2\right)/\left(q_{-1}^2\nu\right)\right)(t^\alpha/\alpha)\right)\right]}{q_1\exp\left[((1/4)\left((pp_{-1})/(q_{-1}\nu)\right)(x^\alpha/\alpha)-(1/8)\left(\left(p^2p_{-1}^2\right)/\left(q_{-1}^2\nu\right)\right)(t^\alpha/\alpha)\right)\right]+q_{-1}\exp\left[-\left((1/4)\left((pp_{-1})/(q_{-1}\nu)\right)(x^\alpha/\alpha)-(1/8)\left(\left(p^2p_{-1}^2\right)/\left(q_{-1}^2\nu\right)\right)(t^\alpha/\alpha)\right)\right]},\tag{40}$$

$$u_{2_6}(x,t)=\frac{p_0+p_{-1}\exp\left[-\left(\left((2cq_{-1})/pp_{-1}\right)(x^\alpha/\alpha)-c\,(t^\alpha/\alpha)\right)\right]}{\left((p_0q_{-1})/p_{-1}\right)+q_{-1}\exp\left[-\left(\left((2cq_{-1})/pp_{-1}\right)(x^\alpha/\alpha)-c\,(t^\alpha/\alpha)\right)\right]},\tag{41}$$

$$u_{2_7}(x,t)=\frac{p_0+p_{-1}\exp\left[(-1/2)\left((pp_{-1})/(q_{-1}\nu)\right)(x^\alpha/\alpha)+(1/4)\left(\left(p^2p_{-1}^2\right)/\left(q_{-1}^2\nu\right)\right)(t^\alpha/\alpha)\right)\right]}{q_1\exp\left[(-1/2)\left((pp_{-1})/(q_{-1}\nu)\right)(x^\alpha/\alpha)+(1/4)\left(\left(p^2p_{-1}^2\right)/\left(q_{-1}^2\nu\right)\right)(t^\alpha/\alpha)\right)\right]+\left(\left(p_{-1}^2q_1+q_{-1}p_0^2\right)/(p_0p_1)\right)+q_{-1}\exp\left[-\left(-(1/2)\left((pp_{-1})/(q_{-1}\nu)\right)(x^\alpha/\alpha)+(1/4)\left(\left(p^2p_{-1}^2\right)/\left(q_{-1}^2\nu\right)\right)(t^\alpha/\alpha)\right)\right]},\tag{42}$$

$$u_{2_8}(x,t)=\frac{p_1\exp\left[\left(\left((2cq_0)/pp_0\right)(x^\alpha/\alpha)-c\,(t^\alpha/\alpha)\right)\right]+p_0+p_{-1}\exp\left[-\left(\left((2cq_0)/pp_0\right)(x^\alpha/\alpha)-c\,(t^\alpha/\alpha)\right)\right]}{\left((p_0q_0)/p_0\right)\exp\left[\left(\left((2cq_0)/pp_0\right)(x^\alpha/\alpha)-c\,(t^\alpha/\alpha)\right)\right]+\ q_0+q_{-1}\exp\left[-\left(\left((2cq_0)/pp_0\right)(x^\alpha/\alpha)-c\,(t^\alpha/\alpha)\right)\right]},\tag{43}$$

$$u_{2_9}(x,t)=\frac{p_1\exp\left[\left(\left((2cq_1)/pp_{-1}\right)(x^\alpha/\alpha)-c\,(t^\alpha/\alpha)\right)\right]+p_{-1}\exp\left[-\left(\left((2cq_1)/pp_{-1}\right)(x^\alpha/\alpha)-c\,(t^\alpha/\alpha)\right)\right]}{\left((p_1q_{-1})/p_{-1}\right)\exp\left[\left(\left((2cq_1)/pp_{-1}\right)(x^\alpha/\alpha)-c\,(t^\alpha/\alpha)\right)\right]+\left((p_{-1}q_0)/p_0\right)\exp\left[-\left(\left((2cq_1)/pp_{-1}\right)(x^\alpha/\alpha)-c\,(t^\alpha/\alpha)\right)\right]}.\tag{44}$$

In particular, if $p_1 = q_{-1} = p_{-1}$ and $p_0 = q_0 = 1$, solution (44) is simplified and offers the kink type solution of the form

$$u_{2_{10}}(x,t)=\tanh\left(\frac{2cq_1}{pp_{-1}}\frac{x^\alpha}{\alpha}-c\,\frac{t^\alpha}{\alpha}\right).\tag{45}$$

The choice of $p_1 = -q_{-1} = -p_{-1}$ and $p_0 = q_0 = 1$ in (44) gives the singular kink solution:

$$u_{2_{11}}(x,t)=\coth\left(\frac{2cq_1}{pp_{-1}}\frac{x^\alpha}{\alpha}-c\,\frac{t^\alpha}{\alpha}\right).\tag{46}$$

It is significant to refer that the traveling wave solutions $u_{2_1} - u_{2_{11}}$ of the considered Burgers' equation are fresh and standard and were not established in the earlier investigations. It is deduced that physical systems should be assigned of unidirectional propagation of weakly nonlinear acoustic waves through a gas-filled tunnel and waves in bubbly fluids.

4.3. Solution Using the Extended Tanh Function Method. The homogeneous symmetry allows solution equation (17) as

$$u(\varepsilon)=a_0+a_1Y+b_1Y^{-1}.\tag{47}$$

Substituting (47) into (22) along with (18) makes the left hand side as a polynomial in Y. Setting each coefficient of this polynomial to zero, resulting a set of algebraic equations (for simplicity, we have omitted them to exhibition) for a_0, a_1, b_1, k, and c. Computing the determined set of equations with the assistance of computer algebra, such as Maple, yields the succeeding results:

$$\begin{aligned}
&\text{Set 1: } c=\ -2k^2\nu\mu, k=k, a_0=-\frac{2k\nu\mu}{p}, a_1=0, \quad \text{and } b_1=-\frac{2k\nu\mu}{p},\\
&\text{Set 2: } c=\ 2k^2\nu\mu, k=k, a_0=\frac{2k\nu\mu}{p}, a_1=0, \quad \text{and } b_1=-\frac{2k\nu\mu}{p},\\
&\text{Set 3: } c=-2k^2\nu\mu, k=k, a_0=-\frac{2k\nu\mu}{p}, a_1=-\frac{2k\nu\mu}{p}, \quad \text{and } b_1=0,\\
&\text{Set 4: } c=-4k^2\nu\mu, k=k, a_0=-\frac{4k\nu\mu}{p}, a_1=-\frac{2k\nu\mu}{p}, \quad \text{and } b_1=-\frac{2k\nu\mu}{p},\\
&\text{Set 5: } c=2k^2\nu\mu, k=k, a_0=\frac{2k\nu\mu}{p}, a_1=-\frac{2k\nu\mu}{p}, \quad \text{and } b_1=0,\\
&\text{Set 6: } c=4k^2\nu\mu, k=k, a_0=\frac{4k\nu\mu}{p}, a_1=-\frac{2k\nu\mu}{p}, \quad \text{and } b_1=-\frac{2k\nu\mu}{p}.
\end{aligned}\tag{48}$$

Using the values of the parameters assembled above into solution (47) together with (18), we achieve the following solitary wave solutions:

$$u_{3_1}(x,t) = -\frac{2k\nu\mu}{p} - \frac{2k\nu\mu}{p}\coth\left(\mu\left(k\frac{x^\alpha}{\alpha} + 2k^2\nu\mu\frac{t^\alpha}{\alpha}\right)\right), \tag{49}$$

$$u_{3_2}(x,t) = \frac{2k\nu\mu}{p} - \frac{2k\nu\mu}{p}\coth\left(\mu\left(k\frac{x^\alpha}{\alpha} - 2k^2\nu\mu\frac{t^\alpha}{\alpha}\right)\right), \tag{50}$$

$$u_{3_3}(x,t) = -\frac{2k\nu\mu}{p} - \frac{2k\nu\mu}{p}\tanh\left(\mu\left(k\frac{x^\alpha}{\alpha} + 2k^2\nu\mu\frac{t^\alpha}{\alpha}\right)\right), \tag{51}$$

$$u_{3_4}(x,t) = -\frac{4k\nu\mu}{p} - \frac{2k\nu\mu}{p}\tanh\left(\mu\left(k\frac{x^\alpha}{\alpha} + 4k^2\nu\mu\frac{t^\alpha}{\alpha}\right)\right) - \frac{2k\nu\mu}{p}\coth\left(\mu\left(k\frac{x^\alpha}{\alpha} + 4k^2\nu\mu\frac{t^\alpha}{\alpha}\right)\right), \tag{52}$$

$$u_{3_5}(x,t) = \frac{2k\nu\mu}{p} - \frac{2k\nu\mu}{p}\tanh\left(\mu\left(k\frac{x^\alpha}{\alpha} - 2k^2\nu\mu\frac{t^\alpha}{\alpha}\right)\right), \tag{53}$$

$$u_{3_6}(x,t) = \frac{4k\nu\mu}{p} - \frac{2k\nu\mu}{p}\tanh\left(\mu\left(k\frac{x^\alpha}{\alpha}4k^2\nu\mu\frac{t^\alpha}{\alpha}\right)\right) - \frac{2k\nu\mu}{p}\coth\left(\mu\left(k\frac{x^\alpha}{\alpha} - 4k^2\nu\mu\frac{t^\alpha}{\alpha}\right)\right). \tag{54}$$

The solutions established above by the extended tanh approach are advanced and progressive. These might be convenient to describe the relativistic electron and the physical processes of unidirectional propagation of weakly nonlinear acoustic waves via a gas-filled tube.

5. Physical Interpretation and Explanation

In this section, we mainly discuss about the physical interpretation of the determined solitary wave solutions, including kink, singular solitons, singular kink, and periodic wave of the NLFEEs. A graph is an effective approach for explaining mathematical concepts. It is capable of describing any circumstances in a straightforward and understandable manner. This segment explains the incidents by portraying 3D plots of some of the solutions that are found. The portraits are precedents of the solutions shown in Figures 1–6 using the computational software, namely, Mathematica.

The results of the time-fractional Burgers' equation include the kink soliton, singular soliton, periodic soliton, and some general solitons which are displayed in Figures 1–6. Figure 1 is the kink shape soliton of solution (26) with the values of the parameters $\lambda = -1$, $\nu = 1$, $p = 1$, $b_1 = 1$, $\sigma = 2$, and $\alpha = 1/2$ within the interval $0 \le x \le 50$ and $0 \le t \le 50$. The kink soliton is a soliton which rises or descends from one asymptotic state to another as $\xi \longrightarrow \infty$. Solution (51) represents the shape of the plane soliton characterized in Figure 2 for the values of parameters $k = 1$, $p = 1$, $\nu = 1$, $\mu = 1$, and $\alpha = (1/2)$ within the interval $-10 \le x \le 10$ and $0 \le t \le 700$. Solution (31) represents the periodic wave solutions, plotted for $\lambda = 1$, $\nu = 1$, $p = 1$, $b_1 = 1$, $\sigma = 2$, and $\alpha = 1/2$ within the interval $0 \le x$ and $t \le 100$ and labeled in Figure 3. When $c = 1$, $p = 1$, $p_{-1} = 2$, $q_1 = 1$, and $\alpha = (1/2)$, solution (46) represents the singular kink type soliton characterized in Figure 4 within $0 \le x$ and $t \le 10$. On the contrary, for the values of $k = 1$, $p = 1$, $\nu = 1$, $\mu = 1$, and $\alpha = (1/2)$, solution (53) also represents the kink soliton illustrated in Figure 5 within the interval $0 \le x$ and $t \le 10$. Finally, outcome (54) also represents the singular kink soliton for the values of parameters $k = 1$, $p = 1$, $\nu = 1$, $\mu = 1$, and $\alpha = (1/2)$ within the range $0 \le x$ and $t \le 1000$, which is labeled as Figure 6. The other figure of the solutions is analogous to the displayed figure; thus, for convenience, these are omitted here.

6. Conclusion

In this article, using three reliable approaches referring conformable the fractional derivative, we have established scores of advanced, further general, and wide-ranging solitary wave solutions to the time-fractional Burgers' equation. The ascertained closed-form solutions of the considered equation include kink, single solitons, periodic solitons, singular kink, and some other kinds of solutions, including some free parameters. The obtained solutions are capable to analyze the phenomena of weakly nonlinear acoustic waves propagating unidirectionally in gas-filled tubes, shallow water waves, and bubbly liquids. The dynamics of solitary waves have been graphically depicted in terms of space and time coordinates which reveal the consistency of the techniques used. The accuracy of the results obtained in this study has been verified using the computational software Maple by placing them back into NLFPDEs and found

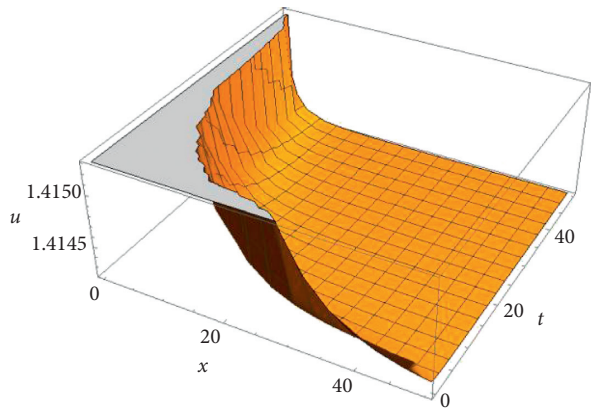

Figure 1: 3D plot of the kink type soliton of (26) sketched within the interval $0 \le x \le 50$ and $0 \le t \le 50$.

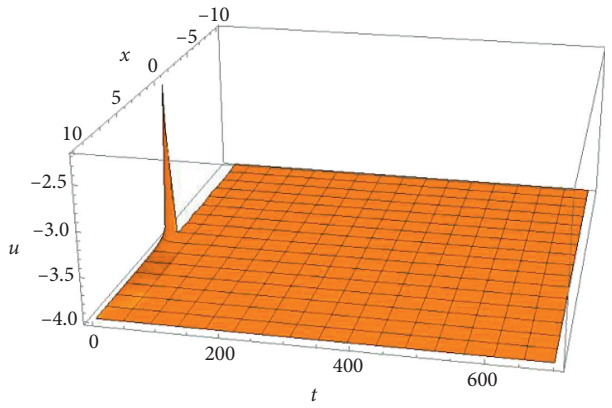

Figure 2: 3D plot of the single soliton solution of (51) sketched within the interval $-10 \le x \le 10$ and $0 \le t \le 700$.

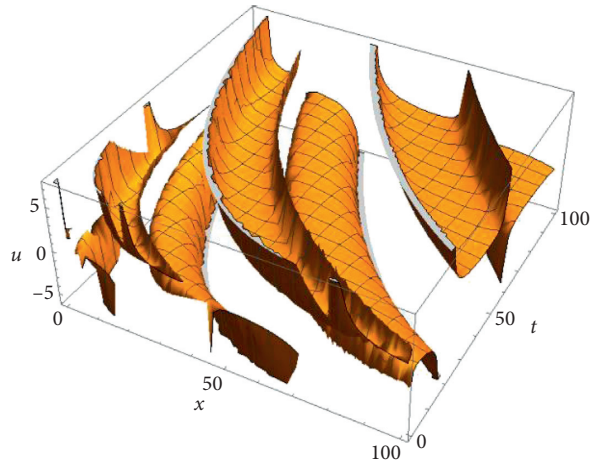

Figure 3: 3D plot of the periodic wave solution of (31) sketched within the interval $0 \le x \le 100$ and $0 \le t \le 100$.

correct. This study shows that all the methods implemented are reliable, effective, functional, and capable of uncovering nonlinear fractional differential equations arising in the field of nonlinear science and engineering. Therefore, we can firmly claim that the implemented methods can be used to

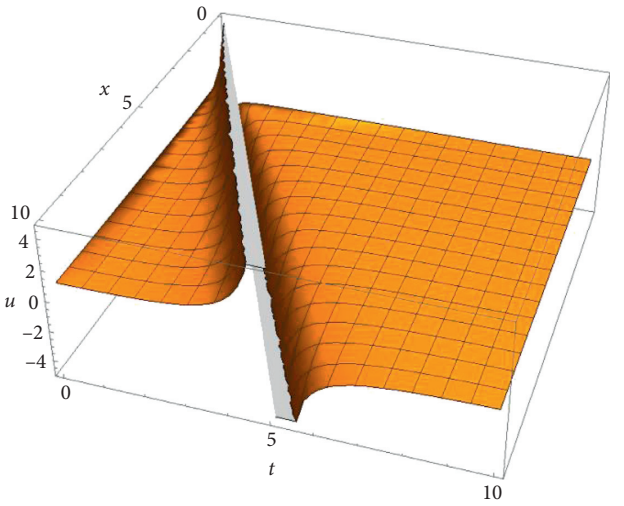

Figure 4: 3D plot of the singular kink type soliton of (46) sketched within the interval $0 \le x$ and $t \le 10$.

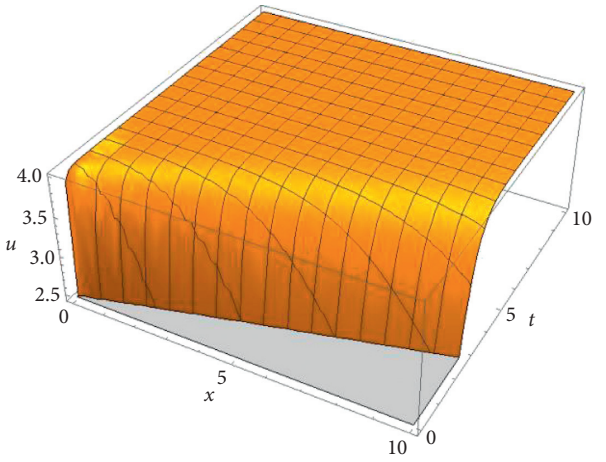

Figure 5: 3D plot of the kink type soliton of (53) sketched within the interval $0 \le x \le 10$ and $0 \le t \le 10$.

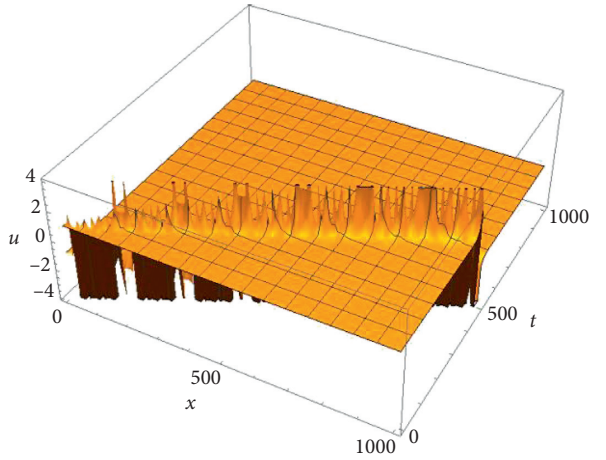

Figure 6: 3D plot of the singular kink type soliton of $0 \le t \le 10$. (54) sketched within the interval $0 \le x \le 1000$ and $0 \le t \le 1000$.

compute exact wave solutions of other nonlinear fractional equations associated with real-world problems, and this is our next contrivance.

Data Availability

No data were used to support this study.

Conflicts of Interest

The authors declare that there are no conflicts of interest regarding the publication of this paper.

References

[1] K. S. Miller and B. Ross, *An Introduction to the Fractional Calculus and Fractional Differential Equations*, Wiley, New York, NY, USA, 1993.

[2] K. B. Oldham and J. Spanier, *The Fractional Calculus*, Academic Press, New York, NY, USA, 1974.

[3] I. Podlubny, *Fractional Differential Equations*, Academic, San Diego, CA, USA, 1999.

[4] R. Hilfer, *Applications of Fractional Calculus in Physics*, World Scientific Publishing, River Edge, NJ, USA, 2000.

[5] K. Diethelm, *The Analysis of Fractional Differential Equations*, Springer-Verlag, Berlin, Germany, 2010.

[6] V. S. Erturk, S. Momani, and Z. Odibat, "Application of generalized differential transform method to multi-order fractional differential equations," *Communications in Nonlinear Science and Numerical Simulation*, vol. 13, no. 8, pp. 1642–1654, 2008.

[7] K.-L. Wang and K.-J. Wang, "A modification of the reduced differential transform method for fractional calculus," *Thermal Science*, vol. 22, no. 4, pp. 1871–1875, 2018.

[8] J. Ji, J. Zhang, and Y. Dong, "The fractional variational iteration method improved with the Adomian series," *Applied Mathematics Letters*, vol. 25, no. 12, pp. 2223–2226, 2012.

[9] M. Inc, "The approximate and exact solutions of the space- and time-fractional Burgers equations with initial conditions by variational iteration method," *Journal of Mathematical Analysis and Applications*, vol. 345, no. 1, pp. 476–484, 2008.

[10] S. Guo and L. Mei, "The fractional variational iteration method using He's polynomials," *Physics Letters A*, vol. 375, no. 3, pp. 309–313, 2011.

[11] S. Guo, L. Mei, Y. Li, and Y. Sun, "The improved fractional sub-equation method and its applications to the space-time fractional differential equations in fluid mechanics," *Physics Letters A*, vol. 376, no. 4, pp. 407–411, 2012.

[12] M. A. Akbar, L. Akinyemi, S. W. Yao et al., "Soliton solutions to the Boussinesq equation through sine-Gordon method and Kudryashov method," *Results Physics*, vol. 25, pp. 1–10, 2021.

[13] K. A. Gepreel, "The homotopy perturbation method applied to the nonlinear fractional Kolmogorov-Petrovskii-Piskunov equations," *Applied Mathematics Letters*, vol. 24, no. 8, pp. 1428–1434, 2011.

[14] P. K. Gupta and M. Singh, "Homotopy perturbation method for fractional Fornberg-Whitham equation," *Computers & Mathematics with Applications*, vol. 61, no. 2, pp. 250–254, 2011.

[15] A. A. M. Arafa, S. Z. Rida, and H. Mohamed, "Homotopy analysis method for solving biological population model," *Communications in Theoretical Physics*, vol. 56, no. 5, pp. 797–800, 2011.

[16] A. Bekir, Ö. Güner, and A. C. Cevikel, "Fractional complex transform and exp-function methods for fractional differential equations," *Abstract and Applied Analysis*, vol. 2013, pp. 1–8, 2013.

[17] M. A. Akbar and N. H. M. Ali, "New solitary and periodic solutions of nonlinear evolution equation by exp-function method," *World Applied Science Journal*, vol. 17, no. 12, pp. 1603–1610, 2012.

[18] M. Wang, X. Li, and J. Zhang, "The ()-expansion method and travelling wave solutions of nonlinear evolution equations in mathematical physics," *Physics Letters A*, vol. 372, no. 4, pp. 417–423, 2008.

[19] F. Batool and G. Akram, "New solitary wave solutions of the time-fractional Cahn-Allen equation via the improved (G'/G)-expansion method," *European Physical Journal - Plus*, vol. 133, no. 5, pp. 1–11, 2018.

[20] M. A. Akbar, N. H. M. Ali, and E. M. E. Zayed, "A generalized and improved (G′/G)-Expansion method for nonlinear evolution equations," *Mathematical Problems in Engineering*, vol. 2012, Article ID 459879, 22 pages, 2012.

[21] M. A. Akbar, N. H. M. Ali, and E. M. E. Zayed, "Abundant exact traveling wave solutions of generalized bretherton equation via improved (G′/G)-Expansion method," *Communications in Theoretical Physics*, vol. 57, no. 2, pp. 173–178, 2012.

[22] M. N. Islam, M. A. Akbar, and B. Spagnolo, "New exact wave solutions to the space-time fractional-coupled Burgers equations and the space-time fractional foam drainage equation," *Cogent Physics*, vol. 5, no. 1, Article ID 1422957, 2018.

[23] M. Hamid, M. Usman, R. U. Haq, and Z. Tian, "A spectral approach to analyze the nonlinear oscillatory fractional order differential equations," *Chaos, Solitons and Fractals*, vol. 146, Article ID 110921, 2021.

[24] M. Hamid, M. Usman, W. Wang, and Z. Tian, "A stable computational approach to analyze semi-relativistic behavior of fractional evolutionary problems," *Numerical Methods for Partial Differential Equations*, pp. 1–15, 2020.

[25] M. Hamid, M. Usman, T. Zubair, R. U. Haq, and A. Shafee, "An efficient analysis for N-soliton, Lump and lump-kink solutions of time-fractional (2+1)-Kadomtsev-Petviashvili equation," *Physica A: Statistical Mechanics and Its Applications*, vol. 528, Article ID 121320, 2019.

[26] M. Usman, M. Hamid, and M. Liu, "Novel operational matrices-based finite difference/spectral algorithm for a class of time-fractional Burger equation in multidimensions," *Chaos, Solitons & Fractals*, vol. 144, Article ID 110701, 2021.

[27] A. R. Seadawy, "The generalized nonlinear higher order of KdV equations from the higher order nonlinear Schrödinger equation and its solutions," *Optik*, vol. 139, pp. 31–43, 2017.

[28] B. Lu, "The first integral method for some time fractional differential equations," *Journal of Mathematical Analysis and Applications*, vol. 395, no. 2, pp. 684–693, 2012.

[29] A. Bekir, O. Guner, and O. Unsal, "The first integral method for exact solutions of nonlinear fractional differential equations," *Journal of Computational and Nonlinear Dynamics*, vol. 10, no. 2, pp. 1–6, 2015.

[30] M. A. Akbar, N. Hj, M. Ali, and A. Wazwaz, "Closed form traveling wave solutions of nonlinear fractional evolution equations through the modified simple equation method," *Thermal Science*, vol. 22, no. 1, pp. 341–352, 2018.

[31] A. Akgül, D. Baleanu, M. Inc, and F. Tchier, "On the solutions of electrohydrodynamic flow with fractional differential equations by reproducing kernel method," *Open Physics*, vol. 14, no. 1, pp. 685–689, 2016.

[32] M. Hafiz Uddin, M. A. Akbar, M. A. Khan, and M. A. Haque, "Close form solutions of the fractional generalized reaction Duffing model and the density dependent fractional diffusion reaction equation," *Applied and Computational Mathematics*, vol. 6, no. 4, pp. 177–184, 2017.

[33] L.-x. Li, E.-q. Li, and M.-l. Wang, "The (G′/G, 1/G)-expansion method and its application to travelling wave solutions of the Zakharov equations," *Applied Mathematics-A Journal of Chinese Universities*, vol. 25, no. 4, pp. 454–462, 2010.

[34] M. Hamid, M. Usman, W. Wang, and Z. Tian, "Hybrid fully spectral linearized scheme for time-fractional evolutionary equations," *Mathematical Methods in the Applied Sciences*, vol. 44, no. 5, pp. 3890–3912, 2021.

[35] A. Bekir and Ö. Güner, "Exact solutions of nonlinear fractional differential equations by (G′/G)-expansion method," *Chinese Physics B*, vol. 22, no. 11, p. 110202, 2013.

[36] H. Bulut, H. M. Baskonus, and Y. Pandir, "The modified trial equation method for fractional wave equation and time fractional generalized burgers equation," *Abstract and Applied Analysis*, vol. 2013, pp. 1–8, 2013.

[37] K. Saad and E. H. Al-Sharif, "Analytical study for time and time-space fractional Burgers' equation," *Advances in Difference Equations*, vol. 2017, no. 1, 2017.

[38] R. Khalil, M. Al Horani, A. Yousef, and M. Sababheh, "A new definition of fractional derivative," *Journal of Computational and Applied Mathematics*, vol. 264, pp. 65–70, 2014.

[39] M. Caputo, "Linear models of dissipation whose Q is almost frequency independent--II," *Geophysical Journal International*, vol. 13, no. 5, pp. 529–539, 1967.

[40] M. Hamid, M. Usman, T. Zubair, R. U. Haq, and W. Wang, "Innovative operational matrices based computational scheme for fractional diffusion problems with the Riesz derivative," *The European Physical Journal Plus*, vol. 134, no. 10, p. 484, 2019.

[41] M. Usman, M. Hamid, R. Ul Haq, and M. Liu, "Linearized novel operational matrices-based scheme for classes of nonlinear time-space fractional unsteady problems in 2D," *Applied Numerical Mathematics*, vol. 162, pp. 351–373, 2021.

[42] A.-M. Wazwaz, "The extended tanh method for abundant solitary wave solutions of nonlinear wave equations," *Applied Mathematics and Computation*, vol. 187, no. 2, pp. 1131–1142, 2007.

Hindawi
Mathematical Problems in Engineering
Volume 2021, Article ID 6645128, 10 pages
https://doi.org/10.1155/2021/6645128

Research Article

Computational Fluid Dynamics Analysis of Flow Patterns, Pressure Drop, and Heat Transfer Coefficient in Staggered and Inline Shell-Tube Heat Exchangers

Shubham Sharma,[1] **Shalab Sharma**,[2] **Mandeep Singh**,[3] **Parampreet Singh**,[4] **Rasmeet Singh**,[5] **Sthitapragyan Maharana**,[6] **Nima Khalilpoor**,[7] **and Alibek Issakhov**[8]

[1]*Department of Mechanical Engineering, IKG Punjab Technical University, Jalandhar-Kapurthala Road, Kapurthala 144603, Punjab, India*
[2]*Department of Mechanical Engineering, DAV University, Jalandhar, Punjab, India*
[3]*School of Mechanical and Mechatronic Engineering, University of Technology Sydney, Sydney, NSW, Australia*
[4]*Department of Mechanical Engineering, Guru Nanak Dev University, Amritsar, India*
[5]*Dr. S.S. Bhatnagar University Institute of Chemical Engineering & Technology, Panjab University, Chandigarh 160 014, India*
[6]*University of Technology Sydney, Sydney, NSW, Australia*
[7]*Department of Energy Engineering, Graduate School of the Environment and Energy, Science and Research Branch, Islamic Azad University, Tehran, Iran*
[8]*Faculty of Mechanics and Mathematics, Department of Mathematical and Computer Modelling, Al-Farabi Kazakh National University, Almaty, Kazakhstan*

Correspondence should be addressed to Shubham Sharma; shubham543sharma@gmail.com and Nima Khalilpoor; nimakhalilpoor@gmail.com

Received 16 November 2020; Revised 28 April 2021; Accepted 18 May 2021; Published 1 June 2021

Academic Editor: Younes Menni

In this numerical study, the heat transfer performance of shell-and-tube heat exchangers (STHXs) has been compared for two different tube arrangements. STHX having 21 and 24 tubes arranged in the inline and staggered grid has been considered for heat transfer analysis. Shell-and-tube heat exchanger with staggered grid arrangement has been observed to provide lesser thermal stratification as compared to the inline arrangement. Further, the study of variation in the mass flow rate of shell-side fluid having constant tube-side flow rate has been conducted for staggered grid structure STHX. The mass flow rate for the shell side has been varied from 0.1 kg/s to 0.5 kg/s, respectively, keeping the tube-side mass flow rate as constant at 0.25 kg/s. The influence of bulk mass-influx transfer rate on heat transfer efficiency, effectiveness, and pressure drop of shell-tube heat exchangers has been analyzed. CFD results were compared with analytical solutions, and it shows a good agreement between them. It has been observed that pressure drop is minimum for the flow rate of 0.1 kg/s, and outlet temperatures at the shell side and tube side have been predicted to be 40.94°C and 63.63°C, respectively.

1. Introduction

Heat transfer analysis of shell-tube heat exchangers is critical owing to their applications in many of the engineering domains like energy production, industrial chemistry, bionics, nanotechnology applications, air conditioning, refrigeration, and food industries [1–3]. It has been reported that around 35% of the total heat exchangers are STHXs [4]. STHX of various sizes is used widely in many industrial applications [3, 5, 6]. The layout model of draft-structure configurations of the shell-and-tube heat exchanger may vary according to the need. Tubular Exchanger Manufacturers Association (TEMA) publishes the standardizing norms or regulations and design configurations regularly.

The Bureau of Indian Standards also suggested a design configuration and standards for shell-and-tube heat exchangers [7]. The shell-side flow inside the STHX is very complicated due to bypass between different flow zones and leakages. The effect of leakages and bypass on the performance of STHX may vary for different shell designs and sizes [8, 9]. Several studies put shell-and-tube heat exchangers in the area of focus due to their vast utilization in the industry, especially in the oil and gas industry [10–12]. Bhuyian et al. [13] reviewed the performance of plate-fin and tubular heat exchangers. Costa and Queiroz [14] investigated the design optimization procedure of the STHX to minimize the thermal surface area. Jozaie et al. [15] investigated the effect of baffle spacing on the heat transfer rate, pressure drop, and cost of the STHX and concluded that the optimal baffle spacing to achieve a higher heat transfer rate, lower pressure drops, and cost would be around 8–12 inches. Li and Kottke [16] studied the variation of baffle spacing on pressure drop and heat transfer coefficient of STHX with staggered tube layout. Rai et al. [17] performed a parametric study on the STHX and monitored that the tube pitch ratio is the main factor for the thermal performance of STHXs. Patel et al. [18] reviewed all the CFD-based studies investigating the heat transfer in the STHXs. Lebele-Alawa and Egwanwo [19] numerically investigated the heat transfer in the heat exchangers and reported high efficiency and accuracy for the presented numerical model. Chalwa and Kadli [20] investigated the effect of vertical baffles on the heat transfer performance and pressure drop of the STHXs. Anand et al. [21] used the Bell-Delaware method to perform an experimental investigation on the performance of STHXs. Yang et al. [22] compared four modeling methods and validated the compared models with experimental results for the rod baffle heat exchangers. Wang et al. [23] studied the effect of installing sealers on the shell side of the STHX. They reported a considerable enhancement in the heat transfer coefficient and energy efficiency of the STHX. Ramezanpour et al. [24] investigated the effect of the staggered tube bundle in a turbulent cross-flow regime to find the optimal layout. Kwak et al. [25] varied the number of tube rows of staggered finned tube bundles and studied their effect on the heat transfer rate and pressure drop. It has been inferred that three rows of tube bundles obtained the least pressure drop among other tested schemes. Beale and Spalding [26] compared the performance of STHX for inline and staggered tube banks under transient flow conditions. Jayawel and Tiwari [27] performed a similar study and compared the performance of inline and staggered tube banks in a 3D model and validated the obtained results with the data available in the literature and reported high accuracy for the presented code.

In the present study, two different types of shell-and-tube heat exchangers, one with an inline tube structure and the other with staggered tube structure, have been studied numerically for heat transfer performance. CFD simulations were performed to analyze the heat transfer efficacy of both heat exchangers. A shell-tube heat exchanger with a staggered grid structure resulted in improvements in heat transfer performance, so it has been considered for further analysis. In the second phase of the study, variation in the bulk mass-transfer flow rate of lateral shell-face fluid has been analyzed, keeping the tube-side flow rate as fixed at 0.25 kg/s. The results and conclusions have been drawn based on the observed outcomes of heat transfer under different bulk mass flow rates varying from 0.1 kg/s to 0.5 kg/s. With the advancement of computer programming and technology, numerical simulation has replaced prototype testing. Nowadays, numerical simulations are being conducted to optimize the efficiency of various devices, tools, and equipment [28–33]. To perform the study, numerical simulation has been done on 3D geometry of STHX using ANSYS FLUENT 15 to know the effect of variation in mass flow rate of shell-tube sided and arrangements of conduit-tube wads or bales in the heat exchangers. CFD results have also been compared with the analytical solutions, and the differences observed have been examined.

2. Modeling Details

In this study, the tubes of shell-tube heat exchangers have been arranged in two different configurations, inline structure and staggered structure having 21 and 24 numbers of tubes, respectively. The shell has dimensions of 94.7 mm in diameter and 810.1 mm in length. Likewise, the outer and inner diameters of the tubes are 12.5 mm and 11 mm, respectively. Water has been considered as drive operating medium fluid for both shell and tube sides. The physical properties of water have been considered as those given in the Fluent database.

2.1. Governing Equations. Steady and incompressible flow conditions have been assumed for the sake of simplifying the numerical analysis. The mass flow rates used in the present study correspond to turbulent flow conditions, and thus turbulence modeling has been done using the two-equation "k-ε" turbulence model. The "k-ε" turbulence model has been used due to its versatility and robustness in handling a wide range of turbulent flows. At the same time, the model is stable and poses lesser convergence difficulties. The governing equations for the flow are given as follows [23–28, 34].

$$\text{Conservation of mass}: \ \nabla.(\rho\vec{V}) = 0. \tag{1}$$

Momentum equation:

X-momentum:

$$\nabla.(\rho u\vec{V}) = -\frac{\partial p}{\partial x} + \frac{\partial \tau_{xx}}{\partial x} + \frac{\partial \tau_{xy}}{\partial y} + \frac{\partial \tau_{xz}}{\partial z}. \tag{2}$$

Y-momentum:

$$\nabla.(\rho v\vec{V}) = -\frac{\partial p}{\partial y} + \frac{\partial \tau_{xy}}{\partial x} + \frac{\partial \tau_{yy}}{\partial y} + \frac{\partial \tau_{zy}}{\partial z} + \rho g. \tag{3}$$

Z-momentum:

$$\nabla.(\rho w\vec{V}) = -\frac{\partial p}{\partial z} + \frac{\partial \tau_{xz}}{\partial x} + \frac{\partial \tau_{yz}}{\partial y} + \frac{\partial \tau_{zz}}{\partial z} \quad (4)$$

Energy equation:

$$\nabla.(\rho e\vec{V}) = -p\nabla.\vec{V} + \nabla.(k\nabla T) + q + \varnothing, \quad (5)$$

where "Ø" is the dissipation function and can be calculated from [23–28, 34]

$$\varnothing = \mu\left[2\left\{\left(\frac{\partial u}{\partial x}\right)^2 + \left(\frac{\partial v}{\partial y}\right)^2 + \left(\frac{\partial w}{\partial z}\right)^2\right\} + \left(\frac{\partial u}{\partial y} + \frac{\partial v}{\partial x}\right)^2 + \left(\frac{\partial u}{\partial z} + \frac{\partial w}{\partial x}\right)^2 + \left(\frac{\partial v}{\partial z} + \frac{\partial w}{\partial y}\right)^2\right] + \lambda(\nabla.\vec{V})^2. \quad (6)$$

2.2. Geometry. The geometry of STHX has been modeled in SolidWorks, and Table 1 describes the dimensions of the heat exchanger. The schematic of STHX with a staggered grid structure and inline grid structure is presented in Figures 1(a) and 1(b). In the present work, the cold fluid has been made to flow in the tubes and hot fluid through the shell. It can also be seen that there are two baffles provided in the shell of the STHX heat exchanger.

2.3. Mesh Generation. The tetrahedral mesh has been generated using Fluent Meshing. The grid generated has been analyzed for aspect ratio and orthogonal quality. The computational grid for STHX has approximately 17,622,730 and 18,233,589 grid elements for the inline and staggered grid. The aforementioned grid density has been obtained after carrying out the necessary grid convergence test.

2.4. Boundary Conditions. The inlet mass flow rate and inlet temperature values have been assigned to the STHX. The shell fluid inlet temperature has been considered as 20°C, and the tube-side fluid inlet temperature is 80°C.

Gauge pressure has been considered to be zero at the outlet. The velocity profile has been assumed to be uniform for simplifying the calculations. The no-slip condition has been considered for all the wall surfaces, and the heat flux value has been assigned as zero for the outer surface of the shell, i.e., the shell-side outer surface has been considered as adiabatic (Table 2).

2.5. Turbulence Model. The mass flow rate used for the flowing stream corresponds to turbulent flow conditions, and hence turbulent effects cannot be ignored. The standard "k-ε" model has been employed for the turbulent transport analysis. The two-equation "k-ε" turbulence model has been used due to its simplicity and faster convergence as compared to other models. In the past literature available on In previous research on CFD studies, the "k-ε" model has been used for almost every flow situation. Thus, the same model has been considered as well. For steady-state conditions, the model equations are [23–29, 34]

Table 1: Design parameters for shell-tube heat exchangers.

Parameters	Design values
Shell diameter, D_s	94.7 mm
Outer-tube diameter, d_o	12.5 mm
Bunch-tube bale structure	Inline and staggered
Pitch	1.5625 cm
Number of tubes, N_t	21 and 24
Heat exchanger length, L	810 mm
Number of baffles, N_b	2
Shell fluid inlet temp., T_{cin}	20°C
Tube fluid inlet temp., T_{hin}	85°C

$$\frac{\partial}{dx_i}(\rho k u_i) = \frac{\partial}{dx_j}\left[\left(\mu + \frac{\mu_t}{\sigma_k}\right)\frac{\partial k}{\partial x_j}\right] + G_k + G_b - \rho\varepsilon + S_k, \quad (7)$$

$$\frac{\partial}{dx_i}(\rho\varepsilon u_i) = \frac{\partial}{dx_j}\left[\left(\mu + \frac{\mu_t}{\sigma_\varepsilon}\right)\frac{\partial \varepsilon}{\partial x_j}\right] + C_{1\varepsilon}\frac{\varepsilon}{k}(G_k - C_{3\varepsilon}G_b) - C_{2\varepsilon}\rho\frac{\varepsilon^2}{k} + S_\varepsilon, \quad (8)$$

$$\mu_t = \rho C_\mu \frac{k^2}{\varepsilon}. \quad (9)$$

Equations (7) and (8) are the transport equations for k and ε, and equation (9) is the equation for turbulent eddy viscosity. In equation (7), $i = 1$, $j = 1$, 2, and 3 represents the space variables in "x," "y," and "z" directions, and the model constants values used in the turbulence model are $C_{1\&\varepsilon} = 1.44$, $C_{2\&\varepsilon} = 1.92$, $C_\mu = 0.09$, $\sigma_k = 1.0$, and $\sigma_{\&\varepsilon} = 1.3$.

3. Results and Discussion

The numerical analysis has been carried out on STHX with inline and staggered tube structure, and a comparison of results shows that the performance of STHX is better with staggered tube structure than that with the inline tube structure. Outlet temperature for shell and tube side is given in Table 3. The effectiveness for the staggered and inline tube heat exchangers is 64.10% and 53.15%, respectively. Based on effectiveness, it is evident that staggered tube heat exchanger is more efficient as compared with aligned tube-conduit heat exchanger, so further calculations have been performed on staggered grid shell-tube type heat exchanger only.

From the results, it can be clearly identified that the heat transfer performance of shell-tube type heat exchanger with staggered grid structure is better than the heat exchanger with inline grid structure (Figures 2(a)–2(c) and Figures 2(d)–2(f)). So, for further analysis of variation in bulk mass-influx flow rate for shell fluid, shell-and-tube heat exchanger with staggered grid structure has been considered. Mass flow rate of shell-side fluid has been varied from

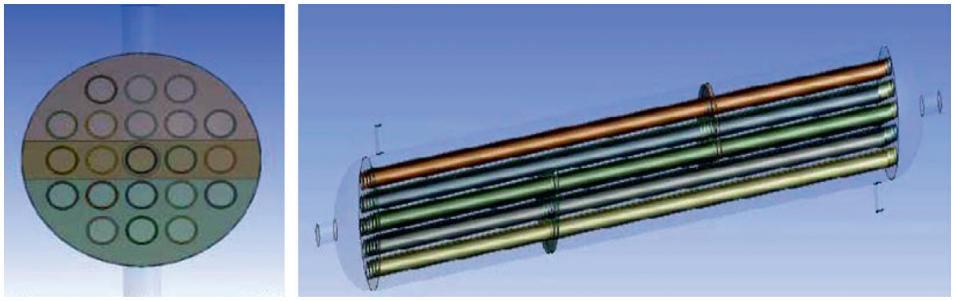

(a)

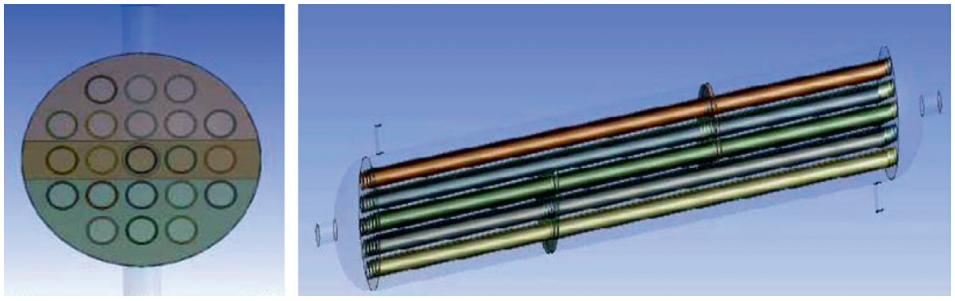

(b)

Figure 1: (a) STHX with staggered grid structure. (b) STHX with inline grid structure.

Table 2: Boundary conditions applied at various faces.

Sr. No.	Physical location	Boundary condition
1	Shell wall	Adiabatic wall boundary condition (no slip) ($\dot{q}'' = 0$; $u = v = w = 0$)
2	Baffle walls	Wall boundary condition (no slip) ($T_b = T_{atm} = 27^{\circ}\text{C}$; $u = v = w = 0$)
3	Shell outlet	Pressure outlet ($P = P_{atm}$; $T = T_{atm}$)
4	Tube outlet	Pressure outlet ($P = P_{atm}$; $T = T_{atm}$)
5	Pipe walls	Conjugate heat transfer
6	Inlets	Mass flow inlets (corresponding to 0.1 kg/s–0.5 kg/s for shell side having fixed inlet temperature $T_{cin} = 20^{\circ}\text{C}$ and 0.25 kg/s for tube side with fixed $T_{hin} = 85^{\circ}\text{C}$)

Table 3: Outlet temperatures of shell-tube heat exchanger.

Zone	STHX with inline tube structure (°C)	STHX with staggered tube structure (°C)
Shell inlet	20.00	20.00
Shell outlet	35.33	42.93
Tube inlet	85.00	85.00
Tube outlet	50.45	43.33

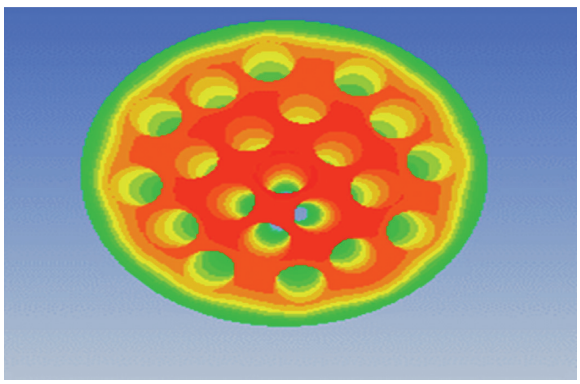

(a)

Figure 2: Continued.

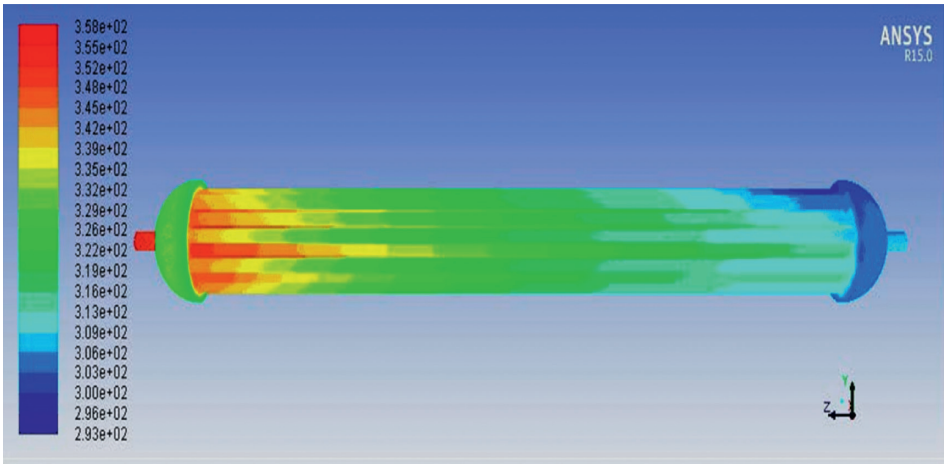

(b)

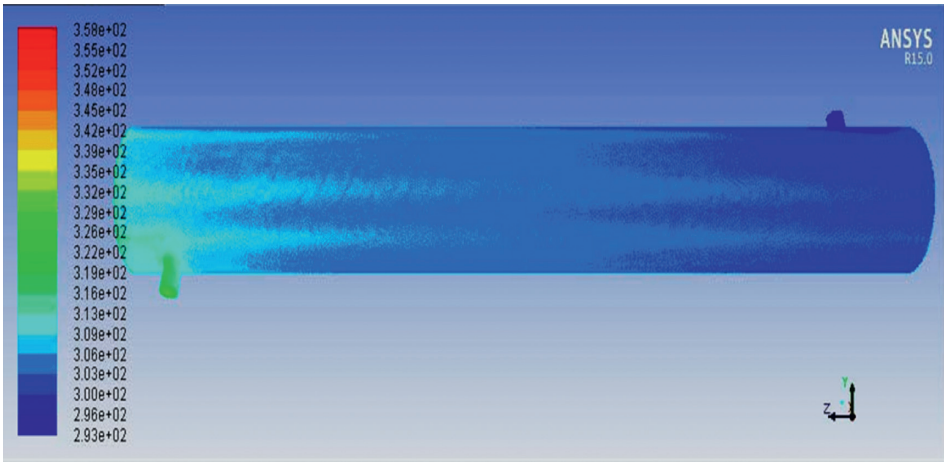

(c)

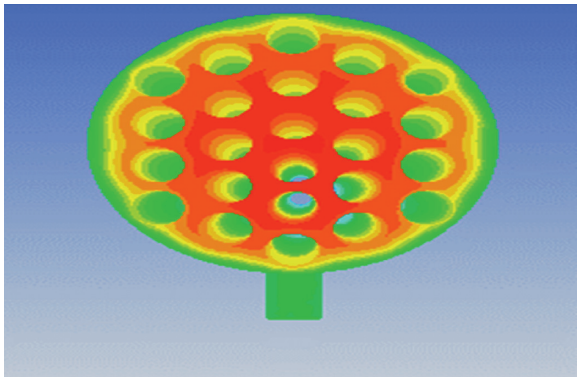

(d)

Figure 2: Continued.

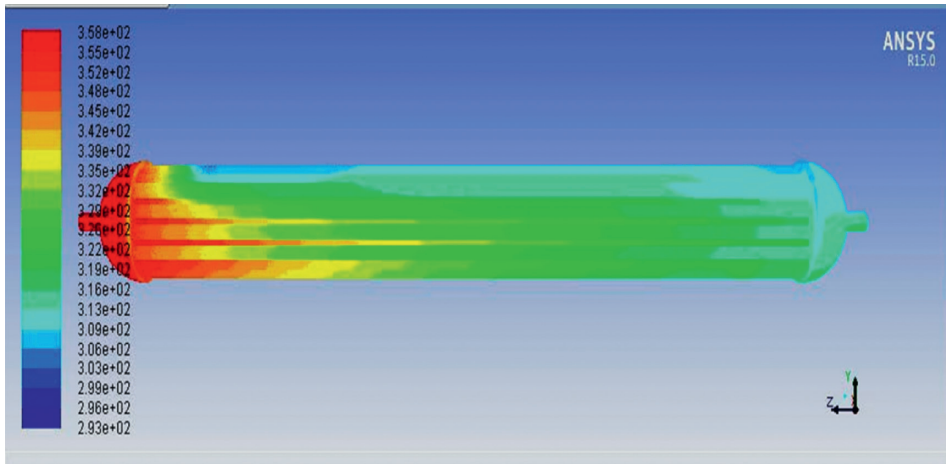

(e)

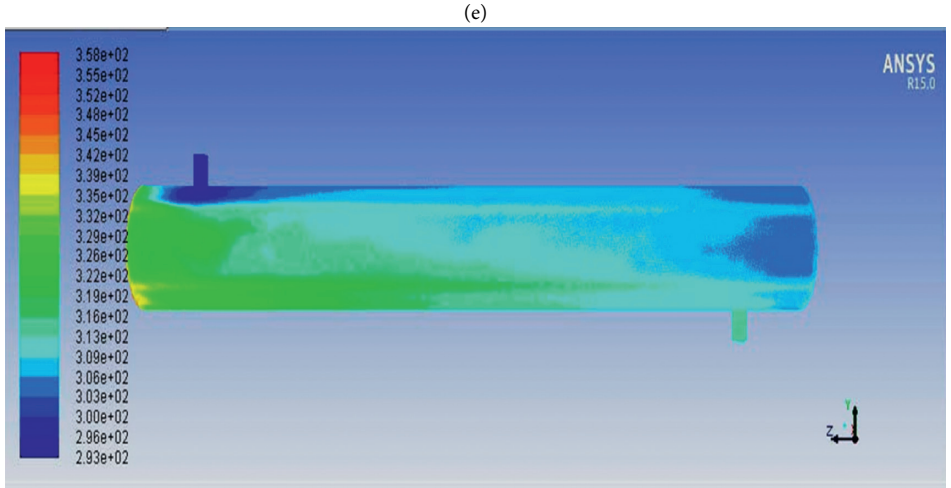

(f)

Figure 2: Static temperature variation in STHX with (a–c) inline grid and (d–f) staggered grid.

Table 4: CFD results for variation in mass flow rate.

Mass flow rate (kg/s)	Outlet temperatures (°C)		Heat transfer coefficient (W/m^{2}K)	Shell-side pressure drop (Pa)	Rate of heat transfer (W)
	T_c	T_h			
0.1	40.94	63.63	714.33	450.9	8750
0.2	32.63	70.90	1045.84	530.4	10557
0.3	29.12	74.05	1307.12	648.6	11443
0.4	27.17	75.53	1531.20	710.1	11989
0.5	25.92	77.17	1731.15	862.2	12365

0.1 kg/s to 0.5 kg/s, and tube-side flow has been taken as constant at 0.25 kg/s.

Table 4 describes the outlet temperatures of the shell-tube heat exchanger for changing mass flow rates. Shell fluid inlet and tube fluid inlet temperatures are kept identical for all cases, which correspond to 20°C and 85°C, respectively. Table 5 describes the effect of variation in mass flow rate on flow parameters such as pressure drop and heat transfer characteristics using respective analytical formulas.

Table 6 presents the percentage discrepancy among the CFD predictions and analytical outcomes by taking the

Table 5: Analytical calculations for variation in mass flow rate on flow and heat transfer.

Mass flow rate (kg/s)	Heat transfer coefficient (W/m^{2}K)	Shell-side pressure drop (Pa)	Rate of heat transfer (W)
0.1	607.11	414.83	7262.5
0.2	941.04	498.57	9739.6
0.3	1202.55	616.17	10921.8
0.4	1453.11	674.95	11624.4
0.5	1678.69	810.46	11991.6

Table 6: Percent difference between CFD analysis and analytical calculations.

Mass flow rate (kg/s)	Heat transfer coefficient (W/m^{2}K)	Shell-side pressure drop (Pa)	Rate of heat transfer (W)
0.1	15.01	8.01	4.88
0.2	10.02	6.20	8.39
0.3	8.00	5.00	4.77
0.4	5.10	4.95	3.13
0.5	3.03	6.00	3.11

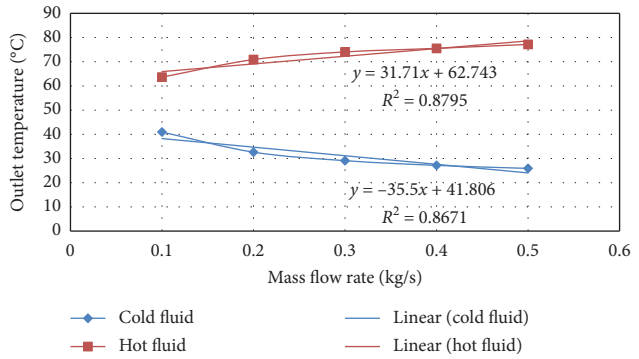

Figure 3: Effect of outlet temperature (°C) against the mass flow rate (Kg/s).

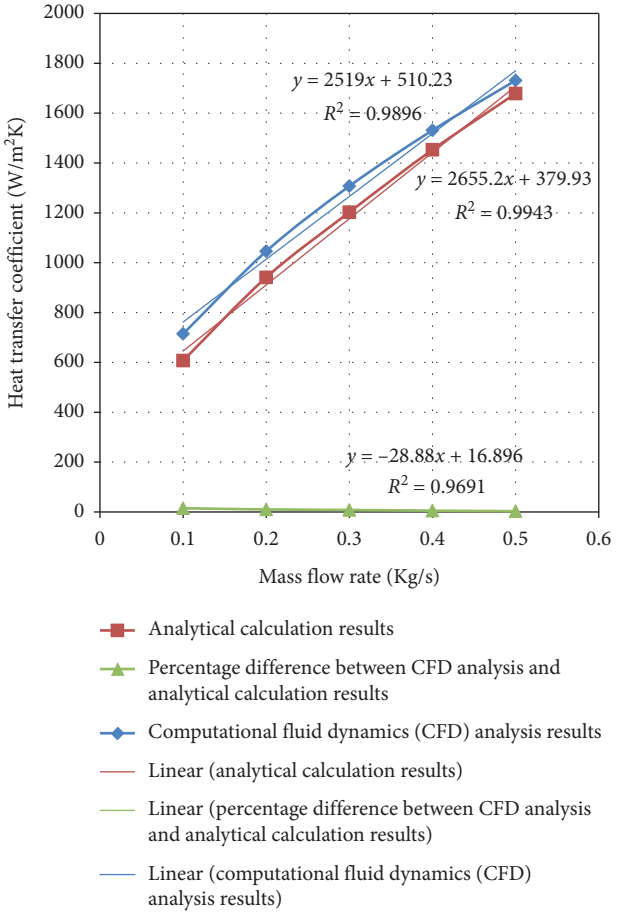

Figure 4: Effect of heat transfer coefficient (W/m^{2}K) against the mass flow rate (Kg/s).

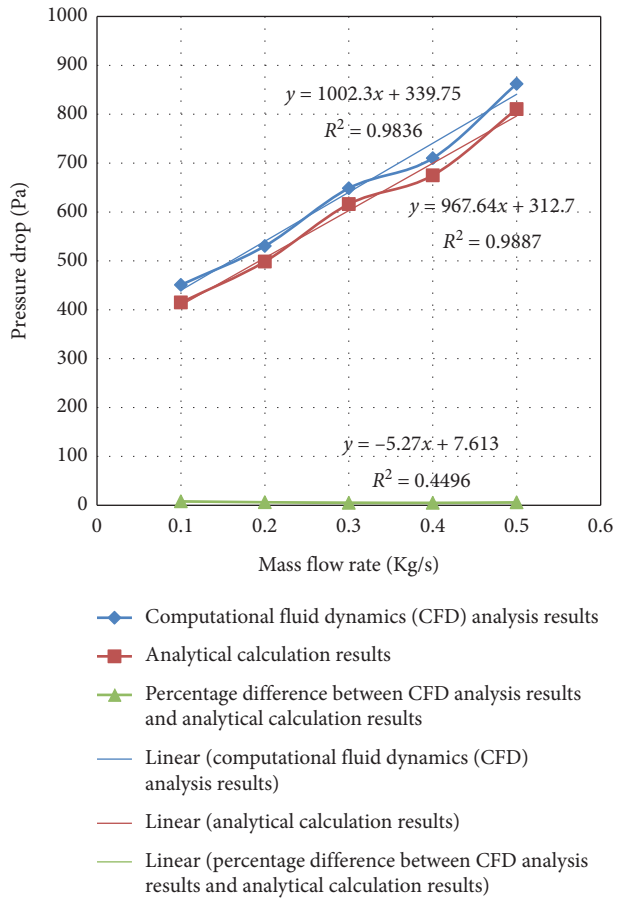

Figure 5: Effect of pressure drop (Pa) against the mass flow rate (Kg/s).

standard analytical results for pressure drop and heat transfer coefficient occurring in internal flows as reference. With the increase in the mass flow rate of shell fluid, both the heat transfer coefficient and pressure drop increase, but the outlet temperature of hot and cold fluid decreases, which ultimately reduces the potential efficiency of a shell-tube heat exchanger. The above results show good agreement between CFD and analytical solutions, and a maximum difference of 15.01% has been noticed in the heat transfer coefficient at the lowest flow rate.

The graphical representation, as illustrated in Figures 3–6, exhibits the influence of mass flow rate variations on outlet temperatures of STHX, pressure drop, heat transfer coefficient, and rate of heat transfer. It has been observed that an increase in mass flow rate of shell fluid leads to a decrease in outlet temperatures of a shell-tube heat exchanger and enhancement of both pressure drop as well as

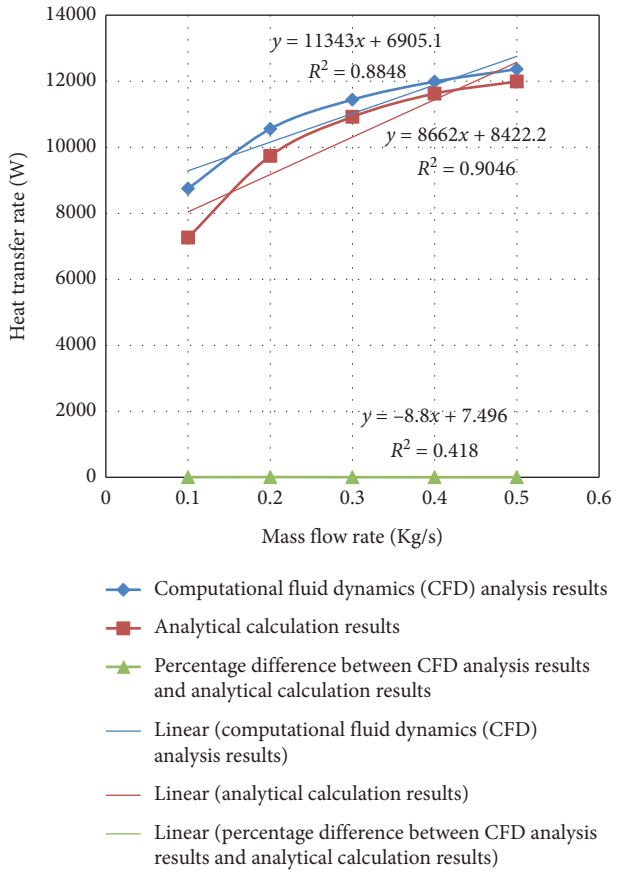

Figure 6: Effect of rate of heat transfer (W) against the mass flow rate (Kg/s).

heat transfer coefficient. The enhancement of pressure drop is expected because of the turbulence in a flow field. The related investigation was reported by Singh et al., which analyzed that the Reynolds averaged N-S eqns.-predicated turbulent simulation in commercial C. F. D. Fluent was being employed for numerical analysis. The three-distinct "k-ε," as well as the shearing-stress-transport (S.S.T.) "k-ω" models, are being used in the analysis. In order to determine the best-efficient and reliable turbulence model, the numerical simulation efficiency analysis was compared with empirical outcomes. For the design topography and configuration in consideration, the influence of alteration of Reynolds number ($\mathrm{Re_p}$), interjet, and separation distance was being contemplated. Such factors influenced the heat transfer coefficient, temp., and turbulence intensity in a stream. Results revealed that the localized "h" levels were being considerably decreased as the separation distance "non-dimensional-impingement separation H/D" escalates. The S.S.T. "k-ω" design model had been reported to be the least important determinant and reliable assessment of empirical outcomes. With an improvement in "H/D" from six-to-ten at "$\mathrm{Re_p}$" $= 9 \times 10^3$ and "interjet-spacing, S/D " of three, the mean of heat transfer performance "h" significantly decreases from 0.021 to 0.0193 W/cm^{2}K. The interjet spacing "S/D " of three was being computed to be the more optimal value predicated upon analytical findings as unveiled by the Singh et al. [34].

4. Conclusions

The STHX has been modeled with staggered and inline tube structures to analyze the heat transfer performance. From the CFD simulations for the shell-tube heat exchanger, outlet temperatures of shell-tube fluids and their effectiveness have been obtained. From the obtained results, the following conclusions can be drawn:

(a) STHX with staggered tube structure is better than the STHX with inline tube structure.

(b) Effect of variation in shell fluid mass flow rate has been analyzed on heat transfer rate, pressure drop, heat transfer coefficient, and outlet temperatures of shell-tube heat structure by varying the shell-side mass flow rate from 0.1 kg/s to 0.5 kg/s and keeping tube-side flow rate as constant at 0.25 kg/s. The results show that with the rise in shell-side mass flow rate, both the pressure drop and heat transfer coefficient enhance and decrease the outlet temperatures.

(c) It has been observed that pressure drop is minimum for a mass flow rate of 0.1 kg/s, and outlet temperatures at the shell side and tube side are 40.94°C and 63.63°C, respectively. The increase in pressure drop for increasing mass flow rate has been attributed to the turbulence, and thus higher shear stresses exist at the surfaces.

(d) It has been observed that there is an excellent accord among CFD and analytical findings. The percentage difference between analytical solution and CFD simulation results shows the highest difference of 15.01% for heat transfer coefficient, 8.01% for shell-side pressure drop, and 8.39% for heat transfer rate.

Abbreviations

x, y, z: Coordinate axis
D_s: Shell diameter (mm)
d_i: Inner diameter of tube (mm)
d_o: Outer diameter of tube (mm)
e: Energy (kJ)
g: Acceleration due to gravity (m/s^2)
G_k: Production term for k (m^2/s^2)
G_b: Buoyancy term for TKE (m^2/s^2)
G_ε: Production term for ε (m^2/s^3)
h: Convective heat transfer coefficient (W/m^2)
i, j: Loop indices
k: Turbulent kinetic energy (m^2/s^2)
L: Length of heat exchanger (mm)
N_b: Number of baffles
N_t: Number of tubes
T: Temperature (°C)
T_{cin}: Temperature of cold fluid (°C)
T_{hin}: Temperature of hot fluid (°C)
P: Pressure (Pa)
q: Heat flux (kW/m^2)
u, v, w: Velocity components (m/s)
CFD: Computational fluid dynamics

STHX: Shell-and-tube heat exchanger
atm: Atmosphere
: **Greek Symbols**
ϕ: Viscous dissipation function
τ_{xy}: Viscous shear stress (Pa)
λ: Second coeff. of viscosity (kg/m-s)
μ_t: Turbulent viscosity (kg/m-s)
μ: Dynamic viscosity (kg/m-s)
ε: Dissipation rate (m^2/s^3)
ρ: Density (kg/m^3)
σ_k: Turbulent Prandtl number for k
σ_ε: Turbulent Prandtl number for ε
∇: Del operator.

Data Availability

The data used to support the findings of this study are available from the corresponding author upon request.

Conflicts of Interest

The authors declare that they have no conflicts of interest.

Acknowledgments

The authors wish to acknowledge the Department of RIC, IKGPTU, Punjab, India, for providing opportunity to conduct this research.

References

[1] B. Sundén, "Computational fluid dynamics in research and design of heat exchangers," *Heat Transfer Engineering*, vol. 28, no. 11, pp. 898–910, 2007.

[2] S. A. Payambarpour, H. Shokouhmand, M. H. Ahmadi, M. El Haj Assad, and L. Chen, "Effect of wetness pattern on the fin-tube heat exchanger performance under partially wet-surface condition," *Thermal Science and Engineering Progress*, vol. 19, Article ID 100619, 2020.

[3] W. H. Alawee, H. A. Dhahad, and K. I. Abass, "Increase the yield of simple solar distillation using the water drip method," *International Journal of Computation and Applied Sciences*, vol. 6, no. 2, pp. 447–445, 2019.

[4] K. J. Bell, "Heat exchanger design for the process industries," *Journal of Heat Transfer*, vol. 126, no. 6, pp. 877–885, 2005.

[5] L. Bellahcene, D. Sahel, and A. Yousfi, "Numerical study of shell and tube heat exchanger performance enhancement using nanofluids and baffling technique," *Journal of Advanced Research in Fluid Mechanics and Thermal Sciences*, vol. 80, no. 2, pp. 42–55, 2021.

[6] S. A. Payambarpour, M. Alhuyi Nazari, M. H. Ahmadi, and A. J. Chamkha, "Effect of partially wet-surface condition on the performance of fin-tube heat exchanger," *International Journal of Numerical Methods for Heat & Fluid Flow*, vol. 29, 2019.

[7] B. B. Gulyani, "Estimating number of shells in shell and tube heat exchangers: a new approach based on temperature cross," *Journal of Heat Transfer*, vol. 122, no. 3, pp. 566–571, 2000.

[8] E. Ozden and I. Tari, "Shell side CFD analysis of a small shell-and-tube heat exchanger," *Energy Conversion and Management*, vol. 51, no. 5, pp. 1004–1014, 2010.

[9] A. M. Ez Abadi, M. Sadi, M. Farzaneh-Gord, M. H. Ahmadi, R. Kumar, and K.-w. Chau, "A numerical and experimental study on the energy efficiency of a regenerative Heat and Mass Exchanger utilizing the counter-flow Maisotsenko cycle," *Engineering Applications of Computational Fluid Mechanics*, vol. 14, no. 1, pp. 1–12, 2020.

[10] M. Kahani, M. H. Ahmadi, A. Tatar, and M. Sadeghzadeh, "Development of multilayer perceptron artificial neural network (MLP-ANN) and least square support vector machine (LSSVM) models to predict Nusselt number and pressure drop of TiO $_2$/water nanofluid flows through non-straight pathways," *Numerical Heat Transfer, Part A: Applications*, vol. 74, pp. 1–17, 2018.

[11] H. Maddah, R. Aghayari, M. Mirzaee, M. H. Ahmadi, M. Sadeghzadeh, and A. J. Chamkha, "Factorial experimental design for the thermal performance of a double pipe heat exchanger using Al2O3-TiO2 hybrid nanofluid," *International Communications in Heat and Mass Transfer*, vol. 97, pp. 92–102, 2018.

[12] E. Jamalei, R. Alayi, A. Kasaeian, F. Kasaeian, and M. H. Ahmadi, "Numerical and experimental study of a jet impinging with axial symmetry with a set of heat exchanger tubes," *Mech India*, vol. 19, 2018.

[13] A. A. Bhuiyan and A. K. M. S. Islam, "Thermal and hydraulic performance of finned-tube heat exchangers under different flow ranges: a review on modeling and experiment," *International Journal of Heat and Mass Transfer*, vol. 101, pp. 38–59, 2016.

[14] A. L. H. Costa and E. M. Queiroz, "Design optimization of shell-and-tube heat exchangers," *Applied Thermal Engineering*, vol. 28, no. 14-15, pp. 1798–1805, 2008.

[15] A. Falav Jozaei, A. Baheri, M. K. Hafshejani, and A. Arad, "Optimization of baffle spacingon heat transfer, pressure drop and estimated price in a shell-and-tube heat exchanger," *World Applied Sciences Journal*, vol. 18, pp. 1727–1736, 2012.

[16] H. Li and V. Kottke, "Effect of baffle spacing on pressure drop and local heat transfer in shell-and-tube heat exchangers for staggered tube arrangement," *International Journal of Heatx and Mass Transfer*, vol. 41, no. 10, pp. 1303–1311, 1998.

[17] D. Rai, S. Bharati, and S. Bux, "To study of parametric analysis of shell and tube heat exchanger," *International Journal of Advance Research and Innovative Ideas*, vol. 1, pp. 383–391, 2015.

[18] D. S. Patel, R. R. Parmar, and V. M. Prajapati, "CFD analysis of shell and tube heat exchangers–a review," *International Research Journal of Engineering and Technology*, vol. 17, 2015.

[19] B. T. Lebele-Alawa and V. Egwanwo, "Numerical Analysis of the Heat Transfer in Heat Exchangers," *Journal of Engineering Physics and Thermophysics*, vol. 2, pp. 1–5, 2009.

[20] V. K. Chalwa and N. Kadli, "Study of variation for pressure drop and temperature distribution in a shell and tube heat exchanger in case of vertical baffle," *Mechanica Confab*, vol. 2, pp. 17–25, 2013.

[21] K. Anand, V. K. Pravin, and P. H. Veena, "Experimental investigation of shell and tube heat exchanger using Bell Delaware," *Method*, vol. 2, pp. 73–85, 2014.

[22] J. Yang, L. Ma, J. Bock, A. M. Jacobi, and W. Liu, "A comparison of four numerical modeling approaches for enhanced shell-and-tube heat exchangers with experimental validation," *Applied Thermal Engineering*, vol. 65, no. 1-2, pp. 369–383, 2014.

[23] S. Wang, J. Wen, and Y. Li, "An experimental investigation of heat transfer enhancement for a shell-and-tube heat

exchanger," *Applied Thermal Engineering*, vol. 29, no. 11-12, pp. 2433–2438, 2009.

[24] A. Ramezanpour, I. Mirzaee, R. Rahmani, and H. Shirvani, "Numerical study of staggered tube bundle in turbulent cross flow for an optimum arrangement," *International Journal of Heat and Mass Transfer*, vol. 7, pp. 37–56, 2006.

[25] K. M. Kwak, K. Torii, and K. Nishino, "Heat transfer and pressure loss penalty for the number of tube rows of staggered finned-tube bundles with a single transverse row of winglets," *International Journal of Heat and Mass Transfer*, vol. 46, no. 1, pp. 175–180, 2003.

[26] S. B. Beale and D. B. Spalding, "A Numerical study of unsteady fluid flow in in-line and staggered tube banks," *Journal of Fluids and Structures*, vol. 13, no. 6, pp. 723–754, 1999.

[27] T. Shaligram, "Numerical study of heat transfer and pressure drop for flow past inline and staggered tube bundles," *International Journal of Numerical Methods for Heat & luid Flow*, vol. 19, pp. 931–949, 2009.

[28] J. M. Hassan, T. A. Mohamed, W. S. Mohammed, and W. H. Alawee, "Experimental and numerical study on the improvement of uniformity flow for three-lateral dividing manifold," in *Proceedings of the World Research and Innovation Convention on Engineering and Technology*, Putrajaya, Malaysia, February 2014.

[29] W. H. Alawee, J. M. Hassan, and W. S. Mohammad, "Experimental and numerical study on the improvement of uniformity flow in a parallel flow channel," *Eng. Technol. J.*vol. 34, pp. 847–856, 2016.

[30] W. H. Alawee, G. F. Al-Sumaily, H. A. Dhahad, and M. C. Thompson, "Numerical analysis of non-Darcian mixed convection flows in a ventilated enclosure filled with a fluid-saturated porous medium," *Thermal Science and Engineering Progress*, vol. 24, Article ID 100922, 2021.

[31] G. F. Al-Sumaily, H. M. Hussen, W. H. Alawee, H. A. Dhahad, and M. C. Thompson, "Non-Darcian Bénard convection in eccentric annuli containing spherical particles," *International Journal of Heat and Fluid Flow*, vol. 86, Article ID 108705, 2020.

[32] W. H. Alawee, B. Yusuf, T. A. Mohammad, and H. A. Dhahad, "Variation of flow along a multiple outlets pipe with various spacing and inflow water head based on physical model," *Journal of Engineering Science and Technology*, vol. 14, pp. 2399–2409, 2019.

[33] J. M. Hassan, W. S. Mohammed, T. A. Mohamed, and W. H. Alawee, "CFD simulation for manifold with tapered longitudinal section," *International Journal of Emerging Technology and Advanced Engineering*, vol. 4, pp. 28–35, 2014.

[34] P. Singh, N. K. Grover, V. Agarwal et al., "Computational fluid dynamics analysis of impingement heat transfer in an inline array of multiple jets," *Mathematical Problems in Engineering*, vol. 2021, Article ID 6668942, 10 pages, 2021.

Hindawi
Mathematical Problems in Engineering
Volume 2021, Article ID 5553732, 9 pages
https://doi.org/10.1155/2021/5553732

Research Article

A Novel Approach for Solving Fuzzy Differential Equations Using Cubic Spline Method

S. Karpagappriya,[1] **Nazek Alessa**,[2] **P. Jayaraman**,[1] **and K. Loganathan**[3]

[1]*Department of Mathematics, Bharathiar University, Coimbatore-641 046, Tamilnadu, India*
[2]*Department of Mathematical Sciences, Faculty of Science, Princess Nourah Bint Abdulrahman University, Riyadh, Saudi Arabia*
[3]*Research and Development Wing, Live4Research, Tiruppur, Tamilnadu 638 106, India*

Correspondence should be addressed to K. Loganathan; loganathankaruppusamy304@gmail.com

Received 5 February 2021; Accepted 2 May 2021; Published 22 May 2021

Academic Editor: José Francisco Gómez Aguilar

Ambiguity in real-world problems can be modeled into fuzzy differential equations. The main objective of this work is to introduce a new class of cubic spline function approach to solve fuzzy initial value problems efficiently. Further, the convergence of this method is shown. As it is a single-step method that converges faster, the complexity of the proposed method is too low. Finally, a numerical example is illustrated in order to validate the effectiveness and feasibility of the proposed method, and the results are compared with the exact as well as Taylor's method of order two.

1. Introduction

The entire real world is complex; it is found that the complexity arises from uncertainty in the form of ambiguity. Uncertainties in the real-world problem can be modeled easily with the help of fuzzy set theory when one lacks complete information about the variables and parameters [1]. This concept of fuzzy set theory was first introduced by Zadeh [2] in 1965. Chang and Zadeh explicated the concept of fuzzy derivatives [3]. The term fuzzy differential equation was formulated by Kandal and Byatt [4] in 1978. These equations help in modeling the propagation of epistemic uncertainty in a dynamical environment [5]. Kaleva [6], Seikkala [7], and Song and Wu [8] have extensively studied the existence and uniqueness of solutions of these equations. A general formulation of the first-order fuzzy initial value problem was given by Buckley and Feuring [9]. Later, the fuzzy initial and boundary value differential equation was given by O'Regan et al. [10].

First-order linear fuzzy differential equations have inspired several authors to focus on solving them numerically since they appear in many real-world applications. These applications include different fields of science such as medical diagnosis, biology, and civil engineering and also in the field of economics [11] where the information are not given in the crisp set [12]. Based on Zadeh's extension principle, a new fuzzy version of Euler's method was developed by Ahamed and Hasan [13]. Solving of these equations by the Taylor method of order p has been studied by Abbasbandy and Viranloo [14], and the same was discussed by Allahviranloo et al. [15] by using the predictor-corrector algorithm. Finally, the authors concluded that a fuzzy differential equation can be modified into a system of ordinary differential equations (ODEs). Also, they found out that there are two solutions for a fuzzy differential equation by solving the associated ODEs. The convergence, consistency, and stability for approximating the solution of fuzzy differential equations with initial value conditions have been studied by Ezzati et al. [16]. All the numerical results of these equations and their applications were summarized by Chakraverty et al. [12].

In this paper, the fuzzy initial value problem is solved numerically by using a new class of function approximation called cubic spline, for better accuracy of the solution.

2. Preliminaries

Let $X' = \{x\}$ where X' is the space of points and x is the generic element of X'.

Definition 1 (see [2]). A fuzzy subset $\mu_{A'}$ of the set A' in X' is a function $\mu_{A'}: A' \longrightarrow [0,1]$.

Definition 2 (see [17]). The α-level set of the fuzzy set A' of X' is a crisp set $[A']^{\alpha} = \{x \in X' | \mu_{A'}(x) \geq \alpha\}$ if $\alpha \in (0,1]$.

Definition 3 (see [17]). Let A' be a triangular fuzzy number (TFN) which is defined as $\langle l, m, n\rangle$ where $[l, n]$ is the support, $\{m\}$ is the core, and the membership function is

$$\mu_{A'}(x) = \begin{cases} \dfrac{x-l}{m-l}, & \text{if} \quad x \in [l,m], \\ \dfrac{n-x}{n-m}, & \text{if} \quad x \in (m,n], \\ 0, & \text{if} \quad x \notin [l,n], \end{cases} \tag{1}$$

where $l < m < n$.

Let us denote the set of all fuzzy numbers on $\mathbb{R}$ as $\mathbb{F}$ which is a fuzzy number such that $\mu: \mathbb{R} \longrightarrow [0,1]$.

Definition 4 (see [18]). Let l and $m \in \mathbb{F}$. If there exists $n \in \mathbb{F}$ such that $l = m + n$, then n is the Hukuhara difference of l and m. This can be denoted as $n = l \ominus m$. To define the differentiability of a fuzzy function, we can make use of this difference as follows.

Let $H: [u,v] \longrightarrow \mathbb{F}$ be differentiable at $t_0 \in (u,v)$. If there exists some element $H'(t_0) \in \mathbb{F}$ such that

$$\lim_{h \longrightarrow 0^+} \frac{H(t_0+h) \ominus H(t_0)}{h} = \lim_{h \longrightarrow 0^+} \frac{H(t_0) \ominus H(t_0-h)}{h} = H'(t_0), \tag{2}$$

then H is said to be Hukuhara differentiable at t_0.

Suppose H is differential at the point $t_0 \in (u,v)$, then all its α-level sets, $H_{\alpha}(t) = [H(t)]^{\alpha}$, are Hukuhara differentiable at t_0 and $[H'(t_0)]^{\alpha} = \mathrm{DH}_{\alpha}(t_0)$, where DH_{α} denotes the Hukuhara derivatives of H_{α} and H_{α} as the multivalued mapping.

Theorem 1 (see [19]). *Let $q(x) \in C^3[u,v]$ and (Δ_k) be a sequence of partitions on $[u,v]$, with $\lim_{k \longrightarrow \infty} \|\Delta_k\| = 0$; then, for the interpolate cubic spline $S_{\Delta_k}(x)$, uniformly for $u \leq x \leq v$,*

$$\left| q^{(p)}(x) - S_{\Delta_k}^{(p)}(x) \right| = O\left(\|\Delta_k\| \right)^{3-p}, \quad \text{for } p = 0, 1, 2, \text{ and } 3. \tag{3}$$

If $q'''(x)$ satisfies the Holder condition on $[u,v]$ with $0 < \alpha < 1$, then

$$\left| y^{(p)}(x) - S_{\Delta_k}^{(p)}(x) \right| = O\left(\|\Delta_k\| \right)^{3+\alpha-p}. \tag{4}$$

Proof. This theorem has been proved in the work by Ahlberg et al. [19] (p. 29). □

2.1. Cubic Spline Function Approximation for Initial Value Problems. Let the given $(n+1)$ data points be (u_i, v_i), $i = 0, 1, 2, \ldots, n$, where $u_0 < u_1 < u_2 < \ldots < u_n$. Let us define the cubic spline $P_i(u)$, which is defined in the interval $[u_{i-1}, u_i]$ as follows.

(i) For $u < u_0$ and $u > u_n$, $P_i(u)$ is a polynomial whose degree is one

(ii) $P_i(u)$ is at most a cubic polynomial in each subinterval $[u_{i-1}, u_i]$, where $i = 1, 2, \ldots, n$

(iii) $P_i(u)$, $P_i'(x)$, and $P_i''(x)$ are continuous at each point (u_i, v_i), where $i = 0, 1, 2, \ldots, n$

(iv) $P_i(u_i) = v_i$, where $i = 0, 1, 2, \ldots, n$

If $P_i''(u_0) = P_i''(u_n) = 0$ and $P_i(u)$, $P_i'(u)$, and $P_i''(u)$ are all continuous in (u_0, u_n), then this cubic spline is called as natural spline [20].

Many applications make use of slopes. So let us denote the cubic spline function that is obtained in terms of first derivatives to be m_i. The cubic spline $P(u)$ formula for an initial value problem in $u_{i-1} \leq u \leq u_i$ in terms of its first derivatives $P'(u_i) = m_i$ can be obtained by using Hermite's interpolation formula as follows [21, 22]:

$$\begin{aligned} P(u) = {} & m_{i-1} \frac{(u_i - u)^2 (u - u_{i-1})}{h^2} - m_i \frac{(u - u_{i-1})^2 (u_i - u)}{h^2} \\ & + v_{i-1} \frac{(u_i - u)^2 [2(u - u_{i-1}) + h]}{h^3} \\ & + v_i \frac{(u - u_{i-1})^2 [2(u_i - u) + h]}{h^3}, \end{aligned} \tag{5}$$

where $h = u_i - u_{i-1}$ for all i:

$$\begin{aligned} P'(u) = {} & \frac{m_{i-1}}{h^2} (u_i - u)(2u_{i-1} + u_i - 3u) \\ & - \frac{m_i}{h^2} (u - u_{i-1})(u_{i-1} + 2u_i - 3u) \\ & + \frac{6}{h^3} (v_i - v_{i-1})(u_i - u)(u - u_{i-1}), \end{aligned} \tag{6}$$

$$\begin{aligned} P''(u) = {} & -2 \frac{m_{i-1}}{h^2} [u_{i-1} + 2u_i - 3u] \\ & - 2 \frac{m_i}{h^2} [2u_{i-1} + u_i - 3u] \\ & + \frac{6}{h^3} (v_i - v_{i-1})[u_{i-1} + u_i - 2u]. \end{aligned} \tag{7}$$

Setting $u = u_i$ and $P(u_i) = v_i$ for all i in (7), we have

$$P''(u_i) = \frac{2m_{i-1}}{h} + \frac{4m_i}{h} - \frac{6}{h^2}(P_i - P_{i-1}). \tag{8}$$

Now consider a differential equation of first order with the initial condition as follows:

$$\frac{dv}{du} = f(u, v) \text{ and } v(u_0) = v_0. \tag{9}$$

On differentiating (9) twice with respect to u,

$$v''(u) = f_u(u, v) + f_v(u, v) f(u, v). \tag{10}$$

Taking $u = u_i$ and $P(u_i) = v_i$, the above equation becomes

$$P''(u_i) = f_u(u_i, P_i) + f_v(u_i, P_i) f(u_i, P_i). \tag{11}$$

On equating (8) and (11), we obtain

$$\frac{2m_{i-1}}{h} + \frac{4m_i}{h} - \frac{6}{h^2}(P_i - P_{i-1}) = f_u(u_i, P_i) + f_v(u_i, P_i) f(u_i, P_i). \tag{12}$$

From this, we can compute P_i's. Substituting these P_i's in (5) gives the required solution. The convergence of this method has been proved by Patricio [21].

3. Fuzzy Initial Value Problem

Consider the first-order fuzzy differential equation as

$$u'(\xi) = f(\xi, u(\xi)), \quad \xi \in [\xi_0, T], T \geq 0, \tag{13}$$

with the initial condition $u(\xi_0) = u_0 \in \mathbb{F}$, where u is a fuzzy function of the crisp variable ξ; that is, $u \in \mathbb{F}$, which is unknown. f: $[\xi_0, T] \times \mathbb{F} \longrightarrow \mathbb{F}$, which is a fuzzy function. u' is the fuzzy derivative of u, and $u(\xi_0)$ is a fuzzy number. Here, let us assume the fuzzy number to be a triangular fuzzy number.

For $\alpha \in [0, 1]$, let us denote the α-level sets:

$$[u(\xi)]_\alpha = [[u(\xi)]_l(\alpha), [u(\xi)]_r(\alpha)], \text{ and } [u(\xi_0)]_\alpha = [[u(\xi_0)]_l(\alpha), [u(\xi_0)]_r(\alpha)]. \tag{14}$$

Also,
$[f(\xi, u(\xi))]_\alpha = [f_1(\xi, u(\xi); \alpha), f_2(\xi, u(\xi); \alpha)]$, where

$$f_1(\xi, u(\xi); \alpha) = \min\{f(\xi, s) \mid s \in [[u(\xi)]_l(\alpha), [u(\xi)]_r(\alpha)]\} = G(\xi, [u(\xi)]_l(\alpha), [u(\xi)]_r(\alpha)), \tag{15}$$

$$f_2(\xi, u(\xi); \alpha) = \max\{f(\xi, s) \mid s \in [[u(\xi)]_l(\alpha), [u(\xi)]_r(\alpha)]\} = H(\xi, [u(\xi)]_l(\alpha), [u(\xi)]_r(\alpha)). \tag{16}$$

The mapping f: $[\xi_0, T] \times \mathbb{F} \longrightarrow \mathbb{F}$ is a fuzzy process, and the derivatives $f^{(i)} \in \mathbb{F}$, for $i = 1, 2, \ldots, p$, are defined as

$$\left[f^{(i)}(\xi, u(\xi))\right]_\alpha = \left[f_1^{(i)}(\xi, u(\xi); \alpha), f_2^{(i)}(\xi, u(\xi); \alpha)\right], \tag{17}$$

where

$$\begin{aligned} f_1^{(i)}(\xi, u(\xi); \alpha) &= \min\left\{f^{(i)}(\xi, s) \mid s \in [[u(\xi)]_l(\alpha), [u(\xi)]_r(\alpha)]\right\}, \\ f_2^{(i)}(\xi, u(\xi); \alpha) &= \max\left\{f^{(i)}(\xi, s) \mid s \in [[u(\xi)]_l(\alpha), [u(\xi)]_r(\alpha)]\right\}. \end{aligned} \tag{18}$$

Equation (13) can be replaced by an equivalent system of equations, and hence,

$$[u'(\xi)](\alpha) = \{[u'(\xi)]_l(\alpha), [u'(\xi)]_r(\alpha)\}, \tag{19}$$

where

$$[u'(\xi)]_l(\alpha) = f_1(\xi, u(\xi); \alpha) = G(\xi, [u(\xi)]_l(\alpha), [u(\xi)]_r(\alpha)), \quad \text{(by (15))}, \tag{20}$$

$$[u'(\xi)]_r(\alpha) = f_2(\xi, u(\xi); \alpha) = H(\xi, [u(\xi)]_l(\alpha), [u(\xi)]_r(\alpha)), \quad \text{(by (16))}. \tag{21}$$

The system of equations (20) and (21) will have a unique solution, $[[u(\xi)]_l(\alpha), [u(\xi)]_r(\alpha)] \in J = C([\xi_0, \mathbb{F}]) \times C([\xi_0, \mathbb{F}])$. Thus, given fuzzy differential equation (13) possesses a unique solution on J.

Usually, equations (20) and (21) can be solved analytically. Yet, in most of the cases, this becomes tedious, and hence, a numerical approach to these systems of equations has to be considered.

4. Cubic Spline Method for Solving Fuzzy Initial Value Problem

Assume that

$$[U(\xi_n)]_\alpha = [[U(\xi_n)]_l(\alpha), [U(\xi_n)]_r(\alpha)], \tag{22}$$

as the exact solution of (13):

$$[P(\xi_n)]_\alpha = [[P(\xi_n)]_l(\alpha), [P(\xi_n)]_r(\alpha)], \tag{23}$$

as the approximated solution of (13) at ξ_n where $0 \le n \le N$.

Now let us calculate the solutions by mesh points at $\xi_0 < \xi_1 < \ldots < \xi_N = T$, $h = (T - \xi_0)/N$, and $\xi_n = \xi_0 + nh$, where $n = 0, 1, 2, \ldots, N$.

The cubic spline function $P(\xi; \alpha)$ for a fuzzy initial value problem in $\xi_{i-1} \le \xi \le \xi_i$ in terms of its first derivatives $P'(\xi_i; \alpha) = m_i$ is given as

$$\begin{aligned} P(\xi; \alpha) = [P(\xi)]_\alpha &= m_{i-1}\frac{(\xi_i - \xi)^2(\xi - \xi_{i-1})}{h^2} - m_i\frac{(\xi - \xi_{i-1})^2(\xi_i - \xi)}{h^2} \\ &+ \left([u(\xi)]_{i-1}(\alpha)\right)\frac{(\xi_i - \xi)^2[2(\xi - \xi_{i-1}) + h]}{h^3} \\ &+ \left([u(\xi)]_i(\alpha)\right)\frac{(\xi - \xi_{i-1})^2[2(\xi_i - \xi) + h]}{h^3}, \end{aligned} \tag{24}$$

where $h = \xi_i - \xi_{i-1}$. But, we know that

$$[P(\xi)]_\alpha = [[P(\xi)]_l(\alpha), [P(\xi)]_r(\alpha)], \tag{25}$$

where

$$\begin{aligned} [P(\xi)]_l(\alpha) &= m_{i-1}\frac{(\xi_i - \xi)^2(\xi - \xi_{i-1})}{h^2} - m_i\frac{(\xi - \xi_{i-1})^2(\xi_i - \xi)}{h^2} \\ &+ \left([[u(\xi)]_l]_{i-1}(\alpha)\right)\frac{(\xi_i - \xi)^2[2(\xi - \xi_{i-1}) + h]}{h^3} \\ &+ \left([[u(\xi)]_l]_i(\alpha)\right)\frac{(\xi - \xi_{i-1})^2[2(\xi_i - \xi) + h]}{h^3}, \end{aligned} \tag{26}$$

$$\begin{aligned} [P(\xi)]_r(\alpha) &= m_{i-1}\frac{(\xi_i - \xi)^2(\xi - \xi_{i-1})}{h^2} - m_i\frac{(\xi - \xi_{i-1})^2(\xi_i - \xi)}{h^2} \\ &+ \left([[u(\xi)]_r]_{i-1}(\alpha)\right)\frac{(\xi_i - \xi)^2[2(\xi - \xi_{i-1}) + h]}{h^3} \\ &+ \left([[u(\xi)]_r]_i(\alpha)\right)\frac{(\xi - \xi_{i-1})^2[2(\xi_i - \xi) + h]}{h^3}. \end{aligned} \tag{27}$$

By carrying out simple and similar calculations for (26) and (27) as given in "cubic spline function approximation for initial value problems" (especially equations from (6)–(12)), we obtain the following set of equations:

$$\frac{2m_{i-1}}{h}+\frac{4m_i}{h}-\frac{6}{h^2}\left([P_l]_i-[P_l]_{i-1}\right)=G_\xi\left(\xi_i,[P_l]_i;\alpha\right)+G_{u(\xi)}\left(\xi_i,[P_l]_i;\alpha\right)G\left(\xi_i,[P_l]_i;\alpha\right), \tag{28}$$

$$\frac{2m_{i-1}}{h}+\frac{4m_i}{h}-\frac{6}{h^2}\left([P_r]_i-[P_r]_{i-1}\right)=H_\xi\left(\xi_i,[P_r]_i;\alpha\right)+H_{u(\xi)}\left(\xi_i,[P_r]_i;\alpha\right)H\left(\xi_i,[P_r]_i;\alpha\right), \tag{29}$$

where $i=1,2,\ldots,n$ and $h=\xi_i-\xi_{i-1}$. From (28), $[P_l]_i$'s can be computed, and they are substituted in (26) to obtain the solution, $[P(\xi)]_l(\alpha)$. Similarly, $[P_r]_i$'s can be evaluated from (29) and are substituted in (27) to yield $[P(\xi)]_r(\alpha)$. Each P_i value depends on $P_{(i-1)}$th value, for $i=1,2,\ldots,n$.

Both these solutions collectively yield the desired solution $[P(\xi)]_\alpha$ of (13) at a fixed $\xi\in[\xi_{i-1},\xi_i]$, $i=1,2,\ldots,n$.

4.1. Convergence of Fuzzy Cubic Spline Method. Let us consider the equations:

$$[P''(\xi_i)]_l(\alpha)=\frac{2m_{i-1}}{h}+\frac{4m_i}{h}-\frac{6}{h^2}\left([P_l]_i-[P_l]_{i-1}\right), \tag{30}$$

$$\begin{aligned}[u''(\xi_i)]_l(\alpha)&=G_\xi\left(\xi_i,[P_l]_i;\alpha\right)\\&\quad+G_{u(\xi)}\left(\xi_i,[P_l]_i;\alpha\right)G\left(\xi_i,[P_l]_i;\alpha\right).\end{aligned} \tag{31}$$

According to the results given in the work by Ahlberg et al. [19] (p. 34) and Theorem 1, if $G(\xi,u(\xi);\alpha)\in C^3[\xi_0,T]$, we have

$$\left|u^{(p)}(\xi)-P^{(p)}(\xi)\right|=O(h)^{4-p},\quad p=0,1,2,\text{ and }3. \tag{32}$$

If $p=2$, then the above equation can be written as

$$\left|u''(\xi)-P''(\xi)\right|=O(h)^2. \tag{33}$$

At $\xi=\xi_i$, for $i=1,2,\ldots,n$, we have

$$\begin{aligned}&\left|u''(\xi_i)-P''(\xi_i)\right|=O(h)^2,\text{ where }h=\max_i h_i\\&\text{(or)}\quad[u''(\xi_i)]_l(\alpha)=O\left(h^2\right)+[P''(\xi_i)]_l(\alpha),\\&\Rightarrow h^2[u''(\xi_i)]_l(\alpha)=2hm_{i-1}+4hm_i-6\left([P_l]_i-[P_l]_{i-1}\right)+O\left(h^4\right).\end{aligned} \tag{34}$$

Again, with (31), we obtain $[P_l]_i$ explicitly or not according to the linearity or nonlinearity of $G(\xi,u(\xi);\alpha)$ in $u(\xi)$. Then, we can write

$$[P_l]_i=c_1+c_2\alpha+O\left(h^4\right), \tag{35}$$

where c_1 and c_2 are constants and $\alpha\in[0,1]$ or

$$r\left([P_l]_i\right)=O\left(h^4\right). \tag{36}$$

Hence, the order of the method is sustained, and it is true for $\xi\in[\xi_0,T]$.

From (26), we have

$$\left|[P(\xi)]_l(\alpha)\right|<\left|m_{j-1}h-m_jh+\left(\left[[u(\xi)]_l\right]_{j-1}(\alpha)\right)+\left(\left[[u(\xi)]_l\right]_j(\alpha)\right)\right|, \tag{37}$$

where $\xi_{j-1}\le\xi\le\xi_j$, $\forall j=0,1,\ldots,n$.

Similarly, by considering the equations,

$$\begin{aligned}[P''(\xi_i)]_r(\alpha)&=\frac{2m_{i-1}}{h}+\frac{4m_i}{h}-\frac{6}{h^2}\left([P_r]_i-[P_r]_{i-1}\right),\\[u''(\xi_i)]_r(\alpha)&=H_\xi\left(\xi_i,[P_r]_i;\alpha\right)+H_{u(\xi)}\left(\xi_i,[P_r]_i;\alpha\right)H\left(\xi_i,[P_r]_i;\alpha\right),\end{aligned} \tag{38}$$

we get

$$\left|[P(\xi)]_r(\alpha)\right| < \left|m_{j-1}h - m_j h + \left([[u(\xi)]_r]_{j-1}(\alpha)\right) + \left([[u(\xi)]_r]_j(\alpha)\right)\right|. \tag{39}$$

Thus, from (24), we obtain

$$\left|[P(\xi)]_\alpha\right| < \left|m_{j-1}h - m_j h + [u(\xi)]_{j-1}(\alpha) + [u(\xi)]_j(\alpha)\right|, \xi \in \left[\xi_{j-1}, \xi_j\right], \quad \forall j = 0, 1, \ldots, n. \tag{40}$$

5. Numerical Illustration (Exponential Decay Problem with Decay Constant as 1)

Consider the fuzzy differential equation

$$y'(\xi) = -y(\xi), \tag{41}$$

with $y(0) = (0.5, 1, 1.5)$ as its fuzzy initial condition. Let us find the solution of (41) at $\xi = 0.2$ and 0.3.

Equation (41) can be modified into a system of ordinary differential equations as follows:

$$[y'(\xi)]_l(\alpha) = -[y(\xi)]_l(\alpha), [y(0)]_l(\alpha) = 0.5\alpha + 0.5, \tag{42}$$

$$[y'(\xi)]_r(\alpha) = -[y(\xi)]_r(\alpha), [y(0)]_r(\alpha) = 1.5 - 0.5\alpha. \tag{43}$$

The solution of these two equations collectively gives the solution of (41). Therefore, the exact solution of (41) is

$$\begin{aligned}[Y(\xi)](\alpha) &= [[Yl(\xi)](\alpha), [Yr(\xi)](\alpha)] \\ &= [(0.5\alpha + 0.5)\exp(-\xi), (1.5 - 0.5\alpha)\exp(-\xi)].\end{aligned} \tag{44}$$

Now let us compute the numerical solution of (41) by using the cubic spline method.

For simplicity, assume $h = 0.1$.

Consider equation (42), here $G(\xi, y; \alpha) = -y$ and so $G_\xi(\xi, y; \alpha) = 0$ and $G_y(\xi, y; \alpha) = -1$.

Also, $G(\xi_i, [P_l]_i; \alpha) = -[P_l]_i$.

Using (28) at $i = 1$ and $\xi = 0.1$, we get

$$20m_0 + 40m_1 - 600\left([P_l]_1 - [P_l]_0\right) = [P_l]_1. \tag{45}$$

Since $m_i = [P_l]'(\xi_i), m_0 = -0.5\alpha - 0.5$ and $m_1 = -[P_l]_1$, the above equation on simplification gives

$$[P_l]_1 = \frac{290\alpha + 290}{641}. \tag{46}$$

Similarly, at $i = 2$ and $\xi = 0.2$, (28) becomes

$$[P_l]_2 = \frac{1}{641^2}(168200\alpha + 168200). \tag{47}$$

This is the approximate solution of (42) at $\xi = 0.2$.

By using (42) at $i = 3$, we obtain

$$20m_2 + 40m_3 - 600\left([P_l]_3 - [P_l]_2\right) = [P_l]_3, \tag{48}$$

where $m_2 = -[P_l]_2$ and $m_3 = -[P_l]_3$. This equation gives the approximate solution of (42) at $\xi = 0.3$.

Now consider equation (43), here $H(\xi, y; \alpha) = -y$, and hence, $H_\xi(\xi, y; \alpha) = 0$, $H_y(\xi, y; \alpha) = -1$, and $H(\xi_i, [P_r]_i; \alpha) = -P_i$.

By using (29) at $i = 1$ and $\xi = 0.1$, we obtain

$$[P_r]_1 = \frac{-290\alpha + 870}{641}, \tag{49}$$

where $m_i = [P_r]'(\xi_i)$, for all i.

From (29), taking $i = 2$ and $\xi = 0.2$, we have

$$\begin{aligned}&20m_1 + 40m_2 - 600\left([P_r]_2 - [P_r]_1\right) = [P_r]_2, \\ &\therefore [P_r]_2 = \frac{1}{641^2}(-168200\alpha + 504600) \text{ (on simplification).}\end{aligned} \tag{50}$$

Similarly, for $i = 3$ and $\xi = 0.3$ in (29), we get

$$20m_2 + 40m_3 - 600\left([P_r]_3 - [P_r]_2\right) = [P_r]_3, \tag{51}$$

where $m_2 = -[P_r]_2$ which is given by (50) and $m_3 = -[P_r]_3$. This equation on further simplification gives the approximate solution of (43) at $\xi = 0.3$.

Tables 1 and 2 represent the comparison of the solutions for equation (41) that are obtained by exact, cubic spline method and Taylor's method of order, $p = 2$ at $\xi = 0.2$ with $h = 0.1$. Comparison of exact and cubic spline solutions at $\xi = 0.2$ is graphically given in Figure 1. Similarly, Figure 2 interprets the compared results of exact and cubic spline at $\xi = 0.3$ of step length $h = 0.1$.

In general, the numerical solution of the fuzzy differential equation by using the cubic spline method can be given as

$$[P_i]_\alpha = [[P_l]_i(\alpha), [P_r]_i(\alpha)], \tag{52}$$

where $i = 1, 2, \ldots, n$, i.e., $[P(\xi)](\alpha) = [[Pl(\xi)](\alpha), [Pr(\xi)](\alpha)]$, for a fixed ξ.

Table 1: Comparison of the results (approximated to 9 decimals) obtained by exact, cubic spline method and Taylor's method of order, $p = 2$ at $\xi = 0.2$ with $h = 0.1$ for equation (42).

α-cut	Exact solution Yl	Cubic spline Pl	Taylor solution Tl for $p = 2$
0.0	0.409365377	0.409364268	0.409512500
0.1	0.450301914	0.450300695	0.450463750
0.2	0.491238452	0.491237122	0.491415000
0.3	0.532174990	0.532173549	0.532366250
0.4	0.573111527	0.573109976	0.573317500
0.5	0.614048065	0.614046403	0.614268750
0.6	0.654984602	0.654982830	0.655220000
0.7	0.695921140	0.695919256	0.696171250
0.8	0.736857678	0.736855683	0.737122500
0.9	0.777794215	0.777792110	0.778073750
1.0	0.818730753	0.818728537	0.819025000

Table 2: Comparison of the results (approximated to 9 decimals) obtained by exact, cubic spline method and Taylor's method of order, $p = 2$ at $\xi = 0.2$ with $h = 0.1$ for equation (43).

α-cut	Exact solution Yr	Cubic spline Pr	Taylor solution Tr for $p = 2$
0.0	1.228096130	1.228092805	1.228537500
0.1	1.187159592	1.187156379	1.187586250
0.2	1.146223054	1.146219952	1.146635000
0.3	1.105286517	1.105283525	1.105683750
0.4	1.064349979	1.064347098	1.064732500
0.5	1.023413441	1.023410671	1.023781250
0.6	0.982476904	0.982474244	0.982830000
0.7	0.941540366	0.941537818	0.941878750
0.8	0.900603828	0.900601391	0.900927500
0.9	0.859667291	0.859664964	0.859976250
1.0	0.818730753	0.818728537	0.819025000

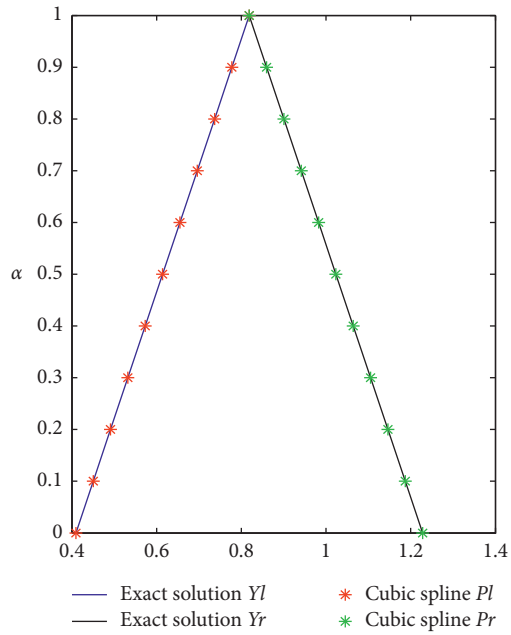

Figure 1: Comparison of exact and cubic spline solutions at $\xi = 0.2$.

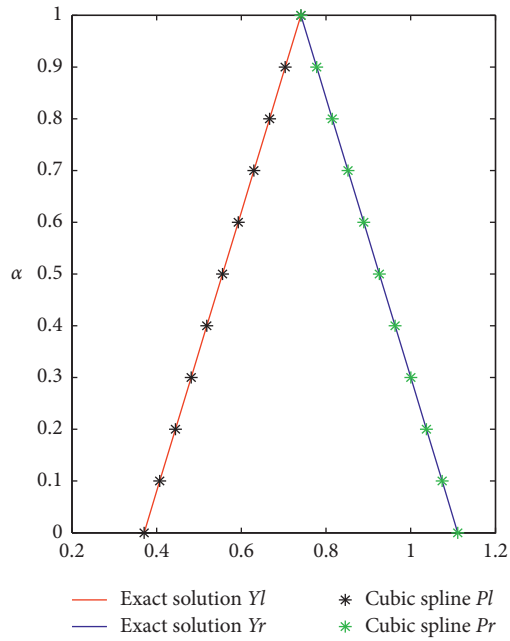

Figure 2: Comparison of exact and cubic spline solutions at $\xi = 0.3$ for $h = 0.1$.

6. Conclusion

In this article, a new class of cubic spline function method is introduced for solving fuzzy differential equations subject to fuzzy initial conditions. The desired solution which is obtained is of $O(h^4)$ convergence based on certain conditions on the derivatives. This numerical method is verified with an example, and the results are compared with the exact as well as with the solution obtained by Taylor's method of order, $p = 2$. From the comparison of results, one can conclude that the proposed method is a single-step method that converges faster and has greater accuracy than the Taylor method of order two. In future, one can extend this method to solve higher-order linear and nonlinear fuzzy initial value problems.

Data Availability

No data were used to support the findings of the study.

Conflicts of Interest

The authors declare that they have no conflicts of interest.

Authors' Contributions

All authors contributed equally to this work. And, all the authors have read and approved the final version manuscript.

Acknowledgments

This research was funded by the Deanship of Scientific Research at Princess Nourah Bint Abdulrahman University through the Fast-Track Research Funding Program.

References

[1] S. N. Sivanandam, S. Sumathi, and S. N. Deepa, *Introduction to Fuzzy Logic Using MATLAB*, Springer, Berlin Heidelberg, 2007.

[2] L. A. Zadeh, "Fuzzy sets," *Information and Control*, vol. 8, no. 3, pp. 338–353, 1965.

[3] S. S. L. Chang and L. A. Zadeh, "On fuzzy mapping and control," *IEEE Transactions on Systems, Man, and Cybernetics*, vol. SMC-2, no. 1, pp. 30–34, 1972.

[4] A. Kandel and W. J. Byatt, "Fuzzy differential equations," in *Proceedings of the International Conference Cybernetics and Society*, pp. 1213–1216, Tokyo-Kyoto, Japan, November 1978.

[5] B. Bede, "Fuzzy differential equations," *Mathematics of Fuzzy Sets and Fuzzy Logic*, vol. 295, pp. 171–191, 2013.

[6] O. Kaleva, "The cauchy problem for fuzzy differential equations," *Fuzzy Sets and Systems*, vol. 35, no. 3, pp. 389–396, 1990.

[7] S. Seikkala, "On the fuzzy initial value problem," *Fuzzy Sets and Systems*, vol. 24, no. 3, pp. 319–330, 1987.

[8] S. Song and C. Wu, "Existence and uniqueness of solutions to Cauchy problem of fuzzy differential equations," *Fuzzy Sets and Systems*, vol. 110, no. 1, pp. 55–67, 2000.

[9] J. J. Buckley and T. Feuring, "Fuzzy differential equations," *Fuzzy Sets and Systems*, vol. 110, no. 1, pp. 43–54, 2000.

[10] D. O'Regan, V. Lakshmikantham, and J. Nieto, "Initial and boundary value problems for fuzzy differential equations," *Nonlinear Analysis: Theory, Methods & Applications*, vol. 54, no. 3, pp. 405–415, 2003.

[11] S. Melliani and L. S. Chadli, "Intuitionistic fuzzy differential equation," *Notes on Intuitionistic Fuzzy Sets*, vol. 6, no. 2, pp. 37–41, 2000.

[12] S. Chakraverty, S. Tapaswini, and D. Behera, *Fuzzy Differential Equations and Applications for Engineers and Scientists*, CRC Press, Taylor & Francis Group, Boca Raton, FL, USA, 2017.

[13] M. Ahamed and M. Hasan, "A new fuzzy version of Euler's method for solving differential equations with fuzzy initial values," *Sians Malaysiana*, vol. 40, pp. 651–657, 2011.
[14] S. Abbasbandy and T. A. Viranloo, "Numerical solutions of fuzzy differential equations by Taylor method," *Computational Methods in Applied Mathematics*, vol. 2, no. 2, pp. 113–124, 2002.
[15] T. Allahviranloo, N. Ahmady, and E. Ahmady, "Numerical solution of fuzzy differential equations by predictor-corrector method," *Information Sciences*, vol. 177, no. 7, pp. 1633–1647, 2007.
[16] R. Ezzati, K. Maleknejad, S. Khezerloo, and M. Khezerloo, "Convergence, consistency and stability in fuzzy differential equations," *Iranian Journal of Fuzzy Systems*, vol. 12, no. 7, pp. 95–112, 2015.
[17] L. T. Gomes, L. Carvalho de Barros, and B. Bede, *Fuzzy Differential Equations in Various Approaches*, Springer, New York, NY, USA, 2015.
[18] O. Kaleva, "A note on fuzzy differential equations," *Nonlinear Analysis: Theory, Methods & Applications*, vol. 64, no. 5, pp. 895–900, 2006.
[19] J. H. Ahlberg, E. N. Nilson, and J. L. Walsh, *The Theory of Splines and Their Applications*, Academic Press INC., London, UK, 1967.
[20] P. Kandaswamy, K. Thilagavathy, and K. Gunavathi, *Numerical Methods*, S. Chand & Company Pvt.Ltd, New Delhi, India, 2008.
[21] F. Patrício, "Cubic spline functions and initial value problems," *BIT*, vol. 18, no. 3, pp. 342–347, 1978.
[22] S. S. Sastry, *Introductory Methods of Numerical Analysis*, PHI Learning Private Limited, New Delhi, India, 5th edition, 2012.

Hindawi
Mathematical Problems in Engineering
Volume 2021, Article ID 5540584, 6 pages
https://doi.org/10.1155/2021/5540584

Research Article

On Some Structural Components of Nilsolitons

Hulya Kadioglu

Department of Mathematics Education, Yildiz Technical University, Esenler 34210, Istanbul, Turkey

Correspondence should be addressed to Hulya Kadioglu; kadiogluhulya@gmail.com

Received 17 February 2021; Accepted 7 April 2021; Published 17 May 2021

Academic Editor: Mustafa Inc

In this paper, we study nilpotent Lie algebras that admit nilsoliton metric with simple pre-Einstein derivation. Given a Lie algebra η, we would like to compute as much of its structure as possible. The structural components we consider in this study are the structure constants, the index, and the rank of the nilsoliton derivations. For this purpose, we prove necessary or sufficient conditions for an algebra to admit such metrics. Particularly, we prove theorems for the computation of the Jacobi identity for a given algebra so that we can solve the system of the equation(s) and find the structure constants of the nilsoliton.

1. Introduction

On any Lie group, it is possible to define several different Riemannian metrics. Considering any Riemannian metrics, Einstein metrics are the most preferable metrics, as the Ricci tensor complies the Einstein metric: $\mathrm{Ric} = cg$, for some constant $c \in \mathbb{R}$. But, it is not possible to define Einstein metrics on nonabelian nilpotent Lie algebras; therefore, we consider the following weaker condition on a left invariant metric g on a nilpotent Lie group G:

$$\mathrm{Ric}_g = \beta I + D, \tag{1}$$

for some $\beta \in \mathbb{R}$ and $D \in \mathrm{Der}(\eta)$, where Ric_g denotes the Ricci operator of (η, g), η is the Lie algebra of G, and $\mathrm{Der}(\eta)$ denotes the Lie algebra of derivations of η. Equation (1) is called the nilsoliton condition, D is called the nilsoliton derivation, and β is called the nilsoliton constant.

Nilsoliton metric Lie algebras are unique up to isometry and scaling. This is one of the reasons that makes nilsolitons an important topic. On the other hand, there is a one to one correspondence between Einstein nilradicals with nilsolitons. In [1], Theorem 2.11 states that a nilpotent Lie algebra η is an Einstein nilradical if and only if η admits a nilsoliton metric. Therefore, it indicates that classification of nilsoliton metrics on a nilpotent Lie algebra is equivalent to the same of Einstein nilradicals. Additionally, if δ is Einstein solvmanifold, then the metric restricted to the submanifold can completely be determined by the nilsoliton metric Lie algebra $\eta = [\delta, \delta]$. On the contrary, any nilsoliton can uniquely extend to an Einstein solvmanifold. Therefore, the study of solvmanifolds is actually the study of nilsolitons. See [1, 2], for a survey on nilsoliton metric Lie algebras.

There are three methods to represent a Lie algebra and its related structures: representing a Lie algebra as a linear Lie algebra, i.e., subalgebra of $\mathrm{gl}(n)$, using table of its structure constants or using generators and relations [3]. In this paper, we use the table of structure constants related to a Lie algebra. The main reason is that this representation helps one to create and classify Lie algebras by the computer software programs as in [4–6]. We vary the Lie algebra structure by finding structure constants. Namely, we determine a Lie algebra η with a fixed basis $\{X_i : 1 \le i \le n\}$ explicitly by given multiplication table, consisting of structure constants α_{ij}^k which are defined by the relations

$$\left[X_i, X_j\right] = \sum \alpha_{ij}^k X_k. \tag{2}$$

In this work, the nonzero structure constants are encoded by using the index set $\Lambda = \left\{(i, j, k) | \alpha_{ij}^k \neq 0, i < j < k\right\}$, ignoring repetitions due to skew-symmetry. While indexing the structure constants, we use triples $(i, j, k) \in \Lambda$ such that $i < j < k$, and if $(i, j, k), (i, j, m) \in \Lambda$, then $k = m$ and $(i, j_1, k), (i, j_2, k) \in \Lambda$, then $j_1 = j_2$. For this purpose, we fix a basis $\{X_1, \ldots, X_n\}$ for a nilpotent Lie algebra η with $[Xi, Xj] = \sum \alpha_{ij}^k X_k \neq 0$ such that for every

$i, j, \#\{k: \alpha_{ij}^k \neq 0\} \leq 1$, and for every $i, k, \#\{j: \alpha_{ij}^k \neq 0\} \leq 1$. Such basis $\{X_j\}$ is called nice and defined by Nikolayevsky in [7]. In our paper, we call this basis as "Nikolayevsky basis." Using this special basis, we do not need to use sum symbol in equation (2).

In this paper, we prove theorems regarding to some structural components of nilsolitons for possible algorithmic approach in classifications. In particular, we present some new concepts and theorems regarding to create Jacobi identity equations for a given nilsoliton metric Lie algebra. We also present methods for the computations of the index and the rank of a nilsoliton. We provide several examples to illustrate the newly proposed concepts and methods.

This paper consists of four sections. In the second section, we present preliminary background. In the third section, we prove necessary theorems that help us to calculate structural elements of nilsolitons. In the last section, we present concluding statements.

2. Preliminaries

Let $(\eta_\mu, <, >)$ be a metric algebra, where $\mu \in \Lambda^2\eta \otimes \eta^*$. Let $B = \{X_i\}_{i=1}^n$ be a $\langle, \rangle$-orthonormal basis of η_μ (we always assume that basis is ordered). The nil-Ricci endomorphism Ric_μ is defined as $\langle \mathrm{Ric}_\mu X, Y\rangle > = \mathrm{ric}_\mu(X, Y)$, where

$$\mathrm{ric}_\mu(X,Y) = -\frac{1}{2}\sum_{i=1}^{n}\langle [X, X_i], [Y, X_i]\rangle + \frac{1}{4}\sum_{i=1}^{n}\langle [X_i, X_j], X\rangle\langle [X_i, X_j], Y\rangle, \tag{3}$$

for $X, Y \in \eta$. When η is a nilpotent Lie algebra, the nil-Ricci endomorphism is the Ricci endomorphism. If all elements of the basis are eigenvectors for the nil-Ricci endomorphism Ric_μ, we call the orthonormal basis a Ricci eigenvector basis.

Let $\mathrm{Der}(\eta)$ denote the derivation algebra of η. A maximal abelian subalgebra of $\mathrm{Der}(\eta)$ comprised of semisimple elements which is called a maximal torus. The dimension of a maximal torus is called the rank of η.

In the following, we define root vectors and root matrix, Gram matrix, Nikolayevsky basis.

Definition 1. Suppose that $\Lambda = \{(i, j, k) | \alpha_{ij}^k \neq 0, i < j < k\}$ is a finite set which indexes the set of nonzero structure constants corresponding to a Lie algebra η, ignoring repetitions due to skew-symmetry. For $1 \leq i, j, k \leq n$, we define $1 \times n$ row vector y_{ij}^k to be $\epsilon_i^T + \epsilon_j^T - \epsilon_k^t$, where $\{\epsilon\}_{i=1}^n$ is the standard orthonormal basis for $\mathbb{R}^n$. We call the vectors in $\{y_{ij}^k | (i, j, k) \in \Lambda\}$ root vectors for Λ. Let $y_1, y_2, \ldots, y_m$ (where $m = |\Lambda|$) be an enumeration of the root vectors in dictionary order. We define root matrix Y_Λ for Λ to be the $m \times n$ matrix whose rows are the root vectors $y_1, y_2, \ldots, y_m$.

The Gram matrix U_Λ for Λ is the $m \times m$ matrix defined by $U_\Lambda = Y_\Lambda Y_\Lambda^T$; the (i, j) entry of U_Λ is the inner product of the i th and j th root vectors (unless otherwise stated, the matrix U means the Gram matrix corresponding to the index set Λ. Therefore, from now on, we do not use U_Λ). From Theorem 5, in [8], we know that U is a symmetric matrix where its all diagonal entries are 3 and its off-diagonal entries are in the set $\{-2, -1, 0, 1, 2\}$.

Nikolayevsky showed that every Lie algebra admitting a derivation with all the eigenvalues of multiplicity one has a nice basis [7]. We use this type of basis in our study. This way our Gram matrices corresponding to metric nilpotent Lie algebras does not have a 2 and -2 as an entree (Lemma 2 in [4]).

Now, suppose that $|\Lambda| = m$ and $[1]_m$ represents a column vector $\begin{bmatrix} 1 & 1 & 1 & \ldots & 1 \end{bmatrix}^T$ in $\mathbb{R}^m$.

Theorem 1 (Theorem 1 in [8]). Let η be a nonabelian metric algebra with Ricci eigenvector basis B. Let U and $[\alpha^2]$ be the Gram matrix and the structure vector for η with respect to B. Then, η satisfies the nilsoliton condition with nilsoliton constant β if and only if $U[\alpha^2] = 2\beta[1]_m$.

The above theorem indicates a Lie algebra η which admits a nilsoliton metric iff there exists a solution $v \in \mathbb{R}^m$ of the linear system $Uv = [1]_m$ where all entries are positive real numbers.

3. The Structural Elements

In this section, we introduce notions and prove theorems for the computation structural elements of the nilsoliton metric Lie algebras.

3.1. The Jacobi Identity(s). Now, we present the theorems which help to create possible Jacobi identity equations.

Theorem 2 (see [8]). Let η be an n-dimensional vector space; $B = \{X_i\}_{i=1}^n$ be a basis for η. Suppose that a set of nonzero structure constants $\alpha_{i,j}^k$ relative to B, indexed by Λ, defines a skew symmetric product on η. Assume that if $(i, j, k) \in \Lambda$, then $i < j < k$. Then, η is a Lie algebra if and only if whenever there exists m so that the inner product of root vectors $\langle y_{ij}^l, y_{lk}^m\rangle = -1$ for triples (i, j, l) and (l, k, m) or (k, l, m) in Λ, the equation

$$\sum_{s<m} \alpha_{i,j}^s \alpha_{s,k}^m + \alpha_{j,k}^s \alpha_{s,i}^m + \alpha_{k,i}^s \alpha_{s,j}^m = 0, \tag{4}$$

holds. Furthermore, a term of form $\alpha_{i,j}^l \alpha_{l,k}^m$ is nonzero if and only if $\langle y_{i,j}^l, y_{l,k}^m\rangle = -1$.

Lemma 1 (Lemma 2.8 in [4]). Let η be an n-dimensional nonabelian nilpotent Lie algebra. Suppose that η admits a derivation D having distinct real positive eigenvalues. Let B be a basis consisting of eigenvectors for the derivation D, and let Λ index the nonzero structure constants with respect to B. Let Y be the $m \times n$ root matrix for Λ. If $\mathrm{rank}(Y) = m$, then the following hold:

(1) $|\Lambda| \leq n - 1$.

(2) *If* $(i_1, j_1, k_1) \in \Lambda$ *and* $(i_2, j_2, k_2) \in \Lambda$, *then* $\langle y_{i_1 j_1}^{k_1}, y_{i_2 j_2}^{k_2}\rangle \neq -1$.

Remark 1. The reverse of Lemma 1 is not true.

Proof. Suppose that η is an algebra which is indexed by the following index set:

$$\Lambda = \{(1,2,5), (1,3,6), (1,5,7), (1,6,8), (2,4,7), (2,5,8), (3,4,8)\}. \tag{5}$$

Its corresponding Gram matrix is as follows:

$$\begin{pmatrix} 3 & 1 & 0 & 1 & 1 & 0 & 0 \\ 1 & 3 & 1 & 0 & 0 & 0 & 1 \\ 0 & 1 & 3 & 1 & 1 & 1 & 0 \\ 1 & 0 & 1 & 3 & 0 & 1 & 1 \\ 1 & 0 & 1 & 0 & 3 & 1 & 1 \\ 0 & 0 & 1 & 1 & 1 & 3 & 1 \\ 0 & 1 & 0 & 1 & 1 & 1 & 3 \end{pmatrix}. \tag{6}$$

It is a singular matrix with nullity = 1. Also, it does not have -1 entry. From Theorem 2, it is a Lie algebra. Also, since the solution space of $U.v = [1]$ is

$$\left\{v = \left(t + \frac{1}{19}, \frac{6}{19} - t, t, \frac{5}{19} - t, \frac{5}{19} - t, \frac{3}{19}, t\right) \mid 0 < t < \frac{5}{19}\right\}, \tag{7}$$

from [8] that it is a nilsoliton metric Lie algebra with the magnitudes of the structure constants

$$\begin{aligned} \left|\alpha_{1,2}^{5}\right| &= t + \frac{1}{19}, \\ \left|\alpha_{1,3}^{6}\right| &= \frac{6}{19} - t, \\ \left|\alpha_{1,5}^{7}\right| &= t, \\ \left|\alpha_{1,6}^{8}\right| &= \frac{5}{19} - t, \\ \left|\alpha_{2,4}^{7}\right| &= \frac{5}{19} - t, \\ \left|\alpha_{2,5}^{8}\right| &= \frac{3}{19}\left|\alpha_{3,4}^{8}\right| = t, \end{aligned} \tag{8}$$

with simple derivation of type $7 < 10 < 13 < 14 < 17 < 20 < 24 < 27$ with singular Gram matrix U and $|\Lambda| = n - 1$. □

The counter example provided in Remark 1 illustrates none of the inner products of root vectors being -1 does not imply that the Gram matrix of the nilsoliton is nonsingular. Additionally, if the cardinality of the index set $|\Lambda| \leq n$, -1 does not imply that the Gram matrix is nonsingular.

3.1.1. Constructing the System of Jacobi Identities. In order an algebra to be a Lie algebra, one needs to satisfy the Jacobi identity. Using our index set Λ, the corresponding Jacobi identity turns into equation (4). Also, there has to be at least two product couples in the Jacobi identity. Otherwise, if there is one product couple in Jacobi identity, it leads to $\alpha_{i,j}^{s}\alpha_{s,k}^{m} = 0$; therefore, it contradicts to the fact that $(i, j, s), (s, k, m) \in \Lambda$. On the other hand, the Jacobi identity is created by each vector triples from the given fixed Nikolayevsky basis. For example, the Jacobi identity for X_i, X_j, X_k is

$$\alpha_{ij}^{s}\alpha_{sk}^{m} + \alpha_{jk}^{s}\alpha_{si}^{m} + \alpha_{ki}^{s}\alpha_{sj}^{m} = 0. \tag{9}$$

Since we use the Nikolayevsky basis, there is a unique k which appears in equation (9). Therefore, each Jacobi identity is created with fixed X_i, X_j, X_k, and $m \in$ AoM. Also, because there has to be at least one product couple in the Jacobi identity, then there exist 2 or three product couples in the Jacobi identity. In equation (9), the product couple $\alpha_{ij}^{s}\alpha_{sk}^{m}$ corresponds to the index triples in Λ such that $(i, j, s), (s, k, m) \in \Lambda$, or $(i, j, s), (k, s, m) \in \Lambda$. In the following definition, we define the set of all product couples P_m related to the Jacobi identity for a given subset X_i, X_j, X_k of the fixed basis. As one can see, there exist at most 3 product couples in the same Jacobi identity.

Definition 2. If there are t product couples in the Jacobi identity for the same m such that $(i, j, s), (s, k, m) \in \Lambda$, or $(i, j, s), (k, s, m) \in \Lambda$, then the Jacobi identity which was created by the basis vectors $\{X_i, X_j, X_k\}$. Now, we define the set of all nonzero product couples for a given index triple basis vectors X_i, X_j, X_k as follows:

$$P_m = \left\{p_s = \left|\alpha_{ij}^{s}\alpha_{s,k}^{m}\right|, 1 \leq s \leq n, p_s \neq 0\right\}. \tag{10}$$

It is called set of product couples for $\#m$ and for in equation (4):

$$\text{AoM} = \{m \in \mathbb{N}: (i, j, s), (s, k, m) \in \Lambda \text{ or } (i, j, s), (k, s, m) \in \Lambda\}. \tag{11}$$

Here, AoM is the matrix of $\#m$ that appears in equation (4).

Remark 2. Let η be an algebra that is indexed by Λ, then the Jacobi identity for a given X_i, X_j, X_k with each $m \in$ AoM is given by

$$p_1 \mp p_2 \mp p_3 = 0. \tag{12}$$

The proof of Remark 2 follows from the definition of Jacobi identity for a given algebra.

Theorem 3. *Let η be an algebra that is indexed by Λ, and U be the Gram matrix related to Λ. Let v_p belong to the solution space to the linear system $Uv = [1]$, then the Jacobi identity for each $m \in$ AoM is given by*

$$\sqrt{v_{i_1}v_{j_1}} \mp \sqrt{v_{i_2}v_{j_2}} \mp \sqrt{v_{i_3}v_{j_3}} = 0, \tag{13}$$

where $1 \leq i_1, i_2, i_3, j_1, j_3 \leq |\Lambda|$.

Proof. Let η be an algebra that is indexed by Λ. By Remark 3, the Jacobi identity for each $m \in$ AoM and each basis vector triple X_i, X_j, X_k is given by

$$p_1 \mp p_2 \mp p_3 = 0. \tag{14}$$

Here, $p_s = \alpha_{ij}^s \alpha_{s,k}^m$. By Theorem 1, the solution vectors of the linear system $Uv = [1]$ are the squares of the structure vectors α_{ij}^s for all $(i, j, s) \in \Lambda$. Therefore, for any v that satisfies $Uv = [1]$ is of form $v = (\alpha_{i,j}^s)^2$. Thus, for each $p_s \in P_m$,

$$p_s = \sqrt{v_a v_b}, \tag{15}$$

where $a, b \in \{i_1, i_2, i_3, j_1, j_3\}$, and $v_a = (\alpha_{ij}^s)^2$ and $v_b = (\alpha_{sk}^m)^2$. Solving the equations for the structure constants, we have

$$\alpha_{ij}^s = \mp\sqrt{v_a}, \tag{16}$$

for all $(i, j, s) \in \Lambda$. Therefore, equation (12) turns into

$$\sqrt{v_{i_1} v_{j_1}} \mp \sqrt{v_{i_2} v_{j_2}} \mp \sqrt{v_{i_3} v_{j_3}} = 0, \tag{17}$$

which finishes the proof. □

In some cases, there can be more than two square root product couples in equation (13), i.e., there is more than one $m \in$ AoM. In that case, we need to consider all the cases of the signs between the product couples $\alpha_{i,j}^s \alpha_{s,k}^m$, $\alpha_{j,k}^s \alpha_{s,i}^m$, and $\alpha_{k,i}^s \alpha_{s,j}^m$. The following lemma deals with this matter.

Lemma 2. *If there are k product couples in the Jacobi identity, then there are $2^{k-1} - 1$ possible sign choices.*

Proof. Suppose that $p_i \in P_m$ for m in equation (4) where P_m is the set of all product couples, as in Definition 2. Therefore, the Jacobi identity turns into $p_1 \mp p_2 \mp p_3 = 0$. Without loss of generality, we assume that $p_1 > 0$. For each $p_s \in P_m$, where $2 \le s \le n$, there are two possible sign choices $\{+, -\}$. Therefore, we have 2^{t-1} possible sign choices. Since all the product couples are nonzero, then they can not all be $+$. Therefore, we drop the case $(+, +, \ldots, +)$. Thus, there are $2^{t-1} - 1$ possible sign choices for the set P_m.

As we know that there is at most three, at least two product couples in the Jacobi identity, the there is at most three different sign choices for a Jacobi identity. □

Definition 3. We define the matrix of all sign choices $SC = [s_{js}] \in M_{(2^{t-1}-1)\times(t-1)}$ matrix where the entries are of the form

$$s_{js} = \begin{cases} 1, & p_s > 0, \\ 0, & p_s < 0, \end{cases} \tag{18}$$

for $1 \le j \le 2^{t-1} - 1$. For example, if $P_m = \{p_1, p_2, p_3\}$, then SC is a 3×2 matrix

$$SC = \begin{pmatrix} 1 & 0 \\ 0 & 1 \\ 0 & 0 \end{pmatrix}. \tag{19}$$

The equations are created by

$$\begin{aligned} p_1 + (-1)^{SC(1,1)}.p_2 + (-1)^{SC(1,2)}.p_3 = 0, \\ p_1 + (-1)^{SC(2,1)}.p_2 + (-1)^{SC(2,2)}.p_3 = 0, \\ p_1 + (-1)^{SC(3,1)}.p_2 + (-1)^{SC(3,2)}.p_3 = 0. \end{aligned} \tag{20}$$

Therefore, we have $p_1 + p_2 - p_3 = 0$, $p_1 - p_2 + p_3 = 0$, and $p_1 - p_2 - p_3 = 0$. If there is more than one array of number m's in equation (4) in Theorem 2, then one needs to find common solutions of at least one Jacobi identity that was created by SC matrix for each m. To illustrate the above procedure, we have the following example.

Example 1. Suppose that

$$\begin{aligned} \Lambda = \{&(1,3,4), (1,4,5), (1,5,6), (2,3,6), (1,6,7), \\ &(2,4,7), (1,7,8), (2,5,8)\}. \end{aligned} \tag{21}$$

The solution of the equation $Uv = [1]$ is of the form

$$\begin{aligned} v &= \left(x + y - 1/5 \;\; 1/55 + x \;\; 1/11 \;\; 31/55 - x - y \;\; 32/55 - x - y \;\; y \;\; 4/11 - x \;\; x \right)^T, \\ &= \left((\alpha_{12}^4)^2 \;\; (\alpha_{13}^5)^2 \;\; (\alpha_{16}^7)^2 \;\; (\alpha_{17}^8)^2 \;\; (\alpha_{25}^6)^2 \;\; (\alpha_{26}^8)^2 \;\; (\alpha_{34}^6)^2 \;\; (\alpha_{45}^8)^2 \right)^T, \end{aligned} \tag{22}$$

where x, y are parameters of the solution system. Then, there are two m's in equation (4). Now, let us denote the set of m as AoM. Therefore, AoM $= \{7, 8\}$. Each $m \in$ AoM corresponds to a Jacobi identity. For $m = 7$, we have two product couples of the triples (i, j, l) and (l, k, m) or (k, l, m) in Λ. They are $(2,3,6)(1,6,7)$ and $(1,3,4)(2,4,7)$. Therefore, the first Jacobi identity is

$$\left(\alpha_{23}^6\right)\left(\alpha_{16}^7\right) \pm \left(\alpha_{13}^4\right)\left(\alpha_{24}^7\right) = 0. \tag{23}$$

For $m = 8$, we have two product couples of the triples (i, j, l) and (l, k, m) or (k, l, m) in Λ. They are $(2,4,7)(1,7,8)$ and $(1,4,5)(2,5,8)$. So, the corresponding Jacobi identity is

$$\left(\alpha_{24}^7\right)\left(\alpha_{17}^8\right) \pm \left(\alpha_{14}^5\right)\left(\alpha_{25}^8\right) = 0. \tag{24}$$

It can easily be seen that there is a unique sign choice for the above equations. The common solution is as follows:

$$\begin{aligned}
\alpha_{13}^{4} &= \sqrt{2/11},\\
\alpha_{14}^{5} &= \sqrt{1/5},\\
\alpha_{15}^{6} &= \sqrt{1/11},\\
\alpha_{23}^{6} &= \sqrt{2/5},\\
\alpha_{16}^{7} &= \sqrt{1/5},\\
\alpha_{24}^{7} &= \sqrt{1/5},\\
\alpha_{17}^{8} &= \sqrt{2/11},\\
\alpha_{25}^{8} &= \sqrt{2/11}.
\end{aligned} \tag{25}$$

3.2. The Rank and the Index of a Nilsoliton. The following proposition and its following corollary help us to compute rank of a nilsoliton metric Lie algebra.

Proposition 1 (see Proposition 4.7 in [9]). Let η be a nonabelian Lie algebra that admits a simple derivation D. Let $B = \{Xi\}_{i=1}^{n}$ be an eigenvector basis with index set Λ, and let Y be the root matrix associated to Λ. Then, the rank of the nilsoliton metric Lie algebra η equals to the nullity of the root matrix Y.

Corollary 1. *Let η be a nonabelian n–dimensional Lie algebra that admits a simple derivation. Let B be an eigenvector basis with index set Λ, and let Y be the root matrix associated to Λ. Then,*

$$\operatorname{rank}(\eta) = n + \operatorname{nullity}\left(YY^{t}\right) - |\Lambda|. \tag{26}$$

Proof. Suppose that η is an n–dimensional nonabelian Lie algebra, admitting a simple derivation. Let B be an eigenvector basis with index set Λ where $|\Lambda| = m$, and let Y be the root matrix associated to Λ. By Proposition 1, the root matrix Y is an $m \times n$ matrix, whose nullity is $\operatorname{rank}(\eta)$. Therefore, from rank-nullity theorem, $\operatorname{rank}(\eta) = n - \operatorname{Rank}(Y)$. We also know that $\operatorname{rank}(Y) = \operatorname{rank}(YY^{T})$; therefore, we have

$$\operatorname{rank}(\eta) = n - \operatorname{Rank}\left(YY^{T}\right). \tag{27}$$

On the other hand, YY^{T} is an $m \times m$ matrix. Therefore, $\operatorname{Rank}(YY^{T}) = m - \operatorname{Nullity}(YY^{T})$. Then, we have

$$\begin{aligned}
\operatorname{rank}(\eta) &= n - \left(m - \operatorname{Nullity}\left(YY^{T}\right)\right)\\
&= n + \operatorname{Nullity}\left(YY^{T}\right) - |\Lambda|.
\end{aligned} \tag{28}$$

□

Definition 4. Let $X \in \eta$, ad_X, denote the adjoint representation and η^{*} denote the dual of the Lie algebra η. Then, the skew symmetric bilinear form Ψ_f, where $f \in \eta^{*}$, is defined by

$$\begin{aligned}
\Psi_f \colon \eta \times \eta &\longrightarrow \mathbb{R}\\
(X, Y) &\longrightarrow \Psi_f(X, Y)\\
&= f([X, Y]).
\end{aligned} \tag{29}$$

The index of a Lie algebra η is the integer $\inf\left\{\dim \eta_f \colon f \in \eta^{*}\right\}$ where $\eta_f = \ker(\Psi_f)$ defined by $\eta_f = \{X \in \eta \colon f([X, Y]) = 0, \forall y \in \eta\}$.

Proposition 2 (see Proposition 4 in [10]). The index of an n-dimensional Lie algebra η is the integer,

$$\operatorname{index}_{\eta} = n - \operatorname{Rank}_{R(\eta)}\left(\left[X_i, X_j\right]\right)_{1 \le i,j \le n}, \tag{30}$$

where $R(\eta)$ is the quotient field of symmetric algebra $S(\eta)$.

Remark 3. above proposition tells us that the index of a Lie algebra is the nullity of the matrix $E_{\eta} = ([X_i, X_j])$.

Now, we present an example regarding to this notion with the use of the index set Λ.

Example 2. Suppose that $\Lambda = \{(1, 2, 3), (1, 3, 4), (2, 3, 5)\}$ is the index set of an algebra η of dimension 6. Its corresponding Gram matrix is

$$\begin{pmatrix} 3 & 0 & 0\\ 0 & 3 & 1\\ 0 & 1 & 3 \end{pmatrix}. \tag{31}$$

Since there is no -1 entry, η is a Lie algebra. The matrix E_{η} is as follows:

$$\begin{pmatrix} 0 & X_3 & X_4 & 0 & 0 & 0\\ -X_3 & 0 & X_5 & 0 & 0 & 0\\ -X_4 & -X_5 & 0 & 0 & 0 & 0\\ 0 & 0 & 0 & 0 & 0 & 0\\ 0 & 0 & 0 & 0 & 0 & 0 \end{pmatrix}. \tag{32}$$

Its rank is 2; therefore, $\operatorname{index}_{\eta} = 4$.

Proposition 3. *For an n–dimensional nilsoliton represented by an index set Λ with a Nikolayevsky basis, the matrix E_{η} has the following properties:*

(1) The matrix is an $n \times n$ matrix with zero diagonal entries

(2) The rank of E_{η} is even

(3) The n^{th} row and column of E_{η} are zero matrices

(4) If $|\Lambda| = K$, then E_{η} has $2K$ nonzero entries

Proof. Suppose that the Nikolayevsky basis is represented by $B = \{X_{\alpha}\}_{1 \le \alpha \le n}$. By the definition of E_{η}, $E_{\eta}(i, j) = [X_i, X_j]$, then

$$\left(E_{\eta}\right)_{ij} = \left[X_i, X_j\right] = -\left[X_j, X_i\right] = -\left(E_{\eta}\right)_{ji}. \tag{33}$$

Therefore, E_{η} is a skew symmetric matrix, which implies the first and second properties. On the other hand, since η is

nilpotent Lie algebra with Nikolayevsky basis, then Λ consists of the elements of form (i, j, k) such that $i < j < k$. Therefore, n cannot appear in the first or the second component of the triples in Λ. Thus, $[X_i, X_n] = [X_n, X_i] = 0$ for all $i \in \{1, 2, \ldots, n\}$, which implies that $(E_\eta)_{in} = (E_\eta)_{ni} = 0$, i.e., the last row and the last column are zero matrices.

The entries of E_η are defined by the index set Λ. If $|\Lambda| = K$, then there exists K non-zero entries on the upper triangular part of E_η. Since the matrix is skew symmetric, then there exists other K nonzero entries in the lower triangular part of the matrix. So, in total, there exists $2K$ nonzero entries in E_η. □

Corollary 2. *Suppose that η is an n–dimensional nilsoliton. Then, index(η) is even, if n is even, and index is odd if n is odd.*

Proof. The index of the nilsoliton is $\text{index}(\eta) = \text{Nullity}(E_\eta) = n - \text{rank}(E_\eta)$. Since E_η is a skew symmetric matrix, its rank is always even, which finishes the proof. □

4. Conclusion

In this paper, we prove theorems for the computations of structural elements of an n-dimensional nilsoliton η. We prove theorems regarding to the Jacobi identity or identities that have to be satisfied, rank, and index of the nilsoliton. In the future, we plan to use these theorems to create a computer algorithm for the classifications of nilsolitons for a given dimension. The theorems appearing in this study will allow us to pare down the number of cases to consider in our procedure.

Data Availability

No data were used in this study.

Conflicts of Interest

The author declares no conflicts of interest.

References

[1] J. Lauret and E. Solvmanifolds, "In Einstein solvmanifolds and nilsolitons," *New Developments in Lie Theory and Geometry*, vol. 23, 2009.

[2] J. Lauret and C. Will, "Einstein solvmanifolds: existence and non-existence questions," *Mathematische Annalen*, vol. 350, no. 1, pp. 199–225, 2011.

[3] De Graaf and A. Willem, *Lie Algebras, Theory and Algorithms*, Elsevier, London, UK, 2000.

[4] H. Kadioglu and T. L. Payne, "Computational methods for nilsoliton metric Lie algebras I," *Journal of Symbolic Computation*, vol. 50, pp. 350–373, 2013.

[5] H. Kadioglu, "Classification of ordered type soliton metric Lie algebras by a computational approach," *Abstract and Applied Analysis*, vol. 2013, 2013.

[6] H. Kadioglu, "A computational procedure on higher-dimensional nilsolitons," *Mathematical Methods in the Applied Sciences*, vol. 42, no. 16, pp. 5390–5397, 2019.

[7] Y. Nikolayevsky, "Einstein solvmanifolds with a simple Einstein derivation," *Geometriae Dedicata*, vol. 135, no. 1, pp. 87–102, 2008.

[8] T. L. Payne, "The existence of soliton metrics for nilpotent Lie groups," *Geometriae Dedicata*, vol. 145, no. 1, pp. 71–88, 2010.

[9] T. L. Payne, "Applications of index sets and Nikolayevsky derivations to positive rank nilpotent Lie algebras," *Journal of Lie Theory*, vol. 24, no. 1, 2014.

[10] H. Adimi and A. Makhlouf, "Computing the index of Lie algebras," *Proceedings of the Estonian Academy of Sciences*, vol. 59, no. 4, pp. 265–271, 2010.

Hindawi
Mathematical Problems in Engineering
Volume 2021, Article ID 6668942, 10 pages
https://doi.org/10.1155/2021/6668942

Research Article

Computational Fluid Dynamics Analysis of Impingement Heat Transfer in an Inline Array of Multiple Jets

Parampreet Singh,[1] Neel Kanth Grover,[2] Vivek Agarwal,[2] Shubham Sharma,[2] Jujhar Singh,[2] Milad Sadeghzadeh,[3] and Alibek Issakhov[4]

[1]*Department of Mechanical Engineering, Dr. BR Ambedkar National Institute of Technology, Jalandhar, India*
[2]*Department of Mechanical Engineering, IK Gujral Punjab Technical University, Main Campus-Kapurthala, Kapurthala, India*
[3]*Department of Renewable Energy and Environmental Engineering, University of Tehran, Tehran, Iran*
[4]*Faculty of Mechanics and Mathematics, Department of Mathematical and Computer Modelling, Al-Farabi Kazakh National University, Almaty, Kazakhstan*

Correspondence should be addressed to Milad Sadeghzadeh; milad.sadeghzadeh@gmail.com

Received 19 November 2020; Revised 21 December 2020; Accepted 30 March 2021; Published 13 April 2021

Academic Editor: Alessandro Mauro

Amid all convective heat transfer augmentation methods employing single phase, jet impingement heat transfer delivers significantly higher coefficient of local heat transfer. The arrangement leading to nine jets in square array has been used to cool a plate maintained at constant heat flux. Numerical study has been carried out using RANS-based turbulence modeling in commercial CFD Fluent software. The turbulent models used for the study are three different "*k*-*ε*" models (STD, RNG, and realizable) and SST "*k*-*ω*" model. The numerical simulation output is equated with the experimental results to find out the most accurate turbulence model. The impact of variation of Reynolds number, inter-jet spacing, and separation distance has been considered for the geometry considered. These parameters affect the coefficient of heat transfer, temperature, and turbulent kinetic energy related to flow. The local "h" values have been noticed to decline with the rise in separation distance "H/*D*." The SST "*k*-*ω*" model has been noticed to be in maximum agreement with the experimental results. The average value of heat transfer coefficient "h" reduces from 210 to 193 W/m^{2}K with increase in "H/*D*" from 6 to 10 at "Re" = 9000 and S/*D* of 3. As per numerical results, inter-jet spacing "S/*D*" of 3 has been determined to be the most optimum value.

1. Introduction

The application of jet impingement because of its higher convection heat transfer rates in processes, namely, mechanical as well as chemical, has steered numerous industry applications, for instance, metal plates cooling/heating, cooling of turbine blades, industrial equipment cleaning, and cooling of Micro Electro Mechanical Systems (MEMS). Jet impingement is normally utilized in numerous industrial applications which include automobile windshield de-icing, electronic component cooling, and glassware. High convective transfer rates associated with the jet impingement has ensured the use of this technology in the fields where the heat fluxes associated are very high and the space is restricted. Heat, Ventilation, and Air-Conditioning (HVAC) is significant for building indoors, not only for adequate comfort levels and quality of air for occupants, but also in terms of the energy consumption [1–3]. Impinging Jet Ventilation (IJV) is the new technique emerging in this field which uses the idea of an impinging jet employed for cooling a heated target surface. Good number of experimental, numerical, and analytical studies have been performed. Outstanding review papers (Viskanta [4] and Zuckerman and Lior [5]) have been published with an emphasis on different issues. The transfer of heat from a single striking jet is bell shaped Gaussian distribution and thus can lead to the formation of hot spots on target surface [4, 5]. Thus, it has been established that multiple impinging jets can give rise to

better heat transfer consistency at the impingement surface. Interactions and thermal characteristics developed in multiple conventional striking jets (MCIJs) have been extensively explored. In multiple jet impingement, each impinging jet may be influenced essentially by two different kinds of interactions. First are inter-jet interactions preceding their impingement on the surface. This type of interaction is important in geometries having small inter-jet spacing and large separation distances. Second type is interaction among the wall jets of impinging jets after their impingement on surface. These primarily occur for array configurations with smaller inter-jet spacing with high velocities.

Metzger and Korstad [6] experimentally determined the effect of cross flow in multiple impinging jets on a horizontal plate. Inline circular jets with varying inter-nozzle distance and separation distance among jets and impingement plate were studied. Heat transfer coefficient is controlled with jet-diameter Reynolds number and inter-jet spacing. Li et al. [7] explored heat transfer from triangular array of jets with varying diameters on a roughened target surface. Goldstein and Timmers [8] studied a geometry of single jet bounded by a hexagonal array of six circular jets with radius of 5 mm. Behbahani and Goldstein [9] stated that at a fixed mass flow rate per jet, decreasing inter-jet spacing resulted in increased area averaged Nusselt number. Experiments carried out by Florschuetz et al. [10] indicated the direct advantages of reducing jet diameter as well as letting free space among jets for directing the spent gas flow. Obot and Trabold [11] examined effects of cross flow employing geometries with minimum, intermediate, and maximum crossflow. Goldstein and Seol [12] stated that local Nusselt number should be higher at smaller separation distance ($H/D = 2$) than at larger distance of $H/D = 6$. Slayzak et al. [13] investigated the interactions between adjacent jets using a twin jet impingement system. By varying the momentum of twin jets, oscillations were observed in the interaction zone. For a round jet at "H/D" = 2, Huber and Viskanta [14] noticed a peak in local "Nu" for a ring formed region around "r/D" = 0.5 and a second smaller peak at "r/D" = 1.6. San and Lai [15] showed that interaction between the jets produced smaller peaks in heat transfer distribution among the stagnation regions because of interactions among neighbouring jets. Geers et al. [16, 17] studied velocity flow field for the multiple array of circular jets striking on a flat horizontal plate. Results revealed interactions taking place among cross flow as well as the wall jets that led to the development of horseshoe vortices. Spring et al. [18] stated that inline arrangement is superior to staggered arrangement of jets mainly attributed to the nature of crossflow existing in the array. San and Chen [19] reported that for the rise of separation distance from 0.5 to 2, the Nusselt number maxima between central and neighbouring jets disappeared attributed mainly to the decreased interactions between adjacent jets. Florschuetz et al. [20] studied the crossflow effects with temperature difference between crossflow and impinging jets. Gardon and Akfirat [21] conducted experiments on slot jet array and presented that the definition of each jet is maintained and the peak values in heat transfer distribution differed slightly from those pertaining to single impinging jets. Lee and Lee [22] established that orifice nozzles lead to high rates of heat transfer rates in comparison to fully developed pipe flow. Weigand et al. [23] conducted experiments on multiple jet impingement instead of a single jet and determined the presence of secondary stagnation zones and vortices that result in the reduction of heat transfer rates. This flow of gas is called spent gas and these wall jets are predominant in the geometries where the small inter-jet spacing, small gap distances among nozzle plate and target plate, and large velocities are used. Chougule et al. [24] determined experimentally that the rise in "H/D" resulted in decreased heat transfer rates. Higher heat transfer rates are visible in lower "H/D" ratios because of the decrease in the impact area as the jet does not mix well with the ambient fluid. Yong et al. [25] experimentally studied the crossflow effects of spent gases in staggered and inline array schemes and demonstrated that the effects of crossflow from upstream rows of jets to downstream rows are more pronounced for a staggered array in contrast to an inline array. Computational fluid dynamics has now emerged as a powerful tool for predicting the flow situations and heat transfer characteristics. Likewise, heat transfer enhancement is also gaining popularity so as to increase the thermal performance of the systems. There are many studies conducted where heat transfer enhancement has been studied by utilizing nano-sized particles and V-ribs for solar panels [26–33]. Jet impingement also focusses on the enhancement of heat transfer using turbulence induced mixing as a means for increased heat transfer coefficient.

The literature review suggests that there are few studies available in which the effects of interactions in larger arrays of impinging jets have been investigated numerically for heat transfer characteristics. Based on this finding, the present work has been performed where an inline array of nine impinging jets has been investigated for studying the impact of interactions upon heat transfer characteristics at different inter-jet spacings ("S/D" = 2, 3, 5, and 7), separation distances ("H/D" = 6, 8, and 10), and Reynolds numbers ("Re" = 7000, 9000, and 11000).

2. Numerical Modeling

The three-dimensional flow situation has been solved using the Navier–Stokes and energy equations along with turbulence models by means of CFD software (FLUENT 6.3.26) to predict the thermal and turbulent flow fields for the flow physics. Equations (1)–(5) have been solved in the commercial Fluent CFD code [34]. The "k-ω" turbulence model has been used with shear stress transport (SST) option, and it has been found to work best for wall bounded flows than other turbulence models available. The "k-ω" turbulence model is selected because of its lesser computation requirements, simplicity, and worldwide acceptability. The flow has been considered as incompressible for the sake of simplicity, and steady-state conditions have been assumed. The gravity and radiation heating are neglected, and temperature dependence for standard thermophysical properties such as specific heat, density, and heat conductivity has

also not been considered. Figure 1(a) illustrates the detail description of the problem with the application of boundary conditions. The bottom wall of computational domain has been given a constant heat flux condition. Nine nozzles, having diameter "D" = 5 mm and length "L" = 25 mm, have been used to supply air in the form of round air jets. The velocity of the air jets has been varied with the use of different Reynolds number. These air jets exit the domain after impingement from the pressure outlets given at the sides of the domain. Likewise, the nozzle plate at the top has been assigned the constant temperature boundary condition. This plate also acts as a semiconfinement for the impinging jets. The schematic details of nozzle plate are given in Figure 1(b) for jet spacing of 15 mm corresponding to nondimensional distance of S/D = 3. The target plate has been maintained at a static heat input rate of 30 W, and all other surfaces except for the top surface are considered to be adiabatic. The governing equations for momentum, pressure, turbulent kinetic energy, specific rate of dissipation, and energy have been discretized using second-order techniques. A tetrahedral meshing scheme having y^+ values less than five and adequate near wall treatment has been employed around wall region so as to precisely resolve viscous sublayer region.

The velocity inlet boundary condition has been specified with the value of measured velocity from the Reynolds number, and static temperature of 300 K has also been assigned at the velocity inlet. No-slip criteria have been implemented at the wall surface for viscous effects. The pressure outlet boundary condition signifies the outflow of the spent flow, and it corresponds to the far field flow conditions with temperature (300 K), gauge pressure of "0" Pa relating to atmospheric conditions, and turbulence intensity of 5%. For the impingement wall, a uniform heat flux of 8333 W/m^2 (30 W for 60 × 60 mm plate) has been specified along with temperature value of 40°C at bottom surface of heat sink. The other heat sink sides are taken to be adiabatic. The temperature values thus obtained at the top surface of base plate have been appended to the computational flow domain, and simulations have been carried out with different conditions of varying inter-jet spacings, H/D, and Reynolds number.

To minimize the computational time and efforts, only quarter of the complete domain is modeled, and by using symmetry boundary conditions, the heat transfer and fluid flow characteristics can be accurately predicted. Figure 2 portrays the computational grid generated for numerical study, and Table 1 highlights different boundary conditions given at various sides of the flow domain. Numbers of cells used for the quarter domain are around 4,34,000, thus resulting in 1.7 million cells for the complete domain which are adequate to model the fluid flow. To minimize the computational efforts, thermophysical properties for air have been approximated to be constant. The SIMPLE algorithm aimed at pressure velocity coupling has been taken for solving the pressure field [34]. The convergence criterion used for residuals in momentum, energy, and turbulence parameters has been specified as 10^{-6}. The numerical calculations have been performed on a computer system having the following configuration: Intel i3 (4 core) processor, 4 GB RAM, 512 GB HDD, and 2 GB graphics. The computation time that has been taken by the computer in solving different mesh sizes is given in Table 2.

2.1. Numerical Procedure. CFD study of the multi nozzle impingement has been conducted by solving the discretized equations of mass, momentum, and energy conservation (equations (1)–(3)). RANS-based momentum equations have been solved for obtaining the flow velocities under steady-state conditions.

2.1.1. Continuity Equation.

$$\nabla.(\rho\vec{V}) = 0. \tag{1}$$

2.1.2. Momentum Equation.

$$\nabla.(\rho\vec{V}\vec{V}) = -\nabla p + \nabla.\left(\mu_{\text{eff}}\nabla\vec{V}\right). \tag{2}$$

2.1.3. Energy Equation. The energy equation is solved to obtain the temperature data in the flow field.

$$\nabla.(\vec{V}(\rho E + p)) = \nabla.\left(k_{\text{eff}}\nabla T - \sum_{j=1}^{N} h_j \vec{J}_j\right). \tag{3}$$

2.1.4. Turbulence Parameters. The turbulence in the flow has been numerically solved using two turbulence models, and the equations used for solving the turbulence parameters are given in equations (4)–(7). The turbulence parameters are calculated or predicted as per the model being used so as to calculate the value of turbulent viscosity which is then used to estimate the value of effective viscosity in equation (2). With the inclusion of this term, the velocity field can be calculated numerically as the equations are now mathematically closed. Equations (4) and (5) represent the transport equations for turbulent kinetic energy (k) and dissipation rate (ε) as used in k-ε models. Likewise, the turbulent parameters (k) and specific dissipation rate (ω) have been estimated for k-ω model as per equations (6) and (7).

$$\nabla(\rho k\vec{V}) = \nabla\left[\alpha_k\mu_{\text{eff}}\nabla k\right] + G_k - \rho\varepsilon, \tag{4}$$

$$\nabla(\rho\varepsilon\vec{V}) = \nabla\left[\alpha_\varepsilon\mu_{\text{eff}}\nabla\varepsilon\right] + C_{1\varepsilon}\frac{\varepsilon}{k}G_k - C_{2\varepsilon}\rho\frac{\varepsilon^2}{k} - R_\varepsilon, \tag{5}$$

$$\nabla(\rho k\vec{V}) = \nabla\left[\alpha_\varepsilon\mu_{\text{eff}}\nabla k\right] + G_k - Y_k + S_k, \tag{6}$$

$$\nabla(\rho\omega\vec{V}) = \nabla\left[\alpha_\varepsilon\mu_{\text{eff}}\nabla\omega\right] + G_\omega - Y_\omega + S_\omega. \tag{7}$$

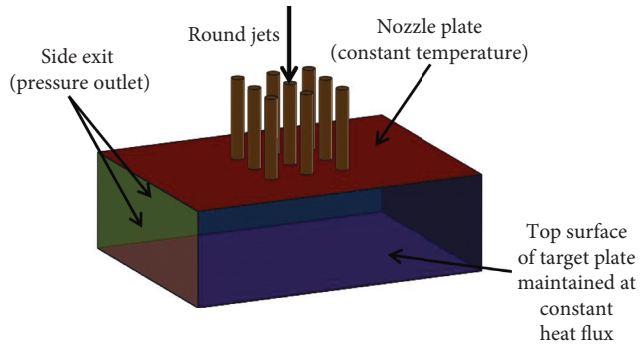

Figure 1: Physical description and boundary conditions at various surfaces.

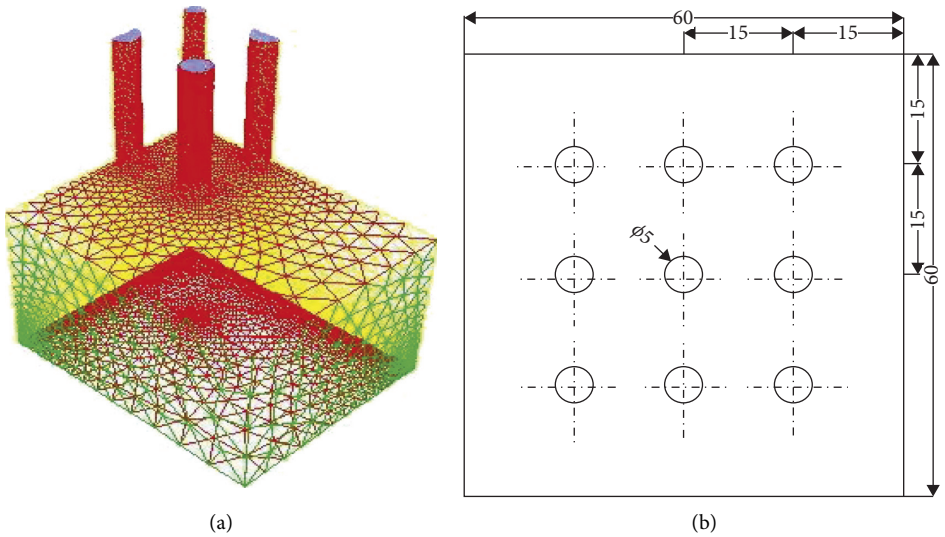

(a) (b)

Figure 2: (a) Computational mesh generated for the numerical computation and (b) schematic view of nozzle plate being used.

3. Numerical Results

Numerical study has been executed to explore the impact of variation in "S/*D*," "H/*D*," and "Re" upon heat transfer characteristics. For the validation of numerical results, Table 3 highlights the average heat transfer coefficient values compared to the experimental output of Chougule et al. [24] along with the errors at fixed conditions corresponding to "H/*D*" of 8, S/*D* of 3, and Re of 9000. On the basis of these results, k-ω "SST" model has been implemented for numerical simulations. Likewise, local coefficient of heat transfer has also been plotted against nondimensional distance along x-axis (Figure 3) for "H/*D*" = 6 and Re = 9000.

3.1. Impact of Separation Distance (H/D). The impact of separation distance (H/*D*) among the nozzle and the target plate has been explored by varying "H/*D*" at the same "S/*D*" and Reynolds number. The rise in separation distance resulted in decreased rate of heat transfer as the increase in the separation improves the interaction among the jets and the surroundings, and thus velocity of the jet decreases owing to increased momentum exchange. The values of coefficient of heat transfer as well as Nusselt number should thus decline at stagnation regions. Figure 4 shows the distribution of heat transfer coefficient and turbulent kinetic energy (TKE) at Reynolds number "Re" = 7000 for numerous values of separation distances ("H/*D*" = 6, 8, and 10) for "*D*" = 5 mm.

The values of local "h" decrease with increasing "H/*D*" at the stagnation region pertaining to the jet at "X/*D*" = 0. The variation shows value of "h" to decrease from 390 W/m^2-K to 270 W/m^2-K as "H/*D*" is increased from 6 to 10.

The value of peak in "TKE" distribution reduces from 15 m^2/s^2 to 2 m^2/s^2 for the separation distance "H/*D*" changing from 6 to 10. Likewise, Figures 5 and 6 portray local "h" and "TKE" distribution intended for different "H/*D*" at fixed "S/*D*" of 3 and Re of 9000 and 11000.

The values of local heat transfer coefficient and turbulent kinetic energy can be seen to be increasing with increasing Reynolds number since the increase in flow velocities tends to increase the turbulent interactions with the atmosphere. The increase in axial flow velocities also results in lesser jet spread and thus lesser thermal dilution leading to higher heat transfer. At the interaction region formed in-between adjacent jets (i.e., "X/*D*" ~ 1.5), the higher flow velocities of wall

Table 1: Boundary conditions used for computation.

Physical location/identity	Boundary type	Mathematical representation
Top plate/nozzle plate	Wall	$u = v = w = 0$; $T_s = 300$ K
Bottom surface/impingement plate	Wall	$u = v = w = 0$; $q'' = 8333$ W/m^2
Side/opening/outlet	Pressure outlet	$P = P_{atm}$
Rear/side surface	Symmetry	$\partial(.)/\partial x_j = 0$
Inlet/velocity inlet	Velocity inlet	As per value of Re at the nozzle
Nozzle walls	Wall	$u = v = w = 0$; $T = 300$ K

Table 2: Computational grids and time taken for convergence.

S. No.	Mesh density/size	Computational time
1	301,720 cells	6 hours (approx.)
2	4,34,000 cells	9 hours (approx.)
3	6,55,600 cells	11 hours 30 minutes (approx.)

Table 3: Comparison of different turbulence models.

Sr. No.	Turbulence models	Average heat transfer coefficient (h)	Error (% age)
1	Experimental value	210 W/m^2-K	—
2	k-ε STD	181 W/m^2-K	13.8
3	k-ε RNG	192 W/m^2-K	8.57
4	k-ε realizable	191 W/m^2-K	9.04
5	k-ω SST	204 W/m^2-K	2.85

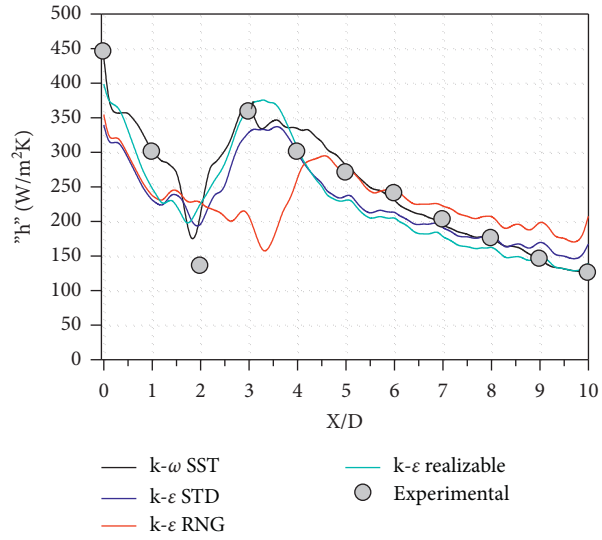

Figure 3: Local heat transfer coefficient (W/m^2-K) distribution with respect to "X/D" for various turbulence models.

jets result in flow separation in form of fountain upwash flow. Due to this flow separation, the value of "h" at this region is very less. One more observation can be made for "H/D" = 10 case that the stagnation region formed here ("X/D" = 0) shows a plateau of high local "h" values instead of depicting a sharp peak as seen for "H/D" = 6 and 8. This happens due to increased jet spread taking place due to the increased space available between nozzle exit and impingement plate for higher separations.

3.2. Impact of Inter-Jet Spacing (S/D). The values of "S/D" considered for the present analysis are "S/D" = 2, 3, 5, and 7. These "S/D" values are sufficient to analyze how the jets will behave for very close, medium, and far inter-jet spacings. The increase in "S/D" will result in decreased interactions among the jets, and therefore the total heat transfer will decrease and the decrease in "S/D" will lead to increased interaction and thus increase in heat transfer. The too small value of "S/D" resulted in array of jets to behave like a large single jet, and thus the heat transfer coefficient value is also high, but study of interaction effects cannot be made properly. The impact of variation in inter-jet spacing is depicted graphically in Figure 7. The graphs show the variation in heat transfer coefficient and temperature at central horizontal axis of the target plate for the nine jets at "S/D" = 2, 3, 5, and 7 for fixed value of Reynolds number, "Re" = 9000, "H/D" = 8, and "D" = 5 mm.

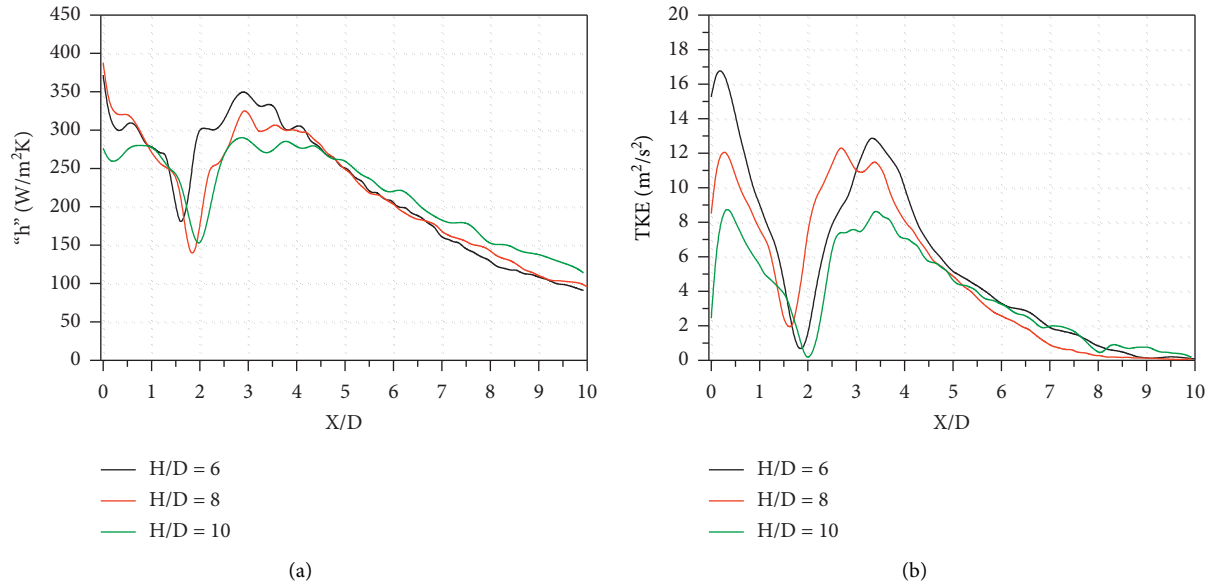

Figure 4: (a) Local heat transfer coefficient (W/m^2-K) and (b) turbulent kinetic energy (m^2/s^2) distribution at fixed "S/*D*" of 3 and "Re" of 7000 for varying separation distances, "H/*D*" of 6, 8, and 10.

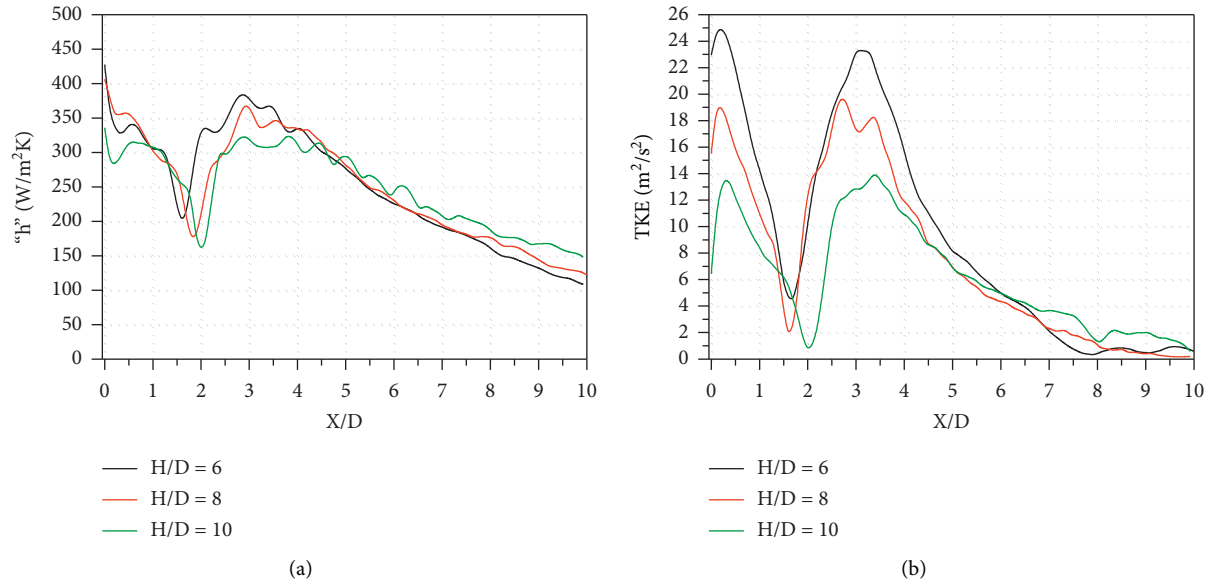

Figure 5: (a) Local heat transfer coefficient (W/m^2-K) and (b) turbulent kinetic energy (m^2/s^2) distribution at fixed "S/*D*" of 3 and "Re" of 9000 for varying separation distances, "H/*D*" of 6, 8, and 10.

Figure 7 shows declining tendencies for the change in heat transfer coefficient by increasing "S/*D*." This reduction in the values of heat transfer coefficient "h" can be anticipated due to decrease in the interaction among the neighbouring jets. At lower values of "S/*D*," the interaction between the jets and lesser spacing results in turbulence and thus increase in heat transfer rates. As the value of "S/*D*" increases, the distance among the jets increases, and thus the rate of heat transfer per unit area decreases. Figure 7 also shows the variation in temperature with respect to "X/*D*." The values of temperature are found to rise with the rise in "S/*D*" at "X/*D*" = 0. Also, the local maxima developed at the interaction region in-between adjacent jets can be seen to show an increase in temperature values with the rise in the value of inter-jet spacing "S/*D*." This is due to the decreased interactions and lesser heat transfer taking place in the interaction region for different "S/*D*" cases here. The decrease in heat transfer leads the surface plate temperature to rise, and thus the cooling of plate is not effective at these interaction regions.

3.3. Impact of Reynolds Number (Re). Impact of Reynolds number on the heat transfer rate has been studied at fixed "H/*D*" of 6 and "S/*D*" of 3, and Reynolds number has been

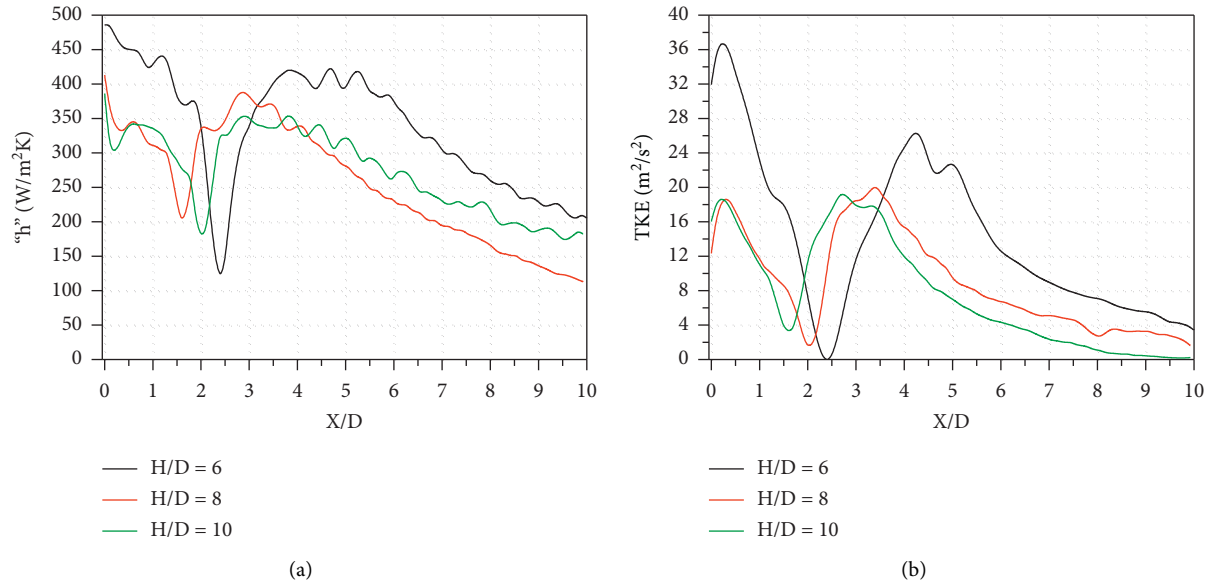

Figure 6: (a) Local heat transfer coefficient (W/m^2-K) and (b) turbulent kinetic energy (m^2/s^2) distribution at fixed "S/D" of 3 and "Re" of 11000 for varying separation distances, "H/D" of 6, 8, and 10.

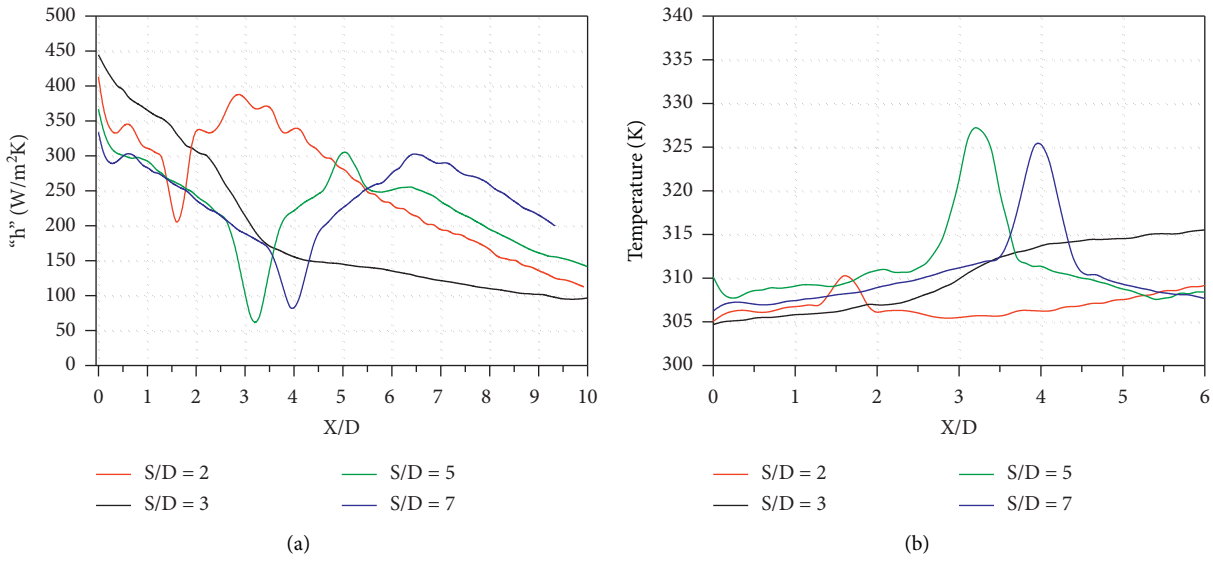

Figure 7: (a) Local heat transfer coefficient (W/m^2-K) and (b) temperature (K) distribution at fixed "H/D" of 8 and "Re" of 9000 for varying separation distances, "S/D" of 2, 3, 5, and 7.

varied as "Re" = 7000, 9000, and 11000. Experimental data analysis suggests a rise in the value of heat transfer rate and thus Nusselt number by increasing Reynolds number at same separation distance.

The impact of Reynolds number on coefficient of heat transfer and turbulent kinetic energy (TKE) is shown in Figure 8. For a fully developed pipe flow, Popiel and Boguslawski [35] revealed that the turbulent intensity as well as kinetic energy rises and achieves their maximum value at "H/D" = 6 for a single jet. This results from high turbulent jet intensity. Even though the jet centerline velocity starts decaying due to its interaction with the ambient, the turbulent intensity continues to increase. The outer peak in heat transfer distribution begins to become less distinctive because the rate of heat transfer at the impact region has developed to so high values that the chances of their further increase as an outcome of transition from laminar to turbulent flow are attenuated. The heat transfer coefficient value "h" at the stagnation region corresponding to central jet increases from 370 W/m^2-K to 495 W/m^2-K with the rise in Reynolds number. Rise in "Re" leads to increased length of potential core region, and thus the axial velocity at the jet centerline is preserved for much greater downstream distances. This marks the increase of heat transfer at the corresponding locations on the target plate. Variation of turbulent kinetic energy shows maximum turbulence at

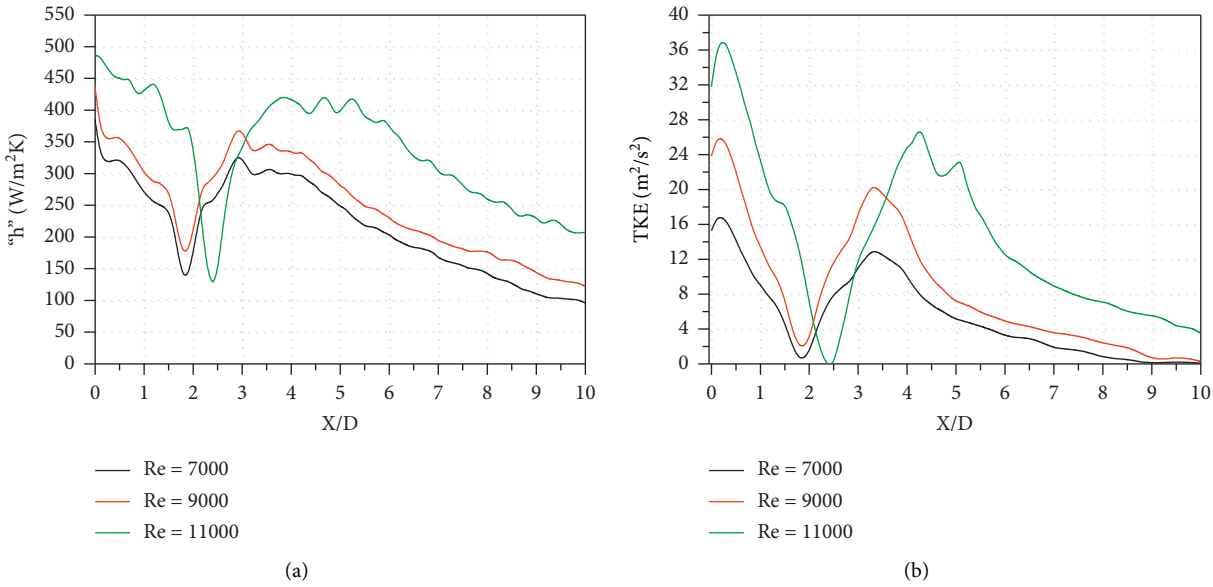

Figure 8: (a) Local heat transfer coefficient (W/m^2-K) and (b) turbulent kinetic energy (m^2/s^2) distribution at fixed "H/D" of 6 and "S/D" of 3 for varying "Re" of 7000, 9000, and 11000.

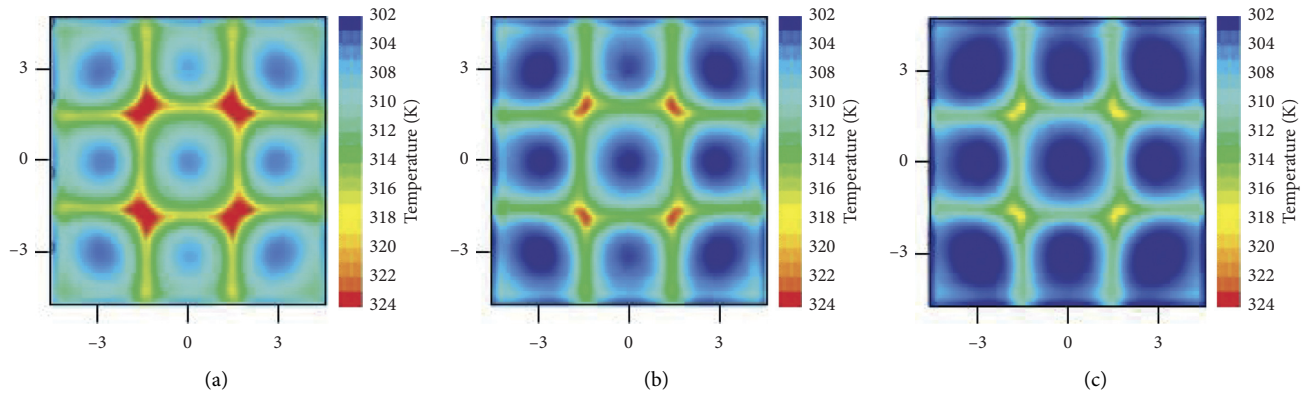

Figure 9: Local contours of temperature (K) developed at the target surface at separation distance "H/D" of 6 and inter-jet spacing "S/D" of 3 for different Reynolds number corresponding to (a) 7000, (b) 9000, and (c) 11000.

Table 4: Averaged heat transfer coefficients for various cases.

Cases	Re = 7000	Re = 9000	Re = 11000
H/D = 6	178 (W/m^2-K)	210 (W/m^2-K)	241 (W/m^2-K)
H/D = 8	174 (W/m^2-K)	204 (W/m^2-K)	219 (W/m^2-K)
H/D = 10	170 (W/m^2-K)	193 (W/m^2-K)	213 (W/m^2-K)
		Inter-jet spacing (S/D)	
Re = 9000 and H/D = 8	2	3	5	7
	205	204	200	182

regions confirming to the location of the jets. Turbulent kinetic energy has been found to be high at the stagnation regions corresponding to the jets, and the values of "TKE" increase from 15.2 m^2/s^2 to 31.8 m^2/s^2 at "X/D" = 0 with the rise in Reynolds number, "Re" from 7000 to 11000.

Figure 9 highlights the temperatures attained by the target plate at different values of Reynolds number for fixed "S/D" of 3 and "H/D" of 6. It can be seen that the plate becomes cooler particularly at the places related to stagnation regions of different impinging jets.

The plate, however, remains relatively hotter at the intersection regions developed in-between four jets and interaction areas in-between each pair of jets. The temperature values decrease from 324 K to 315 K at the regions corresponding to intersection of four jets with increasing values of Reynolds number.

3.4. Averaged Heat Transfer Coefficients "H_{avg}". Averaged heat transfer coefficients at the target surface are given in Table 4.

4. Concluding Remarks

Numerical modeling can be used as an alternative and powerful tool to predict the trend in variation of heat transfer rates as well as fluid flow features in various fluid flow applications. The trends obtained in the current numerical study show the effects of separation distance, inter-jet spacing, and Reynolds number on coefficient of heat transfer and turbulent kinetic energy. Following are the major concluding remarks:

(1) The "k-ω" SST model is observed to match best with the experimental data among different models selected for the study.

(2) The local "h" values have been noticed to decline with the rise in separation distance "H/D." The average value of heat transfer coefficient "h" reduces from 210 to 193 W/m^2-K with increase in "H/D" from 6 to 10 at "Re" = 9000 and S/D of 3.

(3) The values of coefficient of heat transfer "h" and thus Nusselt number rise due to the rise in Reynolds number "Re."

(4) The average value of coefficient of heat transfer "h" is 205, 204, 200, and 182 W/m^2-K at inter-jet spacing "S/D" of 2, 3, 5, and 7, respectively, at "H/D" = 8 and "Re" = 9000. At "S/D" = 2, the multiple jets start behaving as a large single jet.

(5) On the basis of heat transfer features, inter-jet spacing "S/D" = 3 has been determined to be the optimum value for increasing heat transfer.

Nomenclature

X, Y: Coordinate axis on impingement plate
X/D: Nondimensional x-distance
Y/D: Nondimensional y-distance
D: Diameter of nozzle (mm)
H: Impingement separation (mm)
H/D_h: Nondimensional impingement separation
S/D_h: Inter-jet spacing (dimensionless)
T: Temperature (K)
T_s: Surface temperature (K)
T_∞: Ambient temperature (K)
p: Pressure (Pa)
q''L: Heat flux (kW/m^2)
h_{avg}: Averaged heat transfer coefficient (W/m^2-K)
h: Convective heat transfer coefficient
Re: Reynolds number
u, v, w: Velocity components in x, y, and z directions (m/s)
k: Turbulent kinetic energy, TKE (m^2/s^2)
S_k: Source term for TKE
S_ω: Source term for "ω"
Y_k: Dissipation term for k in k-ω model
Y_ω: Dissipation term for ω in k-ω model
k_{eff}: Effective thermal conductivity (W/m-K)

Abbreviations

Nu: Nusselt number
RANS: Reynolds averaged NS equations
Re: Reynolds number
RNG: Renormalization group theory
STD: Standard
SST: Shear stress transport
TKE: Turbulent kinetic energy (W/m^2-K)

Greek Symbols

μ: Dynamic viscosity (kg/m-s)
ε: Dissipation rate (m^2/s^3)
ρ: Density (kg/m^3)
ω: Specific dissipation rate (m^2/s^4).

Data Availability

The data used to support the findings of this study are included within the article.

Conflicts of Interest

The authors declare that they have no conflicts of interest.

References

[1] M. Mirzaee, R. Zare, M. Sadeghzadeh, and H. Maddah, "Thermodynamic analyses of different scenarios in a CCHP system with micro turbine–absorption chiller, and heat exchanger," *Energy Conversion and Management*, vol. 198, 2019.

[2] M. Mehrpooya, M. Sadeghzadeh, A. Rahimi, and M. Pouriman, "Technical performance analysis of a combined cooling heating and power (CCHP) system based on solid oxide fuel cell (SOFC) technology-a building application," *Energy Conversion and Management*, vol. 198, Article ID 111767, 2019.

[3] S. Esbati, M. A. Amooie, M. Sadeghzadeh, M. H. Ahmadi, F. Pourfayaz, and T. Ming, "Investigating the effect of using PCM in building materials for energy saving: case study of Sharif Energy Research Institute," *Energy Science & Engineering*, vol. 1–14, 2019.

[4] R. Viskanta, "Heat transfer to impinging isothermal gas and flame jets," *Experimental Thermal and Fluid Science*, vol. 6, no. 2, pp. 111–134, 1993.

[5] N. Zuckerman and N. Lior, "Jet impingement heat transfer: physics, correlations, and numerical modeling," Edited by G. A. Greene, J. P. Hartnett, A. Bar-Cohen, and Y. I. B. T.-A. Cho, Eds., vol. 39, pp. 565–631, Elsevier, Amsterdam, Netherlands, 2006.

[6] D. E. Metzger and R. J. Korstad, "Effects of crossflow on impingement heat transfer," *Journal of Engineering for Power*, vol. 94, no. 1, pp. 35–41, 1972.

[7] C.-Y. Li and S. V. Garimella, "Prandtl-number effects and generalized correlations for confined and submerged jet

impingement," *International Journal of Heat and Mass Transfer*, vol. 44, no. 18, pp. 3471–3480, 2001.

[8] R. J. Goldstein and J. F. Timmers, "Visualization of heat transfer from arrays of impinging jets," *International Journal of Heat and Mass Transfer*, vol. 25, no. 12, pp. 1857–1868, 1982.

[9] A. I. Behbahani and R. J. Goldstein, "Local heat transfer to staggered arrays of impinging circular air jets," *Heat Transfer; Electric Power*, vol. 4, 1982.

[10] L. W. Florschuetz and C. C. Su, "Effects of crossflow temperature on heat transfer within an array of impinging jets," *Journal of Heat Transfer*, vol. 109, no. 1, pp. 74–82, 1987.

[11] N. T. Obot and T. A. Trabold, "Impingement heat transfer within arrays of circular jets: Part 1-effects of minimum, intermediate, and complete crossflow for small and large spacings," *Journal of Heat Transfer*, vol. 109, no. 4, pp. 872–879, 1987.

[12] R. J. Goldstein and W. S. Seol, "Heat transfer to a row of impinging circular air jets including the effect of entrainment," *International Journal of Heat and Mass Transfer*, vol. 34, no. 8, pp. 2133–2147, 1991.

[13] S. J. Slayzak, R. Viskanta, and F. P. Incropera, "Effects of interaction between adjacent free surface planar jets on local heat transfer from the impingement surface," *International Journal of Heat and Mass Transfer*, vol. 37, no. 2, pp. 269–282, 1994.

[14] A. M. Huber and R. Viskanta, "Effect of jet-jet spacing on convective heat transfer to confined, impinging arrays of axisymmetric air jets," *International Journal of Heat and Mass Transfer*, vol. 37, no. 18, pp. 2859–2869, 1994.

[15] J.-Y. San and M.-D. Lai, "Optimum jet-to-jet spacing of heat transfer for staggered arrays of impinging air jets," *International Journal of Heat and Mass Transfer*, vol. 44, no. 21, pp. 3997–4007, 2001.

[16] L. F. G. Geers, M. J. Tummers, and K. Hanjalic, "Experimental investigation of impinging jet arrays," *Experiments in Fluids*, vol. 36, no. 6, pp. 946–958, 2004.

[17] L. F. G. Geers, K. Hanjalić, and M. J. Tummers, "Wall imprint of turbulent structures and heat transfer in multiple impinging jet arrays," *Journal of Fluid Mechanics*, vol. 546, pp. 255–284, 2006.

[18] S. Spring, Y. Xing, and B. Weigand, "An experimental and numerical study of heat transfer from arrays of impinging jets with surface ribs," *Journal of Heat Transfer*, vol. 134, 2012.

[19] J.-Y. San and J.-J. Chen, "Effects of jet-to-jet spacing and jet height on heat transfer characteristics of an impinging jet array," *International Journal of Heat and Mass Transfer*, vol. 71, pp. 8–17, 2014.

[20] L. W. Florschuetz, C. R. Truman, and D. E. Metzger, "Streamwise flow and heat transfer distributions for jet array impingement with crossflow," *Journal of Heat Transfer*, vol. 103, no. 2, pp. 337–342, 1981.

[21] R. Gardon and J. C. Akfirat, "Heat transfer characteristics of impinging two-dimensional air jets," *Journal of Heat Transfer*, vol. 88, no. 1, pp. 101–107, 1966.

[22] J. Lee and S.-J. Lee, "The effect of nozzle configuration on stagnation region heat transfer enhancement of axisymmetric jet impingement," *International Journal of Heat and Mass Transfer*, vol. 43, no. 18, pp. 3497–3509, 2000.

[23] B. Weigand and S. Spring, "Multiple jet impingement-a review," in *Proceedings of the Int. Symp. Heat Transf. Gas Turbine Syst.*, pp. 2–4, Antalya, Turkey, August 2009.

[24] N. Chougule, G. Parishwad, P. R. Gore, S. Pagnis, and S. Sapali, "CFD analysis of multi-jet air impingement on flat plate," in *Proceedings of the World Congr Eng 2011, WCE*, vol. 3, pp. 2431–2435, London, UK, July 2011.

[25] S. Yong, Z. Jing-zhou, and X. Gong-nan, "Convective heat transfer for multiple rows of impinging air jets with small jet-to-jet spacing in a semi-confined channel," *International Journal of Heat and Mass Transfer*, vol. 86, pp. 832–842, 2015.

[26] A. Mahammedi, H. Ameur, Y. Menni, and D. M. Medjahed, "Numerical study of turbulent flows and convective heat transfer of Al2O3-water nanofluids in A circular tube," *Journal of Advanced Research in Fluid Mechanics and Thermal Sciences*, vol. 77, no. 2, pp. 1–12, 2020.

[27] Y. Menni, M. Ghazvini, H. Ameur, M. H. Ahmadi, M. Sharifpur, and M. Sadeghzadeh, "Numerical calculations of the thermal-aerodynamic characteristics in a solar duct with multiple V-baffles," *Engineering Applications of Computational Fluid Mechanics*, vol. 14, no. 1, pp. 1173–1197, 2020.

[28] H. Ameur, D. Sahel, and Y. Menni, "Enhancement of the cooling of shear-thinning fluids in channel heat exchangers by using the V-baffling technique," *Thermal Science and Engineering Progress*, vol. 18, Article ID 100534, 2020.

[29] N. Sakhri, Y. Menni, A. J. Chamkha et al., "Study of heat and mass transfer through an earth to air heat exchanger equipped with fan in South West of Algeria," *International Journal of Heat and Technology*, vol. 37, no. 3, pp. 689–695, 2019.

[30] H. Ameur and Y. Menni, "Non-Newtonian fluid flows through backward-facing steps," *SN Applied Sciences*, vol. 1, no. 12, Article ID 1717, 2019.

[31] H. Ameur and Y. Menni, "Laminar cooling of shear thinning fluids in horizontal and baffled tubes: effect of perforation in baffles," *Thermal Science and Engineering Progress*, vol. 14, Article ID 100430, 2019.

[32] N. Sakhri, Y. Menni, H. Ameur et al., "Investigation of the natural ventilation of wind catchers with different geometries in arid region houses," *Journal of Mechanical Engineering and Sciences*, vol. 14, no. 3, pp. 7109–7124, 2020.

[33] N. Sakhri, Y. Menni, and H. Ameur, "Experimental investigation of the performance of earth-to-air heat exchangers in arid environments," *Journal of Arid Environments*, vol. 180, Article ID 104215, 2020.

[34] S. V. Patankar, *Numerical Heat Transfer and Fluid Flow*, Routledge, London, UK, 1980.

[35] C. O. Popiel and L. Boguslawski, "Effect of flow structure on the heat or mass transfer on a lat plate in impinging round jet," in *Proceeding of International Heat Transfer Conference 5*, pp. 663–685, University of Strathclyde, Kyongju, Korea, August 1988.

Hindawi
Mathematical Problems in Engineering
Volume 2021, Article ID 6667226, 18 pages
https://doi.org/10.1155/2021/6667226

Research Article

Refinements and Generalizations of Some Fractional Integral Inequalities via Strongly Convex Functions

Ghulam Farid,[1] **Hafsa Yasmeen**,[1] **Chahn Yong Jung**,[2] **Soo Hak Shim**,[3] **and Gaofan Ha**[4]

[1]*Department of Mathematics, COMSATS University Islamabad, Attock Campus, Attock, Pakistan*
[2]*Department of Business Administration, Gyeongsang National University, Jinju 52828, Republic of Korea*
[3]*Department of Refrigeration and Air Conditioning Engineering, Chonnam National University, Yeosu 59626, Republic of Korea*
[4]*School of Mathematics and Statistics, Northeast Normal University, Changchun 130000, China*

Correspondence should be addressed to Chahn Yong Jung; bb5734@gnu.ac.kr

Received 6 November 2020; Revised 13 December 2020; Accepted 4 March 2021; Published 28 March 2021

Academic Editor: Mohammad D. Aliyu

In this article, we have established the Hadamard inequalities for strongly convex functions using generalized Riemann–Liouville fractional integrals. The findings of this paper provide refinements of some fractional integral inequalities. Furthermore, the error bounds of these inequalities are given by using two generalized integral identities.

1. Introduction

Let $f: I \longrightarrow \mathbb{R}$ be a convex function defined on an interval $I \subset \mathbb{R}$ and $x, y \in I$, where $x < y$. Then, the following inequality holds:

$$f\left(\frac{x+y}{2}\right) \leq \frac{1}{y-x}\int_x^y f(v)\mathrm{d}v \leq \frac{f(x)+f(y)}{2}. \tag{1}$$

The above inequality is well-known as the Hadamard inequality. This inequality provides lower and upper estimates for integral average of a convex function. Since the appearance of this result in literature, it has drawn attention of many mathematicians of recent age and it is one of the most extensively studied results for convex functions. In [1, 2], Sarikaya et al. have studied it via Riemann–Liouville fractional integrals of convex functions. After these versions of Hadamard inequality, many researchers were motivated and elegantly produced fractional inequalities using different types of fractional integrals. Also, many new classes of functions have been introduced in the establishment of fractional Hadamard inequalities; for details, we refer the readers to [3–11].

Fractional calculus studies the integrals and derivatives of any arbitrary order, real or complex. Its history begins at the end of seventeenth century, when G. W. Leibniz and Marquis de l'Hospital in 1695 introduced it for first time by discussing the differentiation of functions of order 1/2. However, it experienced a rapid growth over the short span of time. For example, Lagrange, Laplace, Lacroix, Fourier, Abel, Liouville, Riemann, Green, Holmgren, Grunwald, Letnikov, Sonin, Laurent, Nekrassov, Krug, and Weyl made their major contributions to establish a solid foundation of fractional calculus (see [12–14] and references there in). Fractional integral and derivative operators are the key factors in the development of fractional calculus. Recently, the generalizations [15–17], extensions [18–20], and applications [21–23] for fractional operators have been made by many researchers in mathematics, fluid mechanics [24–26], biological population models [27], and numerical methods [28].

Our aim in this paper is to utilize generalized Riemann–Liouville fractional integrals with monotonically increasing function. The Hadamard inequality is studied for these integral operators of strongly convex functions, and

also, by using some integral identities, error bounds are established. Next, we give the definition of strongly convex function introduced by Polyak [29] (see also [30]).

Definition 1. Let D be a convex subset of $\mathbb{X}$, $(\mathbb{X}, \|.\|)$ be a normed space. A function $f: D \subset \mathbb{X} \longrightarrow \mathbb{R}$ will be called strongly convex function with modulus $C \geq 0$ if

$$f(xt + (1-t)y) \leq tf(x) + (1-t)f(y) - Ct(1-t)\|y-x\|^2, \tag{2}$$

holds $\forall x, y \in D \subseteq \mathbb{X}, t \in [0,1]$. For $C = 0$, (2) gives the definition of convex function.

In the following, we give the definition of Riemann–Liouville fractional integrals.

Definition 2. Let $f \in L_1[a,b]$. Then, left-sided and right-sided Riemann–Liouville fractional integrals of a function f of order μ where $\Re(\mu) > 0$ are defined as follows:

$$I_{a^+}^{\mu} f(x) = \frac{1}{\Gamma(\mu)} \int_a^x (x-t)^{\mu-1} f(t)\mathrm{d}t, \quad x > a, \tag{3}$$

$$I_{b^-}^{\mu} f(x) = \frac{1}{\Gamma(\mu)} \int_x^b (t-x)^{\mu-1} f(t)\mathrm{d}t, \quad x < b. \tag{4}$$

The fractional versions of Hadamard inequality by Riemann–Liouville fractional integrals are given in the following theorems.

Theorem 1 (see [1]). *Let $f: [a,b] \longrightarrow \mathbb{R}$ be a positive function with $0 \leq a < b$ and $f \in L_1[a,b]$. If f is a convex function on $[a,b]$, then the following fractional integral inequalities hold:*

$$f\left(\frac{a+b}{2}\right) \leq \frac{\Gamma(\alpha+1)}{2(b-a)^{\alpha}} \left[I_{a^+}^{\alpha} f(b) + I_{b^-}^{\alpha} f(a)\right] \leq \frac{f(a)+f(b)}{2}, \tag{5}$$

with $\alpha > 0$.

Theorem 2 (see [2]). *Let $f: [a,b] \longrightarrow \mathbb{R}$ be a positive function with $0 \leq a < b$ and $f \in L_1[a,b]$. If f is a convex function on $[a,b]$, then the following fractional integral inequalities hold:*

$$f\left(\frac{a+b}{2}\right) \leq \frac{2^{\alpha-1}\Gamma(\alpha+1)}{(b-a)^{\alpha}} \left[I_{(a+b/2)^+}^{\alpha} f(b) + I_{(a+b/2)^-}^{\alpha} f(a)\right] \leq \frac{f(a)+f(b)}{2}, \tag{6}$$

with $\alpha > 0$.

Theorem 3 (see [1]). *Let $f: [a,b] \longrightarrow \mathbb{R}$ be a differentiable mapping on (a,b) with $a < b$. If $|f'|$ is convex on $[a,b]$, then the following fractional integral inequality holds:*

$$\left|\frac{f(a)+f(b)}{2} - \frac{\Gamma(\alpha+1)}{2(b-a)^{\alpha}} \left[I_{a^+}^{\alpha} f(b) + I_{b^-}^{\alpha} f(a)\right]\right| \leq \frac{b-a}{2(\alpha+1)} \left(1 - \frac{1}{2^{\alpha}}\right) \left[|f'(a)| + |f'(b)|\right]. \tag{7}$$

In the following, refinements of Theorem 1–3 are given.

Theorem 4 (see [31]). *Let $f: [a,b] \longrightarrow \mathbb{R}$ be a positive function with $0 \leq a < b$ and $f \in L_1[a,b]$. If f is strongly convex function on $[a,b]$ with modulus $C \geq 0$, then the following fractional integral inequalities hold:*

$$f\left(\frac{a+b}{2}\right) + \frac{C(b-a)^2\left(\alpha^2-\alpha+2\right)}{4(\alpha+1)(\alpha+2)} \leq \frac{\Gamma(\alpha+1)}{2(b-a)^{\alpha}} \left[I_{a^+}^{\alpha} f(b) + I_{b^-}^{\alpha} f(a)\right] \leq \frac{f(a)+f(b)}{2} - \frac{C\alpha(b-a)^2}{(\alpha+1)(\alpha+2)}, \tag{8}$$

with α.

Theorem 5 (see [32]). *Let $f: [a,b] \longrightarrow \mathbb{R}$ be a positive function with $0 \leq a < b$ and $f \in L_1[a,b]$. If f is strongly convex function on $[a,b]$ with modulus $C \geq 0$, then the following fractional integral inequalities hold:*

$$f\left(\frac{a+b}{2}\right) + \frac{C(b-a)^2}{2(\alpha+1)(\alpha+2)} \leq \frac{2^{\alpha-1}\Gamma(\alpha+1)}{(b-a)^{\alpha}} \left[I_{(a+b/2)^+}^{\alpha} f(b) + I_{(a+b/2)^-}^{\alpha} f(a)\right] \leq \frac{f(a)+f(b)}{2} - \frac{C\alpha(b-a)^2(\alpha+3)}{4(\alpha+1)(\alpha+2)}, \tag{9}$$

with α.

Theorem 6 (see [32]). *Let $f: [a,b] \longrightarrow \mathbb{R}$ be a differentiable mapping on (a,b) with $a < b$ and $f \in L_1[a,b]$. If f is strongly convex function on $[a,b]$ with modulus $C \geq 0$, then the following fractional integral inequalities hold:*

$$\left|\frac{f(a)+f(b)}{2} - \frac{\Gamma(\alpha+1)}{2(b-a)^{\alpha}} \left[I_{a^+}^{\alpha} f(b) + I_{b^-}^{\alpha} f(a)\right]\right| \leq \frac{b-a}{2(\alpha+1)} \left(1 - \frac{1}{2^{\alpha}}\right) \left[|f'(a)| + |f'(b)|\right] - \frac{C(b-a)^3}{(\alpha+2)(\alpha+3)} \left(1 - \frac{\alpha+4}{2^{\alpha+2}}\right), \tag{10}$$

with α.

In [33], k-fractional Riemann–Liouville integrals are defined as follows.

Definition 3. Let $f \in L_1[a,b]$. Then, k-fractional Riemann–Liouville integrals of order μ, where $\Re(\mu) > 0$, $k > 0$, are defined by

$$ {}_kI^{\mu}_{a^+} f(x) = \frac{1}{k\Gamma_k(\mu)} \int_a^x (x-t)^{(\mu/k)-1} f(t)\mathrm{d}t, \quad x > a, \tag{11} $$

$$ {}_kI^{\mu}_{b^-} f(x) = \frac{1}{k\Gamma_k(\mu)} \int_x^b (t-x)^{(\mu/k)-1} f(t)\mathrm{d}t, \quad x < b, \tag{12} $$

where $\Gamma_k(.)$ is defined as follows [34]:

$$ \Gamma_k(\mu) = \int_0^{\infty} t^{\alpha-1} e^{-(t^k/k)}\mathrm{d}t, \quad \Re(\mu) > 0. \tag{13} $$

If $k = 1$, (11) and (12) coincide with (3) and (4).

Farid et al. [35, 36] proved the following k-fractional Hadamard inequalities.

Theorem 7 (see [35]). *Let $f: [a,b] \longrightarrow \mathbb{R}$ be a positive function with $0 \le a < b$. If f is a convex function on $[a,b]$, then the following inequalities for k-fractional integrals hold:*

$$ f\left(\frac{a+b}{2}\right) \le \frac{\Gamma_k(\alpha+k)}{2(b-a)^{\alpha/k}} \left[{}_kI^{\alpha}_{a^+} f(b) + {}_kI^{\alpha}_{b^-} f(a)\right] \le \frac{f(a)+f(b)}{2}. \tag{14} $$

Theorem 8 (see [36]). *Let $f: [a,b] \longrightarrow \mathbb{R}$ be a positive function with $0 \le a < b$. If f is a convex function on $[a,b]$, then the following inequalities for k-fractional integrals hold:*

$$ f\left(\frac{a+b}{2}\right) \le \frac{2^{(\alpha/k)-1}\Gamma_k(\alpha+k)}{(b-a)^{(\alpha/k)}} \left[{}_kI^{\alpha}_{(a+b/2)^+} f(b) + {}_kI^{\alpha}_{(a+b/2)^-} f(a)\right] \le \frac{f(a)+f(b)}{2}. \tag{15} $$

Theorem 9 (see [35]). *Let $f: [a,b] \longrightarrow \mathbb{R}$ be a differentiable mapping on (a,b) with $0 \le a < b$. If $|f'|$ is convex on $[a,b]$, then the following inequality for k-fractional integrals hold:*

$$ \left|\frac{f(a)+f(b)}{2} - \frac{\Gamma_k(\alpha+k)}{2(b-a)^{\alpha/k}} \left[{}_kI^{\alpha}_{a^+} f(b) + {}_kI^{\alpha}_{b^-} f(a)\right]\right| \le \frac{b-a}{2((\alpha/k)+1)} \left(1 - \frac{1}{2^{(\alpha/k)}}\right) \left[\left|f'(a)\right| + \left|f'(b)\right|\right]. \tag{16} $$

In the following, we give the definition of generalized Riemann–Liouville fractional integrals by a monotonically increasing function:

Definition 4 (see [37]). Let $f: [a,b] \longrightarrow \mathbb{R}$ be an integrable function. Also, let ψ be an increasing and positive function on $(a,b]$, having a continuous derivative ψ' on (a,b). The left-sided and right-sided fractional integrals of a function f with respect to another function ψ on $[a,b]$ of order μ where $\Re(\mu) > 0$ are defined by

$$ I^{\mu,\psi}_{a^+} f(x) = \frac{1}{\Gamma(\mu)} \int_a^x \psi'(t)(\psi(x)-\psi(t))^{\mu-1} f(t)\mathrm{d}t, \quad x > a, \tag{17} $$

$$ I^{\mu,\psi}_{b^-} f(x) = \frac{1}{\Gamma(\mu)} \int_x^b \psi'(t)(\psi(t)-\psi(x))^{\mu-1} f(t)\mathrm{d}t, \quad x < b. \tag{18} $$

If ψ is identity function, then (17) and (18) coincide with (3) and (4).

The k-analogue of generalized Riemann–Liouville fractional integrals are defined as follows:

Definition 5 (see [38]). *Let $f: [a,b] \longrightarrow \mathbb{R}$ be an integrable function. Also, let ψ be an increasing and positive function on $(a,b]$, having a continuous derivative ψ' on (a,b). The left-sided and right-sided fractional integrals of a function f with respect to another function ψ on $[a,b]$ of order μ where $\Re(\mu) > 0, k > 0$, are defined by*

$$ {}_kI^{\mu,\psi}_{a^+} f(x) = \frac{1}{k\Gamma_k(\mu)} \int_a^x \psi'(t)(\psi(x)-\psi(t))^{(\mu/k)-1} f(t)\mathrm{d}t, \quad x > a, \tag{19} $$

$$ {}_kI^{\mu,\psi}_{b^-} f(x) = \frac{1}{k\Gamma_k(\mu)} \int_x^b \psi'(t)(\psi(t)-\psi(x))^{(\mu/k)-1} f(t)\mathrm{d}t, \quad x < b. \tag{20} $$

If $k = 1$, (19) and (20) coincide with (17) and (18). If ψ is taken as identity function, (19) and (20) coincide with (11) and (12). If ψ is taken as identity function along with $k = 1$, (19) and (20) coincide with (3) and (4). For more details of above defined fractional integrals, one can see [13, 39].

In Section 2, we establish Hadamard inequalities for generalized Riemann–Liouville fractional integrals of strongly convex functions. The particular cases are given as consequences of these inequalities which are connected with already published results. In Section 3, by using two integral identities for generalized fractional integrals, the error bounds of fractional Hadamard inequalities are established. The findings of this paper are connected with results that are explicitly proved in [1, 2, 31, 35, 36, 40–44].

2. Main Results

Theorem 10. *Let $f: [a,b] \longrightarrow \mathbb{R}$ be a positive function with $0 \le a < b$ and $f \in L_1[a,b]$. Also, suppose that f is strongly convex function on $[a,b]$ with modulus $C \ge 0$, ψ is an increasing and positive monotone function on $(a,b]$, having a*

continuous derivative $\psi'(x)$ on (a,b). Then, for $k>0$, the following k-fractional integral inequalities hold:

$$f\left(\frac{a+b}{2}\right)+\frac{C(b-a)^2\left(\alpha^2-k\alpha+2k^2\right)}{4(\alpha+k)(\alpha+2k)}$$
$$\le\frac{\Gamma_k(\alpha+k)}{2(b-a)^{\alpha/k}}\left[{}_kI^{\alpha,\psi}_{\psi^{-1}(a)^+}(f\circ\psi)\left(\psi^{-1}(b)\right)+{}_kI^{\alpha,\psi}_{\psi^{-1}(b)^-}(f\circ\psi)\left(\psi^{-1}(a)\right)\right]$$
$$\le\frac{f(a)+f(b)}{2}-\frac{Ck\alpha(b-a)^2}{(\alpha+k)(\alpha+2k)},\tag{21}$$

with $\alpha>0$.

Proof. Since the function f is strongly convex function, so for $x,y\in[a,b]$, we have

$$f\left(\frac{x+y}{2}\right)\le\frac{f(x)+f(y)}{2}-\frac{C}{4}|x-y|^2.\tag{22}$$

Let $x=at+(1-t)b$, $y=(1-t)a+tb$ for $t\in[0,1]$ in (22) and multiplying the resulting inequality with $t^{(\alpha/k)-1}$ on both sides, we get

$$2f\left(\frac{a+b}{2}\right)t^{(\alpha/k)-1}\le f(at+(1-t)b)t^{(\alpha/k)-1}+f((1-t)a+bt)t^{(\alpha/k)-1}-\frac{C}{2}(b-a)^2(1-2t)^2t^{(\alpha/k)-1}.\tag{23}$$

Integrating (23) over the interval $[0,1]$, we get

$$2f\left(\frac{a+b}{2}\right)\int_0^1 t^{(\alpha/k)-1}\mathrm{d}t\le\int_0^1 f(at+(1-t)b)t^{(\alpha/k)-1}\mathrm{d}t+\int_0^1 f((1-t)a+bt)t^{(\alpha/k)-1}\mathrm{d}t-\frac{C}{2}(b-a)^2\int_0^1(1-2t)^2t^{(\alpha/k)-1}\mathrm{d}t,$$
$$\frac{2k}{\alpha}f\left(\frac{a+b}{2}\right)\le\int_0^1 f(at+(1-t)b)t^{(\alpha/k)-1}\mathrm{d}t+\int_0^1 f((1-t)a+bt)t^{(\alpha/k)-1}\mathrm{d}t-\frac{Ck(b-a)^2\left(\alpha^2-k\alpha+2k^2\right)}{2\alpha(\alpha+k)(\alpha+2k)}.\tag{24}$$

Multiplying (24) by $\alpha/2k$, we get

$$f\left(\frac{a+b}{2}\right)\le\frac{\alpha}{2k}\left(\int_0^1 f(at+(1-t)b)t^{(\alpha/k)-1}\mathrm{d}t+\int_0^1 f((1-t)a+bt)t^{(\alpha/k)-1}\mathrm{d}t\right)-\frac{C(b-a)^2\left(\alpha^2-k\alpha+2k^2\right)}{4(\alpha+k)(\alpha+2k)}.\tag{25}$$

Taking $u\in[a,b]$ so that $\psi(u)=at+b(1-t)$, that is, $t=(b-\psi(u))/(b-a)$, and $v\in[a,b]$ so that $\psi(v)=a(1-t)+bt$, that is, $t=(\psi(v)-a)/(b-a)$, in (25), then by applying Definition 5, we get the following inequality:

$$f\left(\frac{a+b}{2}\right)+\frac{C(b-a)^2\left(\alpha^2-k\alpha+2k^2\right)}{4(\alpha+k)(\alpha+2k)}\le\frac{\Gamma_k(\alpha+k)}{2(b-a)^{\alpha/k}}\left[{}_kI^{\alpha,\psi}_{\psi^{-1}(a)^+}(f\circ\psi)\left(\psi^{-1}(b)\right)+{}_kI^{\alpha,\psi}_{\psi^{-1}(b)^-}(f\circ\psi)\left(\psi^{-1}(a)\right)\right].\tag{26}$$

Since f is strongly convex function, for $t\in[0,1]$, we also have following inequality:

$$f(ta+(1-t)b)+f((1-t)a+tb)\le f(a)+f(b)-2Ct(1-t)(b-a)^2.\tag{27}$$

Multiplying (27) with $t^{(\alpha/k)-1}$ and then integrating over the interval $[0,1]$, we get

$$\int_0^1 t^{(\alpha/k)-1}f(ta+(1-t)b)\mathrm{d}t+\int_0^1 t^{(\alpha/k)-1}f((1-t)a+tb)\mathrm{d}t\le(f(a)+f(b))\int_0^1 t^{(\alpha/k)-1}\mathrm{d}t-2C(b-a)^2\int_0^1 t^{(\alpha/k)}(1-t)\mathrm{d}t,$$
$$\int_0^1 t^{(\alpha/k)-1}f(ta+(1-t)b)\mathrm{d}t+\int_0^1 t^{(\alpha/k)-1}f((1-t)a+tb)\mathrm{d}t\le\frac{k(f(a)+f(b))}{\alpha}-\frac{2Ck^2(b-a)^2}{(\alpha+k)(\alpha+2k)}.\tag{28}$$

Multiplying (28) by $\alpha/2k$, we get

$$\frac{\alpha}{2k}\left(\int_0^1 t^{(\alpha/k)-1}f(ta+(1-t)b)\mathrm{d}t+\int_0^1 t^{(\alpha/k)-1}f((1-t)a+tb)\mathrm{d}t\right)\le\frac{f(a)+f(b)}{2}-\frac{Ck\alpha(b-a)^2}{(\alpha+k)(\alpha+2k)}.\tag{29}$$

Again taking $\psi(u)=at+b(1-t)$, that is, $t=(b-\psi(u)/b-a)$, and $\psi(v)=a(1-t)+bt$, that is, $t=(\psi(v)-a/(b-a))$, in (29), then by applying Definition 5, we get the following inequality:

$$\frac{\Gamma_k(\alpha+k)}{2(b-a)^{\alpha/k}}\left[{}_kI^{\alpha,\psi}_{\psi^{-1}(a)^+}(f\circ\psi)\left(\psi^{-1}(b)\right)+{}_kI^{\alpha,\psi}_{\psi^{-1}(b)^-}(f\circ\psi)\left(\psi^{-1}(a)\right)\right]\le\frac{f(a)+f(b)}{2}-\frac{Ck\alpha(b-a)^2}{(\alpha+k)(\alpha+2k)}.\tag{30}$$

Combining (26) and (30), we get (21). □

Remark 1. Under the assumption of Theorem 10, one can get the following results:

(i) If $C = 0$, $k = 1$, and ψ is identity function in (21), then Theorem 1 is obtained.

(ii) If $C = 0$ and ψ is identity function in (21), then Theorem 7 is obtained.

(iii) If $k = 1$ and ψ is identity function in (21), then Theorem 4 is obtained.

(iv) If $\alpha = 1$, $k = 1$, $C = 0$, and ψ is identity function in (21), then Hadamard inequality is obtained.

(v) If $C = 0$ in (21), then the inequality (Theorem 1) stated in [41] is obtained.

(vi) If $C = 0$ and $k = 1$ in (21), then the inequality (Theorem 2.1) stated in [40] is obtained.

(vii) If $k = 1$, $\alpha = 1$, and ψ is identity function in (21), then the inequality (Theorem 6) stated in [44] is obtained.

Corollary 1. *Under the assumption of Theorem 10 with $k = 1$ in (21), the following inequality holds:*

$$f\left(\frac{a+b}{2}\right)+\frac{C(b-a)^2\left(\alpha^2-\alpha+2\right)}{4(\alpha+1)(\alpha+2)} \le \frac{\Gamma(\alpha+1)}{2(b-a)^{\alpha}}\left[I^{\alpha,\psi}_{\psi^{-1}(a)^+}(f\circ\psi)\left(\psi^{-1}(b)\right)+I^{\alpha,\psi}_{\psi^{-1}(b)^-}(f\circ\psi)\left(\psi^{-1}(a)\right)\right] \le \frac{f(a)+f(b)}{2}-\frac{C\alpha(b-a)^2}{(\alpha+1)(\alpha+2)}. \tag{31}$$

Corollary 2. *Under the assumption of Theorem 10 with ψ as identity function in (21), the following inequality holds:*

$$f\left(\frac{a+b}{2}\right)+\frac{C(b-a)^2\left(\alpha^2-k\alpha+2k^2\right)}{4(\alpha+k)(\alpha+2k)} \le \frac{\Gamma_k(\alpha+k)}{2(b-a)^{\alpha/k}}\left[{}_kI^{\alpha}_{a^+}f(b)+{}_kI^{\alpha}_{b^-}f(a)\right] \le \frac{f(a)+f(b)}{2}-\frac{Ck\alpha(b-a)^2}{(\alpha+k)(\alpha+2k)}. \tag{32}$$

Theorem 11. *Let $f\colon [a,b] \longrightarrow \mathbb{R}$ be a positive function with $0 \le a < b$ and $f \in L_1[a,b]$. Also, suppose that f is strongly convex function on $[a,b]$ with modulus $C \ge 0$ and ψ is an increasing and positive monotone function on $(a,b]$, having a continuous derivative $\psi'(x)$ on (a,b). Then, for $k > 0$, the following k-fractional integral inequalities hold:*

$$f\left(\frac{a+b}{2}\right)+\frac{k^2C(b-a)^2}{2(\alpha+k)(\alpha+2k)} \le \frac{2^{(\alpha/k)-1}\Gamma_k(\alpha+k)}{(b-a)^{(\alpha/k)}}\left[{}_kI^{\alpha,\psi}_{\psi^{-1}(a+b/2)^+}(f\circ\psi)\left(\psi^{-1}(b)\right)+{}_kI^{\alpha,\psi}_{\psi^{-1}(a+b/2)^-}(f\circ\psi)\left(\psi^{-1}(a)\right)\right] \le \frac{f(a)+f(b)}{2}-\frac{C\alpha(b-a)^2(\alpha+3k)}{4(\alpha+k)(\alpha+2k)}, \tag{33}$$

with $\alpha > 0$.

Proof. Let $x = (at/2) + (2-t/2)b$ and $y = (2-t/2)a + (bt/2)$ in (22), and multiplying the resulting inequality with $t^{(\alpha/k)-1}$, we get

$$f\left(\frac{a+b}{2}\right)t^{(\alpha/k)-1} \le \frac{1}{2}\left[f\left(\frac{at}{2}+\left(\frac{2-t}{2}\right)b\right)t^{(\alpha/k)-1}+f\left(\left(\frac{2-t}{2}\right)a+\frac{bt}{2}\right)t^{(\alpha/k)-1}\right] -\frac{C}{4}(b-a)^2(1-t)^2t^{(\alpha/k)-1}. \tag{34}$$

Integrating (34) over $[0,1]$, we get

$$\frac{2k}{\alpha} f\left(\frac{a+b}{2}\right) \leq \int_0^1 f\left(\frac{at}{2}+\left(\frac{2-t}{2}\right)b\right) t^{(\alpha/k)-1}\mathrm{d}t + \int_0^1 f\left(a\left(\frac{2-t}{2}\right)+\frac{bt}{2}\right) t^{(\alpha/k)-1}\mathrm{d}t - \frac{k^3 C(b-a)^2}{\alpha(\alpha+k)(\alpha+2k)}. \tag{35}$$

Multiplying above inequality with $\alpha/2k$, we get

$$f\left(\frac{a+b}{2}\right) + \frac{Ck^2(b-a)^2}{2(\alpha+k)(\alpha+2k)} \leq \frac{\alpha}{2k}\left(\int_0^1 f\left(\frac{at}{2}+\left(\frac{2-t}{2}\right)b\right) t^{(\alpha/k)-1}\mathrm{d}t + \int_0^1 f\left(a\left(\frac{2-t}{2}\right)+\frac{bt}{2}\right) t^{(\alpha/k)-1}\mathrm{d}t\right). \tag{36}$$

Taking $u \in [a,b]$ so that $\psi(u) = (at/2) + b(2-t/2)$, that is, $t = (2(b-\psi(u))/b-a)$, and $v \in [a,b]$ so that $\psi(v) = a(2-t/2) + (bt/2)$, that is, $t = (2(\psi(v)-a)/b-a)$, in (36), then by applying Definition 5, we get following inequality:

$$f\left(\frac{a+b}{2}\right) + \frac{Ck^2(b-a)^2}{2(\alpha+k)(\alpha+2k)} \leq \frac{2^{(\alpha/k)-1}\Gamma_k(\alpha+k)}{(b-a)^{(\alpha/k)}}\left[{}_kI^{\alpha,\psi}_{\psi^{-1}(a+b/2)^+}(f\circ\psi)\left(\psi^{-1}(b)\right) + {}_kI^{\alpha,\psi}_{\psi^{-1}(a+b/2)^-}(f\circ\psi)\left(\psi^{-1}(a)\right)\right]. \tag{37}$$

Since f is strongly convex function on $[a,b]$, for $t \in [0,1]$, we have the following inequality:

$$f\left(\frac{at}{2}+\left(\frac{2-t}{2}\right)b\right) + f\left(a\left(\frac{2-t}{2}\right)+\frac{bt}{2}\right) \leq f(a) + f(b) - \frac{Ct(2-t)(b-a)^2}{2}. \tag{38}$$

Multiplying (38) with $t^{(\alpha/k)-1}$ on both sides and integrating over $[0,1]$, we get

$$\int_0^1 f\left(\frac{at}{2}+\left(\frac{2-t}{2}\right)b\right) t^{(\alpha/k)-1}\mathrm{d}t + \int_0^1 f\left(a\left(\frac{2-t}{2}\right)+\frac{bt}{2}\right) t^{(\alpha/k)-1}\mathrm{d}t \leq (f(a)+f(b))\int_0^1 t^{(\alpha/k)-1}\mathrm{d}t - \frac{C(b-a)^2}{2}\int_0^1 (2-t)t^{(\alpha/k)}\mathrm{d}t. \tag{39}$$

Multiplying (39) with $\alpha/2k$ on both sides, we get

$$\frac{\alpha}{2k}\left(\int_0^1 f\left(\frac{at}{2}+\left(\frac{2-t}{2}\right)b\right) t^{(\alpha/k)-1}\mathrm{d}t + \int_0^1 f\left(\left(\frac{2-t}{2}\right)a+\frac{bt}{2}\right) t^{(\alpha/k)-1}\mathrm{d}t\right) \leq \frac{f(a)+f(b)}{2} - \frac{C\alpha(b-a)^2(\alpha+3k)}{4(\alpha+k)(\alpha+2k)}. \tag{40}$$

Again taking $\psi(u) = (at/2) + b(2-t/2)$, that is, $t = (2(b-\psi(v))/b-a)$, and $\psi(v) = a(2-t/2) + (bt/2)$, that is, $t = (2(\psi(v)-a)/b-a)$, in (40), then by applying Definition 5, we get the following inequality:

$$\frac{2^{\alpha/k}\Gamma_k(\alpha+k)}{2(b-a)^{\alpha/k}}\left[{}_kI^{\alpha,\psi}_{\psi^{-1}(a+b/2)^+}(f\circ\psi)\left(\psi^{-1}(b)\right) + {}_kI^{\alpha,\psi}_{\psi^{-1}(a+b/2)^-}(f\circ\psi)\left(\psi^{-1}(a)\right)\right] \leq \frac{f(a)+f(b)}{2} - \frac{C\alpha(b-a)^2(\alpha+3k)}{4(\alpha+k)(\alpha+2k)}. \tag{41}$$

Combining (37) and (41), (33) is obtained. □

Remark 2. Under the assumption of Theorem 11, one can get the following results:

(i) If $k = 1$, $C = 0$, and ψ is identity function in (33), then Theorem 2 is obtained.

(ii) If $k = 1$ and ψ is identity function in (33), then Theorem 5 is obtained.

(iii) If $C = 0$ and ψ is identity function in (33), then inequality (Theorem 2.1) stated in [36] is obtained.

(iv) If $k = 1$, $C = 0$, $\alpha = 1$, and ψ is identity function in (33), then Hadamard inequality is obtained.

(v) If $k = 1$, $\alpha = 1$, and ψ is identity function in (33), then the inequality (Theorem 6) stated in [44] is obtained.

Corollary 3. *Under the assumption of Theorem 11 with $C = 0$ in (33), the following inequality holds:*

$$f\left(\frac{a+b}{2}\right) \leq \frac{2^{(\alpha/k)-1}\Gamma_k(\alpha+k)}{(b-a)^{(\alpha/k)}}\left[{}_kI^{\alpha,\psi}_{\psi^{-1}(a+b/2)^+}(f\circ\psi)\left(\psi^{-1}(b)\right) + {}_kI^{\alpha,\psi}_{\psi^{-1}(a+b/2)^-}(f\circ\psi)\left(\psi^{-1}(a)\right)\right] \leq \frac{f(a)+f(b)}{2}. \tag{42}$$

Corollary 4. *Under the assumption of Theorem 11 with $k = 1$ in (33), the following inequality holds:*

$$f\left(\frac{a+b}{2}\right) + \frac{C(b-a)^2}{2(\alpha+1)(\alpha+2)} \leq \frac{2^{\alpha-1}\Gamma(\alpha+1)}{(b-a)^{\alpha}}\left[I^{\alpha,\psi}_{\psi^{-1}(a+b/2)^+}(f\circ\psi)\left(\psi^{-1}(b)\right) + I^{\alpha,\psi}_{\psi^{-1}(a+b/2)^-}(f\circ\psi)\left(\psi^{-1}(a)\right)\right] \leq \frac{f(a)+f(b)}{2} - \frac{C\alpha(b-a)^2(\alpha+3)}{4(\alpha+1)(\alpha+2)}. \tag{43}$$

Corollary 5. *Under the assumption of Theorem 11 with ψ as identity function in (33), the following inequality holds:*

$$f\left(\frac{a+b}{2}\right) + \frac{Ck^2(b-a)^2}{2(\alpha+k)(\alpha+2k)} \leq \frac{2^{(\alpha/k)-1}\Gamma_k(\alpha+k)}{(b-a)^{(\alpha/k)}}\left[{}_kI^{\alpha}_{(a+b/2)^+}f(b) + {}_kI^{\alpha}_{(a+b/2)^-}f(a)\right] \leq \frac{f(a)+f(b)}{2} - \frac{C\alpha(b-a)^2(\alpha+3k)}{4(\alpha+k)(\alpha+2k)}. \tag{44}$$

3. Error Bounds of Hadamard Inequalities for Strongly Convex Functions

In this section, we provide the error bounds of fractional Hadamard inequalities using generalized Riemann–Liouville fractional integrals via strongly convex functions. Estimations here are further refined as compared to those already established for convex functions. The following lemma is useful to prove the next result.

Lemma 1 (see [41]). *Let $a < b$ and $f\colon [a,b] \longrightarrow \mathbb{R}$ be a differentiable mapping on (a,b). Also, suppose that $f' \in L[a,b]$, ψ is an increasing and positive monotone function on $(a,b]$, having a continuous derivative $\psi'(x)$ on (a,b), and $\alpha \in (0,1)$. Then, for $k > 0$, the following identity holds:*

$$\frac{f(a)+f(b)}{2} - \frac{\Gamma_k(\alpha+k)}{2(b-a)^{\alpha/k}}\left[{}_kI^{\alpha,\psi}_{\psi^{-1}(a)^+}(f\circ\psi)\left(\psi^{-1}(b)\right) + {}_kI^{\alpha,\psi}_{\psi^{-1}(b)^-}(f\circ\psi)\left(\psi^{-1}(a)\right)\right] = \frac{b-a}{2}\int_0^1\left[(1-t)^{\alpha/k} - t^{\alpha/k}\right]f'(ta+(1-t)b)\mathrm{d}t. \tag{45}$$

Theorem 12. *Let $f:[a,b]\longrightarrow\mathbb{R}$ be a differentiable mapping on (a,b) with $a<b$. Also, suppose that $|f'|$ is strongly convex function on $[a,b]$ with modulus $C\geq 0$ and $\psi(x)$ is an increasing and positive monotone function on $(a,b]$, having a continuous derivative $\psi'(x)$ on (a,b). Then, for $k>0$, the following k-fractional integral inequalities hold:*

$$\left|\frac{f(a)+f(b)}{2}-\frac{\Gamma_k(\alpha+k)}{2(b-a)^{\alpha/k}}\left[{}_kI^{\alpha,\psi}_{\psi^{-1}(a)^+}(f\circ\psi)\left(\psi^{-1}(b)\right)+{}_kI^{\alpha,\psi}_{\psi^{-1}(b)^-}(f\circ\psi)\left(\psi^{-1}(a)\right)\right]\right| \leq\frac{b-a}{2((\alpha/k)+1)}\left(1-\frac{1}{2^{(\alpha/k)}}\right)\left[|f'(a)|+|f'(b)|\right]-\frac{C(b-a)^3}{((\alpha/k)+2)((\alpha/k)+3)}\left(1-\frac{(\alpha/k)+4}{2^{(\alpha/k)+2}}\right), \tag{46}$$

with $\alpha>0$.

Proof. From Lemma 1 and strongly convexity of $|f'|$, we have

$$\begin{aligned}&\left|\frac{f(a)+f(b)}{2}-\frac{\Gamma_k(\alpha+k)}{2(b-a)^{(\alpha/k)}}\left[{}_kI^{\alpha,\psi}_{\psi^{-1}(a)^+}(f\circ\psi)\left(\psi^{-1}(b)\right)+{}_kI^{\alpha}_{\psi^{-1}(b)^-}(f\circ\psi)\left(\psi^{-1}(b)\right)\right]\right|\\&\leq\frac{b-a}{2}\int_0^1\left|(1-t)^{(\alpha/k)}-t^{(\alpha/k)}\right|\left|f'(ta+(1-t))\right|\mathrm{d}t\\&\leq\frac{b-a}{2}\int_0^1\left|(1-t)^{(\alpha/k)}-t^{(\alpha/k)}\right|\left(t\left|f'(a)\right|+(1-t)\left|f'(b)\right|-Ct(1-t)|b-a|^2\right)\mathrm{d}t\\&=\frac{b-a}{2}\int_0^{1/2}\left((1-t)^{(\alpha/k)}-t^{(\alpha/k)}\right)\left(t\left|f'(a)\right|+(1-t)\left|f'(b)\right|-Ct(1-t)|b-a|^2\right)\mathrm{d}t\\&\quad+\int_{1/2}^1\left(t^{(\alpha/k)}-(1-t)^{(\alpha/k)}\right)\left(t\left|f'(a)\right|+(1-t)\left|f'(b)\right|-Ct(1-t)|b-a|^2\right)\mathrm{d}t.\end{aligned} \tag{47}$$

It can be noted that

$$\begin{aligned}&\int_0^{1/2}\left((1-t)^{\alpha/k}-t^{\alpha/k}\right)\left(t\left|f'(a)\right|+(1-t)\left|f'(b)\right|-Ct(1-t)|b-a|^2\right)\mathrm{d}t\\&=\left|f'(a)\right|\int_0^{1/2}\left(t(1-t)^{\alpha/k}-t^{(\alpha/k)+1}\right)\mathrm{d}t+\left|f'(b)\right|\int_0^{1/2}\left((1-t)^{(\alpha/k)+1}-(1-t)t^{\alpha/k}\right)\mathrm{d}t\\&\quad-C(b-a)^2\left(\int_0^{1/2}t(1-t)^{(\alpha/k)+1}\mathrm{d}t-\int_0^{1/2}(1-t)t^{(\alpha/k)+1}\mathrm{d}t\right)\\&=\left|f'(a)\right|\left(\frac{1}{((\alpha/k)+1)((\alpha/k)+2)}-\frac{(1/2)^{(\alpha/k)+1}}{(\alpha/k)+1}\right)+\left|f'(b)\right|\left(\frac{1}{(\alpha/k)+2}-\frac{(1/2)^{(\alpha/k)+1}}{(\alpha/k)+1}\right)\\&\quad-\frac{C(b-a)^2}{((\alpha/k)+2)((\alpha/k)+3)}\left(1-\frac{(\alpha/k)+4}{2^{(\alpha/k)+2}}\right).\end{aligned} \tag{48}$$

By similar evaluation, one can have

$$\begin{aligned}
&\int_{1/2}^{1}\left(t^{(\alpha/k)}-(1-t)^{(\alpha/k)}\right)\left(t\left|f'(a)\right|+(1-t)\left|f'(b)\right|-Ct(1-t)|b-a|^{2}\right)\mathrm{d}t\\
&=\left|f'(a)\right|\left(\frac{1}{(\alpha/k)+2}-\frac{(1/2)^{(\alpha/k)+1}}{(\alpha/k)+1}\right)+\left|f'(b)\right|\left(\frac{1}{((\alpha/k)+1)((\alpha/k)+2)}-\frac{(1/2)^{(\alpha/k)+1}}{(\alpha/k)+1}\right)\\
&\quad-\frac{C(b-a)^{2}}{((\alpha/k)+2)((\alpha/k)+3)}\left(1-\frac{(\alpha/k)+4}{2^{(\alpha/k)+2}}\right).
\end{aligned}\tag{49}$$

Therefore, (47) implies

$$\begin{aligned}
&\left|\frac{f(a)+f(b)}{2}-\frac{\Gamma_k(\alpha+k)}{2(b-a)^{(\alpha/k)}}\left[{}_kI^{\alpha,\psi}_{\psi^{-1}(a)^{+}}(f\circ\psi)\left(\psi^{-1}(b)\right)+{}_kI^{\alpha}_{\psi^{-1}(b)^{-}}(f\circ\psi)\left(\psi^{-1}(b)\right)\right]\right|\\
&\le\frac{b-a}{2}\left[\left|f'(a)\right|\left(\frac{1}{((\alpha/k)+1)((\alpha/k)+2)}-\frac{(1/2)^{(\alpha/k)+1}}{(\alpha/k)+1}\right)+\left|f'(b)\right|\left(\frac{1}{(\alpha/k)+2}-\frac{(1/2)^{(\alpha/k)+1}}{(\alpha/k)+1}\right)\right.\\
&\quad-\frac{C(b-a)^{2}}{((\alpha/k)+2)((\alpha/k)+3)}\left(1-\frac{(\alpha/k)+4}{2^{(\alpha/k)+2}}\right)+\left|f'(a)\right|\left(\frac{1}{(\alpha/k)+2}-\frac{(1/2)^{(\alpha/k)+1}}{(\alpha/k)+1}\right)\\
&\quad\left.+\left|f'(b)\right|\left(\frac{1}{((\alpha/k)+1)((\alpha/k)+2)}-\frac{(1/2)^{(\alpha/k)+1}}{(\alpha/k)+1}\right)-\frac{C(b-a)^{2}}{((\alpha/k)+2)((\alpha/k)+3)}\left(1-\frac{(\alpha/k)+4}{2^{(\alpha/k)+2}}\right)\right].
\end{aligned}\tag{50}$$

From which after a little computation, one can get (46). □

Remark 3. Under the assumption of Theorem 12, one can get the following results:

(i) If $k=1$ and ψ is identity function in (46), then Theorem 6 is obtained.

(ii) If $C=0$ and ψ is identity function in (46), then Theorem 9 is obtained.

(iii) If $k=1$, $C=0$, and ψ is identity function in (46), then Theorem 3 is obtained.

(iv) If $k=1$, $C=0$, $\alpha=1$, and ψ is identity function in (46), then Theorem 2.2 in [42] is obtained.

(v) If $k=1$ and ψ is identity function in (46), then Theorem 6 is obtained.

Corollary 6. *Under the assumption of Theorem 12 with $C=0$ in (46), the following inequality holds:*

$$\begin{aligned}
&\left|\frac{f(a)+f(b)}{2}-\frac{\Gamma_k(\alpha+k)}{2(b-a)^{(\alpha/k)}}\left[{}_kI^{\alpha,\psi}_{\psi^{-1}(a)^{+}}(f\circ\psi)\left(\psi^{-1}(b)\right)+{}_kI^{\alpha,\psi}_{\psi^{-1}(b)^{-}}(f\circ\psi)\left(\psi^{-1}(a)\right)\right]\right|\\
&\le\frac{b-a}{2((\alpha/k)+1)}\left(1-\frac{1}{2^{(\alpha/k)}}\right)\left[\left|f'(a)\right|+\left|f'(b)\right|\right].
\end{aligned}\tag{51}$$

Corollary 7. *Under the assumption of Theorem 12 with $k=1$ in (46), the following inequality holds:*

$$\begin{aligned}
&\left|\frac{f(a)+f(b)}{2}-\frac{\Gamma(\alpha+1)}{2(b-a)^{\alpha}}\left[I^{\alpha,\psi}_{\psi^{-1}(a)^{+}}(f\circ\psi)\left(\psi^{-1}(b)\right)+I^{\alpha,\psi}_{\psi^{-1}(b)^{-}}(f\circ\psi)\left(\psi^{-1}(a)\right)\right]\right|\\
&\le\frac{b-a}{2(\alpha+1)}\left(1-\frac{1}{2^{\alpha}}\right)\left[\left|f'(a)\right|+\left|f'(b)\right|\right]-\frac{C(b-a)^{3}}{(\alpha+2)(\alpha+3)}\left(1-\frac{\alpha+4}{2^{\alpha+2}}\right).
\end{aligned}\tag{52}$$

Corollary 8. *Under the assumption of Theorem 12 with ψ as identity function in (46), the following inequality holds:*

$$\left|\frac{f(a)+f(b)}{2}-\frac{\Gamma_k(\alpha+k)}{2(b-a)^{\alpha/k}}\left[{}_kI^{\alpha}_{a^+}f(b)+{}_kI^{\alpha}_{b^-}f(a)\right]\right| \leq \frac{b-a}{2((\alpha/k)+1)}\left(1-\frac{1}{2^{\alpha/k}}\right)\left[\left|f'(a)\right|+\left|f'(b)\right|\right]-\frac{C(b-a)^3}{((\alpha/k)+2)((\alpha/k)+3)}\left(1-\frac{(\alpha/k)+4}{2^{(\alpha/k)+2}}\right). \tag{53}$$

We now derive a new fractional integral identity for fractional integrals (19) and (20).

Lemma 2. *Let $a<b$ and $f\colon [a,b]\longrightarrow \mathbb{R}$ be a differentiable mapping on (a,b). Also, suppose that $f'\in L[a,b]$ and ψ is an increasing and positive monotone function on $(a,b]$, having a continuous derivative $\psi'(x)$ on (a,b). Then, for $k>0$, the following identity holds:*

$$\frac{2^{(\alpha/k)-1}\Gamma_k(\alpha+k)}{(b-a)^{(\alpha/k)}}\left[{}_kI^{\alpha,\psi}_{\psi^{-1}(a+b/2)^+}(f\circ\psi)\left(\psi^{-1}(b)\right)+{}_kI^{\alpha,\psi}_{\psi^{-1}(a+b/2)^-}(f\circ\psi)\left(\psi^{-1}(a)\right)\right]-f\left(\frac{a+b}{2}\right) =\frac{b-a}{4}\left[\int_0^1 t^{(\alpha/k)}f'\left(\frac{at}{2}+\left(\frac{2-t}{2}\right)b\right)\mathrm{d}t -\int_0^1 t^{(\alpha/k)}f'\left(\left(\frac{2-t}{2}\right)a+\frac{bt}{2}\right)\mathrm{d}t\right], \tag{54}$$

with $\alpha>0$.

Proof. Let

$$I_1=\frac{2^{(\alpha/k)-1}\Gamma_k(\alpha+k)}{(b-a)^{(\alpha/k)}}\left[{}_kI^{\alpha,\psi}_{\psi^{-1}(a+b/2)^+}(f\circ\psi)\left(\psi^{-1}(b)\right)\right],$$

$$I_2=\frac{2^{(\alpha/k)-1}\Gamma_k(\alpha+k)}{(b-a)^{(\alpha/k)}}\left[{}_kI^{\alpha,\psi}_{\psi^{-1}(a+b/2)^-}(f\circ\psi)\left(\psi^{-1}(a)\right)\right]. \tag{55}$$

Then, we have

$$I_1=\frac{2^{(\alpha/k)-1}\alpha}{k(b-a)^{(\alpha/k)}}\left[\int_{\psi^{-1}(a+b/2)}^{\psi^{-1}(b)}\psi'(v)(b-\psi(v))^{(\alpha/k)-1}(f\circ\psi)(v)\mathrm{d}v\right] =\frac{-2^{(\alpha/k)-1}}{(b-a)^{(\alpha/k)}}\left[\int_{\psi^{-1}(a+b/2)}^{\psi^{-1}(b)}f(\psi(v))d(b-\psi(v))^{(\alpha/k)}\right] =\frac{1}{2}f\left(\frac{a+b}{2}\right)+\frac{1}{2}\int_{\psi^{-1}(a+b/2)}^{\psi^{-1}(b)}f'(\psi(v))\left(\frac{2(b-\psi(v))}{b-a}\right)^{(\alpha/k)}\psi'(v)\mathrm{d}v. \tag{56}$$

By substituting $t=(2(b-\psi(v))/b-a)$, we will get

$$I_1 = \frac{1}{2} f\left(\frac{a+b}{2}\right) + \frac{b-a}{4} \int_0^1 t^{\alpha/k} f'\left(\frac{at}{2} + \left(\frac{2-t}{2}\right)b\right) \mathrm{d}t. \tag{57}$$

We also have

$$\begin{aligned} I_2 &= \frac{2^{(\alpha/k)-1}\alpha}{k(b-a)^{(\alpha/k)}} \left[\int_{\psi^{-1}(a)}^{\psi^{-1}(a+b/2)} \psi'(v)(\psi(v)-a)^{(\alpha/k)-1} f \circ \psi(v) \mathrm{d}v \right] \\ &= \frac{2^{(\alpha/k)-1}}{(b-a)^{(\alpha/k)}} \left[\int_{\psi^{-1}(a)}^{\psi^{-1}(a+b/2)} d(\psi(v)-a)^{(\alpha/k)} (f(\psi(v))) \right] \\ &= \frac{1}{2} f\left(\frac{a+b}{2}\right) - \frac{1}{2} \int_{\psi^{-1}(a)}^{\psi^{-1}(a+b/2)} f'(\psi(v)) \left(\frac{2(\psi(v))-a)}{b-a}\right)^{(\alpha/k)} \psi'(v) \mathrm{d}v. \end{aligned} \tag{58}$$

By substituting $s = (2(\psi(v) - a)/b - a)$, we will get

$$I_2 = \frac{1}{2} f\left(\frac{a+b}{2}\right) - \frac{b-a}{4} \int_0^1 f'\left(a\left(\frac{2-s}{2}\right) + \frac{bs}{2}\right) s^{\alpha/k} \mathrm{d}s. \tag{59}$$

By summing (57) and (59), we get (54). □

Remark 4. Under the assumption of Lemma 2, one can get the following results:

(i) If $k = 1$ and ψ is identity function in (54), then the identity (Lemma 3) stated in [2] is obtained.

(ii) If $k = 1$, $\alpha = 1$, and ψ is identity function in (54), then the identity (Corollary 1) stated in [2] is obtained.

(iii) If ψ is identity function in (54), then the identity (Lemma 3.1) stated in [36] is obtained.

Corollary 9. *Under the assumption of Lemma 2 with $k = 1$ in (54), the following identity holds:*

$$\begin{aligned} &\frac{2^{\alpha-1}\Gamma(\alpha+1)}{(b-a)^{\alpha}} \left[I^{\alpha,\psi}_{\psi^{-1}(a+b/2)^+} (f \circ \psi)\left(\psi^{-1}(b)\right) - I^{\alpha,\psi}_{\psi^{-1}(a+b/2)^-} (f \circ \psi)\left(\psi^{-1}(a)\right) \right] - f\left(\frac{a+b}{2}\right) \\ &= \frac{b-a}{4} \left[\int_0^1 t^{\alpha} f'\left(\frac{at}{2} + \left(\frac{2-t}{2}\right)b\right) \mathrm{d}t + \int_0^1 t^{\alpha} f'\left(\left(\frac{2-t}{2}\right)a + \frac{bt}{2}\right) \mathrm{d}t \right]. \end{aligned} \tag{60}$$

Using above lemma, we give the following error bounds of the k-fractional Hadamard inequality.

Theorem 13. *Let $f: I \longrightarrow \mathbb{R}$ be a differentiable mapping on (a,b) with $a < b$. Also, suppose that $|f'|^q$ is strongly convex function on $[a,b]$ with modulus $C \geq 0$ for $q \geq 1$, and ψ is an increasing and positive monotone function on $(a,b]$, having a continuous derivative $\psi'(x)$ on (a,b). Then, for $k > 0$, the following k-fractional integral inequalities hold:*

$$\begin{aligned} &\left| \frac{2^{(\alpha/k)-1}\Gamma_k(\alpha+k)}{(b-a)^{(\alpha/k)}} \left[{}_kI^{\alpha,\psi}_{\psi^{-1}(a+b/2)^+} (f \circ \psi)\left(\psi^{-1}(b)\right) + {}_kI^{\alpha,\psi}_{\psi^{-1}(a+b/2)^-} (f \circ \psi)\left(\psi^{-1}(a)\right) \right] - f\left(\frac{a+b}{2}\right) \right| \\ &\leq \frac{b-a}{4((\alpha/k)+1)} \left(\frac{1}{2((\alpha/k)+2)} \right)^{1/q} \left[\left(\left(\frac{\alpha}{k}+1\right) |f'(a)|^q + \left(\frac{\alpha}{k}+3\right) |f'(b)|^q \right. \right. \\ &\quad \left. - \frac{C(b-a)^2((\alpha/k)+1)((\alpha/k)+4)}{2((\alpha/k)+3)} \right)^{1/q} + \left(\left(\frac{\alpha}{k}+3\right) |f'(a)|^q + \left(\frac{\alpha}{k}+1\right) |f'(b)|^q \right. \\ &\quad \left. \left. - \frac{C(b-a)^2((\alpha/k)+1)((\alpha/k)+4)}{2((\alpha/k)+3)} \right)^{1/q} \right], \end{aligned} \tag{61}$$

with $\alpha > 0$.

Proof. From Lemma 2 and strongly convexity of $|f'|$, let $q = 1$, we have

$$\begin{aligned}
&\left|\frac{2^{(\alpha/k)-1}\Gamma_k(\alpha+k)}{(b-a)^{(\alpha/k)}}\left[{}_kI^{\alpha,\psi}_{\psi^{-1}(a+b/2)^+}(f\circ\psi)\left(\psi^{-1}(b)\right)+{}_kI^{\alpha,\psi}_{\psi^{-1}(a+b/2)^-}(f\circ\psi)\left(\psi^{-1}(a)\right)-f\left(\frac{a+b}{2}\right)\right]\right| \\
&\le\frac{b-a}{4}\left[\int_0^1 t^{(\alpha/k)}\left|f'\left(\frac{at}{2}+\left(\frac{2-t}{2}\right)b\right)\right|\mathrm{d}t+\int_0^1 t^{(\alpha/k)}\left|f'\left(a\left(\frac{2-t}{2}\right)+\frac{bt}{2}\right)\right|\mathrm{d}t\right] \\
&\le\frac{b-a}{4}\left[\left(|f'(a)|+\left|f'(b)\right|\right)\int_0^1 t^{(\alpha/k)}\mathrm{d}t-\frac{C}{2}(b-a)^2\int_0^1 t^{(\alpha/k)+1}(2-t)\mathrm{d}t\right] \\
&\le\frac{b-a}{4((\alpha/k)+1)}\left[\left(|f'(a)|+\left|f'(b)\right|\right)-\frac{C(b-a)^2((\alpha/k)+4)((\alpha/k)+1)}{((\alpha/k)+2)((\alpha/k)+k)}\right].
\end{aligned} \tag{62}$$

Now, for $q > 1$, we proceed as follows.

From Lemma 2 and using power mean inequality, we get

$$\begin{aligned}
&\left|\frac{2^{(\alpha/k)-1}\Gamma_k(\alpha+k)}{(b-a)^{\alpha/k}}\left[{}_kI^{\alpha,\psi}_{\psi^{-1}(a+b/2)^+}(f\circ\psi)\left(\psi^{-1}(b)\right)+{}_kI^{\alpha,\psi}_{\psi^{-1}(a+b/2)^-}(f\circ\psi)\left(\psi^{-1}(a)\right)-f\left(\frac{a+b}{2}\right)\right]\right| \\
&\le\frac{b-a}{4}\left(\int_0^1 t^{(\alpha/k)}\mathrm{d}t\right)^{1-(1/q)}\left[\left(\int_0^1 t^{(\alpha/k)}\left|f'\left(\frac{at}{2}+\left(\frac{2-t}{2}\right)b\right)\right|^q\mathrm{d}t\right)^{(1/q)}\right. \\
&\left.+\left(\int_0^1 t^{(\alpha/k)}\left|f'\left(\left(\frac{2-t}{2}\right)a+\frac{bt}{2}\right)\right|^q\mathrm{d}t\right)^{(1/q)}\right].
\end{aligned} \tag{63}$$

Strongly convexity of $|f'|^q$ gives

$$\begin{aligned}
&\left|\frac{2^{(\alpha/k)-1}\Gamma(\alpha+k)}{(b-a)^{(\alpha/k)}}\left[{}_kI^{\alpha,\psi}_{\psi^{-1}(a+b/2)^+}(f\circ\psi)\left(\psi^{-1}(b)\right)+{}_kI^{\alpha,\psi}_{\psi^{-1}(a+b/2)^-}(f\circ\psi)\left(\psi^{-1}(a)\right)-f\left(\frac{a+b}{2}\right)\right]\right| \\
&\le\frac{b-a}{4((\alpha/k)+1)^{1/p}}\left[\left(|f'(a)|^q\int_0^1\frac{t^{(\alpha/k)+1}}{2}\mathrm{d}t+|f'(b)|^q\int_0^1\left(\frac{2t^{(\alpha/k)}-t^{(\alpha/k)+1}}{2}\right)\mathrm{d}t\right.\right. \\
&\left.-\frac{C(b-a)^2}{4}\int_0^1 t^{(\alpha/k)+1}(2-t)\mathrm{d}t\right)^{1/q}+\left(|f'(a)|^q\int_0^1\left(\frac{2t^{(\alpha/k)}-t^{(\alpha/k)+1}}{2}\right)\mathrm{d}t\right. \\
&\left.\left.+|f'(b)|^q\int_0^1\frac{t^{(\alpha/k)+1}}{2}\mathrm{d}t-\frac{C(b-a)^2}{4}\int_0^1 t^{(\alpha/k)+1}(2-t)\mathrm{d}t\right)^{1/q}\right] \\
&\le\frac{b-a}{4((\alpha/k)1)^{1/p}}\left[\left(\frac{|f'(a)|^q}{2((\alpha/k)+2)}+\frac{|f'(b)|^q((\alpha/k)+3)}{2((\alpha/k)+1)((\alpha/k)+2)}-\frac{C(b-a)^2((\alpha/k)+4)}{4((\alpha/k)+2)((\alpha/k)+3)}\right)^{1/q}\right. \\
&\left.+\left(\frac{|f'(a)|^q((\alpha/k)+3)}{2((\alpha/k)+1)((\alpha/k)+2)}+\frac{|f'(b)|^q}{2((\alpha/k)+2)}-\frac{C(b-a)^2((\alpha/k)+4)}{4((\alpha/k)+2)((\alpha/k)+3)}\right)^{1/q}\right],
\end{aligned} \tag{64}$$

which after a little computation gives the required result. □

Remark 5. Under the assumption of Theorem 13, one can get the following results:

(i) If $C = 0$ and ψ is identity function in (61), then the inequality (Theorem 3.1) stated in [36] is obtained.

(ii) If $C = 0$, $k = 1$, and ψ is identity function in (61), then the inequality (Theorem 5) stated in [2] is obtained.

(iii) If $q = 1$, $C = 0$, $k = 1$, $\alpha = 1$, and ψ is identity function in (61), then the inequality (Theorem 2.2) stated in [43] is obtained.

Corollary 10. *Under the assumption of Theorem 13 with $C = 0$ in (61), the following inequality holds:*

$$\begin{aligned}&\left|\frac{2^{(\alpha/k)-1}\Gamma_k(\alpha+k)}{(b-a)^{(\alpha/k)}}\left[{}_kI^{\alpha,\psi}_{\psi^{-1}(a+b/2)^+}(f\circ\psi)\left(\psi^{-1}(b)\right)+{}_kI^{\alpha,\psi}_{\psi^{-1}(a+b/2)^-}(f\circ\psi)\left(\psi^{-1}(a)\right)\right]-f\left(\frac{a+b}{2}\right)\right|\\&\le\frac{b-a}{4((\alpha/k)+1)}\left(\frac{1}{2((\alpha/k)+2)}\right)^{1/q}\left[\left(\left(\frac{\alpha}{k}+1\right)\left|f'(a)\right|^q\right.\right.\\&\left.\left.+\left(\frac{\alpha}{k}+3\right)\left|f'(b)\right|^q\right)^{1/q}+\left(\left(\frac{\alpha}{k}+3\right)\left|f'(a)\right|^q+\left(\frac{\alpha}{k}+1\right)\left|f'(b)\right|^q\right)^{1/q}\right].\end{aligned}\tag{65}$$

Corollary 11. *Under the assumption of Theorem 13 with $k = 1$ in (61), the following inequality holds:*

$$\begin{aligned}&\left|\frac{2^{\alpha-1}\Gamma(\alpha+1)}{(b-a)^{\alpha}}\left[I^{\alpha,\psi}_{\psi^{-1}(a+b/2)^+}(f\circ\psi)\left(\psi^{-1}(b)\right)+I^{\alpha,\psi}_{\psi^{-1}(a+b/2)^-}(f\circ\psi)\left(\psi^{-1}(a)\right)\right]-f\left(\frac{a+b}{2}\right)\right|\\&\le\frac{b-a}{4(\alpha+1)}\left(\frac{1}{2(\alpha+2)}\right)^{1/q}\left[\left((\alpha+1)\left|f'(a)\right|^q+(\alpha+3)\left|f'(b)\right|^q\right.\right.\\&\left.\left.-\frac{C(b-a)^2((\alpha/k)+1)(\alpha+4)}{2(\alpha+3)}\right)^{1/q}+\left((\alpha+3)\left|f'(a)\right|^q+(\alpha+1)\left|f'(b)\right|^q\right.\right.\\&\left.\left.-\frac{C(b-a)^2(\alpha+1)(\alpha+4)}{2(\alpha+3)}\right)^{1/q}\right].\end{aligned}\tag{66}$$

Corollary 12. *Under the assumption of Theorem 13 with ψ is identity function in (61), the following inequality holds:*

$$\begin{aligned}&\left|\frac{2^{(\alpha/k)-1}\Gamma_k(\alpha+k)}{(b-a)^{(\alpha/k)}}\left[{}_kI^{\alpha}_{(a+b/2)^+}f(b)-{}_kI^{\alpha}_{(a+b/2)^-}f(a)\right]-f\left(\frac{a+b}{2}\right)\right|\\&\le\frac{b-a}{4((\alpha/k)+1)}\left(\frac{1}{2((\alpha/k)+2)}\right)^{1/q}\left[\left(\left(\frac{\alpha}{k}+1\right)\left|f'(a)\right|^q+\left(\frac{\alpha}{k}+3\right)\left|f'(b)\right|^q\right.\right.\\&\left.\left.-\frac{C(b-a)^2((\alpha/k)+1)((\alpha/k)+4)}{2((\alpha/k)+3)}\right)^{1/q}+\left(\left(\frac{\alpha}{k}+3\right)\left|f'(a)\right|^q+\left(\frac{\alpha}{k}+1\right)\left|f'(b)\right|^q-\frac{C(b-a)^2((\alpha/k)+1)((\alpha/k)+4)}{2((\alpha/k)+3)}\right)^{1/q}\right].\end{aligned}\tag{67}$$

Corollary 13. *Under the assumption of Theorem 13 with $k = 1$, $q = 1$, $\alpha = 1$, and ψ as identity function in (61), the following inequality holds:*

$$\left|\frac{1}{b-a}\int_a^b f(v)\mathrm{d}v - f\left(\frac{a+b}{2}\right)\right| \leq \frac{b-a}{8}\left[\left|f'(a)\right| + \left|f'(b)\right| - \frac{5C(b-a)^2}{12}\right]. \tag{68}$$

Theorem 14. *Let $f: I \longrightarrow \mathbb{R}$ be a differentiable mapping on (a,b) with $a<b$. Also, suppose that $|f'|^q$ is strongly convex function on $[a,b]$ for $q>1$, and ψ is an increasing and positive monotone function on $(a,b]$, having a continuous derivative $\psi'(x)$ on (a,b). Then, for $k>0$, the following k-fractional integral inequalities hold:*

$$\begin{aligned}&\left|\frac{2^{(\alpha/k)-1}\Gamma_k(\alpha+k)}{(b-a)^{(\alpha/k)}}\left[{}_kI^{\alpha,\psi}_{\psi^{-1}(a+b/2)^+}(f\circ\psi)\left(\psi^{-1}(b)\right) + {}_kI^{\alpha,\psi}_{\psi^{-1}(a+b/2)^-}(f\circ\psi)\left(\psi^{-1}(a)\right)\right] - f\left(\frac{a+b}{2}\right)\right| \\ &\leq \frac{b-a}{16}\left(\frac{4}{(\alpha p/k)+1}\right)^{1/p}\left[\left(\left(\left|f'(a)\right| + 3^{1/q}\left|f'(b)\right|\right)^q - \frac{2C(b-a)^2}{3}\right)^{1/q}\right. \\ &\left. + \left(\left(3^{1/q}\left|f'(a)\right| + \left|f'(b)\right|\right)^q - \frac{2C(b-a)^2}{3}\right)^{1/q}\right],\end{aligned} \tag{69}$$

with $\alpha>0$.

Proof. From Lemma 2 and using the property of modulus, we get

$$\begin{aligned}&\left|\frac{2^{(\alpha/k)-1}\Gamma_k(\alpha+k)}{(b-a)^{(\alpha/k)}}\left[{}_kI^{\alpha,\psi}_{\psi^{-1}(a+b/2)^+}\left(f\left(\psi^{-1}(b)\right)\right) + {}_kI^{\alpha,\psi}_{\psi^{-1}(a+b/2)^-}(f\circ\psi)\left(\psi^{-1}(a)\right) - f\left(\frac{a+b}{2}\right)\right]\right| \\ &\leq \frac{b-a}{4}\left[\int_0^1\left|t^{(\alpha/k)}f'\left(\frac{t}{2}a + \left(\frac{2-t}{2}\right)b\right)\right|\mathrm{d}t + \int_0^1\left|t^{(\alpha/k)}f'\left(\left(\frac{2-t}{2}\right)a + \frac{t}{2}b\right)\right|\mathrm{d}t\right].\end{aligned} \tag{70}$$

Now applying *Hölder's* inequality for integrals, we get

$$\begin{aligned}&\left|\frac{2^{(\alpha/k)-1}\Gamma_k(\alpha+k)}{(b-a)^{(\alpha/k)}}\left[{}_kI^{\alpha,\psi}_{\psi^{-1}(a+b/2)^+}(f\circ\psi)\left(\psi^{-1}(b)\right) + {}_kI^{\alpha,\psi}_{g^{-1}(a+b/2)^-}(f\circ\psi)\left(\psi^{-1}(a)\right) - f\left(\frac{a+b}{2}\right)\right]\right| \\ &\leq \frac{b-a}{4}\left[\left(\int_0^1 t^{\alpha p/k}\mathrm{d}t\right)^{1/p}\left[\int_0^1\left|f'\left(\frac{t}{2}a + \left(\frac{2-t}{2}\right)b\right)\right|^q\mathrm{d}t\right]^{1/q}\right. \\ &\left. + \left(\int_0^1 t^{\alpha p/k}\mathrm{d}t\right)^{1/p}\left[\int_0^1\left|f'\left(\left(\frac{2-t}{2}\right)a + \frac{t}{2}b\right)\right|^q\mathrm{d}t\right]^{1/q}\right].\end{aligned} \tag{71}$$

Using strongly convexity of $|f'|^q$, we get

$$\begin{aligned}
&\left|\frac{2^{(\alpha/k)-1}\Gamma_k(\alpha+k)}{(b-a)^{(\alpha/k)}}\left[{}_kI^{\alpha,\psi}_{\psi^{-1}(a+b/2)^+}(f\circ\psi)\left(\psi^{-1}(b)\right)+{}_kI^{\alpha,a+b/2}_{\psi^{-1}(a+b/2)^-}(f\circ\psi)\left(\psi^{-1}(a)\right)-f\left(\frac{a+b}{2}\right)\right]\right| \\
&\le\frac{b-a}{4}\left(\frac{1}{(\alpha p/k)+1}\right)^{1/p}\left[\left(|f'(a)|^q\int_0^1\frac{t}{2}\mathrm{d}t+|f'(b)|^q\int_0^1\frac{2-t}{2}\mathrm{d}t\right.\right. \\
&\left.\left.-\frac{C(b-a)^2}{4}\int_0^1 t(2-t)\mathrm{d}t\right)^{1/q}+\left(|f'(a)|^q\int_0^1\frac{2-t}{2}\mathrm{d}t+|f'(b)|^q\int_0^1\frac{t}{2}\mathrm{d}t\frac{C(b-a)^2}{4}\int_0^1 t(2-t)\mathrm{d}t\right)^{1/q}\right] \\
&=\frac{b-a}{4}\left(\frac{1}{(\alpha p/k)+1}\right)^{1/p}\left[\left(|f'(a)|^q+3|f'(b)|^q-\frac{2C(b-a)^2}{3}\right)^{1/q}\right. \\
&\left.+\left(3|f'(a)|^q+|f'(b)|^q-\frac{2C(b-a)^2}{3}\right)^{1/q}\right] \\
&\le\frac{b-a}{4}\left(\frac{1}{(\alpha p/k)+1}\right)^{1/p}\left[\left(\left(|f'(a)|+3^{1/q}|f'(b)|\right)^q-\frac{2C(b-a)^2}{3}\right)^{1/q}\right. \\
&\left.+\left(\left(3^{1/q}|f'(a)|+|f'(b)|\right)^q-\frac{2C(b-a)^2}{3}\right)^{1/q}\right].
\end{aligned}\tag{72}$$

Here, we have used the fact $a^q+b^q\le(a+b)^q$, for $q>1$, $a,b\ge0$. This completes the proof. □

Remark 6. Under the assumption of Theorem 14, one can get the following results:

(i) If $C=0$ and ψ is identity function in (69), then the inequality (Theorem 3.2) stated in [36] is obtained.

(ii) If $k=1$, $C=0$, $\alpha=1$ and ψ is identity function in (69), then the inequality (Theorem 2.3) stated in [43] is obtained.

Corollary 14. *Under the assumption of Theorem 14 with $C=0$ in (69), the following inequality holds:*

$$\begin{aligned}
&\left|\frac{2^{(\alpha/k)-1}\Gamma_k(\alpha+k)}{(b-a)^{(\alpha/k)}}\left[{}_kI^{\alpha,\psi}_{\psi^{-1}(a+b/2)^+}(f\circ\psi)\left(\psi^{-1}(b)\right)+{}_kI^{\alpha,\psi}_{\psi^{-1}(a+b/2)^-}(f\circ\psi)\left(\psi^{-1}(a)\right)-f\left(\frac{a+b}{2}\right)\right]\right| \\
&\le\frac{b-a}{4}\left(\frac{4}{(\alpha p/k)+1}\right)^{1/p}\left[|f'(a)|+|f'(b)|\right].
\end{aligned}\tag{73}$$

Corollary 15. *Under the assumption of Theorem 14 with $k=1$ in (69), the following inequality holds:*

$$\begin{aligned}
&\left|\frac{2^{\alpha-1}\Gamma(\alpha+1)}{(b-a)^{\alpha}}\left[I^{\alpha,\psi}_{\psi^{-1}(a+b/2)^+}(f\circ\psi)\left(\psi^{-1}(b)\right)+I^{\alpha,\psi}_{\psi^{-1}(a+b/2)^-}\left(\psi^{-1}(a)\right)-f\left(\frac{a+b}{2}\right)\right]\right| \\
&\le\frac{b-a}{16}\left(\frac{4}{\alpha p+1}\right)^{1/p}\left[\left(\left(|f'(a)|+3^{1/q}|f'(b)|\right)^q-\frac{2C(b-a)^2}{3}\right)^{1/q}\right. \\
&\left.+\left(\left(3^{1/q}|f'(a)|+|f'(b)|\right)^q-\frac{2C(b-a)^2}{3}\right)^{1/q}\right].
\end{aligned}\tag{74}$$

Corollary 16. *Under the assumption of Theorem 14 with $C = 0$ and $k = 1$ in (69), the following inequality holds:*

$$\left|\frac{2^{\alpha-1}\Gamma(\alpha+1)}{(b-a)^{\alpha}}\left[I^{\alpha,\psi}_{\psi^{-1}(a+b/2)^{+}}(f\circ\psi)\left(\psi^{-1}(b)\right)+I^{\alpha,\psi}_{\psi^{-1}(a+b/2)^{-}}(f\circ\psi)\left(\psi^{-1}(a)\right)-f\left(\frac{a+b}{2}\right)\right]\right| \leq \frac{b-a}{4}\left(\frac{4}{\alpha p+1}\right)^{1/p}\left[\left|f'(a)\right|+\left|f'(b)\right|\right]. \tag{75}$$

Corollary 17. *Under the assumption of Theorem 14 with ψ is identity function in (69), the following inequality holds:*

$$\left|\frac{2^{(\alpha/k)-1}\Gamma_k(\alpha+k)}{(b-a)^{(\alpha/k)}}\left[{}_kI^{\alpha}_{(a+b/2)^{+}}f(b)+{}_kI^{\alpha}_{(a+b/2)^{-}}f(a)-f\left(\frac{a+b}{2}\right)\right]\right| \leq \frac{b-a}{16}\left(\frac{4}{(\alpha p/k)+1}\right)^{1/p}\left[\left(\left(\left|f'(a)\right|+3^{1/q}\left|f'(b)\right|\right)^{q}-\frac{2C(b-a)^2}{3}\right)^{1/q}+\left(\left(3^{1/q}\left|f'(a)\right|+\left|f'(b)\right|\right)^{q}-\frac{2C(b-a)^2}{3}\right)^{1/q}\right]. \tag{76}$$

Corollary 18. *Under the assumption of Theorem 14 with $k = 1$, $\alpha = 1$, and ψ is identity function in (69), the following inequality holds:*

$$\left|\frac{1}{b-a}\int_a^b f(t)\mathrm{d}t-f\left(\frac{a+b}{2}\right)\right| \leq \frac{b-a}{16}\left(\frac{4}{p+1}\right)^{1/p}\left[\left(\left(\left|f'(a)\right|+3^{1/q}\left|f'(b)\right|\right)^{q}-\frac{2C(b-a)^2}{3}\right)^{1/q}+\left(\left(3^{1/q}\left|f'(a)\right|+\left|f'(b)\right|\right)^{q}-\frac{2C(b-a)^2}{3}\right)^{1/q}\right]. \tag{77}$$

4. Conclusion

In this paper, we have studied Hadamard inequalities and their error estimations using generalized Riemann–Liouville fractional integrals of strongly convex functions. The Hadamard inequalities obtained in this work are refinements as well as generalizations of many well-known inequalities. The error estimations of the Hadamard inequalities for differentiable strongly convex functions are better as compared to those which are obtained for convex functions. The authors are analyzing other well-known fractional integral operators for several kinds of functions in their future work.

Data Availability

No additional data are required.

Conflicts of Interest

The authors declare that they have no conflicts of interest.

References

[1] M. Z. Sarikaya, E. Set, H. Yaldiz, and N. Başak, "Hermite-Hadamard's inequalities for fractional integrals and related fractional inequalities," *Mathematical and Computer Modelling*, vol. 57, no. 9-10, pp. 2403–2407, 2013.

[2] M. Z. Sarikaya and H. S. Yildirim, "On Hermite-Hadamard type inequalities for Riemann-Liouville fractional integrals," *Miskolc Mathematical Notes*, vol. 17, no. 2, pp. 1049–1059, 2017.

[3] E. Set and I. Mumcu, "Hermite-Hadamard-Fejér type inequalities for conformable fractional integrals," *Miskolc Mathematical Notes*, vol. 20, no. 1, pp. 475–488, 2019.

[4] G. Farid, "Hadamard and Fejér-Hadamard inequalities for generalized fractional integrals involving special functions," *Konuralp Journal of Mathematics*, vol. 4, no. 1, pp. 108–113, 2016.

[5] G. Rahman, T. Abdeljawad, F. Jarad, A. Khan, and K. S. Nisar, "Certain inequalities via generalized proportional Hadamard fractional integral operators," *Advances in Difference Equations*, vol. 2019, p. 454, 2019.

[6] H. Chen and U. N. Katugampola, "Hermite-Hadamard and Hermite-Hadamard-Fejér type inequalities for generalized fractional integrals," *Journal of Mathematical Analysis and Applications*, vol. 446, no. 2, pp. 1274–1291, 2017.

[7] J. Wang, X. Li, and C. Zhu, "Refinements of Hermite-Hadamard type inequalities involving fractional integrals," *Bulletin of the Belgian Mathematical Society—Simon Stevin*, vol. 20, no. 4, pp. 655–666, 2013.

[8] M. Avci, H. Kavurmaci, and M. Emin Raciila, "New inequalities of Hermite-Hadamard type via s-convex functions in the second sense with applications," *Applied Mathematics and Computation*, vol. 217, no. 12, pp. 5171–5176, 2011.

[9] N. Mehreen and M. Anwar, "Hermite-Hadamard and Hermite-Hadamard-Fejer type inequalities for p-convex functions via new fractional conformable integral operators," *Journal of Mathematics and Computer Science*, vol. 19, no. 4, pp. 230–240, 2019.

[10] P. O. Mohammed, M. Z. Sarikaya, and D. Baleanu, "On the generalized Hermite-Hadamard inequalities via the tempered fractional integrals," *Symmetry*, vol. 12, no. 4, p. 595, 2020.

[11] S. Mubeen, S. Iqbal, and M. Tomar, "On Hermite-Hadamard type inequalities via fractional integrals of a function with respect to another function and k-parameter," *Journal of Inequalities and Applications*, vol. 10, p. 5, 2016.

[12] K. Oldham and J. Spanier, *The Fractional Calculus*, Academic Press, New York, NY, USA, 1974.

[13] K. S. Miller and B. Ross, *An Introduction to the Fractional Calculus and Fractional Differential Equations*, John Wiley & Sons, New York, NY, USA, 1993.

[14] S. Das, "Introduction to fractional calculus," in *Functional Fractional Calculus,* Springer, Berlin, Heidelberg, 2011.

[15] K. S. Nisar, D. Baleanu, and M. M. Al Qurashi, "Fractional calculus and application of generalized Struve function," *Springerplus*, vol. 5, no. 1, p. 910, 2016.

[16] K. S. Nisar, G. Rahman, J. Choi, S. Mubeen, and M. Arshad, "Generalized hypergeometric k-functions via (k,s)-fractional calculus," *The Journal of Nonlinear Sciences and Applications*, vol. 10, no. 4, pp. 1791–1800, 2017.

[17] P. Agarwal, M. Chand, J. Choi, and G. Singh, "Certain fractional integrals and image formulas of generalized-kBessel function," *Communications of the Korean Mathematical Society*, vol. 33, no. 2, pp. 423–436, 2018.

[18] D. Baleanu and G. C. Wu, "Some further results of the Laplace transform for variable-order fractional difference equations," *Fractional Calculus and Applied Analysis*, vol. 22, no. 6, pp. 1641–1654, 2019.

[19] D. Baleanu, S. Rezapour, and Z. Saberpour, "On fractional integro-differential inclusions via the extended fractional Caputo-Fabrizio derivation, bound," *Boundary Value Problems*, vol. 2019, no. 1, p. 79, 2019.

[20] G. Singh, P. Agarwal, S. Araci, and M. Acikgoz, "Certain fractional calculus formulas involving extended generalized Mathieu series," *Advances in Difference Equations*, vol. 2018, p. 144, 2018.

[21] A. A. El-Sayed and P. Agarwal, "Numerical solution of multiterm variable-order fractional differential equations via shifted Legendre polynomials," *Mathematical Methods in the Applied Sciences*, vol. 42, no. 2, pp. 3978–3991, 2019.

[22] H. Khalil, R. A. Khan, D. Baleanu, and M. M. Rashidi, "Some new operational matrices and its application to fractional order Poisson equations with integral type boundary constrains," *Computers & Mathematics with Applications*, vol. 78, no. 6, pp. 1826–1837, 2019.

[23] K. S. Nisar, G. Rahman, and K. Mehrez, "Chebyshev type inequalities via generalized fractional conformable integrals," *Journal of Inequalities and Applications*, vol. 2019, p. 245, 2019.

[24] M. U. Farooq, M. S. Khan, M. S. Khan, and A. Hajizadeh, "Flow of viscous fluid over an infinite plate with Caputo-Fabrizio derivatives," *Open Journal of Mathematical Sciences*, vol. 3, no. 1, pp. 115–120, 2019.

[25] V. V. Kulish and J. L. Lage, "Application of fractional calculus to fluid mechanics," *Journal of Fluids Engineering*, vol. 124, no. 3, pp. 803–806, 2002.

[26] Z. Odibat and S. Momani, "The variational iteration method: an efficient scheme for handling fractional partial differential equations in fluid mechanics," *Computational and Applied Mathematics*, vol. 58, no. 11-12, pp. 2199–2208, 2009.

[27] C. N. Angstmann, B. I. Henry, and A. V. McGann, "A fractional-order interactivity and recovery SIR model," *Fractal and Fractional*, vol. 1, no. 1, p. 11, 2017.

[28] A. Akgül, A. Kilicman, and D. Baleanu, "A new approach for one-dimensional sine-Gordon equation," *Advances in Difference Equations*, vol. 2016, no. 8, p. 8, 2016.

[29] B. T. Polyak, "Existence theorems and convergence of minimizing sequences in extremum problems with restrictions," *Soviet Mathematics. Doklady*, vol. 7, pp. 72–75, 1966.

[30] J. P. Vial, "Strong convexity of sets and functions," *Journal of Mathematical Economics*, vol. 9, no. 1-2, pp. 187–205, 1982.

[31] M. U. Awan, M. A. Noor, T.-S. Du, and K. I. Noor, "New refinements of fractional Hermite-Hadamard inequality," *Revista de la Real Academia de Ciencias Exactas, Físicas y Naturales. Serie A. Matemáticas*, vol. 113, no. 1, pp. 21–29, 2019.

[32] F. Zhang, G. Farid, and S. B. Akbar, "Inequalities for Riemann-Liouville fractional integrals of strongly (s,m)-convex functions," *Journal of Mathematics*, vol. 2021, Article ID 5577203, 14 pages, 2021.

[33] S. Mubeen and G. M. Habibullah, "k Fractional integrals and applications," *International Journal of Contemporary Mathematical Sciences*, vol. 7, pp. 89–94, 2012.

[34] S. Mubeen and A. Rehman, "A note on k-Gamma function and Pochhammer k-symbol," *Journal of Mathematical Sciences*, vol. 6, no. 2, pp. 93–107, 2014.

[35] G. Farid, A. U. Rehman, and M. Zahra, "On Hadamard-type inequalities for k-fractional integrals," *Nonlinear Functional Analysis and Applications*, vol. 21, no. 3, pp. 463–478, 2016.

[36] G. Farid, A. U. Rehman, and M. Zahra, "On Hadamard inequalities for k-fractional integrals," *Konuralp Journal of Mathematics*, vol. 4, no. 2, pp. 79–86, 2016.

[37] A. A. Kilbas, H. M. Srivastava, and J. J. Trujillo, *Theory and Applications of Fractional Differential Equations*, North-Holland Math. Stud., Elsevier, New York, NY, USA, 2006.

[38] Y. C. Kwun, G. Farid, W. Nazeer, S. Ullah, and S. M. Kang, "Generalized Riemann-Liouville k-fractional integrals associated with ostrowski type inequalities and error bounds of hadamard inequalities," *IEEE Access*, vol. 6, pp. 64946–64953, 2018.

[39] S. G. Samko, A. A. Kilbas, and O. I. Marichev, *Fractional Integrals and Derivatives, Theory and Applications*, Gordon and Breach Science Publishers, London, UK, 1993.

[40] K. Liu, J. Wang, and D. O'regan, "On the Hermite-Hadamard type inequality for ψ-Riemann-Liouville fractional integrals via convex functions," *Journal of Inequalities and Applications*, vol. 2019, p. 27, 2019.

[41] M. U. Awan, S. Talib, Y. M. Chu, M. A. Noor, and K. I. Noor, "Some new refinements of Hermite-Hadamard-type inequalities involving ψ_k-Riemann-Liouville fractional integrals and applications," *Journal of Mathematical Problems in Engineering*, vol. 2020, no. 1, pp. 1–10, 2020.

[42] S. S. Dragomir and R. P. Agarwal, "Two inequalities for differentiable mappings and applications to special means of real numbers and to trapezoidal formula," *Applied Mathematics Letters*, vol. 11, no. 5, pp. 91–95, 1998.

[43] U. S. Kirmaci, "Inequalities for differentiable mappings and applications to special means of real numbers and to midpoint formula," *Applied Mathematics and Computation*, vol. 147, no. 1, pp. 137–146, 2004.

[44] N. Merentes and K. Nikodem, "Remarks on strongly convex functions," *Aequationes Mathematicae*, vol. 80, no. 1-2, pp. 193–199, 2010.

Hindawi
Mathematical Problems in Engineering
Volume 2021, Article ID 6687064, 12 pages
https://doi.org/10.1155/2021/6687064

Research Article

Investigation of Counterflow Microchannel Heat Exchanger with Hybrid Nanoparticles and PCM Suspension as a Coolant

Mushtaq I. Hasan,[1] Mohammad J. Khafeef,[1] Omid Mohammadi,[2] Suvanjan Bhattacharyya,[3] and Alibek Issakhov[4]

[1]*Mechanical Engineering Department, College of Engineering, University of Thi-Qar, Nasiriyah, Iraq*
[2]*Department of Mechanical Engineering, Sharif University of Technology, Tehran, Iran*
[3]*Center for Renewable Energy and Environment Development, Department of Mechanical Engineering, Birla Institute of Technology & Science, Pilani Campus, Vidya Vihar, Pilani, Rajasthan 333 031, India*
[4]*Faculty of Mechanics and Mathematics, Department of Mathematical and Computer Modelling, Al-Farabi Kazakh National University, Almaty, Kazakhstan*

Correspondence should be addressed to Omid Mohammadi; omidmohmm@alum.sharif.edu

Received 19 November 2020; Revised 23 December 2020; Accepted 10 March 2021; Published 25 March 2021

Academic Editor: Younes Menni

The effect of the hybrid suspension on the intrinsic characteristics of microencapsulated phase change material (MEPCM) slurry used as a coolant in counterflow microchannel heat exchanger (CFMCHE) with different velocities is investigated numerically. The working fluid used in this paper is a hybrid suspension consisting of nanoparticles and MEPCM particles, in which the particles are suspended in pure water as a base fluid. Two types of hybrid suspension are used (Al_2O_3 + MEPCM and Cu + MEPCM), and the hydrodynamic and thermal characteristics of these suspensions flowing in a CFMCHE are numerically investigated. The results indicated that using hybrid suspension with high flow velocities improves the performance of the microchannel heat exchanger while resulting in a noticeable increase in pressure drop. Thereupon, it causes a decrease in the performance index. Moreover, it was found that the increment of the nanoparticles' concentration can rise the low thermal conductivity of the MEPCM slurry, but it also leads to a noticeable increase in pressure drop. Furthermore, it was found that as the thermal conductivity of Cu is higher than that for Al_2O_3, the enhancement in heat transfer is higher in case of adding Cu particles compared with Al_2O_3 particles. Therefore, the effectiveness of these materials depends strongly on the application at which CFMCHE is employed.

1. Introduction

The need for cooling devices in various industries such as building [1], electronic devices [2], and solar applications [3–6] has increased so that various researches have been conducted on this field. Thus, enhancing the performance of heat transfer and thermal storage systems is very important and has gained lots of interest [7]. The geometry and working flow are the most noteworthy methods for improvement. Using metal and carbon nanofluids, due to the high thermal conductivity of these materials, has intensified their application in modern heat transfer systems. Phase change materials (PCMs) could improve the heat storage capacity of the fluid and can enhance the heat storage and heat transfer potential of the working fluid by absorbing and releasing heat at a constant temperature. A point to be noted is that the weak thermal conductivity of PCM has limited severely the heat transfer of these materials during both discharging and charging processes in thermal storage systems. A wide range of investigations was conducted to enhance the thermal conductivity of PCMs. From these methods, the use of nanoparticles to increase the heat transfer rates is of high significance [8]. Kashani et al. [9] carried out a numerical investigation into the discharging of

Nanoenhanced Phase Change Material (NEPCM) inside an enclosure. They used different types of nanofluids at concentrations of $\phi = 0\%$, 2.5%, and 5% in a cavity in which the left wall is under constant heat flux, and the other sides were thermally insulated. It was illustrated that the heat transfer rate of the enclosure improves, as the nanoparticles are added to the system. Gujarathi [10] studied the characteristics of PCM enriched by nanoparticles to be used in a data center cooling system. Thus, wide ranges of concentration of copper were added to the paraffin as the PCM. The dispersion of nanoparticles into the paraffin increased its thermal conductivity when compared with conventional PCM. As a result, the heat transfer and melting rate were improved in the presence of nanoparticles. A point to be mentioned is that since concentration is associated with viscosity increment, the lower concentrations of nanoparticles showed better heat transfer properties in comparison with higher concentrations. Using high latent heat capacity of PCM along with high thermal conductivity of nanoparticles was stated as a promising potential in data center cooling applications. Farsani et al. [11] compared the impacts using nanoalumina at the concentration of 0.01, 0.02, and 0.03 by volume on the melting and solidification of PCM. They employed the enthalpy-porosity method to predict the PCM behavior. It was found that the overall performance of the phase change exceeds at the concentration of 0.02, which is due to the dominance of conduction improvement over the convection weakening.

In fact, dispersing carbon and metal nanoparticles into the base fluid could improve the thermal conductivity, and dispersing microencapsulated PCM (MEPCM) could enhance the heat storage capacity of the base fluid.

There are numerous studies regarding the performance of microchannel heat exchangers by using MEPCM suspension, nanofluids, and hybrid suspensions. Hasan et al. [12] numerically studied the performance of a counterflow microchannel heat exchanger (CFMCHE) charged with nanofluid as a coolant fluid. Two types of nanofluids including Al_2O_3-water and Cu-water were studied at concentrations of 1% to 5% by volume. It was inferred that using the nanofluids as a coolant medium results in the enhancement of the thermal performance of CFMCHE, with no rise in pressure drop because of low concentrations and also the ultrafine solid particles. The effectiveness of nanoparticles was higher in lower concentrations than in high concentrations. In other words, the effectiveness decreased with increasing the concentration. They also concluded that the best nanoparticle to be used is the one with higher thermal conductivity. Hasan [13] numerically investigated a CFMCHE with MEPCM suspension as the working fluid. The MEPCM suspension used in his research was made of microcapsules constructed from n-octadecane and polymethylmethacrylate as the core and shell materials, respectively. These capsules were dispersed in pure water at a concentration range of 0 to 20%. From their results, it was found that using MEPCM suspension as a cooling medium results in improvement of thermal performance of the CFMCHE but increasing the pressure drop significantly. As well, in order to obtain the benefits of melting of phase change material (PCM) and releasing the latent heat, it is favorable to use the MEPCM suspension with low concentration. Ho et al. [14] employed a hybrid suspension as a working fluid, consisting of Al_2O_3 nanoparticles and MEPCM particles and water as the base fluid. The thermal properties of hybrid suspension, including the thermal conductivity, specific heat, dynamic viscosity, latent heat of fusion, and density, were experimentally examined. It was concluded that increasing the concentration of Al_2O_3 nanoparticles increases the thermal conductivity of the PCM suspension. Ho et al. [15] experimentally investigated the effect of using a hybrid nanofluid on the natural convection in a circular tube. They employed pure water, PCM suspension (wPCM = 2, 5, and 10 wt.%), and nanofluids (wnp = 2, 6, and 10 wt.%) as cooling fluids and investigated the convection in the tube. The nanofluid decreased the specific heat and increased the thermal conductivity while PCM suspension weakened the thermal conductivity and increased the specific heat. The dominance of the thermal conductivity over specific heat in nanofluid and also specific heat over thermal conductivity in PCM suspension led to the improvement of the heat transfer of the working fluid. Ho et al. [16] experimentally used a hybrid nanofluid containing Al_2O_3 nanoparticles along with MEPCM particles to investigate their effects on the laminar convective cooling performance in a circular tube. A significant enhancement in cooling was obtained by using the hybrid nanofluid compared with the pure PCM suspension, Al_2O_3 nanofluid, and water. However, as the concentration rose, because of viscosity increment, the pressure drop increased, and thus, the effect of utilizing hybrid suspension decreased. Meanwhile, the dependency of pressure drop on concentration was higher in case of hybrid suspension than the nanofluid or pure PCM suspension. Elbahjaoui and El Qarnia [17] studied a shell and tube thermal storage system. They used water as the heat transfer fluid and n-octadecane embedded in shell space as the PCM. They investigated two cases of stationary and pulsating heat transfer fluid (HTF) on the storage characteristics and, thus, used nanoparticles with concentrations ranging from 0 to 7% by volume and HTF with dimensionless frequency from 0.01 to 3. The best performance was obtained in a volume fraction of 7% and pulsating frequency of 1. In the optimum case, the melting time was reduced up to 14.4%.

Augmenting convective heat transfer by using a swirl generator is one of the most popular techniques in the HVAC&R industry [18–23]. Hao and Tao [24] numerically investigated the mixed convective heat transfer. A square cavity with partial slip-filled kerosene–cobalt nanofluid is used for the study. The horizontal walls of the cavity are kept insulated while the vertical wall is partially heated. It was reported that heat flow was affected by the change in volume concentration of ferrofluid.

Goel et al. [25] numerically investigated the free convective heat transfer and flow of MHD Alumina-Cu/water nanofluid filled in a square cavity. The cavity contains a corrugated conductive cylinder. The left wall of the cavity is given constant heat. Corcione correlation is used for determining the thermal conductivity and viscosity of the

hybrid nanofluid. It was reported from the results that the presence of a wavy block in the cavity influences the flow and thermal characteristics. Local Thermal Nonequilibrium model has been utilized by Tsai and Chein [26] to investigate the heat transport through convection in a porous medium filled with Ag–MgO/H_2O nanofluid. The influencing parameters investigated in the study are Rayleigh number, porosity, the volume fraction of nanoparticles, interface convective heat transfer coefficient, and thermal conductivity ratio. The study concluded that vortex strength is increased with an increase in Ra while the dispersion of combined Ag–MgO nanoparticles in the fluid reduces the flow and thermal transport in the cavity as compared with Ag and MgO nanoparticles individually. Lee and Mudawar [27] numerically inspected the effect of MHD flow of second-grade fluid on the convective heat transfer in a vertical channel filled with porous medium. The results are analyzed with respect to velocity, temperature, volume concentration, skin friction, and heat and mass flow rate. It was revealed that increasing the permeability results in an increase in skin friction.

Manikandan and Rajan [28] experimentally investigated the double pipe HE, shell and tube HE, and plate HE for the same surface area under the same condition with the same nanofluids for thermal and flow characteristics. The results obtained from the experiments showed that minimum pressure drop was obtained with plate-type HE at 27% enhancement while maximum pressure drop was observed with double pipe HE with 85% enhancement in thermal transport. Sadeghi et al. [29] numerically revealed the benefits of using multilayer PCMs. 15 sets of experiments have been conducted to investigate the effect of various arrangements and thickness of the layer of phase change materials. It was revealed that the single layer saves 23% of inlet energy while three layers of PCM save 41% of inlet energy. Dogonchi et al. [30] utilize controlled volume-based FEM for investigating the presence of nanoparticles in a square cavity fitted with an elliptical cylinder for free convective heat transfer. The results obtained from the simulation show that, at a specific aspect ratio, enhancement in heat transfer and Nu was observed.

Ghalambaz et al. [31] numerically investigated the impact of Ag–MgO/water hybrid nanofluid filled in a square cavity fitted with a solid conductive layer at a hot wall for free convection. The parameters used for the study are volume concentration of nanoparticles, Rayleigh number, and thermal conductivity ratio. The study concluded that adding the hybrid nanoparticles in the base fluid and increasing the Ra and thermal conductivity ratio lead to the enhancement of heat transport. Ishak et al. [32] investigated the effect of wall thickness on heat transfer and entropy production in a square cavity filled with Al_2O_3 nanofluid. A moving heat source is present at the lower wall, which allows partial isothermal heating while other walls remain insulated. It was revealed from the obtained results that thermal conductivity and thickness of the wall are key parameters to control the optimal heat transfer and pressure drop.

Rejvani et al. [33] experimentally reveal the effect of the addition of SiO_2, and MWCNT in 10 W 40 engine oil. The viscosity of the resulting hybrid nanofluid was tested for various concentrations at different temperature ranges. The results show a 35% increase in the viscosity of the hybrid nanofluid comparative to base fluid.

Alsabery et al. [34] computationally studied the convective heat transfer and entropy production in a trapezoidal cavity filled with nanohomogenous Al_2O_3-water nanofluid under the influence of a magnetic field. The governing PDEs are solved using Galerkin weighted residual FEM. The parameters studied are Rayleigh No., the concentration of nanoparticles, Hartmann No., thermal conductivity, and height of the trapezoidal body. It was revealed that streamlines show more sensitive behavior for Hartmann as compared with the change in volume fraction.

Mehryan et al. [35] revealed the impact of MWCNT-Fe_2O_3/H_2O nanofluid on the convective heat transfer under the influence of an inclined magnetic field. The parameters that influence the thermal and flow characteristics are studied. An increase in average Nusselt's number was up to $Ra = 10^4$ while an increase in viscosity due to the addition of nanoparticles decreases the average Nu. Hoseinzadeh et al. [36] numerically investigated porous rectangular fin and run the simulation for analyzing the thermal transport. The results obtained from Runge-Kutta numerical analysis are compared with results obtained through collocation method (CM), homotopy perturbation method (HPM), and homotopy analysis method (HAM). It was revealed from the study that on increasing the porosity, convection, and radiation; temperature gradient and heat flow increase along the fin length. Taamneh et al. [37] computationally investigated the thermal and flow behavior of Al_2O_3-H_2O nanofluid in a triangular duct. The Reynolds number varied between 4000 and 10000. 20% increase in friction factor was observed with the addition of nanoparticles in comparison to base fluid while pressure drop was increased by 85% for $Re = 10000$. Besides this, a 40% increase in the production of entropy was also observed when varying the concentration of nanoparticles from 0.05 to 0.1%. Raza et al. [38] investigated the effect of MoS_2–H_2O nanofluid in a channel with different shapes of nanoparticles. A magnetic field influenced the flow. The results obtained from the analysis show that increasing the concentration of nanoparticles in the base fluid increases the Nu while increasing the value of wall expansion ratio results in augmentation of velocity profile between bottom wall and center.

Giwa et al. [39] investigated the impact of ferrous hybrid nanofluid on the convective thermal and flow performance in the rectangular cavity under the influence of a magnetic field. The thermal properties of hybrid nanofluid are also analyzed for different particle concentrations. The magnetic field enhances the average Nu by 4.9% while increasing the strength of the magnetic field further enhances the thermal transport. The authors also noticed that the use of hybrid nanofluid shows better results in comparison to mono nanofluid. Giwa et al. [40] in another work investigated the thermal performance of Alumina-MWCNT/water nanofluid filled in a square enclosure. The nanofluid has been investigated for the different weight ratios of nanoparticles. It was revealed that nanofluid with a 60–40 weight ratio of Al_2O_3-MWCNT

nanoparticles gives the best results. The hybrid nanofluid also promotes convective heat transfer with the cavity. Osman et al. [41] experimentally investigated a uniformly heated rectangular channel for convective heat transfer in a turbulent flow regime. Alumina-water nanofluid is used as a working fluid for the investigation. The Re varied from 200 to 7000. It was revealed from the results that a maximum heat transfer of 54% was observed in transition flow for nanofluids having 1% of nanoparticles. Mahadevi et al. [42] numerically investigated the effect of different inclination angles of the circular tube on the mixed convection heat transfer of Al_2O_3-water nanofluid. It was observed that maximum deposition of nanoparticles takes place at a 30^o inclination angle for all concentrations. It was revealed that inclination angles have a little effect on HTC up to 35^o. Further increase in the inclination angle decreases the HTC.

Sharifpur et al. [43] optimized the concentration of TiO_2-water nanofluid for maximum convective heat transfer in a square cavity. The upper and lower walls of the cavity are insulated while a temperature gradient exists between the left wall and right wall. It was found that the addition of TiO_2 nanoparticles enhances the heat transport for all concentrations while the maximum heat transfer of 8.2% was observed at 0.05% concentration. Sharifpur et al. [44] experimentally investigate the impact of the size of Al_2O_3 nanoparticles on the thermal conductivity of Al_2O_3-glycerol nanofluid. The nanofluid prepared with 3 different sizes of nanoparticles for concentration varied between 0.5 and 4%. It was revealed from the experiments that maximum augmentation of thermal conductivity was observed at 4% concentration for 31 nm nanoparticles. It was also found that thermal conductivity is influenced by volume concentration and size of nanoparticles, while temperature variation shows negligible impact.

After a wide review of previous research, the researcher did not find a previous study regarding the usage of hybrid suspension in the heat exchanger of microchannels. Thus, it is a source of modernity for this paper. In fact, by using the hybrid suspension, both advantages of nanoparticles and microcapsules are obtained. MEPCM can improve the heat capacity of the cooling fluids, and on the other hand, nanofluid can improve the thermal conductivity; thereupon, using a mixture of these materials may lead to a significant increase in heat transfer of microchannel heat exchanger.

2. Mathematical Model

Figure 1 represents the schematic structure of CFMCHE used in this study with square channels carrying cold and hot fluids. To study the fully CFMCHE, numerically, a huge amount of time is required due to its complication. As shown in Figure 2, given that there is a symmetry between the cold and hot channel rows, geometrically and thermally, assuming a part of the geometry as the model studied is acceptable, since it gives an adequate indication for the whole heat exchanger performance. Hence, two channels in the cold and hot fluids flow, and the separating wall between them is considered as the studied cases and modeled numerically [18, 19].

The assumptions used to solve this model are 3D, laminar, steady-state, incompressible fluid, continuum flow, constant properties, and thermally isolated from the ambient.

3. Governing Equations

The governing equations are continuity, momentum, and energy used for the flow of pure fluids, nanofluid, MEPCM suspension, and hybrid suspension as follows [13, 20, 21].

3.1. Governing Equations for Pure Water and Nanofluids

The continuity equation is

$$\frac{\partial u_j}{\partial x} + \frac{\partial v_j}{\partial y} + \frac{\partial w_j}{\partial z} = 0. \tag{1}$$

The momentum equations are

$$u_j\frac{\partial u_j}{\partial x} + v_j\frac{\partial u_j}{\partial y} + w_j\frac{\partial u_j}{\partial z} = \frac{1}{\rho_j}\frac{\partial P}{\partial x} + \frac{\mu_j}{\rho_j}\left(\frac{\partial^2 u_j}{\partial x^2} + \frac{\partial^2 u_j}{\partial y^2} + \frac{\partial^2 u_j}{\partial z^2}\right), \tag{2}$$

$$u_j\frac{\partial v_j}{\partial x} + v_j\frac{\partial v_j}{\partial y} + w_j\frac{\partial v_j}{\partial z} = \frac{1}{\rho_j}\frac{\partial P}{\partial y} + \frac{\mu_j}{\rho_j}\left(\frac{\partial^2 v_j}{\partial x^2} + \frac{\partial^2 v_j}{\partial y^2} + \frac{\partial^2 v_j}{\partial z^2}\right), \tag{3}$$

$$u_j\frac{\partial w_j}{\partial x} + v_j\frac{\partial w_j}{\partial y} + w_j\frac{\partial w_j}{\partial z} = \frac{1}{\rho_j}\frac{\partial P}{\partial z} + \frac{\mu_j}{\rho_j}\left(\frac{\partial^2 w_j}{\partial x^2} + \frac{\partial^2 w_j}{\partial y^2} + \frac{\partial^2 w_j}{\partial z^2}\right), \tag{4}$$

where j stands for h for the hot and c for the cold fluids, respectively.

The energy equation for fluids in heat exchanger is

$$\rho c\left(u\frac{\partial T}{\partial x} + v\frac{\partial T}{\partial y} + w\frac{\partial T}{\partial z}\right) = \Phi + k\left(\frac{\partial^2 T}{\partial x^2} + \frac{\partial^2 T}{\partial y^2} + \frac{\partial^2 T}{\partial z^2}\right). \tag{5}$$

The energy equation for solid walls in heat exchanger is

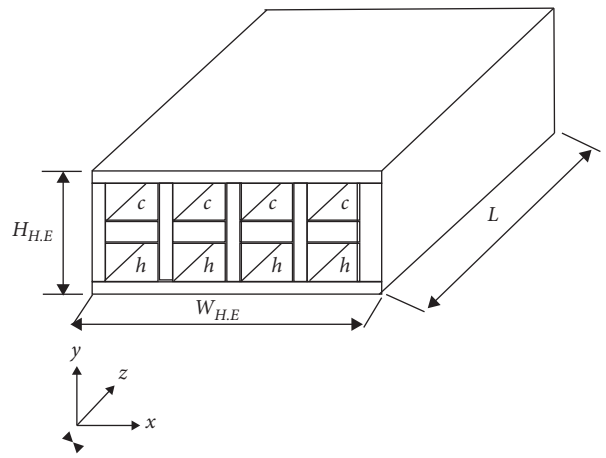

Figure 1: A schematic model of the counterflow MCHE.

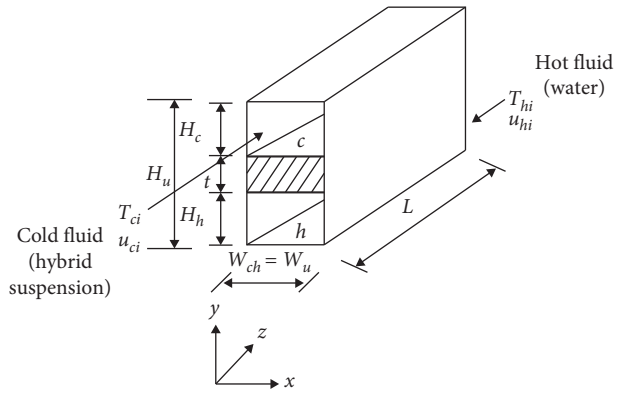

Figure 2: A schematic of the heat exchange unit.

$$k_s \nabla^2 T_s = 0. \tag{6}$$

3.2. Governing Equations for MEPCM and Hybrid Suspensions. The governing equations used for pure fluid (equations 1 to 4 and 6) are also used MEPCM and hybrid suspension.

The enthalpy-based energy equation is written as follows:

$$\nabla \cdot \left[\vec{v}\left(\rho_f H_e\right)\right] = \nabla \cdot \left(k_f \nabla T_f\right). \tag{7}$$

It also can be defined as

$$\rho_f \left[u\frac{\partial H_e}{\partial x} + v\frac{\partial H_e}{\partial y} + w\frac{\partial H_e}{\partial z}\right] = k_f \left[\frac{\partial^2 T_f}{\partial x^2} + \frac{\partial^2 T_f}{\partial y^2} + \frac{\partial^2 T_f}{\partial z^2}\right]. \tag{8}$$

The enthalpy of the slurry (H_e) is shown by equation (9) and computed as follows:

$$\mathrm{He} = \mathrm{he} + \Delta H. \tag{9}$$

The sensible heat is calculated by equation (10), in which h_{ref} is the reference enthalpy at T_{ref} [21].

$$h_e = h_{\mathrm{ref}} + \int_{T_{\mathrm{ref}}}^{t} Cp_f \mathrm{d}T. \tag{10}$$

The slurry's latent heat (ΔH) is calculated by equation (11), where (β) is the mass ratio of molten to the total PCM in the slurry, (Φ) is the MEPCM mass fraction, and (L) is the fusion latent heat. The PCM begins to melt at T_{solidus} where the liquid fraction is zero and melting ends at $\mathrm{T_{lquidus}}$. At this point, the liquid fraction reaches one.

$$\Delta H = \beta \phi L, \tag{11}$$

where $\beta = 0$ if $T_f < T_{\mathrm{solidus}}$, and $\beta = 1$ if $T_f > T_{\mathrm{lquidus}}$.

$$\beta = \frac{T_f - T_{\mathrm{solidus}}}{T_{\mathrm{liquidus}} - T_{\mathrm{solidus}}}, \quad \text{if } T_{\mathrm{solidus}} < T_f < T_{\mathrm{liquidus}}. \tag{12}$$

3.3. Model Boundary Conditions. The working fluids enter the channels at a defined velocity and temperature. Pure water is the hot fluid used in hot channels while the cold fluid in the cold channels is tested (pure water, Nanofluid, MEPCM suspension, and hybrid suspension). The boundary conditions of the model are given in Tables 1–3.

In the present study, to solve the boundary conditions and also governing equations, the finite volume method (FVM) is employed. Computational fluid dynamics (CFD) is employed to solve the model and also determine the profile of the fluid flow, temperature, and pressure fields in the CFMCHE. Meanwhile, the dimensions of the square channel used in this model are $W = 100\,\mu$m, $H = 100\,\mu$m, $L = 10$ mm, and $t = 50\,\mu$m. W, H, L, and t are width, channel height, length, and wall thickness, respectively.

Performance parameters have been calculated as follows.

The ratio of the experimental heat transfer to the maximum heat that is possible to be transferred is defined as heat exchanger effectiveness (ε).

$$\varepsilon = \frac{c_h\left(T_{hi} - T_{ho}\right)}{c_{\min}\left(T_{hi} - T_{ci}\right)} - \frac{c_c\left(T_{co} - T_{ci}\right)}{c_{\min}\left(T_{hi} - T_{ci}\right)}, \tag{13}$$

where $C_c = mCp_{\mathrm{c}}$ and $\mathrm{C}_h = mCp_{\mathrm{h.}}$

In the heat exchange cell, the total pressure drop is

$$\Delta P_t = \Delta P_h + \Delta P_c = \left(P_{hi} - P_{ho}\right) - \left(P_{ci} - P_{co}\right). \tag{14}$$

In order to investigate the overall performance of the CFMCHE, both hydrodynamic and thermal performances must be taken into account. Thus, performance index is defined as the effectiveness of CFMCHE to the total pressure drop of heat exchanger [19]:

$$\eta = \frac{\varepsilon}{\Delta pt}. \tag{15}$$

The input power required for the pump to circulate fluids in the microchannel heat exchanger is

$$PP = V\Delta Pt. \tag{16}$$

Flow rate ($\mathrm{m^3/s}$) is defined as follows:

Table 1: Bottom channel (hot fluid) ($0 \le y \le Hh$).

Location	Boundary condition	Comments
At $x = 0$	$u_h = u_{hi},\ v_h = w_h = 0,\ T_h = T_{hi}$	Hot fluid inflow
At $x = L$	$(\partial u_h/\partial x) = v_h = w_h = 0,\ (\partial T_h/\partial x) = 0$	Hot fluid outflow (fully developed flow, end of the channel)
At $y = 0$	$u_h = v_h = w_h = 0,\ (\partial T_h/\partial y) = 0$	No-slip, adiabatic wall
At $y = H_h$	$u_h = v_h = w_h = 0,\ -k_h(\partial T_h/\partial y) = -k_s(\partial T_s/\partial y),\ T_h = T_s$	Fluid-solid interface (no-slip, conjugate heat transfer)
At $z = 0$	$u_h = v_h = w_h = 0,\ (\partial T_h/\partial z) = 0$	No-slip, adiabatic wall
At $z = W_{ch}$	$u_h = v_h = w_h = 0,\ (\partial T_h/\partial z) = 0$	No-slip, adiabatic wall

Table 2: Top channel (cold fluid) ($Hh + t \le y \le Hh + t + Hc$).

Location	Boundary condition	Comments
At $x = 0$	$(\partial u_c/\partial x) = v_c = w_c = 0,\ (\partial T_c/\partial x) = 0$	Cold fluid outflow (fully developed flow, end of the channel
At $x = L$	$u_c = u_{ci},\ v_c = w_c = 0,\ T_c = T_{ci}$	Cold fluid inflow
At $y = H_h + t$	$u_c = v_c = w_c = 0,\ -k_c(\partial T_c/\partial y) = -k_s(\partial T_s/\partial y), T_c = T_s$	Fluid-solid interface (no-slip, conjugate heat transfer)
At $y = H_h + t + H_c$	$u_c = v_c = w_c = 0,\ (\partial T_c/\partial y) = 0$	No-slip, adiabatic wall
At $z = 0$	$u_c = v_c = w_c = 0,\ (\partial T_c/\partial z) = 0$	No-slip, adiabatic wall
At $z = W_{ch}$	$u_c = v_c = w_c = 0,\ (\partial T_c/\partial z) = 0$	No-slip, adiabatic wall

Table 3: Solid wall separating two channels ($Hh \le y \le Hh + t$).

Location	Boundary condition	Comments
At $x = 0$	$(\partial T_s/\partial x) = 0$	Adiabatic wall
At $x = L$	$(\partial T_s/\partial x) = 0$	Adiabatic wall
At $y = H_h$	$-k_h(\partial T_h/\partial y) = -k_s(\partial T_s/\partial y), T_h = T_s$	Fluid-solid interface
At $y = H_h + t$	$-k_c(\partial T_c/\partial y) = -k_s(\partial T_s/\partial y), T_c = T_s$	Fluid-solid interface
At $z = 0$	$(\partial T_s/\partial z) = 0$	Adiabatic wall
At $z = W_{ch}$	$(\partial T_s/\partial z) = 0$	Adiabatic wall

$$V = v_{in}A. \tag{17}$$

There is another factor called performance factor defined as the heat transfer rate to the pumping power ratio and used to investigate the overall performance of the CFMCHE and also verify the obtained results of the performance index [19]:

$$\eta^* = \frac{q(W)}{P \cdot P(W)}. \tag{18}$$

4. Properties of Fluids

4.1. Properties of MEPCM Suspension. MEPCM particles are made of a polymer shell surrounding a core of PCM, preventing PCM from leakage, and keeping the form during phase change. Figure 3 represents a schematic of a microcapsule during the phase change process [13]. Herein, the average diameter of MEPCM particles is 5 μm. The selection of core and shell materials of the microcapsule corresponds to the transporter fluid. N-octadecane with a melting temperature of about 301 K is used as PCM in the core of the capsule, and the shell is made up of polymethylmethacrylate (PMMA) [22–24]. Given that the physical properties of the wall material and PCM affect the properties of the MEPCM particle, different components must be taken into account while calculating the properties of MPCM.

The densities of solid and liquid PCM were assumed to be the same as the density of n-octadecane. Moreover, energy and mass balances were utilized to calculate the density and specific heat of the microcapsules, respectively [25].

$$Cp_{\mathrm{PCM}} = \frac{(7Cp_c + 3Cp_{\mathrm{wall}})p_c p_{\mathrm{wall}}}{(3p_c + 7p_{\mathrm{wall}})\rho_{\mathrm{PCM}}}, \tag{19}$$

$$\rho_{\mathrm{PCM}} = \frac{10}{7}\left(\frac{d_c}{d_{\mathrm{PCM}}}\right)^3 p_c. \tag{20}$$

The thermal conductivity of microcapsules is also represented as follows:

$$\frac{1}{k_{\mathrm{PCM}}d_{\mathrm{PCM}}} = \frac{1}{k_c d_c} + \frac{d_{\mathrm{PCM}} - d_c}{k_{\mathrm{wall}}d_{\mathrm{PCM}}d_c}. \tag{21}$$

PCM stands for the whole (capsule = wall + core) and the wall is the wall of the capsule (polymer). C is the core material (PCM) and d is the diameter.

The suspension properties are a function of the properties of water (base fluid) and properties of the microcapsules. Hence, the specific heat and density are determined using a mass and energy balance [22–25].

$$\rho_f = c\rho_{\mathrm{PCM}} + (1 - c)\rho_w, \tag{22}$$

$$C\rho_f = \phi c\rho_{\mathrm{PCM}} + (1 - \phi)C\rho_w. \tag{23}$$

The viscosity of the suspension is also determined using

$$\mu_f = \mu_w\left(1 - c - 1.16c^2\right)^{-2.5}. \tag{24}$$

The thermal conductivity of the suspension is calculated as

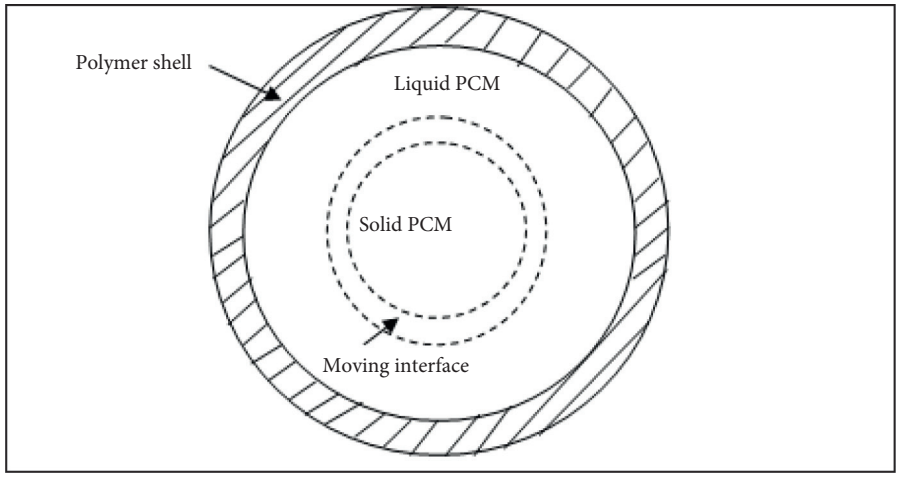

Figure 3: Schematic diagram of single MEPCM particles during melting.

$$k_f = \frac{2k_w + k_{\mathrm{PCM}} + 2c\left(k_{\mathrm{PCM}} - k_w\right)}{2 + \left(k_{\mathrm{PCM}}/k_w\right) - c\left(\left(k_{\mathrm{PCM}}/k_w\right) - 1\right)}. \tag{25}$$

The mass fraction can be calculated from

$$\phi = \frac{c\rho_{\mathrm{PCM}}}{\left(\rho_w + c\left(\rho_{\mathrm{PCM}} - \rho_w\right)\right)}. \tag{26}$$

4.2. Properties of Nanofluids. According to the previous studies [26, 27], the thermophysical properties of the nanofluids are a function of the properties of solid particles, the base fluid, particles shape, and volume fraction of the solid particles in the suspension. The properties of nanofluids are determined using the following relations:

Thermal conductivity:

$$k_{nf} = k_f\left(\frac{k_p + (SH-1)k_f - (SH-1)c\left(k_f - k_p\right)}{k_p + (SH-1)k_f + c\left(k_f - k_p\right)}\right). \tag{27}$$

Viscosity:

$$\mu_{nf} = \mu_f\left(1 + 2.5c\right). \tag{28}$$

Density:

$$\rho_{nf} = c\rho_p + (1-c)\rho_f. \tag{29}$$

Specific heat:

$$C\rho_{nf} = cC\rho_p + (1-c)C\rho_f. \tag{30}$$

In equation (27), SH indicates the solid particle shape factor.

$$\mathrm{SH} = \frac{3}{\psi}. \tag{31}$$

ψ represents the ratio of the surface area of a sphere (with the same volume of the particle) to the surface area of the particle. Thus, for the spherical particles, SH is 3.

k_p, k_f, and k_{nf} are thermal conductivities of the solid particles, base fluid, and nanofluid, respectively.

4.3. Properties of Hybrid Suspensions. To determine the viscosity and thermal conductivity properties of hybrid suspension, the following relations are used [28]:

Thermal conductivity:

$$k_{hs} = \frac{k_{nf}\left(1 - 3c\right)}{2}. \tag{32}$$

Viscosity:

$$\mu_{hs} = \mu_{nf}\left(1 + 7.85\phi\right). \tag{33}$$

To calculate the specific heat and density of the suspension, we use the following relations [14].

Specific heat:

$$Cp_{hs} = \left[\frac{c_{np}\rho_{np}cp_{np} + c_{\mathrm{MEPCM}}\rho_{\mathrm{MEPCM}}cp_{\mathrm{MEPCM}} + \left(1 - c_{np} - c_{\mathrm{MEPCM}}\right)c\rho_{bf}p_{bf}}{p_{hs}}\right]. \tag{34}$$

Density:

$$p_{hs} = c_{np}\rho_{np} + c_{\mathrm{MEPCM}}\rho_{\mathrm{MEPCM}} + \left(1 - c_{np} - c_{\mathrm{MEPCM}}\right)p_{bf}, \quad (35)$$

where *hs*, *np*, MEPCM, and *bf* refer to hybrid suspension, nanoparticle, microencapsulated phase change material, and base fluid, respectively. In Table 4, the rheological and thermal properties of the materials employed are listed.

5. Numerical Model

Governing equations were transformed into algebraic equations using the finite volume method. The SIMPLE algorithm was employed to handle the mass conservation equation and get the pressure field. Computational fluid dynamic software (FLUENT 19.1) was used to determine the fields of velocity, pressure, and temperature distribution along the CFMCHE. Afterward, all the computational domain (two channels and the separating wall) was meshed with suitable size, and then using a mesh refinement process, the generated mesh was refined.

6. Results and Discussion

In order to investigate the effectiveness of the nanofluids, the model was firstly operated with pure water. The inlet temperatures of cold and hot fluids flowing in the channels were set as the boundary conditions with values of $T_{ci} = 293$ K and $T_{hi} = 373$ K. Then, we repeated operating the model by using nanofluid and MEPCM suspensions with volume fractions of (2%, 4%, 6%, and 8%). Noting that a core material of PCM is n-octadecane which has $T_{\mathrm{solidus}} = 297$ K and $T_{\mathrm{liquidus}} = 302$ K; also, latent heat $\Delta H = 245{,}000$ (J/kg). And then, we repeated again operating the model by adding nanoparticles of (Cu and Al_2O_3) with volume fractions of (2% and 4%) to the MEPCM suspension to form the hybrid suspension.

To examine the validity of the present model, the model presented by Kashani et al. [9] was solved, and a comparison was made between the obtained results and those presented by them. The numerical model that used them is a microchannel heat exchanger composed of rectangular microchannels with hydraulic diameter $D_h = 100\,\mu$m, channel height $H = 100\,\mu$m, channel width $W = 100\,\mu$m, and length $L = 10$ mm. A silicon wall with a thickness of $50\,\mu$m separates the channels, and the inlet velocity of the fluid was chosen to be $Vi = 1$ m/s.

Figure 4 illustrates the heat transfer rate distribution in terms of volume concentration for two cases of the present study and the numerical model of [9]. According to the figure, it is evident that the two models are in good agreement with each other, and the average error is 1.16% which is attributed to the end effect. Thereupon, the present model has acceptable accuracy and could be used as a reliable model to examine the impact of different nanofluids, including MEPCM and hybrid suspension on the performance of CFMCHE.

Table 4: Properties of materials.

Material	p (kg/m^3)	Cp (J/kg.K)	K (W/m.K)	Mμ (kg/m.s)
Pure water	981.3	4189	0.643	0.00059
n-octadecane (MEPCM core)	solid = 850 liquid = 780	2000	0.18	—
PMMA (MEPCM wall)	1190	1470	0.21	—
MEPCM particles	867.2	1899	0.1643	—
Cupper (cu)	8930	383.1	386	—
Al_2O_3	3600	765	36	—

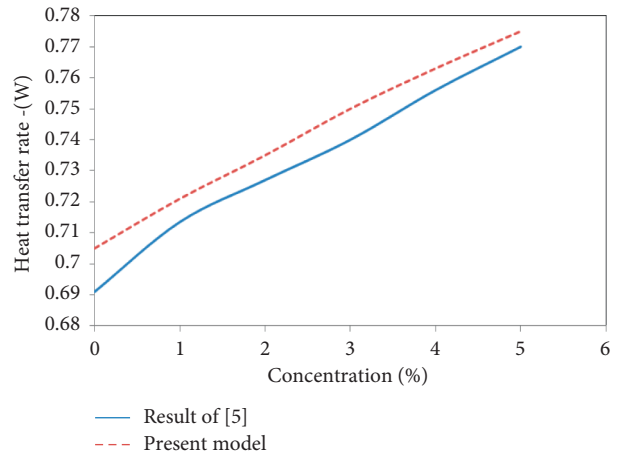

Figure 4: Variation of heat transfer rate distribution with concentration as a comparison between the present model and [5].

The heat transfer rate versus inlet velocity for pure MEPCM suspension at a concentration of 4% and enhanced (hybrid) suspension with the addition of 2% and 4% of Cu and Al_2O_3 nanoparticles is shown in Figure 5.

It is inferred that, for all cases, the heat transfer rate rises with increasing the velocity, which is because of the increase in flow rate. Also, results reveal that the heat transfer rises with adding nanoparticles, due to enhancing the thermal properties of suspension, especially thermal conductivity which increases with the increment of the amount of nanoparticles volume concentration. Furthermore, it could be noted that the enhancement in heat transfer is higher in case of adding Cu particles compared with Al_2O_3 particles because of the higher value of thermal conductivity of Cu compared with that of Al_2O_3.

The variation of pressure drop with inlet velocity for pure MEPCM suspension at a concentration of 4% and enhanced (hybrid) suspension with adding 2% and 4% of Cu and Al_2O_3 nanoparticles is portrayed in Figure 6.

From Figure 6, it is found that the pressure drop increases with the increment of inlet velocity for all cases, which is attributed to the increase in the frictional and dynamic losses. Also, it is shown that adding nanoparticles to the fluid leads to a higher pressure drop due to an increase in the dynamic

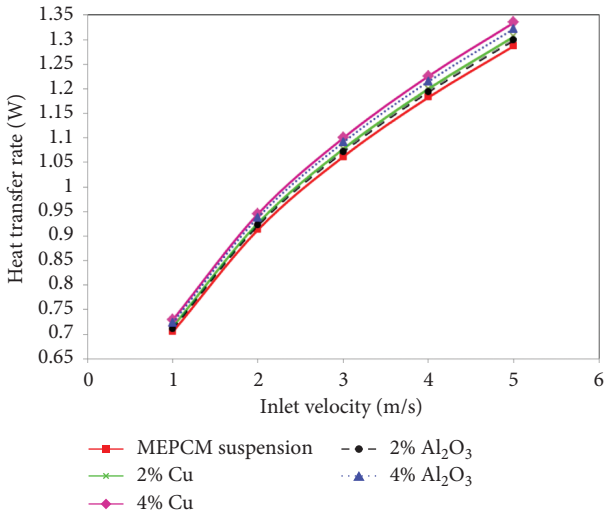

Figure 5: Variation of heat transfer rate with inlet velocity for different concentrations of nanoparticles at concentration 4% MEPCM suspension.

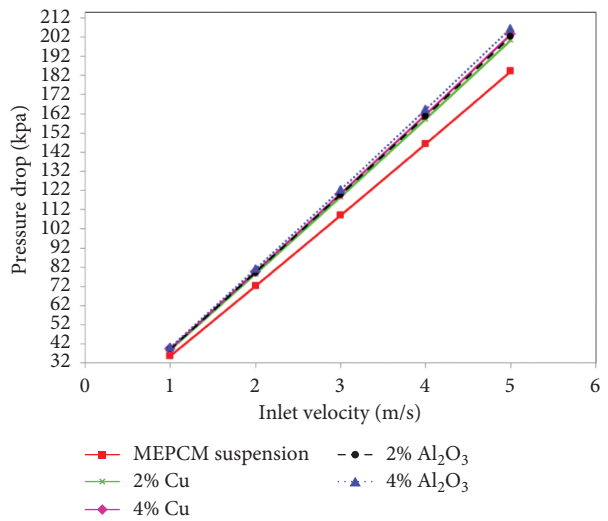

Figure 6: Variation of pressure drop with inlet velocity for different concentrations of nanoparticles at concentration 4% MEPCM suspension.

viscosity. This trend increased with the increment of concentration. A slight difference was discovered between pressure drop in case of adding Cu particles compared with Al_2O_3 particles resulting from the difference between the densities.

Figure 7 shows the effectiveness versus inlet velocity for pure MEPCM suspension (at a concentration of 4%) and enhanced (hybrid) suspension by adding 2% and 4% of Cu and Al_2O_3 nanoparticles, respectively.

As depicted in Figure 7, for all cases, as the inlet velocity increased, the effectiveness decreased. In fact, in high velocities, there is not enough time for all the particles to melt completely. As a result, the thermal energy was absorbed during melting, and also the effectiveness of MEPCM decreases. It is also evident that the effectiveness rises slightly with adding nanoparticles due to the enhancement of the thermal properties of suspension,

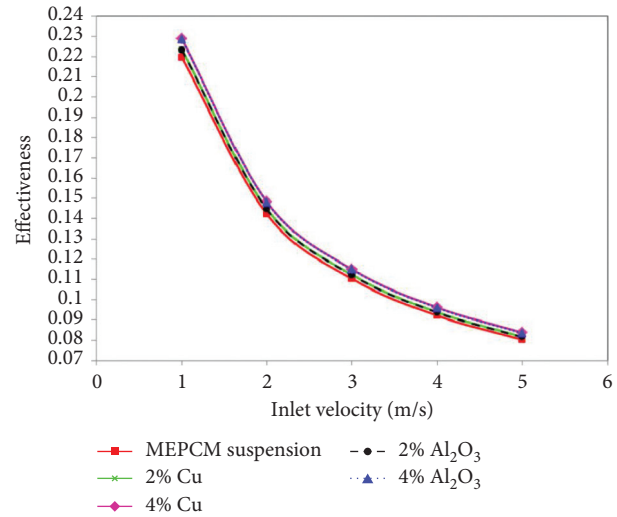

Figure 7: Variation of effectiveness with inlet velocity for different concentrations of nanoparticles at concentration 4% MEPCM suspension.

especially thermal conductivity. A point to be mentioned is that, in high flow rates, the impact of nanoparticles on the development of the boundary layer decreases, resulting in better heat transfer of the suspension in higher velocities. In fact, in high velocities, the volume flow rate is dominated, and the effect of nanoparticles is weakened.

Figure 8 represents the performance index in terms of inlet velocity for pure MEPCM suspension (at a concentration of 4%) and enhanced (hybrid) suspension by adding 2% and 4% of Cu and Al_2O_3 nanoparticles, respectively.

As shown in Figure 8, the performance index (η) for all cases decreases with an increment of inlet velocity. It is due to the higher increment of pressure drop than effectiveness. Also, the increase in pressure drop for hybrid suspensions is higher in comparison with that of MEPCM suspension resulting in a higher performance index of MEPCM suspension than that of hybrid suspensions.

Figure 9 indicates the variation of pumping power with inlet velocity for pure MEPCM suspension at a concentration of 4% and enhanced (hybrid) suspension by adding 2% and 4% of Cu and Al_2O_3 nanoparticles, respectively.

From Figure 9, it is found that as the inlet velocity increases, pressure drop increases and thus pumping power rises. Also, the pumping power increases with adding nanoparticles because of the increase in dynamic viscosity that results in an increment of pressure drop. Moreover, the more the number of nanoparticles, the more pumping power. Since there is no noticeable difference between the density values of Cu and Al_2O_3, a slight difference was seen between pumping power in case of adding Cu particles compared with Al_2O_3 particles.

The variation of performance factor in terms of inlet velocity for pure MEPCM suspension (at a concentration of 4%) and enhanced (hybrid) suspension with adding 2% and 4% of Cu and Al_2O_3 nanoparticles is depicted in Figure 10, respectively.

It is inferred that the performance factor (□) for all cases decreases with the increment of inlet velocity since the effect

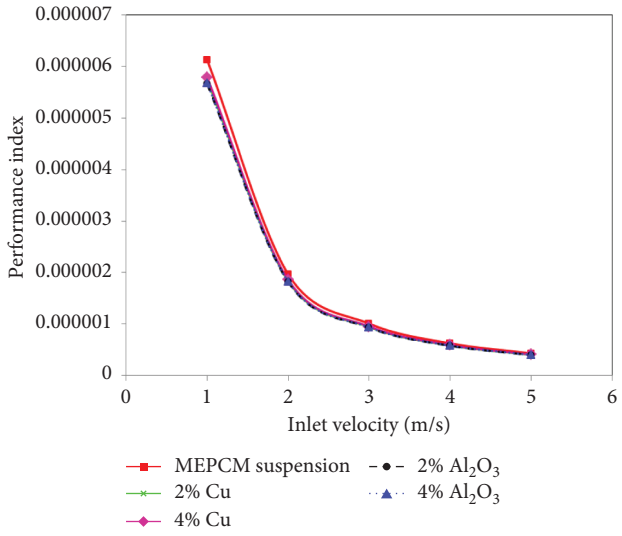

Figure 8: Variation of performance index with inlet velocity for different concentrations of nanoparticles at concentration 4% MEPCM suspension.

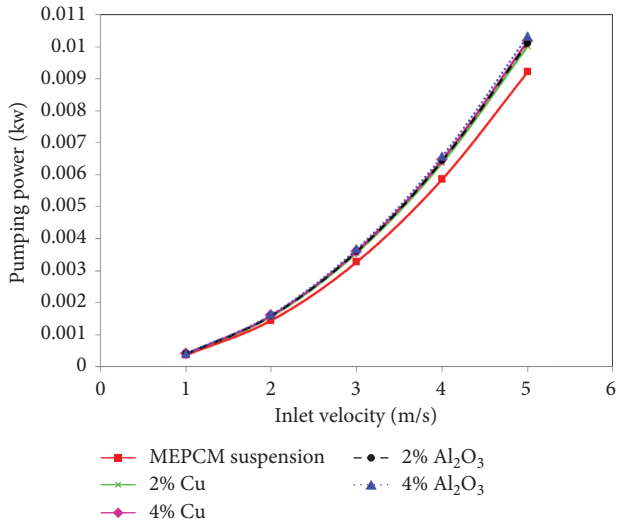

Figure 9: Variation of pumping power with inlet velocity for different concentrations of nanoparticles at concentration 4% MEPCM suspension.

of inlet velocity on the increment of pumping power is higher in comparison with that on heat transfer rate. Also, the performance factor of MEPCM suspension is higher than that of the hybrid suspensions. It is due to the higher increment of pumping power for hybrid suspensions than MEPCM suspensions.

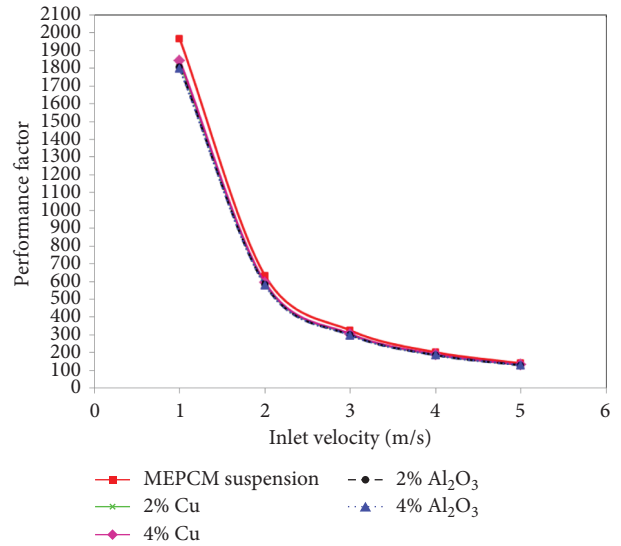

Figure 10: Variation of performance factor with inlet velocity for different concentrations of nanoparticles at concentration 4% MEPCM suspension.

7. Conclusions

The following conclusions are drawn:

(1) The MEPCM suspension can be enhanced by adding nanoparticles to obtain a hybrid suspension.

(2) Using higher thermal conductivity nanoparticles leads to obtaining extra enhancement in heat transfer rates for MEPCM suspension.

(3) Using hybrid suspension leads to the enhancement of heat transfer rates in CFMCHE.

(4) Also, the hybrid suspension causes an extra rise in pressure drop, which dominates the thermal performance.

(5) Using hybrid suspension with high velocities leads to an increase in heat transfer rates of the microchannel heat exchanger. On the other hand, it significantly raises the pressure drop and, hence, causes a decrease in the performance index.

Nomenclature

A: Cross-sectional area (m^2)
C: Volume fraction%
Cp: Specific heat capacity (J/kg·K)
Dh: Hydraulic diameter (m)
H: Channel height (m)

He: Enthalpy of suspension (W)
he: Sensible heat (W)
K: Thermal conductivity (W/m K)
L: Heat exchanger length (m)
M: Mass flow rate (kg/s)
P: Total pressure (Pa)
Q: Heat transfer rate (W)
t: Separating wall thickness (m)
T: Temperature (K)
u: Fluid x-component velocity (m/s)
v: Fluid y-component velocity (m/s)
w: Fluid z-component velocity (m/s)
x: Axial coordinate (m)
y: Vertical coordinate (m)
z: Horizontal coordinate (m)
Wch: Channel width (m)
ΔP: Pressure drop (Pa)
ΔH: Latent heat (W)

Greek letters

ρ: Density (kg/m^3)
Φ: Mass fraction
m: Flow rate
η: Performance index (1/Pa)
$ß$: Melted fraction
μ: Dynamic viscosity (m^2/s)

Subscripts

c: Cold
f: Suspension
h: Hot
i: Inlet
ch: Channel
Max: Maximum
o: Outlet
p: Particle
t: Total.

Data Availability

No data availability statement is assigned.

Conflicts of Interest

The authors declare that they have no conflicts of interest.

References

[1] I. Vigna, L. Bianco, F. Goia, and V. Serra, "Phase change materials in transparent building envelopes: a strengths, weakness, opportunities and threats (SWOT) analysis," *Energies*, vol. 11, no. 1, p. 111, 2018.

[2] W. Zhang, A. Maleki, A. K. Birjandi, M. Alhuyi Nazari, and O. Mohammadi, "Discrete optimization algorithm for optimal design of a solar/wind/battery hybrid energy conversion scheme," *International Journal of Low-Carbon Technologies*, vol. 60, 2020.

[3] O. A. Babar, V. K. Arora, and P. K. Nema, "Selection of phase change material for solar thermal storage application: a comparative study," *Journal of the Brazilian Society of Mechanical Sciences and Engineering*, vol. 41, no. 9, p. 355, 2019.

[4] V. Saikrishnan, A. Karthikeyan, N. Beemkumar, S. Ganesan, and D. Yuvarajan, "The thermal performance analyses of the solar energy-powered thermal energy storage system with $MgCl_2{\cdot}6H_2$ O as PCM," *Journal of the Brazilian Society of Mechanical Sciences and Engineering*, vol. 42, no. 1, p. 31, 2020.

[5] F. Moradi Gharghani, M. A. Bijarchi, O. Mohammadi, and M. B. Shafii, "An experimental investigation into a novel small-scale device for energy harvesting using vortex-induced vibration," *International Journal of Low-Carbon Technologies*, vol. 60, 2020.

[6] H. Jafari Mosleh, "A comprehensive comparative investigation on solar heating and cooling technologies from a thermo-economic viewpoint-a dynamic simulation," *Energy Science & Engineering*, vol. 9, no. 3, 2021.

[7] H. Hosseininaveh, O. Mohammadi, S. Faghiri, and M. B. Shafii, "A comprehensive study on the complete charging-discharging cycle of a phase change material using intermediate boiling fluid to control energy flow," *Journal of Energy Storage*, vol. 35, Article ID 102235, 2021.

[8] L. Selvam and D. Ramalingam, "Experimental study on the cascaded thermal energy storage system using MWCNT-enhanced phase change materials," *Journal of the Brazilian Society of Mechanical Sciences and Engineering*, vol. 41, no. 12, p. 572, 2019.

[9] S. Kashani, A. A. Ranjbar, M. Abdollahzadeh, and S. Sebti, "Solidification of nano-enhanced phase change material (NEPCM) in a wavy cavity," *Heat and Mass Transfer*, vol. 48, no. 7, pp. 1155–1166, 2012.

[10] H. Gujarathi, "Use of nanoparticle enhanced phase change material (nepcm) for data center cooling application," *Fluids*, vol. 6, no. 1, p. 31, 2017.

[11] R. Y. Farsani, A. Raisi, and A. Mahmoudi, "Successive melting and solidification of paraffin–alumina nanomaterial in a cavity as a latent heat thermal energy storage," *Journal of the Brazilian Society of Mechanical Sciences and Engineering*, vol. 41, no. 9, p. 368, 2019.

[12] M. I. Hasan, A. Rageb, and M. Yaghoubi, "Investigation of a counter flow microchannel heat exchanger performance with using nanofluid as a coolant," *Journal of Electronics Cooling and Thermal Control*, vol. 02, no. 03, pp. 35–43, 2012.

[13] M. I. Hasan, "Numerical investigation of counter flow microchannel heat exchanger with MEPCM suspension," *Applied Thermal Engineering*, vol. 31, no. 6-7, pp. 1068–1075, 2011.

[14] C. J. Ho, J. B. Huang, P. S. Tsai, and Y. M. Yang, "Preparation and properties of hybrid water-based suspension of Al_2O_3 nanoparticles and MEPCM particles as functional forced convection fluid," *International Communications in Heat and Mass Transfer*, vol. 37, no. 5, pp. 490–494, 2010.

[15] C. J. Ho, J. B. Huang, P. S. Tsai, and Y. M. Yang, "Water-based suspensions of Al_2O_3 nanoparticles and MEPCM particles on convection effectiveness in a circular tube," *International Journal of Thermal Sciences*, vol. 50, no. 5, pp. 736–748, 2011.

[16] C. Ho, J. Huang, P. Tsai, and Y. Yang, "On laminar convective cooling performance of hybrid water-based suspensions of Al_2O_3 nanoparticles and MEPCM particles in a circular tube," *International Journal of Heat and Mass Transfer*, vol. 54, no. 11-12, pp. 2397–2407, 2011.

[17] R. Elbahjaoui and H. El Qarnia, "Melting of nanoparticle-enhanced phase change material in a shell-and-tube latent heat storage unit heated by laminar pulsating fluid flow," *Computational Thermal Sciences: An International Journal*, vol. 9, no. 4, 2017.

[18] M. I. Hasan, M. Yaghoubi, and A. R. Abdul Muhsen, "Improving thermal performance of a counter flow microchannel heat exchanger by using nanofluid," in *Proceedings of the*

Fourth International Conference on Thermal Engineering: Theory and Applications, Abu Dhabi, UAE, January 2009.

[19] M. I. Hasan, A. A. Rageb, M. Yaghoubi, and H. Homayoni, "Influence of channel geometry on the performance of a counter flow microchannel heat exchanger," *International Journal of Thermal Sciences*, vol. 48, no. 8, pp. 1607–1618, 2009.

[20] M. I. Hasan and D. M. Muter, "Study the micro heat sink with pin fins and different coolants: a comparative study," *International Journal of Engineering & Technology*, vol. 7, no. 4, pp. 4856–4865, 2018.

[21] M. J. Moran, H. N. Shapiro, D. D. Boettner, and M. B. Bailey, *Fundamentals of Engineering Thermodynamics*, John Wiley & Sons, Hoboken, NJ, USA, 2010.

[22] Y. Rao, F. Dammel, P. Stephan, and G. Lin, "Convective heat transfer characteristics of microencapsulated phase change material suspensions in minichannels," *Heat and Mass Transfer*, vol. 44, no. 2, pp. 175–186, 2007.

[23] Y. Yamagishi, H. Takeuchi, A. T. Pyatenko, and N. Kayukawa, "Characteristics of microencapsulated PCM slurry as a heat-transfer fluid," *AichE Journal*, vol. 45, no. 4, pp. 696–707, 1999.

[24] Y. L. Hao and Y. X. Tao, "A numerical model for phase-change suspension flow in microchannels," *Numerical Heat Transfer, Part A: Applications*, vol. 46, no. 1, pp. 55–77, 2004.

[25] M. Goel, S. K. Roy, and S. Sengupta, "Laminar forced convection heat transfer in microcapsulated phase change material suspensions," *International Journal of Heat and Mass Transfer*, vol. 37, no. 4, pp. 593–604, 1994.

[26] T.-H. Tsai and R. Chein, "Performance analysis of nanofluid-cooled microchannel heat sinks," *International Journal of Heat and Fluid Flow*, vol. 28, no. 5, pp. 1013–1026, 2007.

[27] J. Lee and I. Mudawar, "Assessment of the effectiveness of nanofluids for single-phase and two-phase heat transfer in micro-channels," *International Journal of Heat and Mass Transfer*, vol. 50, no. 3-4, pp. 452–463, 2007.

[28] S. Manikandan and K. S. Rajan, "New hybrid nanofluid containing encapsulated paraffin wax and sand nanoparticles in propylene glycol-water mixture: potential heat transfer fluid for energy management," *Energy Conversion and Management*, vol. 137, pp. 74–85, 2017.

[29] H. M. Sadeghi, M. Babayan, and A. Chamkha, "Investigation of using multi-layer PCMs in the tubular heat exchanger with periodic heat transfer boundary condition," *International Journal of Heat and Mass Transfer*, vol. 147, p. 118970, 2020.

[30] A. S. Dogonchi, M. K. Nayak, N. Karimi, A. J. Chamkha, and D. D. Ganji, "Numerical simulation of hydrothermal features of Cu-H_2O nanofluid natural convection within a porous annulus considering diverse configurations of heater," *Journal of Thermal Analysis and Calorimetry*, vol. 141, no. 5, pp. 2109–2125, 2020.

[31] M. Ghalambaz, A. Doostani, E. Izadpanahi, and A. J. Chamkha, "Conjugate natural convection flow of Ag-MgO/water hybrid nanofluid in a square cavity," *Journal of Thermal Analysis and Calorimetry*, vol. 139, no. 3, pp. 2321–2336, 2020.

[32] M. S. Ishak, A. I. Alsabery, A. Chamkha, and I. Hashim, "Effect of finite wall thickness on entropy generation and natural convection in a nanofluid-filled partially heated square cavity," *International Journal of Numerical Methods for Heat and Fluid Flow*, vol. 30, no. 3, pp. 1518–1546, 2020.

[33] M. Rejvani, S. Saedodin, S. M. Vahedi, S. Wongwises, and A. J. Chamkha, "Experimental investigation of hybrid nano-lubricant for rheological and thermal engineering applications," *Journal of Thermal Analysis and Calorimetry*, vol. 138, no. 2, pp. 1823–1839, 2019.

[34] A. I. Alsabery, R. Mohebbi, A. J. Chamkha, and I. Hashim, "Impacts of magnetic field and non-homogeneous nanofluid model on convective heat transfer and entropy generation in a cavity with heated trapezoidal body," *Journal of Thermal Analysis and Calorimetry*, vol. 138, no. 2, pp. 1371–1394, 2019.

[35] S. A. M. Mehryan, M. Izadi, Z. Namazian, and A. J. Chamkha, "Natural convection of multi-walled carbon nanotube-Fe_3O_4/water magnetic hybrid nanofluid flowing in porous medium considering the impacts of magnetic field-dependent viscosity," *Journal of Thermal Analysis and Calorimetry*, vol. 138, no. 2, pp. 1541–1555, 2019.

[36] S. Hoseinzadeh, P. S. Heyns, A. J. Chamkha, and A. Shirkhani, "Thermal analysis of porous fins enclosure with the comparison of analytical and numerical methods," *Journal of Thermal Analysis and Calorimetry*, vol. 138, no. 1, pp. 727–735, 2019.

[37] Y. Taamneh, A. E. Kabeel, N. Prakash, R. Sathyamurthy, and A. J. Chamkha, "Thermal and hydraulic characteristics of a triangular duct using an Al_2O_3 nanofluid in a turbulent flow regime," *Heat Transfer-Asian Research*, vol. 48, no. 6, pp. 2639–2654, 2019.

[38] J. Raza, F. Mebarek-Oudina, and A. J. Chamkha, "Magnetohydrodynamic flow of molybdenum disulfide nanofluid in a channel with shape effects," *Multidiscipline Modeling in Materials and Structures*, vol. 15, no. 4, pp. 737–757, 2019.

[39] S. O. Giwa, M. Sharifpur, and J. P. Meyer, "Effects of uniform magnetic induction on heat transfer performance of aqueous hybrid ferrofluid in a rectangular cavity," *Applied Thermal Engineering*, vol. 170, p. 115004, 2020.

[40] S. O. Giwa, M. Sharifpur, and J. P. Meyer, "Experimental study of thermo-convection performance of hybrid nanofluids of Al_2O_3-MWCNT/water in a differentially heated square cavity," *International Journal of Heat and Mass Transfer*, vol. 148, p. 119072, 2020.

[41] S. Osman, M. Sharifpur, and J. P. Meyer, "Experimental investigation of convection heat transfer in the transition flow regime of aluminium oxide-water nanofluids in a rectangular channel," *International Journal of Heat and Mass Transfer*, vol. 133, pp. 895–902, 2019.

[42] M. Mahdavi, I. Garbadeen, M. Sharifpur, M. H. Ahmadi, and J. P. Meyer, "Study of particle migration and deposition in mixed convective pipe flow of nanofluids at different inclination angles," *Journal of Thermal Analysis and Calorimetry*, vol. 135, no. 2, pp. 1563–1575, 2019.

[43] M. Sharifpur, A. B. Solomon, T. L. Ottermann, and J. P. Meyer, "Optimum concentration of nanofluids for heat transfer enhancement under cavity flow natural convection with TiO_2-water," *International Communications in Heat and Mass Transfer*, vol. 98, pp. 297–303, 2018.

[44] M. Sharifpur, N. Tshimanga, J. P. Meyer, and O. Manca, "Experimental investigation and model development for thermal conductivity of α-Al_2O_3-glycerol nanofluids," *International Communications in Heat and Mass Transfer*, vol. 85, pp. 12–22, 2017.

Hindawi
Mathematical Problems in Engineering
Volume 2021, Article ID 5514535, 10 pages
https://doi.org/10.1155/2021/5514535

Research Article

On Conformable Laplace's Equation

Francisco Martínez,[1] Inmaculada Martínez,[1] Mohammed K. A. Kaabar,[2] and Silvestre Paredes[1]

[1]*Department of Applied Mathematics and Statistics, Technological University of Cartagena, Cartagena 30203, Spain*
[2]*Jabalia Camp, UNWRA Palestinian Refugee Camp, Gaza Strip Jabalya, State of Palestine*

Correspondence should be addressed to Mohammed K. A. Kaabar; mohammed.kaabar@wsu.edu

Received 30 January 2021; Revised 11 February 2021; Accepted 23 February 2021; Published 12 March 2021

Academic Editor: Mustafa Inc

The most important properties of the conformable derivative and integral have been recently introduced. In this paper, we propose and prove some new results on conformable Laplace's equation. We discuss the solution of this mathematical problem with Dirichlet-type and Neumann-type conditions. All our obtained results will be applied to some interesting examples.

1. Introduction

The idea of fractional derivative was first raised by L'Hospital in 1695. After introducing this idea, many new definitions have been formulated. The most well-known ones are Riemann–Liouville and Caputo fractional definitions. For more background information about these definitions, we refer the reader to [1, 2]. A new definition of derivative and integral has been recently formulated by Khalil et al. in [3]. This new definition is a type of local fractional derivative [4]. This definition was proposed to overcome some of difficulties associated with solving the equations formulated in the sense of classical nonlocal fractional definitions where the solutions can be difficult to obtain or even impossible to obtain. As a result, various research studies have been conducted on the mathematical analysis of functions of a real variable formulated in the sense of conformable definition such as Rolle's theorem, mean value theorem, chain rule, power series expansion, and integration by parts formulas [3, 5, 6]. In [7], the conformable partial derivative of the order $\alpha \in (0, 1]$ of the real-valued functions of several variables and the conformable gradient vector has been proposed, and conformable Clairaut's theorem for partial derivative has also been investigated. In [8], the Jacobian matrix has been defined in the context of conformable definition, and the chain rule for multivariable conformable derivative has been also proposed. In [9], conformable Euler's theorem on homogeneous has been successfully introduced.

Furthermore, many research studies have been conducted on the theoretical and practical elements of conformable differential equations shortly after the proposition of this new definition [4, 10–26]. Conformable derivative has also been applied in modeling and investigating phenomena in applied sciences and engineering such as the deterministic and stochastic forms of coupled nonlinear Schrödinger equations [27] and regularized long wave Burgers equation [28] and the analytical and numerical solutions for $(1 + 3)$-Zakharov–Kuznetsov equation with power-law nonlinearity [29].

Laplace's equation is used as indicator of the equilibrium in applications such as heat conduction and heat transfer [30]. Generally, to solve the Laplace equation, Legendre's differential equation, particularly the Legendre function or as commonly known as Legendre polynomials, is used to find a solution to the Laplace equation that indicates spherical symmetry in the physical systems [31]. Laplace equation can be widely seen in the field of heat transfer where the temperature is at different locations when the body's heat transfer is at the equilibrium point [30]. According to our knowledge, there are not many research studies that have been done on investigating Laplace's

equation in the sense of conformable derivative; therefore, all our results are considered new and worthy.

This paper is organized as follows. In the next section, the main concepts of conformable fractional calculus are presented. Next, we successively discuss the solution of conformable Laplace's partial differential equation with Dirichlet and Neumann conditions. Finally, the above results will be applied in some interesting examples to validate their applicability.

2. Basic Definitions and Tools

Definition 1. Given a function $f:[0,\infty)\longrightarrow R$. Then, the conformable derivative of order α [3] is defined by

$$\left(T_\alpha f\right)(t)=\lim_{\varepsilon\longrightarrow 0}\frac{f\left(t+\varepsilon t^{1-\alpha}\right)-f(t)}{\varepsilon}, \tag{1}$$

for all $t>0$, $0<\alpha\le 1$. If f is $\alpha-$ differentiable in some $(0, a)$, $a>0$, and $\lim_{t\longrightarrow 0h+}(T_a f)(t)$ exists, then it is defined as

$$\left(T_\alpha f\right)(0)=\lim_{t\longrightarrow 0}+\left(T_\alpha f\right)(t). \tag{2}$$

Theorem 1 (see [3]). *If a function $f:[0, \infty)\longrightarrow R$ is α-differentiable at $t0>0$, $0\alpha\le 1$, then f is continuous at t_0.*

Theorem 2 (see [3]). *Let $0\alpha\le 1$ and let f, g be $\alpha-$differentiable at a point $t>0$. Then, we have*

(i) $T_\alpha(af+bg)=a(T_\alpha f)+b(T_\alpha g),\quad \forall a,b\in R.$

(ii) $T_\alpha(t^p)=pt^{p-\alpha},\quad \forall p\in R.$

(iii) $T_\alpha(\lambda)=0$, *for all constant functions* $f(t)=\lambda$.

(iv) $T_\alpha(fg)=f(T_\alpha g)+g(T_\alpha f).$

(v) $T_\alpha(f/g)=g(T_\alpha f)-f(T_\alpha g)/g^2.$

(vi) If, in addition, f is differentiable, then $(T_\alpha f)(t)=t^{1-\alpha}(df/dt)(t).$

The conformable derivative of certain functions using the above definition is given as follows:

(i) $T_\alpha(1)=0.$

(ii) $T_\alpha(\sin(at))=at^{1-\alpha}\cos(at).$

(iii) $T_\alpha(\cos(at))=-at^{1-\alpha}\sin(at).$

(iv) $T_\alpha(e^{at})=ae^{at},\quad a\in R.$

Definition 2. The (left) conformable derivative starting from a of a given function $f:[a,\infty)\longrightarrow R$ of order $0<\alpha\le 1$ [5] is defined by

$$\left(T_\alpha^a f\right)(t)=\lim_{\epsilon\longrightarrow 0}\frac{f\left(t+\varepsilon(t-a)^{1-\alpha}\right)-f(t)}{\varepsilon}. \tag{3}$$

When $a=0$, it is expressed as $(T_\alpha f)(t)$. If f is $\alpha-$differentiable in some a, b, then the following can be defined:

$$\left(T_\alpha^a f\right)(a)=\lim_{t\longrightarrow a}+\left(T_\alpha^a f\right)(t). \tag{4}$$

Theorem 3 (chain rule) (see [5]). *Let $f, g:(a,\infty)\longrightarrow R$ be (left) α-differentiable functions, where $0<\alpha\le 1$. By letting $h(t)=f(g(t))$, $h(t)$ is α-differentiable for all $t\ne a$ and $g(t)\ne 0$; therefore, we have the following:*

$$\left(T_\alpha^a h\right)(t)=\left(T_\alpha^a f\right)(g(t))\cdot\left(T_\alpha^a g\right)(t)\cdot(g(t))^{\alpha-1}. \tag{5}$$

If $t=a$, then we obtain

$$\left(T_\alpha^a h\right)(a)=\lim_{t\longrightarrow a^+}\left(T_\alpha^a f\right)(g(t))\cdot\left(T_\alpha^a g\right)(t)\cdot(g(t))^{\alpha-1}. \tag{6}$$

Theorem 4 (see [5]). *Assume f is infinitely α-differentiable function, for some $0<\alpha\le 1$ at the neighborhood of a point t_0. Then, f has the following fractional power series expansion:*

$$f(t)=\sum_{k=0}^{\infty}\frac{\left({}^kT_\alpha^{t_0}\right)(t_0)}{a^k k!}(t-t_0)^{k\alpha},\quad t_0<t<t_0+\frac{1}{R^\alpha}, \tag{7}$$

Here, $({}^{(k)}T_\alpha^{t_0})(t_0)$ means the application of the conformable derivative k times.

The following definition is the conformable α-integral of a function f starting from $a\ge 0$.

Definition 3. $I_\alpha^a(f)(t)=\int_{k=0}^{t}(f(x)/x^{1-\alpha})\cdot dx$, where the integral is the usual Riemann improper integral, and $\alpha\in 0, 1$ [2].

According to the above definition, the following can be shown.

Theorem 5. $T_\alpha^a I_\alpha^a(f)(t)=f(t),\quad$ *for $t\ge a$, where f is any continuous function in the domain of $I\alpha$ [3].*

Lemma 6. *Let $f: (a, b)\longrightarrow R$ be differentiable, and $\alpha\in 0, 1$. Then, for all $a>0$, we have [5]*

$$I_\alpha^a T_\alpha^a(f)(t)=f(t)-f(a). \tag{8}$$

From [7, 8], the conformable partial derivative of a real-valued function with several variables is defined as follows.

Definition 4. Let f be a real-valued function with n variables and $a=(a_1,\ldots,a_n)\in R^n$ be a point whose ith component is positive. Then, the limit can be expressed as follows:

$$\lim_{\epsilon\longrightarrow 0}\frac{f\left(a_1,\ldots,a_i+\varepsilon a_i^{1-\alpha},\ldots a_n\right)-f(a_1,\ldots,a_n)}{\varepsilon}. \tag{9}$$

If the above limit exists, then we have the ith conformable partial derivative of f of the order $\alpha\in(0, 1]$ at a, denoted by $(\partial^\alpha/\partial x_i^\alpha)f(a)$.

Finally, some results on conformable Fourier series will be recalled [22] as follows.

Let $\alpha\in(0, 1$, and $\varphi:0,\infty)\longrightarrow R$ be defined by

$$\varphi(t)=\frac{t^\alpha}{\alpha}, \tag{10}$$

and $g:[0, \infty)\longrightarrow R$ be any function. Let f: $[0,\infty)\longrightarrow R$ be defined by $f(t)=g(\varphi(t))$.

Definition 5. A function ft is called α-periodical with period p if we have

$$f(t) = g(\varphi(t)) = g\left(\varphi(t) + \frac{p^{\alpha}}{\alpha}\right). \tag{11}$$

Definition 6. Two functions f, h are called α-orthogonal on $[0, b]$ if $\int_0^b (f(t)h(t)/t^{1-\alpha})\mathrm{d}t = 0$.

Definition 7. Let f: $[0, \infty) \longrightarrow$ R be a given piecewise continuous α-periodical with a period p. Then, we define the following:

(i) The cosine α-Fourier coefficients of f are expressed as $a_n = 2\alpha/\quad p^{\alpha}\int_0^p f(t)\cos(nt^{\alpha}/\alpha)(\mathrm{d}t/t^{1-\alpha}), \quad n = 1, 2, 3, \ldots$.

(ii) The sine α-Fourier coefficients of f are expressed as $b_n = 2\alpha/\quad p^{\alpha}\int_0^p f(t)\sin(n(t^{\alpha}/\alpha))\mathrm{d}t/t^{1-\alpha}, \quad n = 1, 2, 3, \ldots$.

Remark 1. The following can be proven easily:

(i) $\cos(n(t^{\alpha}/\alpha))$ and $\cos(m(t^{\alpha}/\alpha))$ are orthogonal on $[0, (\alpha 2\pi)^{(1/\alpha)}]$, for all $n \neq m$.

(ii) $\sin(n(t^{\alpha}/\alpha))$ and $\sin(m(t^{\alpha}/\alpha))$ are orthogonal on $[0, (\alpha 2\pi)^{(1/\alpha)}]$, for all $n \neq m$.

(iii) $\sin(n(t^{\alpha}/\alpha))$ and $\cos(m(t^{\alpha}/\alpha))$ are orthogonal on $[0, (\alpha 2\pi)^{(1/\alpha)}]$, for all n, m.

Definition 8. Let f: $[0, \infty) \longrightarrow$ R be a given piecewise continuous function which is α-periodical with period p. Then, the conformable α–Fourier series of f associated with the interval $[0, p]$ is expressed as

$$S(f)(t) = \frac{a_0}{2} + \sum_{n=1}^{\infty}\left(a_n \cos\left(n\frac{t^{\alpha}}{\alpha}\right) + b_n \sin\left(n\frac{t^{\alpha}}{\alpha}\right)\right), \tag{12}$$

where a_n and b_n, are as stated in Definition 7.

Theorem 6. *The conformable Fourier series of a piecewise continuous α-periodical function converges pointwise to the average limit of the function at each point of discontinuity and to the function at each point of continuity.*

3. Conformable Laplace's Partial Differential Equation

In this section, we solve the two-dimensional conformable Laplace's partial differential equation which is expressed in the following form:

$$\frac{\partial^{\alpha}}{\partial x^{\alpha}}\left(\frac{\partial^{\alpha}u(x,y)}{\partial x^{\alpha}}\right) + \frac{\partial^{\alpha}}{\partial y^{\alpha}}\left(\frac{\partial^{\alpha}u(x,y)}{\partial y^{\alpha}}\right) = 0. \tag{13}$$

As in the classical case, we propose this equation only with boundary conditions at the limit of the enclosure where the equation is fulfilled, which must have a certain regularity. These boundary conditions can be of two types:

(i) Dirichlet conditions: these are conditions in the function $u(x, y)$.

(ii) Neumann conditions: these are conditions imposed on the conformable partial derivatives of $u(x, y)$ of the order $\partial^{\alpha}u(x, y)/\partial x^{\alpha}$or $\partial^{\alpha}u(x, y)/\partial y^{\alpha}$.

The geometry of the region R where equation (13) is satisfied is very important, and we can only calculate solutions if they have certain regularity conditions.

3.1. Dirichlet Conditions. Let us discuss the solution of the following conformable Laplace's partial differential equation:

$$\begin{aligned}
&\frac{\partial^{\alpha}}{\partial x^{\alpha}}\left(\frac{\partial^{\alpha}u(x,y)}{\partial x^{\alpha}}\right) + \frac{\partial^{\alpha}}{\partial y^{\alpha}}\left(\frac{\partial^{\alpha}u(x,y)}{\partial y^{\alpha}}\right) = 0, \quad 0 \le x \le a, 0 \le y \le b,\\
&u(x,0) = u(x,b) = 0, \quad 0 \le x \le a,\\
&u(0,y) = 0, \quad 0 \le y \le b,\\
&u(a,y) = f(y), \quad 0 \le y \le b.
\end{aligned} \tag{14}$$

We will use the separation of variables technique [22].

So, let $u(x, y) = P(x)Q(y)$. By substituting it in equation (13), we obtain the following:

$$\frac{\mathrm{d}^{\alpha}}{\mathrm{d}x^{\alpha}}\left(\frac{\mathrm{d}^{\alpha}p(x)}{\mathrm{d}x^{\alpha}}\right)Q(y) + P(x)\frac{\mathrm{d}^{\alpha}}{\mathrm{d}y^{\alpha}}\left(\frac{\mathrm{d}^{\alpha}Q(y)}{\mathrm{d}y^{\alpha}}\right) = 0. \tag{15}$$

By ignoring the trivial solution $u \equiv 0$ and assuming that $P(x) \neq 0$ and $Q(x) \neq 0$, we have

$$\frac{1}{P(x)}\frac{\mathrm{d}^{\alpha}}{\mathrm{d}x^{\alpha}}\left(\frac{\mathrm{d}^{\alpha}P(x)}{\mathrm{d}x^{\alpha}}\right) = -\frac{1}{Q(y)}\frac{\mathrm{d}^{\alpha}}{\mathrm{d}y^{\alpha}}\left(\frac{\mathrm{d}^{\alpha}Q(y)}{\mathrm{d}y^{\alpha}}\right). \tag{16}$$

Hence, for some constant λ,

$$\frac{1}{P(x)}\frac{\mathrm{d}^{\alpha}}{\mathrm{d}x^{\alpha}}\left(\frac{\mathrm{d}^{\alpha}P(x)}{\mathrm{d}x^{\alpha}}\right) = -\frac{1}{Q(y)}\frac{\mathrm{d}^{\alpha}}{\mathrm{d}y^{\alpha}}\left(\frac{\mathrm{d}^{\alpha}Q(y)}{\mathrm{d}y^{\alpha}}\right) = \lambda. \tag{17}$$

Consequently, we have

$$\frac{\mathrm{d}^{\alpha}}{\mathrm{d}x^{\alpha}}\left(\frac{\mathrm{d}^{\alpha}P(x)}{\mathrm{d}x^{\alpha}}\right)-\lambda P(x)=0,$$
$$\frac{\mathrm{d}^{\alpha}}{\mathrm{d}y^{\alpha}}\left(\frac{d^{\alpha}Q(y)}{\mathrm{d}y^{\alpha}}\right)+\lambda Q(y)=0. \tag{18}$$

The boundary conditions can be written as follows:

$$u(x,0)=P(x)Q(0)=0,$$
$$u(x,b)=P(x)Q(b)=0. \tag{19}$$

Since x is arbitrary, it follows that

$$Q(0)=Q(b)=0. \tag{20}$$

Thus, we have the following contour problem:

$$\frac{\mathrm{d}^{\alpha}}{\mathrm{d}y^{\alpha}}\left(\frac{\mathrm{d}^{\alpha}Q(y)}{\mathrm{d}y^{\alpha}}\right)+\lambda Q(y)=0,$$
$$Q(0)=0,$$
$$Q(b)=0, \tag{21}$$

whose solution depends on the separation parameter, λ. Now, we have the following:

(1) $\lambda=0$. Then, equation (18) becomes $(\mathrm{d}^{\alpha}/\mathrm{d}y^{\alpha})(\mathrm{d}^{\alpha}Q(y)/\mathrm{d}y^{\alpha})=0$, whose general solution is obtained by integrating twice with respect to x.

$$Q(y)=A\frac{y^{\alpha}}{\alpha}+B. \tag{22}$$

By using the following boundary conditions, we have:

$$Q(0)=0\Longrightarrow B=0,$$
$$Q(b)=0\Longrightarrow Ab+B=0. \tag{23}$$

Since $b\neq 0\lambda=-\mu^2$, the solution of the previous system is $A=B=0$, and we obtain $Q(y)=0$. Hence, there is no nontrivial solution when $\lambda=0$.

(2) $\lambda<0$, say $\lambda=-\mu^2$. Then, equation (18) becomes $(\mathrm{d}^{\alpha}/\mathrm{d}y^{\alpha})(\mathrm{d}^{\alpha}Q(y)/\mathrm{d}y^{\alpha})-\mu^2Q(y)=0$, which has a general solution as follows:

$$Q(y)=Ae^{\mu(y^{\alpha}/\alpha)}+Be^{-\mu(y^{\alpha}/\alpha)}. \tag{24}$$

By using the following boundary conditions, we have:

$$Q(0)=0\Longrightarrow A+B=0,$$
$$Q(b)=0\Longrightarrow Ae^{\mu(b^{\alpha}/\alpha)}+Be^{-\mu(b^{\alpha}/\alpha)}=0. \tag{25}$$

The previous equations form a homogeneous linear system in the unknowns A and B. The determinant of the matrix of the coefficients is expressed as

$$\begin{vmatrix}1 & 1\\ e^{\mu(b^{\alpha}/\alpha)} & e^{-\mu(b^{\alpha}/\alpha)}\end{vmatrix}=e^{\mu(b^{\alpha}/\alpha)}-e^{-\mu(b^{\alpha}/\alpha)}=2\sinh\left(\mu\left(\frac{b^{\alpha}}{\alpha}\right)\right), \tag{26}$$

and since $\mu\neq 0$, the only solution of the system is the trivial $A=B=0$, and we obtain $Q(y)=0$. Hence, there is no nontrivial solution when $\lambda<0$.

(3) $\lambda>0$, say $\lambda=\mu^2$ Then, equation (18) becomes $(\mathrm{d}^{\alpha}/\mathrm{d}y^{\alpha})(\mathrm{d}^{\alpha}Q(y)/\mathrm{d}y^{\alpha})+\mu^2Q(y)=0$, which has a general solution as follows:

$$Q(y)=A\cos\left(\mu\frac{y^{\alpha}}{\alpha}\right)+B\sin\left(\mu\frac{y^{\alpha}}{\alpha}\right). \tag{27}$$

By using the following boundary conditions, we have:

$$Q(0)=0\Longrightarrow A=0,$$
$$Q(b)=0\Longrightarrow A\cos\left(\mu\frac{b^{\alpha}}{\alpha}\right)+B\sin\left(\mu\frac{b^{\alpha}}{\alpha}\right)=0, \tag{28}$$

where

$$B\sin\left(\mu\frac{b^{\alpha}}{\alpha}\right)=0. \tag{29}$$

Since we do not want the trivial solution, $B=0$ and

$$\sin\left(\mu\frac{b^{\alpha}}{\alpha}\right)=0\Longleftrightarrow\left(\mu\frac{b^{\alpha}}{\alpha}\right)=n\pi,\quad n\in N, \tag{30}$$

and then we obtain

$$\mu=n\pi\frac{\alpha}{b^{\alpha}}, \tag{31}$$

and the value of $\lambda=\mu^2$ is written as

$$\lambda=n^2\pi^2\frac{\alpha^2}{b^{2\alpha}},\quad n\in N. \tag{32}$$

Since λ was an arbitrary constant, then for each $n\in\mathrm{N}$, we would have a possible solution of the conformable ordinary differential equation as follows:

$$\lambda_n=n^2\pi^2\frac{\alpha^2}{b^{2\alpha}}\Longrightarrow Q_n(y)=B_n\sin\left(n\pi\left(\frac{y}{b}\right)^{\alpha}\right). \tag{33}$$

Substituting these values for λ_n in the other conformal differential equation, we have

$$\frac{\mathrm{d}^{\alpha}}{\mathrm{d}x^{\alpha}}\left(\frac{\mathrm{d}^{\alpha}P(x)}{\mathrm{d}x^{\alpha}}\right)-n^2\pi^2\frac{\alpha^2}{b^{2\alpha}}p(x)=0, \tag{34}$$

whose solution for each $n\in\mathrm{N}$ is of the following form:

$$P_n(x)=C_ne^{n\pi(x/b)^{\alpha}}+D_ne^{-n\pi(x/b)^{\alpha}},\quad C_n,D_n\in R. \tag{35}$$

By using the initial condition $u\,(0,\,y)=0$, we have

$$u(0,y)=P(0)Q(y)=0, \tag{36}$$

which by arbitrary y leads to $P\,(0)=0$, and therefore, we obtain

$$P_n(0)=C_n+D_n=0\Longrightarrow D_n=-C_n, \tag{37}$$

and the function $P_n\,(x)$ is given by

$$P_n(x)=C_n\left(e^{n\pi(x/b)^\alpha}-e^{-n\pi(x/b)^\alpha}\right)=2C_n\sinh\left(n\pi\left(\frac{x}{b}\right)^\alpha\right). \tag{38}$$

The solution of the partial derivative equation will be, for each n, of the following form:

$$\begin{aligned}u_n(x,y)&=P_n(x)Q_n(y)\\&=2C_n\sinh\left(n\pi\left(\frac{x}{b}\right)^\alpha\right)B_n\sin\left(n\pi\left(\frac{y}{b}\right)^\alpha\right)\\&=c_n\sinh\left(n\pi\left(\frac{x}{b}\right)^\alpha\right)\sin\left(n\pi\left(\frac{y}{b}\right)^\alpha\right),\end{aligned} \tag{39}$$

with $c_n=2C_nB_n$.

Since the equation is linear, any linear combination of solutions is another solution; therefore, we can consider it as a formal general solution:

$$u(x,y)=\sum_{n=1}^{\infty}C_n\sinh\left(n\pi\left(\frac{x}{b}\right)^\alpha\right)\sin\left(n\pi\left(\frac{y}{b}\right)^\alpha\right), \tag{40}$$

and using the last boundary condition $u(a,y)=f(y)$, we have

$$\begin{aligned}u(a,y)&=\sum_{n=1}^{\infty}c_n\sinh\left(n\pi\left(\frac{a}{b}\right)^\alpha\right)\sin\left(n\pi\left(\frac{y}{b}\right)^\alpha\right)\\&=\sum_{n=1}^{\infty}d_n\sin\left(n\pi\left(\frac{y}{b}\right)^\alpha\right)=f(y).\end{aligned} \tag{41}$$

Finally, we can calculate the value of the coefficients d_n, if we observe the expression as the conformable $\alpha-$ Fourier series of the odd extension of $f\,(y)$; therefore, we obtain

$$d_n=c_n\sinh\left(n\pi\left(\frac{a}{b}\right)^\alpha\right)=\frac{2\alpha}{b^\alpha}\int_0^b f(y)\sin\left(n\pi\left(\frac{y}{b}\right)^\alpha\right)\frac{dy}{y^{1-\alpha}}, \tag{42}$$

where

$$d_n=\frac{2\alpha}{b^\alpha\sinh\left(n\pi(a/b)^\alpha\right)}\int_0^b f(y)\sin\left(n\pi\left(\frac{y}{b}\right)^\alpha\right)\frac{dy}{y^{1-\alpha}}. \tag{43}$$

3.2. Neumann Conditions. Let us discuss the solution of the following problem with Neumann-type conditions:

$$\frac{\partial^\alpha}{\partial x^\alpha}\left(\frac{\partial^\alpha u(x,y)}{\partial x^\alpha}\right)+\frac{\partial^\alpha}{\partial y^\alpha}\left(\frac{\partial^\alpha u(x,y)}{\partial y^\alpha}\right)=0,\quad 0\le x\le a,0\le y\le b, \tag{44}$$

$$\begin{aligned}\left(\frac{\partial^\alpha u(x,0)}{\partial y^\alpha}\right)&=0,\quad 0\le x\le a,\\\left(\frac{\partial^\alpha u(x,b)}{\partial y^\alpha}\right)&=0,\quad 0\le x\le a,\\\left(\frac{\partial^\alpha u(0,y)}{\partial x^\alpha}\right)&=f(y),\quad 0\le y\le b,\\\left(\frac{\partial^\alpha u(a,y)}{\partial x^\alpha}\right)&=0,\quad 0\le y\le b.\end{aligned} \tag{45}$$

We can see in this case that the boundary conditions involve the conformable partial derivatives of u.

All conditions are boundary. As we did previously, we use the method of separation of variables [22]:

$$u(x,y)=P(x)Q(y), \tag{46}$$

which will lead us to the following two conformable ordinary differential equations:

$$\frac{d^\alpha}{dx^\alpha}\left(\frac{d^\alpha P(x)}{dx^\alpha}\right)-\lambda P(x)=0, \tag{47}$$

$$\frac{d^\alpha}{dy^\alpha}\left(\frac{d^\alpha Q(y)}{dy^\alpha}\right)+\lambda Q(y)=0. \tag{48}$$

The differences with the Dirichlet-type conditions appear when establishing the boundary conditions of these problems. Observe that in this case, $(\partial^\alpha u(x,0)/\partial y^\alpha)=0$ and $(\partial^\alpha u(x,b)/\partial y^\alpha)=0$; therefore, the boundary conditions for the conformable differential equations are obtained as follows:

$$\frac{\partial^\alpha u(x,y)}{\partial y^\alpha}=P(x)\frac{d^\alpha}{dy^\alpha}\left(\frac{d^\alpha Q(y)}{dy^\alpha}\right)\Longrightarrow\begin{cases}\dfrac{\partial^\alpha u(x,0)}{\partial y^\alpha}=P(x)\dfrac{d^\alpha}{dy^\alpha}\left(\dfrac{d^\alpha Q(0)}{dy^\alpha}\right)\Longrightarrow\dfrac{d^\alpha}{dy^\alpha}\left(\dfrac{d^\alpha Q(0)}{dy^\alpha}\right)=0,\\[2ex]\dfrac{\partial^\alpha u(x,b)}{\partial y^\alpha}=P(x)\dfrac{d^\alpha}{dy^\alpha}\left(\dfrac{d^\alpha Q(b)}{dy^\alpha}\right)\Longrightarrow\dfrac{d^\alpha}{dy^\alpha}\left(\dfrac{d^\alpha Q(b)}{dy^\alpha}\right)=0.\end{cases} \tag{49}$$

We verify the following:

$$\frac{\partial^{\alpha}u(a,y)}{\partial x^{\alpha}}=\frac{\mathrm{d}^{\alpha}}{\mathrm{d}x^{\alpha}}\left(\frac{\mathrm{d}^{\alpha}P(a)}{\mathrm{d}x^{\alpha}}\right)Q(y)=0\Longrightarrow\frac{\mathrm{d}^{\alpha}}{\mathrm{d}x^{\alpha}}\left(\frac{\mathrm{d}^{\alpha}P(a)}{\mathrm{d}x^{\alpha}}\right)=0. \tag{50}$$

Using equation (48) and the conditions found for $(\mathrm{d}^{\alpha}/\mathrm{d}y^{\alpha})(\mathrm{d}^{\alpha}Q(y)/\mathrm{d}y^{\alpha})$, we have the following boundary problem:

$$\begin{aligned}\frac{\mathrm{d}^{\alpha}}{\mathrm{d}y^{\alpha}}\left(\frac{\mathrm{d}^{\alpha}Q(y)}{\mathrm{d}y^{\alpha}}\right)+\lambda Q(y)&=0,\\ \left(\frac{\mathrm{d}^{\alpha}Q(0)}{\mathrm{d}y^{\alpha}}\right)&=0,\\ \left(\frac{\mathrm{d}^{\alpha}Q(b)}{\mathrm{d}y^{\alpha}}\right)&=0.\end{aligned} \tag{51}$$

We distinguish according to the value of λ. Now, we obtain the following:

(1) $\lambda=0$. Then, equation (48) becomes $(d^{\alpha}/dy^{\alpha})(d^{\alpha}Q(y)/dy^{\alpha})=0$, whose general solution is obtained by integrating twice with respect to y:

$$Q(y)=A\frac{y^{\alpha}}{\alpha}+B, \tag{52}$$

with $A, B\in R$ arbitrary constants. By using the following boundary conditions, we have:

$$\left.\begin{aligned}\left(\frac{\mathrm{d}^{\alpha}Q(0)}{\mathrm{d}y^{\alpha}}\right)&=0,\\ \left(\frac{\mathrm{d}^{\alpha}Q(b)}{\mathrm{d}y^{\alpha}}\right)&=0,\end{aligned}\right\}\Leftrightarrow A=0. \tag{53}$$

Therefore, $Q(y)=B$, and then $u(x,y)=P(x)B$. Using equation (44), we obtain

$$\left.\begin{aligned}&\frac{\partial^{\alpha}u(x,y)}{\partial x^{\alpha}}=\left(\frac{\mathrm{d}^{\alpha}P(x)}{\mathrm{d}x^{\alpha}}\right)B\Longrightarrow\frac{\partial^{\alpha}}{\partial x^{\alpha}}\left(\frac{\partial^{\alpha}u(x,y)}{\partial x^{\alpha}}\right)=\frac{\mathrm{d}^{\alpha}}{\mathrm{d}x^{\alpha}}\left(\frac{\mathrm{d}^{\alpha}P(x)}{\mathrm{d}x^{\alpha}}\right)B\left(\frac{\partial^{\alpha}u(x,y)}{\partial y^{\alpha}}\right)=0\Longrightarrow\frac{\partial^{\alpha}}{\partial y^{\alpha}}\left(\frac{\partial^{\alpha}u(x,y)}{\partial y^{\alpha}}\right)=0\\ &\frac{\partial^{\alpha}}{\partial x^{\alpha}}\left(\frac{\partial^{\alpha}u(x,y)}{\partial x^{\alpha}}\right)+\frac{\partial^{\alpha}}{\partial y^{\alpha}}\left(\frac{\partial^{\alpha}u(x,y)}{\partial y^{\alpha}}\right)=\frac{\mathrm{d}^{\alpha}}{\mathrm{d}x^{\alpha}}\left(\frac{\mathrm{d}^{\alpha}P(x)}{\mathrm{d}x^{\alpha}}\right)B+0=0,\end{aligned}\right\} \tag{54}$$

where either $B=0$, but then we should have the null solution, or $(\mathrm{d}^{\alpha}/\mathrm{d}x^{\alpha})(\mathrm{d}^{\alpha}P(x)/\mathrm{d}x^{\alpha})=0$, and therefore, we have

$$P(x)=Cx+D. \tag{55}$$

We have as a possible solution:

$$u(x,y)=P(x)Q(y)=ACx+A\ D=\rho x+\sigma, \tag{56}$$

with $\rho=\mathrm{AC}$ and $\sigma=\mathrm{AD}$. If we now use the boundary condition $(\partial^{\alpha}u(a,y)/\partial x^{\alpha})=0$, we have

$$\frac{\partial^{\alpha}u(x,y)}{\partial x^{\alpha}}=\rho\Longrightarrow\frac{\partial^{\alpha}u(a,y)}{\partial x^{\alpha}}=0\Longrightarrow\rho=0. \tag{57}$$

In this case, equation (44) has the following solution:

$$u(x,y)=\sigma. \tag{58}$$

(2) $\lambda<0$, say $\lambda=-\mu^{2}$. Then, the equations are written as follows:

$$\begin{aligned}\frac{\mathrm{d}^{\alpha}}{\mathrm{d}y^{\alpha}}\left(\frac{\mathrm{d}^{\alpha}Q(y)}{dy^{\alpha}}\right)-\mu^{2}Q(y)&=0,\\ \left(\frac{\mathrm{d}^{\alpha}Q(0)}{\mathrm{d}y^{\alpha}}\right)&=0,\\ \left(\frac{\mathrm{d}^{\alpha}Q(b)}{\mathrm{d}y^{\alpha}}\right)&=0,\end{aligned} \tag{59}$$

which has the following general solution:

$$Q(y)=Ae^{\mu\left(y^{\alpha}/\alpha\right)}+Be^{-\mu\left(y^{\alpha}/\alpha\right)}, \tag{60}$$

By using the following boundary conditions, we obtain:

$$\frac{\mathrm{d}^{\alpha}Q(y)}{\mathrm{d}y^{\alpha}}=A\mu e^{\mu\left(y^{\alpha}/\alpha\right)}-B\mu e^{-\mu\left(y^{\alpha}/\alpha\right)}. \tag{61}$$

So,

$$\left.\begin{aligned}\frac{\mathrm{d}^{\alpha}Q(0)}{\mathrm{d}y^{\alpha}} &= A\mu - B\mu = 0 \Longrightarrow \mu(A-B) = 0 \Longrightarrow A - B = 0\\ \frac{\mathrm{d}^{\alpha}Q(b)}{\mathrm{d}y^{\alpha}} &= A\mu e^{\mu(b^{\alpha}/\alpha)} - B\mu e^{-\mu(b^{\alpha}/\alpha)} = 0 \Longrightarrow \mu\left(Ae^{\mu(b^{\alpha}/\alpha)} - Be^{-\mu(b^{\alpha}/\alpha)}\right) = 0 \Longrightarrow Ae^{\mu(b^{\alpha}/\alpha)} - Be^{-\mu(b^{\alpha}/\alpha)} = 0\end{aligned}\right\}. \tag{62}$$

From the first equation above, $A = B$, and by substituting it in the second equation, we have

$$Ae^{\mu(b^{\alpha}/\alpha)} - Be^{-\mu(b^{\alpha}/\alpha)} = 0 \Longrightarrow A\left(e^{-\mu(b^{\alpha}/\alpha)} - e^{-\mu(b^{\alpha}/\alpha)}\right) = 0. \tag{63}$$

In this case, we will have two options:

$$\begin{aligned}A = 0 &\Longrightarrow \text{trivial solution},\\ e^{\mu(b^{\alpha}/\alpha)} - e^{-\mu(b^{\alpha}/\alpha)} = 0 &\Longrightarrow e^{\mu(b^{\alpha}/\alpha)} = e^{-\mu(b^{\alpha}/\alpha)} \Longrightarrow b = 0 \Longrightarrow \text{trivial solution}.\end{aligned} \tag{64}$$

(3) $\lambda > 0$, say $\lambda = \mu^2$.

Then, the equations are expressed as follows:

$$\begin{aligned}\frac{\mathrm{d}^{\alpha}}{\mathrm{d}y^{\alpha}}\left(\frac{\mathrm{d}^{\alpha}Q(y)}{\mathrm{d}y^{\alpha}}\right) - \mu^2 Q(y) &= 0,\\ \left(\frac{\mathrm{d}^{\alpha}Q(0)}{\mathrm{d}y^{\alpha}}\right) &= 0,\\ \left(\frac{\mathrm{d}^{\alpha}Q(b)}{\mathrm{d}y^{\alpha}}\right) &= 0,\end{aligned} \tag{65}$$

which has the following general solution:

$$Q(y) = A\cos\left(\mu\frac{y^{\alpha}}{\alpha}\right) + B\sin\left(\mu\frac{y^{\alpha}}{\alpha}\right). \tag{66}$$

We need the following equation:

$$\frac{\mathrm{d}^{\alpha}Q(y)}{\mathrm{d}y^{\alpha}} = -\mu A\sin\left(\mu\frac{y^{\alpha}}{\alpha}\right) + B\mu\cos\left(\mu\frac{y^{\alpha}}{\alpha}\right), \tag{67}$$

to be able to use the boundary conditions as follows:

$$\left.\begin{aligned}\frac{\mathrm{d}^{\alpha}Q(y)}{\mathrm{d}y^{\alpha}} &= \mu B = 0\\ \frac{\mathrm{d}^{\alpha}Q(b)}{\mathrm{d}y^{\alpha}} &= -\mu A\ \sin\left(\mu\frac{b^{\alpha}}{\alpha}\right) + B\mu\cos\left(\mu\frac{b^{\alpha}}{\alpha}\right)\end{aligned}\right\} \Longrightarrow \left.\begin{aligned}B &= 0\\ -\mu A\sin\left(\mu\frac{b^{\alpha}}{\alpha}\right) &= 0\end{aligned}\right\} \Longrightarrow \mu\frac{b^{\alpha}}{\alpha} = n\pi, \tag{68}$$

and therefore, we have

$$\mu = n\pi\frac{\alpha}{b^{\alpha}}, \quad n \in N, \tag{69}$$

and for each value of n, we will have the following function:

$$Q_n(y) = A_n\cos\left(n\pi\left(\frac{y}{b}\right)^{\alpha}\right). \tag{70}$$

With these values and equation (47), we obtain

$$\frac{\mathrm{d}^{\alpha}}{\mathrm{d}x^{\alpha}}\left(\frac{\mathrm{d}^{\alpha}P(x)}{\mathrm{d}x^{\alpha}}\right) - \mu^2 P(x) = 0 \Longrightarrow \frac{\mathrm{d}^{\alpha}}{\mathrm{d}x^{\alpha}}\left(\frac{\mathrm{d}^{\alpha}P(x)}{\mathrm{d}x^{\alpha}}\right) - n^2\pi^2\frac{\alpha}{b^{2\alpha}}P(x) = 0, \tag{71}$$

which has as a general solution as follows:

$$P(x) = Ce^{\mu(x^{\alpha}/\alpha)} + De^{-\mu(x^{\alpha}/\alpha)}. \tag{72}$$

As we have seen before: $(d^{\alpha}P(a)/dx^{\alpha}) = 0$.

$$\frac{d^{\alpha}P(x)}{dx^{\alpha}} = C\mu e^{\mu(x^{\alpha}/\alpha)} - D\mu\ e^{-\mu(x^{\alpha}/\alpha)} \Longrightarrow \frac{d^{\alpha}P(a)}{dx^{\alpha}} = C\mu e^{\mu(a^{\alpha}/\alpha)} - D\mu\ e^{-\mu(a^{\alpha}/\alpha)} = 0 \Longrightarrow Ce^{\mu(a^{\alpha}/\alpha)} = De^{-\mu(a^{\alpha}/\alpha)}. \tag{73}$$

Then for each n, we have

$$P_n(x) = C_n\left(e^{n\pi(x/b)^{\alpha}} + e^{-n\pi(x/b)^{\alpha}}e^{2n\pi(a/b)^{\alpha}}\right). \tag{74}$$

The formal solution is the linear combination of all solutions that we have obtained in the case $\lambda = 0$.

$$\begin{aligned} u(x,y) &= \sigma + \sum_{n=1}^{\infty} A_n \cos\left(n\pi\left(\frac{y}{b}\right)^{\alpha}\right) C_n\left(e^{n\pi(x/b)^{\alpha}} + e^{-n\pi(x/b)^{\alpha}}\right), \\ &= \sigma + \sum_{n=1}^{\infty} C_n \cos\left(n\pi\left(\frac{y}{b}\right)^{\alpha}\right)\left(e^{n\pi(x/b)^{\alpha}} + e^{-n\pi(x/b)^{\alpha}}e^{2n\pi(a/b)^{\alpha}}\right), \end{aligned} \tag{75}$$

where $c_n = A_nC_n$ has been taken.

The values of c_n are obtained using the boundary condition: $(\partial^{\alpha}u(0,y)/\partial x^{\alpha}) = f(y)$

$$\begin{aligned} \frac{\partial^{\alpha}u(x,y)}{\partial x^{\alpha}} &= \sum_{n=1}^{\infty} c_n n\pi \frac{\alpha}{b^{\alpha}} \cos\left(n\pi\left(\frac{y}{b}\right)^{\alpha}\right)\left(e^{n\pi(x/b)^{\alpha}} - e^{-n\pi(x/b)^{\alpha}}e^{2n\pi(a/b)^{\alpha}}\right), \\ \frac{\partial^{\alpha}u(0,y)}{\partial x^{\alpha}} &= \sum_{n=1}^{\infty} C_n n\pi \frac{\alpha}{b^{\alpha}}\left(1 - e^{2n\pi(a/b)^{\alpha}}\right)\cos\left(n\pi\left(\frac{y}{b}\right)^{\alpha}\right) \\ &= \sum_{n=1}^{\infty} d_n \cos\left(n\pi\left(\frac{y}{b}\right)^{\alpha}\right) = f(y), \\ d_n &= C_n n\pi \frac{\alpha}{b^{\alpha}}\left(1 - e^{2n\pi(a/b)^{\alpha}}\right), \end{aligned} \tag{76}$$

All values of c_n are obtained from the boundary condition: ..., which are known as the coefficients of the conformable α-Fourier series of the even extension of the even extension of $f(y)$; therefore, we obtain

$$d_n = C_n n\pi \frac{\alpha}{b^{\alpha}}\left(1 - e^{2n\pi(a/b)^{\alpha}}\right) = \frac{2\alpha}{b^{\alpha}} \int_0^a f(y)\cos\left(n\pi\left(\frac{y}{b}\right)^{\alpha}\right)\frac{dy}{y^{1-\alpha}}, \tag{77}$$

where

$$c_n = \frac{2}{n\pi\left(1 - e^{2n\pi(a/b)^{\alpha}}\right)} \int_0^a f(y)\cos\left(n\pi\left(\frac{y}{b}\right)^{\alpha}\right)\frac{dy}{y^{1-\alpha}}. \tag{78}$$

Note that in this case, it must be satisfied that the independent term of the conformable α–Fourier series $d_0/2$ must be 0; therefore, for the solution of the problem with the Neumann conditions to be $u(x, y)$, the following compatibility condition must be verified as follows:

$$d_0 = \frac{2\alpha}{b^{\alpha}} \int_0^a f(y)\frac{dy}{y^{1-\alpha}} = 0 \Longrightarrow \int_0^a f(y)\frac{dy}{y^{1-\alpha}} = 0. \tag{79}$$

4. Examples

In this section, we will use the above results to solve some conformable Laplace partial differential equations.

Example 1. Let us solve the solution of the following problem with Dirichlet-type conditions:

$$\begin{aligned} \frac{\partial^{\alpha}}{\partial x^{\alpha}}\left(\frac{\partial^{\alpha}u(x,y)}{\partial x^{\alpha}}\right) + \frac{\partial^{\alpha}}{\partial y^{\alpha}}\left(\frac{\partial^{\alpha}u(x,y)}{\partial y^{\alpha}}\right) &= 0, \quad 0 \le x \le 1, 0 \le y \le 1, \\ u(x,0) = u(x,1) &= 0, \quad 0 \le x \le 1, \\ u(0,y) &= 0 \quad 0 \le y \le 1, \\ u(1,y) &= 100, \quad 0 \le y \le 1, \end{aligned} \tag{80}$$

where $\alpha \in (0, 1]$.

Solution. Using equations (40) and (43), we get

$$u(x, y) = \sum_{n=1}^{\infty} c_n \sinh\left(n\pi\left(\frac{x}{b}\right)^{\alpha}\right) \sin\left(n\pi\left(\frac{y}{b}\right)^{\alpha}\right), \tag{81}$$

where

$$c_n = \frac{200\alpha}{\sinh(n\pi)} \int_0^1 \sin\left(n\pi y^{\alpha}\right) \frac{dy}{y^{1-\alpha}} = \frac{200\left(1-(-1)^n\right)}{n\pi \sinh(n\pi)}, n \in N. \tag{82}$$

Example 2. Let us solve the solution of the following problem with Neumann-type conditions:

$$\begin{aligned} \frac{\partial^{\alpha}}{\partial x^{\alpha}}\left(\frac{\partial^{\alpha} u(x, y)}{\partial x^{\alpha}}\right) + \frac{\partial^{\alpha}}{\partial y^{\alpha}}\left(\frac{\partial^{\alpha} u(x, y)}{\partial y^{\alpha}}\right) &= 0, \quad 0 \le x \le a, 0 \le y \le b, \\ \left(\frac{\partial^{\alpha} u(x, 0)}{\partial y^{\alpha}}\right) &= 0, \quad 0 \le x \le a, \\ \left(\frac{\partial^{\alpha} u(x, b)}{\partial y^{\alpha}}\right) &= 0 \quad 0 \le x \le a, \\ \left(\frac{\partial^{\alpha} u(0, y)}{\partial x^{\alpha}}\right) &= \frac{b^{\alpha}}{2} - y^{\alpha}, \quad 0 \le y \le b, \\ \left(\frac{\partial^{\alpha} u(a, y)}{\partial x^{\alpha}}\right) &= 0, 0 \le y \le b, \end{aligned} \tag{83}$$

where $\alpha \in (0, 1]$.

Solution. First, note that the function $f(y) = (b^{\alpha}/2) - y^{\alpha}$ satisfies the compatibility condition given by equation (30).

$$\int_0^b \left(\frac{b^{\alpha}}{2} - y^{\alpha}\right) \frac{dy}{y^{1-\alpha}} = 0. \tag{84}$$

The formal solution of this problem is given by

$$u(x, y) = \sigma + \sum_{n=1}^{\infty} c_n \cos\left(n\pi\left(\frac{y}{b}\right)^{\alpha}\right)\left(e^{n\pi(x/b)^{\alpha}} + e^{-n\pi(x/b)^{\alpha}} e^{2n\pi(a/b)^{\alpha}}\right), \tag{85}$$

where

$$c_n = \frac{2}{n\pi\left(1 - e^{2n\pi(a/b)^{\alpha}}\right)} \int_0^b \left(\frac{b^{\alpha}}{2} - y^{\alpha}\right) \cos\left(n\pi\left(\frac{y}{b}\right)^{\alpha}\right) \frac{dy}{y^{1-\alpha}} = \frac{2b^{2\alpha}\left((-1)^n - 1\right)}{\alpha n^3 \pi^3 \left(1 - e^{2n\pi(a/b)^{\alpha}}\right)}. \tag{86}$$

5. Conclusion

In this research paper, we have proposed some results referring to the conformable Laplace's partial differential equation. The definitions of conformable derivative and integral have been applied to construct some of the results and relationships in our study. The solution of conformable Laplace's partial differential equation with Dirichlet-type and Neumann-type conditions has been successfully established. The findings of this research study indicate that the results obtained in the sense of conformable derivative coincide with the results obtained in classical integer-order case. Finally, some interesting examples are presented to show the validity and potentiality of our obtained results to be applied in future research works in various applications in the field of natural sciences or engineering.

Data Availability

No data were used to support this study.

Conflicts of Interest

The authors declare that they have no conflicts of interest.

References

[1] A. Kilbas, H. Srivastava, and J. Trujillo, *Theory and Applications of Fractional Differential Equations*, North-Holland, New York, NY, USA, 2006.

[2] K. S. Miller, *An Introduction to Fractional Calculus and Fractional Differential Equations*, J. Wiley and Sons, New York, NY, USA, 1993.

[3] R. Khalil, M. Al Horani, A. Yousef, and M. Sababheh, "A new definition of fractional derivative," *Journal of Computational and Applied Mathematics*, vol. 264, pp. 65–70, 2014.

[4] M. Kaabar, "Novel methods for solving the conformable wave equation," *Journal of New Theory*, vol. 31, pp. 56–85, 2020.

[5] T. Abdeljawad, "On conformable fractional calculus," *Journal of Computational and Applied Mathematics*, vol. 279, pp. 57–66, 2015.

[6] O. S. Iyiola and E. R. Nwaeze, "Some new results on the new conformable fractional calculus with application using D'Alambert approach," *Progress in Fractional Differentiation and Applications*, vol. 2, no. 2, pp. 1–7, 2016.

[7] A. Atangana, D. Baleanu, and A. Alsaedi, "New properties of conformable derivative," *Open Math*, vol. 13, pp. 57–63, 2015.

[8] N. Yazici and U. Gözütok, "Multivariable conformable fractional calculus," *Filomat*, vol. 32, no. 1, pp. 45–53, 2018.

[9] F. Martínez, I. Martínez, and S. Paredes, "Conformable Euler's Theorem on homogeneous functions," *Computational and Mathematical Methods*, vol. 1, no. 5, pp. 1–11, 2018.

[10] E. Ünal, A. an, and E. Çelik, "Solutions of sequential conformable fractional differential equations around an ordinary point and conformable fractional hermite differential equation," *British Journal of Applied Science & Technology*, vol. 10, no. 2, pp. 1–11, 2015.

[11] M. Al Masalmeh, "Series method to solve conformable fractional ric-cati differential equations," *International Journal of Applied Mathematical Research*, vol. 6, no. 1, pp. 30–33, 2017.

[12] M. Al Horani and R. Khalil, "Total fractional differential with applications to exact fractional differential equations," *International Journal of Computer Mathematics*, vol. 95, no. 6-7, pp. 1444–1452, 2018.

[13] M. Al Horani, M. Abu Hammad, and R. Khalil, "Variation of parameters for local fractional nonhomogenous linear-differential equations," *Journal of Mathematics and Computer Science*, vol. 16, no. 02, pp. 147–153, 2016.

[14] R. Khalil, M. Al Horani, and D. Anderson, "Undetermined coefficients for local fractional differential equations," *Journal of Mathematics and Computer Science*, vol. 16, no. 02, pp. 140–146, 2016.

[15] M. A. Hammad and R. Khalil, "Abel's formula and wronskian for conformable fractional differential equations," *International Journal of Differential Equations and Applications*, vol. 13, no. 2, pp. 177–183, 2014.

[16] M. A. Hammad and R. Khalil, "Legendre fractional differential equation and Legendre fractional polynomials," *International Journal of Applied Mathematical Research*, vol. 3, no. 3, pp. 214–219, 2014.

[17] F. S. Silva, M. D. Moreira, and M. A. Moret, "Conformable Laplace transform of fractional differential equations," *Axioms*, vol. 7, no. 55, 2018.

[18] Z. Al-Zhour, N. Al-Mutairi, F. Alrawajeh, and R. Alkhasawneh, "Series solutions for the Laguerre and Lane-Emden fractional differential equations in the sense of conformable fractional derivative," *Alexandria Engineering Journal*, vol. 58, no. 4, 2019.

[19] M. A. Hammad, H. Alzaareer, H. Al-Zoubi, and H. Dutta, "Fractional Gauss hypergeometric differential equation," *Journal of Interdisciplinary Mathematics*, vol. 22, no. 7, pp. 1113–1121, 2019.

[20] F. Martínez, I. Martínez, and S. Paredes, "A note on integrating factors of a conformable fractional differential equation," *International Journal of Applied Physics and Mathematics*, vol. 10, no. 4, pp. 143–152, 2020.

[21] F. Martínez, I. Martínez, M. K. A. Kaabar, and S. Paredes, "Some new results on conformable fractional power series," *Asia Pacific Journal of Mathematics*, vol. 7, no. 3, pp. 1–14, 2020.

[22] I. Abu Hammad and R. Khalil, "fractional fourier series with applications," *American Journal of Computational and Applied Mathematics*, vol. 4, no. 6, pp. 187–191, 2014.

[23] I. Abu Hammad and R. Khalil, "Some new results on conformable fractional differential equations," *International Journal of Pure and Applied Mathematics*, vol. 94, no. 2, pp. 215–314, 2020.

[24] R. Khalil and H. Abu-Shaab, "Solution of some conformable fractional power series," *Asia Pacific Journal of Mathematics*, vol. 103, no. 4, pp. 667–673, 2015.

[25] F. Martínez, I. Martínez, I. Martínez, M. K. A. Kaabar, and S. Paredes, "New results on complex conformable integral," *AIMS Mathematics*, vol. 5, no. 6, pp. 7695–7710, 2020.

[26] F. Martínez, I. Martínez, M. K. A. Kaabar, R. Ortíz-Munuera, and S. Paredes, "Note on the conformable fractional derivatives and integrals of complex-valued functions of a real variable," *IAENG International Journal of Applied Mathematics*, vol. 50, pp. 509–615, 2020.

[27] Z. Korpinar, A. S. Alshomrani, M. Inc, and D. Baleanu, "The deterministic and stochastic solutions of the Schrodinger equation with time conformable derivative in birefrigent fibers," *AIMS Mathematics*, vol. 5, no. 3, pp. 2326–2345, 2020.

[28] Z. Korpinar, A. S. Alshomrani, and D. Baleanu, "On exact special solutions for the stochastic regularized long wave-Burgers equation," *Advances in Difference Equations*, vol. 2020, no. 1, pp. 1–12, 2020.

[29] M. M. A. Khater, Y.-M. Chu, R. A. M. Attia, M. Inc, and D. Lu, "On the analytical and numerical solutions in the quantum magnetoplasmas: the atangana conformable derivative (1+3)-ZK equation with power-law nonlinearity," *Advances in Mathematical Physics*, vol. 2020, pp. 1–10, 2020.

[30] E. Amoupour, E. A. Toroqi, and H. S. Najafi, "Numerical experiments of the Legendre polynomial by generalized differential transform method for solving the Laplace equation," *Communications of the Korean Mathematical Society*, vol. 33, no. 2, pp. 639–650, 2018.

[31] Y. Song and H. Kim, "Legendre's equation expressed by the initial value by using integral transforms," *Applied Mathematical Sciences*, vol. 8, no. 11, pp. 531–540, 2014.

Hindawi
Mathematical Problems in Engineering
Volume 2021, Article ID 5516392, 10 pages
https://doi.org/10.1155/2021/5516392

Research Article

An Analytical View of Fractional-Order Fisher's Type Equations within Caputo Operator

Nehad Ali Shah [1,2]

[1]*Informetrics Research Group, Ton Duc Thang University, Ho Chi Minh City, Vietnam*
[2]*Faculty of Mathematics & Statistics, Ton Duc Thang University, Ho Chi Minh City, Vietnam*

Correspondence should be addressed to Nehad Ali Shah; nehadali199@yahoo.com

Received 30 January 2021; Revised 5 February 2021; Accepted 25 February 2021; Published 8 March 2021

Academic Editor: Mustafa Inc

The present research article is related to the analytical investigation of some nonlinear fractional-order Fisher's equations. The homotopy perturbation technique and Shehu transformation are implemented to discuss the fractional view analysis of Fisher's equations. For a better understanding of the proposed procedure, some examples related to Fisher's equations are presented. The identical behavior of the derived and actual solutions is observed. The solutions at different fractional are calculated, which describe some useful dynamics of the given problems. The proposed technique can be modified to study the fractional view analysis of other problems in various areas of applied sciences.

1. Introduction

In mathematical science, the construction of exact and explicit solutions to nonlinear fractional-order partial differential equations (PDEs) is very significant and is one of the most exciting and especially active fields of study. It is well recognized that it is possible to divide all nonlinear PDEs into two parts: the nonintegrable ones and the integrable partial differential equations. There is an infinite number of exact solutions to the first form, i.e., the integrable equations. The most well-known problems among them are the sine-Gordon equation, Korteweg-de Vries equation, Boussinesq equations, Kawahara type equations, and nonlinear Schrodinger equation and the list can be expanded with other fundamental integrable problems, but it is not our purpose to give all the lists [1–5]. Nonlinear PDEs are considered to be in the class of nonintegrable partial differential equations with certain precise solutions or without precise solutions and will need special care to achieve their solutions because of the shape of the nonlinear differential equation and the pole of its solution. The Fitzhugh-Nagumo equation, Fisher equation, Burger-Huxley equation, and Ginzburg-Landau equation can be mentioned as the well-known nonintegrable PDEs among them all [6–13].

Over the last few decades, considerable progress has been made in developing methods for obtaining precise solutions to nonlinear equations, but the progress accomplished is insufficient. Since, from our point of view, there is no single optimal way to achieve correct solutions to nonlinear differential equations of all forms. Based on the researchers' expertise and the sympathy for the method used, each method has its benefits and shortcomings. Also, all these techniques can be seen to be problem-dependent, namely, that certain techniques perform well on some concerns, but others do not. Therefore, it is very important to apply certain well-known methods to nonlinear partial differential equations in the literature that are not solved with that method to look for potential new exact solutions or to check current solutions with different approaches [14–17].

Fisher-Kolmogorov-Petrovsky-Piscounov (Fisher-KPP) equation was first introduced by Fisher [18] and was later renamed Fisher equation. FEs have numerous applications in the fields of engineering and science [19–22]. The researchers investigated some important generalizations of this equation [23–25]. Numerous reaction-diffusion equations have wavefronts that show a vital part in explaining chemical, physical, and biological phenomena [26, 27]. The reaction-diffusion systems can explain how changes in the

concentration of one or more chemicals occur. One is the local chemical reactions that transform the substances into each other and the other is the diffusion, which allows the substances to spread through the air.

The simplest equation for reaction-diffusion in one spatial dimension,

$$\psi_{\mathfrak{J}} = P\psi_{\mu\mu} + Q(\psi), \tag{1}$$

where $\psi(\mu, \mathfrak{J})$ shows single material concentration, P represents diffusion coefficients, and Q represents all local reactions. If $R(\psi) = \psi(1-\psi)$, we get FE which is used to define the biological populations dispersion. The Fisher-KPP advection equation is used to define population dynamics in advective environments [28]. The partial differential equation proposed by Fisher is nonlinear as

$$\psi_{\mathfrak{J}} = D\psi_{\mu\mu} + \psi(1-\psi). \tag{2}$$

Fisher proposed equation (2) as a model for gene selection, with ψ denoting the population density. The same equation also arises in the autocatalytic chemical reactions, nuclear reactor theory, flame propagation, neurophysiology, and Brownian motion process. The Fisher equation is considered to be an important equation because of its vast number of applications in the field of engineering.

The homotopy perturbation technique was developed by He [29, 30] in 1998. HPM provides the solution as a sum of the sequence having an infinite sum that converges rapidly to the exact results. HPM can be used to solve PDEs of higher dimensions and nonlinearity effectively.

In the present research article, effective utilization of the new developed technique, the homotopy perturbation method and Shehu transform, has been implemented to solve fractional FEs. The suggested technique is very effective for the solutions of other fractional PDEs because its required small computational work and higher degree accuracy. Moreover, the obtained results are in close resemblance with the actual solution of all fractional FEs.

2. Preliminaries

2.1. Definition. The fractional-order Riemann–Liouville integral is define by [31, 32]

$$I_0^{\delta} h(\tau) = \frac{1}{\Gamma(\alpha)} \int_0^{\eta} (\eta - s)^{\alpha-1} h(s)\mathrm{d}s. \tag{3}$$

2.2. Definition. The fractional-order Caputo's derivative of $h(\eta)$ is given as [31, 32]

$$D_{\eta}^{\alpha} h(\eta) = I^{n-\alpha} f^n, \quad n-1 < \alpha < n, n \in \mathbb{N},$$
$$\frac{d^n}{d\eta^n} h(\eta), \quad \alpha = n, n \in \mathbb{N}. \tag{4}$$

2.3. Definition. The integral of Shehu transformation is new and similar to other integral transformation which is described for exponential order functions. In set A, we take a function which is described by [33–35]

$$A = \left\{ \nu(\eta): \exists, \rho_1, \rho_2 > 0, |\nu(\eta)| < Me^{(|\eta|/\rho_i)}, \quad \text{if } \eta \in [0, \infty). \right. \tag{5}$$

The Shehu transformation which is defined by $S(\cdot)$ for a function $\nu(\eta)$ is given as

$$S\{\nu(\eta)\} = V(s,\mu) = \int_0^{\infty} e^{(-s\eta/\mu)} \nu(\eta)\mathrm{d}\eta, \quad \eta > 0, s > 0. \tag{6}$$

The Shehu transformation of a function $\nu(\eta)$ is $V(s,\mu)$, and then $\nu(\eta)$ is known as the inverse of $V(s,\mu)$ which is define as

$$S^{-1}\{V(s,\mu)\} = \nu(\eta), \quad \text{for } \eta \geq 0, S^{-1} \text{ is inverse Shehu transformation.} \tag{7}$$

2.4. Definition. The Shehu transformation for nth derivatives is defined as [33–35]

$$S\left\{\nu^{(n)}(\eta)\right\} = \frac{s^n}{u^n} V(s,u) - \sum_{k=0}^{n-1} \left(\frac{s}{u}\right)^{n-k-1} \nu^{(k)}(0). \tag{8}$$

2.5. Definition. The fractional-order derivatives of Shehu transformation are given as [33–35]

$$S\left\{\nu^{(\alpha)}(\eta)\right\} = \frac{s^{\alpha}}{u^{\alpha}} V(s,u) - \sum_{k=0}^{n-1} \left(\frac{s}{u}\right)^{\alpha-k-1} \nu^{(k)}(0), \quad 0 < \beta \leq n. \tag{9}$$

2.6. Definition. The Mittag-Leffler function of $E_{\alpha}(z)$ for $\alpha > 0$ is given as

$$E_{\alpha}(z) = \sum_{m=0}^{\infty} \frac{z^m}{\Gamma(\alpha m + 1)}, \quad \alpha > 0, z \in \mathbb{C}. \tag{10}$$

3. Homotopy Perturbation Transform Method

To explain the fundamental ideas of this method, we get the following equation:

$$D_{\mathfrak{J}}^{\alpha} \psi(\mu, \mathfrak{J}) + M\psi(\mu, \mathfrak{J}) + N\psi(\mu, \mathfrak{J}) = h(\mu, \mathfrak{J}), \quad \mathfrak{J} > 0, 0 < \alpha \leq 1,$$
$$\psi(\mu, 0) = g(\mu), \quad \mu \in \Re, \tag{11}$$

where $D_{\mathfrak{J}}^{\alpha} = (\partial^{\alpha}/\partial\mathfrak{J}^{\alpha})$ is Caputo's derivative, M, N is the linear and nonlinear operator in μ, and $h(\mu, \mathfrak{J})$ is the source function.

By taking Shehu transformation, we can write (11) as

$$S\left[D^{\alpha}_{\mathfrak{T}}\psi(\mu,\mathfrak{T})+M\psi(\mu,\mathfrak{T})+N\psi(\mu,\mathfrak{T})\right]=S[h(\mu,\mathfrak{T})],$$

$$R(\mu,s,u)=\frac{g(\mu)}{s}+\frac{u^{\alpha}}{s^{\alpha}}S[h(\mu,\mathfrak{T})]-\frac{u^{\alpha}}{s^{\alpha}}S[M\psi(\mu,\mathfrak{T})+N\psi(\mu,\mathfrak{T})]. \tag{12}$$

Now, using inverse Shehu transformation, we get

$$\psi(\mu,\mathfrak{T})=F(\mu,\mathfrak{T})-S^{-1}\left[\frac{u^{\alpha}}{s^{\alpha}}S\{M\psi(\mu,\mathfrak{T})+N\psi(\mu,\mathfrak{T})\}\right], \tag{13}$$

where

$$\begin{aligned}F(\mu,\mathfrak{T})&=S^{-1}\left[\frac{g(\mu)}{s}+\frac{u^{\alpha}}{s^{\alpha}}S[h(\mu,\mathfrak{T})]\right]\\&=g(\mu)+S^{-1}\left[\frac{u^{\alpha}}{s^{\alpha}}S[h(\mu,\mathfrak{T})]\right].\end{aligned} \tag{14}$$

Now, if ρ is the parameter perturbation, we can write as

$$\psi(\mu,\mathfrak{T})=\sum_{k=0}^{\infty}\rho^{k}\psi_{k}(\mu,\mathfrak{T}), \tag{15}$$

where ρ is the perturbation parameter and $\rho\in[0,1]$.

The nonlinear term can be decomposed as

$$N\psi(\mu,\mathfrak{T})=\sum_{k=0}^{\infty}\rho^{k}H_{n}(\psi), \tag{16}$$

where H_n are He's polynomials of the form $\psi_0,\psi_1,\psi_2,\ldots,\psi_n$, and can be determined as

$$H_{n}(\psi_{0},\psi_{1},\ldots,\psi_{n})=\frac{1}{n!}\frac{\partial^{n}}{\partial p^{n}}\left[N\left(\sum_{k=0}^{\infty}\rho^{k}\psi_{k}\right)\right]_{\rho=0}. \tag{17}$$

Using relations (15) and (16) in (2) and constructing the homotopy, we get

$$\sum_{k=0}^{\infty}\rho^{k}\psi_{k}(\mu,\mathfrak{T})=F(\mu,\mathfrak{T})-\rho\times\left[S^{-1}\left\{\frac{u^{\alpha}}{s^{\alpha}}S\left\{M\sum_{k=0}^{\infty}\rho^{k}\psi_{k}(\mu,\mathfrak{T})+\sum_{k=0}^{\infty}\rho^{k}H_{k}(\psi)\right\}\right\}\right]. \tag{18}$$

On comparing coefficient of ρ on both sides, we obtain

$$\begin{aligned}&\rho^{0}\colon\ \psi_{0}(\mu,\mathfrak{T})=F(\mu,\mathfrak{T}),\\&\rho^{1}\colon\ \psi_{1}(\mu,\mathfrak{T})=S^{-1}\left[\frac{u^{\alpha}}{s^{\alpha}}S\{M\psi_{0}(\mu,\mathfrak{T})+H_{0}(\psi)\}\right],\\&\rho^{2}\colon\ \psi_{2}(\mu,\mathfrak{T})=S^{-1}\left[\frac{u^{\alpha}}{s^{\alpha}}S\{M\psi_{1}(\mu,\mathfrak{T})+H_{1}(\psi)\}\right],\\&\qquad\vdots\\&\rho^{k}\colon\ \psi_{n}(\mu,\mathfrak{T})=S^{-1}\left[\frac{u^{\alpha}}{s^{\alpha}}S\{M\psi_{k-1}(\mu,\mathfrak{T})+H_{k-1}(\psi)\}\right],\\&\qquad\qquad k>0,k\in N.\end{aligned} \tag{19}$$

The component $\psi_k(\mu,\mathfrak{T})$ can be calculated easily, which leads us to the convergent series rapidly. By taking $\rho\longrightarrow 1$, we obtain

$$\psi(\mu,\mathfrak{T})=\lim_{M\longrightarrow\infty}\sum_{k=1}^{M}\psi_{k}(\mu,\mathfrak{T}). \tag{20}$$

The obtained result is in the form of series and easily converges to exact solution of the problem.

4. Test Problems

To show the validity of the suggested technique, the following test problems are solved.

4.1. Example. Consider the fractional-order Fisher equation is given by

$$D^{\alpha}_{\mathfrak{T}}\psi=\psi_{\mu\mu}+\psi(1-\psi),\quad 0<\alpha\le 1, \tag{21}$$

with initial condition

$$\psi(\mu,0)=\beta. \tag{22}$$

Applying Shehu transform to (21), we have

$$\frac{s^{\alpha}}{u^{\alpha}}S[\psi(\mu,\mathfrak{T})]-\frac{s^{\alpha-1}}{u^{\alpha}}\psi(\mu,0)=S\left(\psi_{\mu\mu}+\psi(1-\psi)\right).$$

$$S[\psi(\mu,\mathfrak{T})]=\frac{\beta}{s}+\frac{u^{\alpha}}{s^{\alpha}}\left[S\left(\psi_{\mu\mu}+\psi(1-\psi)\right)\right]. \tag{23}$$

Using inverse Shehu transformation, we get

$$\psi(\mu,\mathfrak{T})=\beta+S^{-1}\left[\frac{u^{\alpha}}{s^{\alpha}}\left\{S\left(\psi_{\mu\mu}+\psi(1-\psi)\right)\right\}\right]. \tag{24}$$

Applying the abovementioned homotopy perturbation technique as in (18), we get

$$\sum_{k=0}^{\infty}\rho^{k}\psi_{k}(\mu,\mathfrak{T})=\beta+\rho\left[S^{-1}\left\{\frac{u^{\alpha}}{s^{\alpha}}S\left(\left(\sum_{k=0}^{\infty}\rho^{k}\psi_{k}(\mu,\mathfrak{T})\right)_{\mu\mu}+\sum_{k=0}^{\infty}\rho^{k}\psi_{k}(\mu,\mathfrak{T})\left(1-\sum_{k=0}^{\infty}\rho^{k}\psi_{k}(\mu,\mathfrak{T})\right)\right)\right\}\right]. \tag{25}$$

Comparing the coefficient of power ρ, we get

$$\begin{aligned}
&\rho^0\colon \psi_0(\mu,\mathfrak{F}) = \beta,\\
&\rho^1\colon \psi_1(\mu,\mathfrak{F}) = S^{-1}\left[\frac{u^\alpha}{s^\alpha}S\left\{\psi_{0\mu\mu}+\psi_0-\psi_0^2\right\}\right] = \beta(1-\beta)\frac{\mathfrak{F}^\alpha}{\Gamma(\alpha+1)},\\
&\rho^2\colon \psi_2(\mu,\mathfrak{F}) = S^{-1}\left[\frac{u^\alpha}{s^\alpha}S\left\{\psi_{1\mu\mu}+\psi_1-2\psi_0\psi_1\right\}\right] = \beta(1-\beta)(1-2\beta)\frac{\mathfrak{F}^{2\alpha}}{\Gamma(2\alpha+1)},\\
&\rho^3\colon \psi_3(\mu,\mathfrak{F}) = S^{-1}\left[\frac{u^\alpha}{s^\alpha}S\left\{\psi_{2\mu\mu}+\psi_2-\psi_1^2-2\psi_0\psi_2\right\}\right] = \left(\beta-5\beta^2+8\beta^3-4\beta^4\right)\frac{\mathfrak{F}^{3\alpha}}{\Gamma(3\alpha+1)}\\
&\qquad -\left(\beta^2-2\beta^3+\beta^4\right)\frac{\Gamma(2\alpha+1)}{\Gamma(\alpha+1)^2}\frac{\mathfrak{F}^{3\alpha}}{\Gamma(3\alpha+1)}.\\
&\quad\vdots
\end{aligned} \tag{26}$$

Now, by taking $\rho \longrightarrow 1$, we obtain convergent series form solution as

$$\begin{aligned}
&\psi(\mu,\mathfrak{F}) = \psi_0+\psi_1+\psi_2+\psi_3+\cdots,\\
&\psi(\mu,\mathfrak{F}) = \beta+\beta(1-\beta)\frac{\mathfrak{F}^\alpha}{\Gamma(\alpha+1)}+\beta(1-\beta)(1-2\beta)\\
&\qquad\frac{\mathfrak{F}^{2\alpha}}{\Gamma(2\alpha+1)}+\left(\beta-5\beta^2+8\beta^3-4\beta^4\right)\frac{\mathfrak{F}^{3\alpha}}{\Gamma(3\alpha+1)}\\
&\qquad-\left(\beta^2-2\beta^3+\beta^4\right)\left(\frac{\Gamma(2\alpha+1)}{\Gamma(\alpha+1)^2}\right)\frac{\mathfrak{F}^{3\alpha}}{\Gamma(3\alpha+1)}+\cdots.
\end{aligned} \tag{27}$$

Putting $\alpha = 1$, we get the same solution,

$$\psi(\mu,\mathfrak{F}) = \frac{\beta\ \exp^\mu}{1-\beta+\beta\ \exp^{\mathfrak{F}}}. \tag{28}$$

Figure 1 compares the exact solution and approximate solution for the nonlinear fractional-order Fisher equation at $\alpha = 1$. Figure 2 represents the graph of 2D of exact and analytical solutions and the second graph in Figure 2 shows the different fractional-order graphs of α.

4.2. Example. Consider the fractional-order Fisher equation is given by

$$D^\alpha_{\mathfrak{F}}\psi = \psi_{\mu\mu}+6\psi(1-\psi),\quad 0<\alpha\le 1, \tag{29}$$

with initial conditions

$$\psi(\mu,0) = \frac{1}{\left(1+\ \exp^\mu\right)^2}. \tag{30}$$

Applying Shehu transform of (29), we have

$$\begin{aligned}
&\frac{s^\alpha}{u^\alpha}S[\psi(\mu,\mathfrak{F})]-\frac{s^{\alpha-1}}{u^\alpha}\psi(\mu,0) = S\left(\psi_{\mu\mu}+6\psi(1-\psi)\right).\\
&S[\psi(\mu,\mathfrak{F})] = \frac{1}{s}\frac{1}{\left(1+\ \exp^\mu\right)^2}+\frac{u^\alpha}{s^\alpha}\\
&\qquad\cdot\left[S\left(\psi_{\mu\mu}+6\psi(1-\psi)\right)\right].
\end{aligned} \tag{31}$$

Using inverse Shehu transformation, we get

$$\psi(\mu,\mathfrak{F}) = \frac{1}{\left(1+\ \exp^\mu\right)^2}+S^{-1}\left[\frac{u^\alpha}{s^\alpha}\left\{S\left(\psi_{\mu\mu}+6\psi(1-\psi)\right)\right\}\right]. \tag{32}$$

Applying the abovementioned homotopy perturbation technique as in (18), we get

$$\sum_{k=0}^{\infty}\rho^k\psi_k(\mu,\mathfrak{F}) = \frac{1}{\left(1+\ \exp^\mu\right)^2}+\rho\left[S^{-1}\left\{\frac{u^\alpha}{s^\alpha}S\left(\left(\sum_{k=0}^{\infty}\rho^k\psi_k(\mu,\mathfrak{F})\right)_{\mu\mu}+6\sum_{k=0}^{\infty}\rho^k\psi_k(\mu,\mathfrak{F})\left(1-\sum_{k=0}^{\infty}\rho^k\psi_k(\mu,\mathfrak{F})\right)\right)\right\}\right]. \tag{33}$$

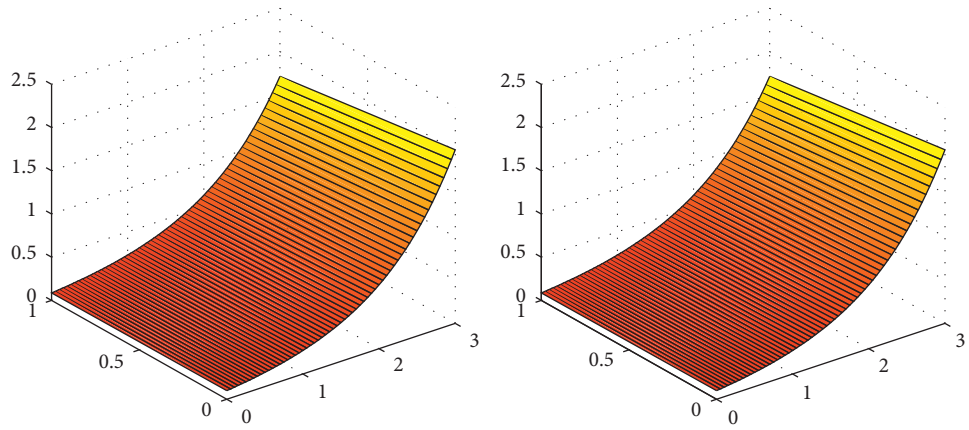

Figure 1: The graphs of exact and HPTM solutions for equation (21) at $\alpha = 1$.

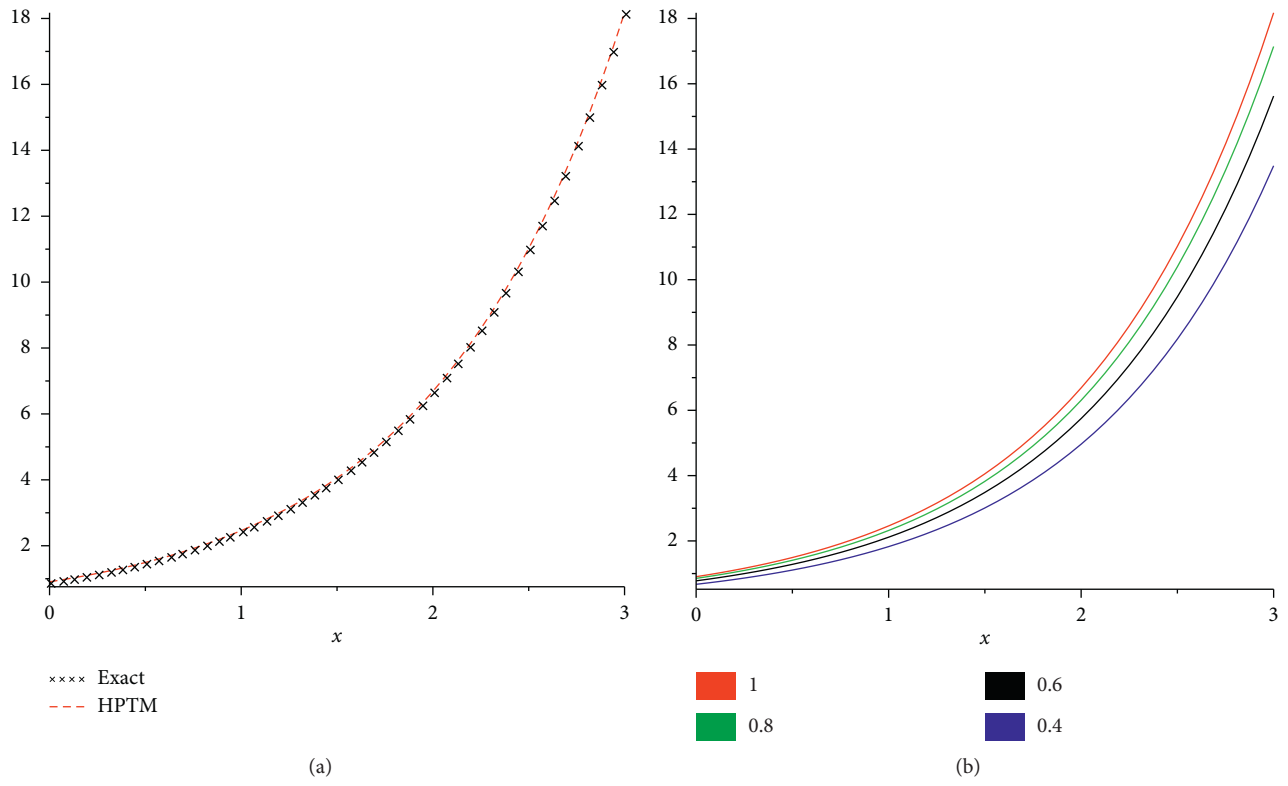

Figure 2: The graphs of exact and HPTM solutions and different fractional-order α of example 1.

Comparing the coefficient of power ρ, we get

$$\begin{aligned}
\rho^0&: \psi_0(\mu,\mathfrak{F}) = \frac{1}{\left(1+\ \exp^{\mu}\right)^2},\\
\rho^1&: \psi_1(\mu,\mathfrak{F}) = S^{-1}\left[\frac{u^{\alpha}}{s^{\alpha}}S\left\{\psi_{0\mu\mu}+6\psi_0-6\psi_0^2\right\}\right] = 10\frac{\exp^{\mu}}{\left(1+\ \exp^{\mu}\right)^3}\frac{\mathfrak{F}^{\alpha}}{\Gamma(\alpha+1)},\\
\rho^2&: \psi_2(\mu,\mathfrak{F}) = S^{-1}\left[\frac{u^{\alpha}}{s^{\alpha}}S\left\{\psi_{1\mu\mu}+6\psi_1-12\psi_0\psi_1\right\}\right] = 50\frac{\exp^{\mu}\left(-1+2\ \exp^{\mu}\right)}{\left(1+\ \exp^{\mu}\right)^4}\frac{\mathfrak{F}^{2\alpha}}{\Gamma(2\alpha+1)},\\
\rho^3&: \psi_3(\mu,\mathfrak{F}) = S^{-1}\left[\frac{u^{\alpha}}{s^{\alpha}}S\left\{\psi_{2\mu\mu}+6\psi_2-6\psi_1^2-12\psi_0\psi_2\right\}\right] = 50\exp^{\mu}\left(5-6\ \exp^{\mu}\right.\\
&\qquad\left.-15\ \exp^{2\mu},n+20\ \exp^{3\mu}-12\ \exp^{\mu}\frac{\Gamma(2\alpha+1)}{(\Gamma(\alpha+1))^2}\right)\frac{\mathfrak{F}^{3\alpha}}{\left(1+\ \exp^{\mu}\right)^6\ \Gamma(3\alpha+1)}.\\
&\ \ \vdots
\end{aligned} \tag{34}$$

Now, by taking $\rho \longrightarrow 1$, we obtain convergent series form solution as

$$\begin{aligned}
\psi(\mu,\mathfrak{F}) &= \psi_0+\psi_1+\psi_2+\psi_3+\cdots\\
&= \frac{1}{\left(1+\ \exp^{\mu}\right)^2}+10\frac{\exp^{\mu}}{\left(1+\ \exp^{\mu}\right)^3}\frac{\mathfrak{F}^{\alpha}}{\Gamma(\alpha+1)}+50\frac{\exp^{\mu}\left(-1+2\ \exp^{\mu}\right)}{\left(1+\ \exp^{\mu}\right)^4}\frac{\mathfrak{F}^{2\alpha}}{\Gamma(2\alpha+1)}\\
&\quad+50\exp^{\mu}\left(5-6\ \exp^{\mu}-15\ \exp^{2\mu}+20\ \exp^{3\mu}-12\ \exp^{\mu}\frac{\Gamma(2\alpha+1)}{(\Gamma(\alpha+1))^2}\right)\frac{\mathfrak{F}^{3\alpha}}{\left(1+\ \exp^{\mu}\right)^6\ \Gamma(3\alpha+1)}+\cdots.
\end{aligned} \tag{35}$$

Putting $\alpha = 1$, we get the same solution

$$\psi(\mu,\mathfrak{F}) = \frac{1}{\left(1-\ \exp^{\mu-5\mathfrak{F}}\right)^2}. \tag{36}$$

Figure 3 compares the exact solution and approximate solution for the nonlinear fractional-order Fisher equation at $\alpha = 1$. Figure 3 represents the graph of 2D of exact and analytical solutions and the second graph in Figure 3 shows the different fractional-order graphs of α of example 2.

4.3. Example. Consider the fractional-order Fisher equation is given by

$$D_{\mathfrak{F}}^{\alpha}\psi = \psi_{\mu\mu}+\psi\left(1-\psi^6\right),\quad 0<\alpha\le 1, \tag{37}$$

with initial conditions

$$\psi(\mu,0) = \frac{1}{\left(1+\ \exp^{(3/2)\mu}\right)^{(1/3)}}. \tag{38}$$

Applying Shehu transform of (37), we have

$$\begin{aligned}
\frac{s^{\alpha}}{u^{\alpha}}S[\psi(\mu,\mathfrak{F})]-\frac{s^{\alpha-1}}{u^{\alpha}}\psi(\mu,0) &= S\left(\psi_{\mu\mu}+\psi\left(1-\psi^6\right)\right),\\
S[\psi(\mu,\mathfrak{F})] &= \frac{1}{s}\frac{1}{\left(1+\ \exp^{(3/2)\mu}\right)^{(1/3)}}+\frac{u^{\alpha}}{s^{\alpha}}\\
&\quad\cdot\left[S\left(\psi_{\mu\mu}+\psi\left(1-\psi^6\right)\right)\right].
\end{aligned} \tag{39}$$

Using inverse Shehu transformation, we get

$$\begin{aligned}
\psi(\mu,\mathfrak{F}) &= \frac{1}{\left(1+\ \exp^{(3/2)\mu}\right)^{(1/3)}}+S^{-1}\\
&\quad\cdot\left[\frac{u^{\alpha}}{s^{\alpha}}\left\{S\left(\psi_{\mu\mu}+\psi\left(1-\psi^6\right)\right)\right\}\right].
\end{aligned} \tag{40}$$

Applying the abovementioned homotopy perturbation technique as in (18), we get

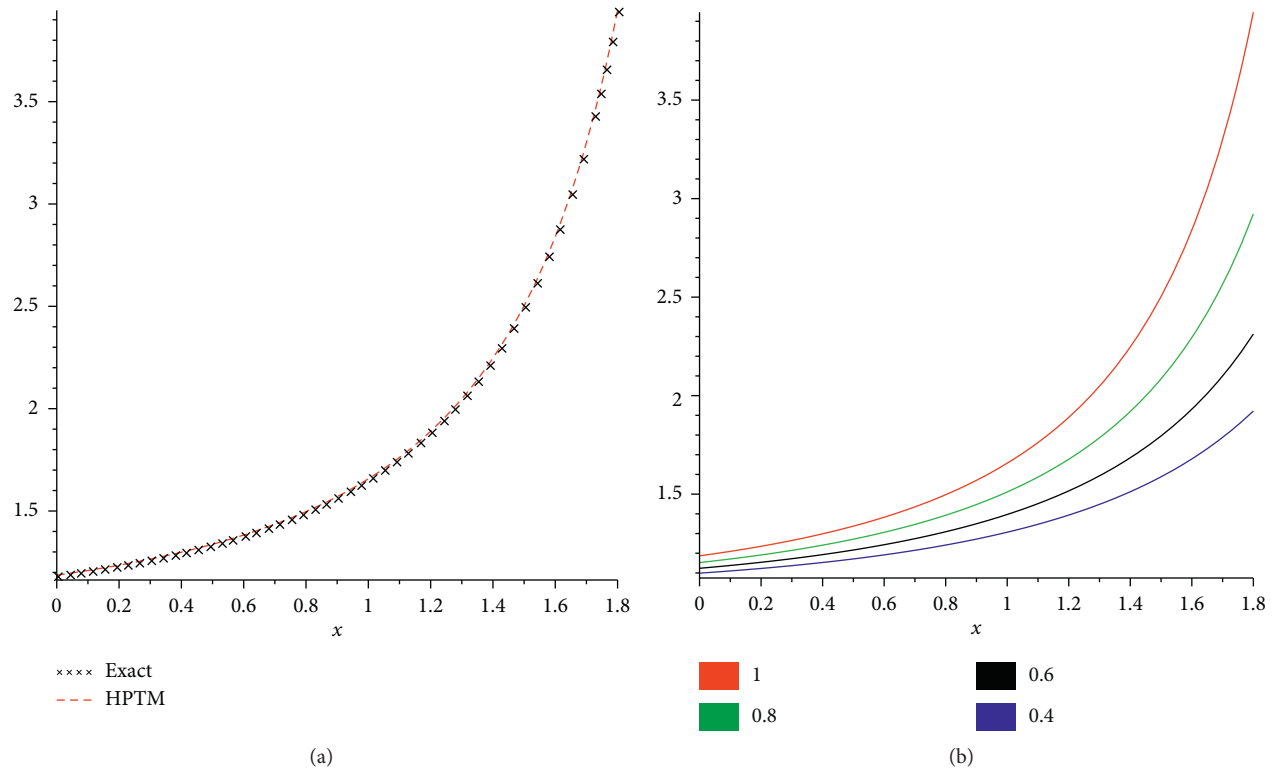

Figure 3: The graphs of exact and HPTM solutions and different fractional-order α for equation (29).

$$\sum_{k=0}^{\infty}\rho^k\psi_k(\mu,\mathfrak{F}) = \frac{1}{\left(1+\exp^{(3/2)\mu}\right)^{(1/3)}} + \rho\left[S^{-1}\left\{\frac{u^\alpha}{s^\alpha}S\left(\left(\sum_{k=0}^{\infty}\rho^k\psi_k(\mu,\mathfrak{F})\right)_{\mu\mu} + \sum_{k=0}^{\infty}\rho^k\psi_k(\mu,\mathfrak{F})\left(1-\left(\sum_{k=0}^{\infty}\rho^k\psi_k(\mu,\mathfrak{F})\right)^6\right)\right)\right\}\right]. \tag{41}$$

Comparing the coefficient of the same power of ρ, we get

$$\begin{aligned}
\rho^0&: \psi_0(\mu,\mathfrak{F}) = \frac{1}{\left(1+\exp^{(3/2)\mu}\right)^{(1/3)}},\\
\rho^1&: \psi_1(\mu,\mathfrak{F}) = S^{-1}\left[\frac{u^\alpha}{s^\alpha}S\left\{\psi_{0\mu\mu}+\psi_0-\psi_0^7\right\}\right] = \frac{5\exp^{(3/2)\mu}}{4\left(1+\exp^{(3/2)\mu}\right)^{(4/3)}}\frac{\mathfrak{F}^\alpha}{\Gamma(\alpha+1)},\\
\rho^2&: \psi_2(\mu,\mathfrak{F}) = S^{-1}\left[\frac{u^\alpha}{s^\alpha}S\left\{\psi_{1\mu\mu}+\psi_1-7\psi_0^6\psi_1\right\}\right] = \frac{25\exp^{(3/2)\mu}\left(\exp^{(3/2)\mu}-3\right)}{16\left(1+\exp^{(3/2)\mu}\right)^{(7/3)}}\frac{\mathfrak{F}^{2\alpha}}{\Gamma(2\alpha+1)},\\
&\vdots
\end{aligned} \tag{42}$$

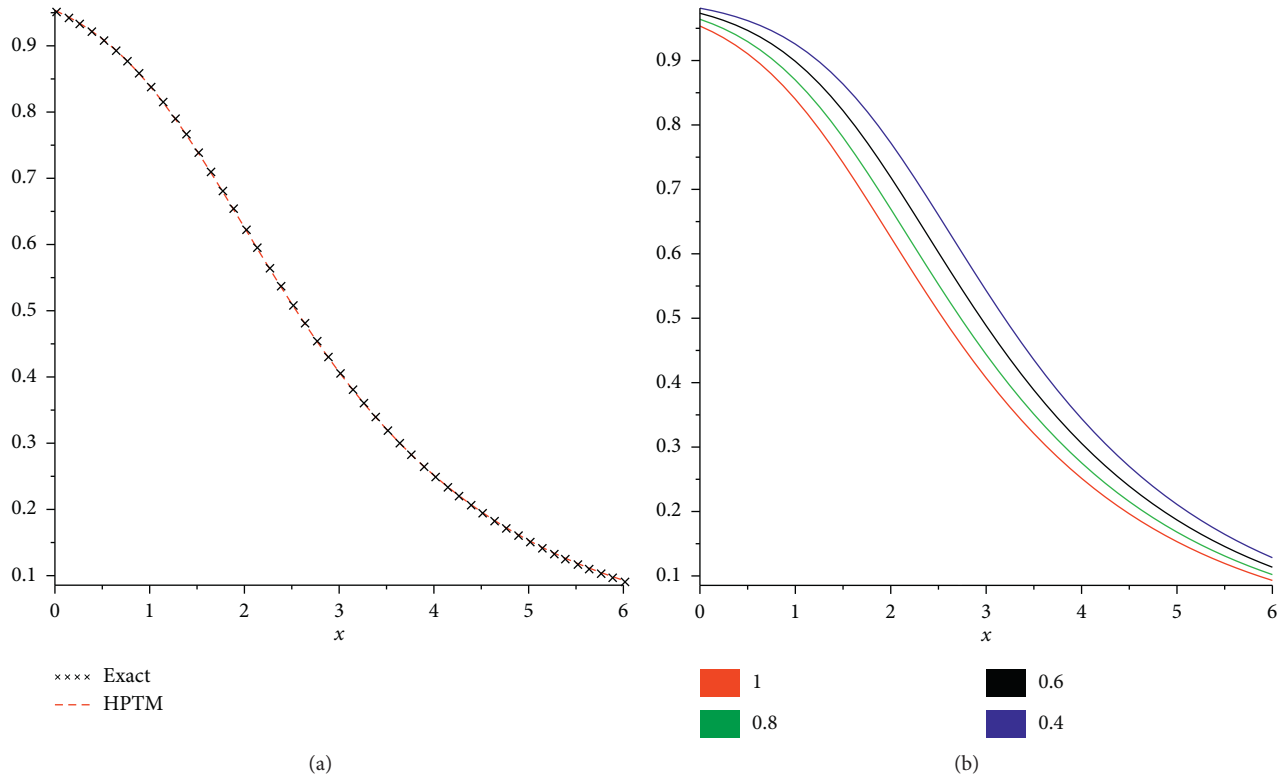

Figure 4: The graphs of exact and HPTM solutions and different fractional-order α for equation (37).

Now, by taking $\rho \longrightarrow 1$, we obtain convergent series form solution as

$$\psi(\mu, \mathfrak{F}) = \psi_0 + \psi_1 + \psi_2 + \psi_3 + \cdots.$$

$$\psi(\mu, \mathfrak{F}) = \frac{1}{\left(1 + \exp^{(3/2)\mu}\right)^{1/3}} + \frac{5 \exp^{(3/2)\mu}}{4\left(1 + \exp^{(3/2)\mu}\right)^{4/3}} \frac{\mathfrak{F}^{\alpha}}{\Gamma(\alpha+1)} + \frac{25 \exp^{(3/2)\mu}\left(\exp^{(3/2)\mu} - 3\right)}{16\left(1 + \exp^{(3/2)\mu}\right)^{(7/3)}} \frac{\mathfrak{F}^{2\alpha}}{\Gamma(2\alpha+1)} + \cdots. \tag{43}$$

Putting $\alpha = 1$, we get the same solution

$$\psi(\mu, \mathfrak{F}) = \left\{\frac{1}{2}\tanh\left(\frac{15}{8}\mathfrak{F} - \frac{3}{4}\mu\right) + \frac{1}{2}\right\}^{(1/3)}. \tag{44}$$

Figure 4 compares the exact solution and approximate solution for the nonlinear fractional-order Fisher equation at $\alpha = 1$. Figure 4 represents the graph of 2D of exact and analytical solutions and the second graph in Figure 4 shows the different fractional-order graphs of α.

5. Conclusion

In this paper, some computational works have been done to analyze Fisher's equations' fractional view analysis. For this purpose, the Shehu transformation is mixed with the homotopy perturbation method and derived a useful hybrid technique to handle the solution. The graphical representation of the solution of some illustrative examples is shown to be in closed contact. The fractional problem solution is convergent toward the integer-order solutions. Moreover, the accuracy of the proposed method is high and required less number of calculations. The suggested method can solve other fractional-order problems because of its simple and straight forward implementation.

Data Availability

The data used to support the findings of this study are available from the corresponding author upon request.

Conflicts of Interest

The authors declare that they have no conflicts of interest.

References

[1] D. Agirseven and T. Ozis, "An analytical study for Fisher type equations by using homotopy perturbation method," *Computers & Mathematics with Applications*, vol. 60, no. 3, pp. 602–609, 2010.

[2] M. Inc, M. Miah, S. A. Akher Chowdhury, H. Rezazadeh, M. A. Akinlar, and Y. M. Chu, "New exact solutions for the Kaup-Kupershmidt equation," *AIMS Mathematics*, vol. 5, no. 6, pp. 6726–6738, 2020.

[3] M. Inc, H. Rezazadeh, J. Vahidi et al., "New solitary wave solutions for the conformable Klein-Gordon equation with quantic nonlinearity," *AIMS Mathematics*, vol. 5, no. 6, pp. 6972–6984, 2020.

[4] N. Panagant and S. Bureerat, "Solving partial differential equations using a new differential evolution algorithm," *Mathematical Problems in Engineering*, vol. 2014, Article ID 747490, 10 pages, 2014.

[5] M. Inc, N. Bouteraa, M. A. Akinlar et al., "New positive solutions of nonlinear elliptic PDEs," *Applied Sciences*, vol. 10, no. 14, p. 4863, 2020.

[6] T. Elnaqeeb, N. A. Shah, and I. A. Mirza, "Natural convection flows of carbon nanotubes nanofluids with Prabhakar-like thermal transport," *Mathematical Methods in the Applied Sciences*, Wiley, New York, NY, USA, 2020.

[7] A. Yusuf, M. Inc, A. I. Aliyu, and D. Baleanu, "Efficiency of the new fractional derivative with nonsingular Mittag-Leffler kernel to some nonlinear partial differential equations," *Chaos, Solitons & Fractals*, vol. 116, pp. 220–226, 2018.

[8] T. Elnaqeeb, N. A. Shah, and A. Rauf, "Natural convection flows of carbon nanotube Prabhakar-like fractional second grade nanofluids over an infinite plate with Newtonian heating," *Mathematical Methods in the Applied Sciences*, Wiley, New York, NY, USA, 2020.

[9] M. Inc, A. Yusuf, A. I. Aliyu, and D. Baleanu, "Investigation of the logarithmic-KdV equation involving Mittag-Leffler type kernel with AtanganaŰBaleanu derivative," *Physica A: Statistical Mechanics and Its Applications*, vol. 506, pp. 520–531, 2018.

[10] T. Elnaqeeb, N. A. Shah, and D. Vieru, "Heat transfer enhancement in natural convection flow of nanofluid with Cattaneo thermal transport," *Physica Scripta*, vol. 95, no. 11, Article ID 115705, 2020.

[11] A. Yusuf, B. Acay, U. T. Mustapha, M. Inc, and D. Baleanu, "Mathematical modeling of pine wilt disease with Caputo fractional operator," *Chaos, Solitons & Fractals*, vol. 143, Article ID 110569, 2021.

[12] N. A. Shah, T. Elnaqeeb, and S. Wang, "Effects of Dufour and fractional derivative on unsteady natural convection flow over an infinite vertical plate with constant heat and mass fluxes," *Computational and Applied Mathematics*, vol. 37, no. 4, pp. 4931–4943, 2018.

[13] S. Qureshi, A. Yusuf, A. A. Shaikh, and M. Inc, "Transmission dynamics of varicella zoster virus modeled by classical and novel fractional operators using real statistical data," *Physica A: Statistical Mechanics and Its Applications*, vol. 534, Article ID 122149, 2019.

[14] N. Bertrand, J. Sabatier, O. Briat, and J. M. Vinassa, "An implementation solution for fractional partial differential equations," *Mathematical Problems in Engineering*, vol. 2013, Article ID 795651, 4 pages, 2013.

[15] M. Inc, A. I. Aliyu, A. Yusuf, and D. Baleanu, "Gray optical soliton, linear stability analysis and conservation laws via multipliers to the cubic nonlinear Schrödinger equation," *Optik*, vol. 164, pp. 472–478, 2018.

[16] M. Inç, H. Khan, D. Baleanu, and A. Khan, "Modified variational iteration method for straight fins with temperature dependent thermal conductivity," *Thermal Science*, vol. 22, 2018.

[17] M. Inc, A. I. Aliyu, A. Yusuf, and D. Baleanu, "Optical solitons for Biswas-Milovic Model in nonlinear optics by Sine-Gordon equation method," *Optik*, vol. 157, pp. 267–274, 2018.

[18] R. A. Fisher, "The wave of advance of advantageous genes," *Annals of Eugenics*, vol. 7, no. 4, pp. 355–369, 1937.

[19] D. A. B. Frank-Kamenetskii, *Diffusion and Heat Transfer in Chemical Kinetics*, Plenum Press, New York, NY, USA, 1969.

[20] A. J. Ammerman and L. L. Cavalli-Sforza, *Measuring the Rate of Spread of Early Farming in Europe*, pp. 674–688, University of London, London, UK, 1971.

[21] M. D. Bramson, "Maximal displacement of branching Brownian motion," *Communications on Pure and Applied Mathematics*, vol. 31, no. 5, pp. 531–581, 1978.

[22] J. Canosa, "Diffusion in nonlinear multiplicative media," *Journal of Mathematical Physics*, vol. 10, no. 10, pp. 1862–1868, 1969.

[23] X. Y. Wang, "Exact and explicit solitary wave solutions for the generalised Fisher equation," *Physics Letters A*, vol. 131, no. 4-5, pp. 277–279, 1988.

[24] J. R. Branco, J. A. Ferreira, and P. De Oliveira, "Numerical methods for the generalized Fisher-Kolmogorov-Petrovskii-Piskunov equation," *Applied Numerical Mathematics*, vol. 57, no. 1, pp. 89–102, 2007.

[25] J. E. Macías-Díaz, I. E. Medina-Ramírez, and A. Puri, "Numerical treatment of the spherically symmetric solutions of a generalized FisherŰKolmogorovŰPetrovskyŰPiscounov equation," *Journal of Computational and Applied Mathematics*, vol. 231, no. 2, pp. 851–868, 2009.

[26] A. M. Wazwaz and A. Gorguis, "An analytic study of Fisher's equation by using Adomian decomposition method," *Applied Mathematics and Computation*, vol. 154, no. 3, pp. 609–620, 2004.

[27] V. F. Zaitsev and A. D. Polyanin, *Handbook of Nonlinear Partial Differential Equations*, CRC Press, Boca Raton, FL, USA, 2003.

[28] H. Gu, B. Lou, and M. Zhou, "Long time behavior of solutions of Fisher-KPP equation with advection and free boundaries," *Journal of Functional Analysis*, vol. 269, no. 6, pp. 1714–1768, 2015.

[29] J. H. He, "Homotopy perturbation technique," *Computer Methods in Applied Mechanics and Engineering*, vol. 178, no. 3-4, pp. 257–262, 1999.

[30] J. H. He, "A coupling method of a homotopy technique and a perturbation technique for non-linear134 problems," *International Journal of Non-linear Mechanics*, vol. 35, no. 1, pp. 37–43, 2000.

[31] J. A. T. Machado, B. Dumitru, W. Chen, and Jocelyn Sabatier, "New trends in fractional dynamics," *Journal of Vibration and Control*, vol. 20, p. 963, 2014.

[32] D. Baleanu, Z. B. Güvenç, and J. A. T. Machado, Eds., *New Trends in Nanotechnology and Fractional Calculus Applications*, Springer, New York, NY, USA, 2010.

[33] S. Maitama and W. Zhao, "New integral transform: shehu transform a generalization of sumudu and laplace transform for solving differential equations," 2019, http://arxiv.org/abs/1904.11370.

[34] A. Bokhari, "Application of Shehu transform to atangana-baleanu derivatives," *Journal of Mathematical and Computational Science*, vol. 20, pp. 101–107, 2019.

[35] R. Belgacem, B. Dumitru, and B. Ahmed, "Shehu transform and applications to caputo-fractional differential equations," *International Journal of Analysis and Applications*, vol. 17, no. 6, pp. 917–927, 2019.

Hindawi
Mathematical Problems in Engineering
Volume 2021, Article ID 6610645, 8 pages
https://doi.org/10.1155/2021/6610645

Research Article

Matrix Factorization Recommendation Algorithm Based on Multiple Social Relationships

Sheng Bin and Gengxin Sun

School of Data Science and Software Engineering, Qingdao University, Qingdao 266071, China

Correspondence should be addressed to Sheng Bin; binsheng@qdu.edu.cn

Received 4 December 2020; Revised 30 January 2021; Accepted 19 February 2021; Published 26 February 2021

Academic Editor: Mustafa Inc

With the widespread use of social networks, social recommendation algorithms that add social relationships between users to recommender systems have been widely applied. Existing social recommendation algorithms only introduced one type of social relationship to the recommendation system, but in reality, there are often multiple social relationships among users. In this paper, a new matrix factorization recommendation algorithm combined with multiple social relationships is proposed. Through experiment results analysis on the Epinions dataset, the proposed matrix factorization recommendation algorithm has a significant improvement over the traditional and matrix factorization recommendation algorithms that integrate a single social relationship.

1. Introduction

With the development of big data technology, data redundancy has seriously interfered with obtaining effective information. The recommendation system solves the problem well and becomes a research hotspot in related fields. The recommendation system recommends items or information that may be of interest to users based on their hobbies, demand information, and consumer behavior [1, 2]. At present, the recommender system had been widely used in different industries, such as Amazon product recommendation, iTunes music recommendation, and Netflix movie recommendation because the recommendation algorithm can filter according to the mass of user history information, mine the deep relationship between users and users or items, and produce more accurate personalized recommendation with preference characteristics, which can better meet the needs of users. The algorithms used by the recommendation system consist of three types: collaborative filtering recommendation algorithms [3, 4], content-based recommendation algorithms [5], and hybrid recommendation algorithms [6]. Among them, collaborative filtering recommendation algorithm is currently the most popular, and it consists of three types: item-based collaborative filtering [7], user-based collaborative filtering [8], and matrix factorization collaborative filtering [9]. The matrix factorization collaborative filtering recommendation algorithm has attracted more and more researchers' attention because of its outstanding performance in the Netflix Prize competition. However, in practical applications, only a small number of users will rate or comment on a small number of items. Therefore, the matrix factorization recommendation algorithm has obvious data sparsity problem and item cold-start problem. The algorithm expresses the user's scorings of items in matrix form and factorizes the matrix to mine low-dimensional hidden feature space and then get user feature matrix and item feature matrix, finally through inner product operation of the two low-dimensional feature matrixes to describe the relation between users and items. Although the existing recommendation algorithms had obtained a good recommendation result, these traditional recommendation algorithms ignored the influence of social relationships among users on recommendation results. Since social relationships can reflect the similarity between users' preferences, simply considering the user's scoring of the items can no longer meet the recommendation needs, so the social recommendation algorithm that introduces social relationship into recommendation algorithm became

current research hotspots in recommendation systems [10]. Hao et al. [11] proposed a weighted bipartite graph recommendation algorithm that used the monotonic saturation function as the weight and used the true value of the number of target users and other items to score relative to the total number of users as the traditional similarity coefficient. Chen et al. [12] calculated the similarity between users and items through similar tags and proposed a joint probability matrix factorization recommendation algorithm that merged the neighbor perception of social tags, effectively using the semantics of the tag improved the recommendation quality. Lin et al. [13] used the principle of trust generation in social psychology, based on the trust extension method of user credibility, to alleviate the sparseness of data, and proposed a matrix recommendation algorithm with enhanced trust. Korpinar et al. [14] based on the shared representation method of user feature matrix, proposed a novel social recommendation model based on shared representation of user feature matrix, which effectively improved the accuracy of recommendation.

Most existing social recommendation algorithms only introduce a social relationship, but each added social relationship affects the recommendation result differently, so introduction of multiple social relationships would definitely improve recommendation accuracy. In this paper, a multiple relationships social network is constructed through a multi-subnet composite complex network model [15], a shared user feature matrix is used to introduce multiple social relationships into the recommendation algorithm, and a matrix factorization recommendation algorithm that integrates multiple social relationships is proposed.

2. Methodology

2.1. Traditional Matrix Factorization Model. Assuming that the recommendation system includes m customers and n commodities, $R_{m\times n} = [R_{ij}]_{m\times n}$ represents the customer-commodity scoring matrix, which is shown as Figure 1. R_{ij} represents the rating of customer i to item j, where $R_{ij} \in [1, 5]$. Usually, there many empty elements in $R_{m\times n}$, and it will cause a sparse matrix of customer-commodity scoring.

	v_1	v_2	v_3	v_4	v_5
u_1		5	2		
u_2	4			3	
u_3			2		4
u_4	5			3	
u_5		5	5		2

Figure 1: Customer-commodity scoring matrix.

	u_1	u_2	u_3	u_4	u_5
u_1		1		1	
u_2	1			1	
u_3					1
u_4	1	1			1
u_5			1	1	

Figure 2: Customer social relationship matrix.

In social networks, as shown in Figure 2, the social relationship between customers can be represented by a matrix C: $C = [C_{ik}]_{m\times m}$, the value of C_{ik} is 0 or 1, and if $C_{ik} = 0$, it means that there is no social relationship between customers.

The flowchart of traditional matrix factorization algorithm [8] is shown in Figure 3.

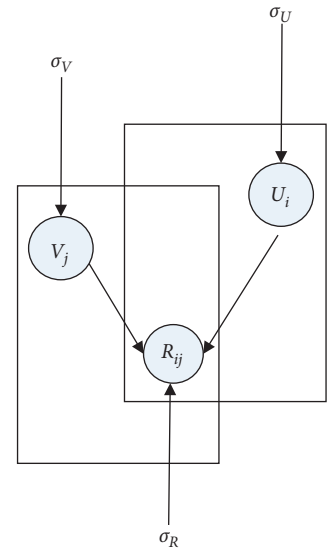

Figure 3: Flowchart of probabilistic matrix factorization.

Matrix $R_{m\times n}$ can be factorized into user feature matrix $U_{m\times k}$ and item feature $V_{k\times n}$, respectively. k represents dimension of vector, in general, it is much smaller than m and n, and then dimensionality reduction can be realized. U_i and V_j represent the potential feature spaces of corresponding users u_i and items v_j, respectively. The null value in scoring matrix can be forecast through $U_i^T V_j$, and then the prediction scoring matrix could be obtained.

For the convenience of research, the function $f(a) = 1/R_{\max}$ is used to map the customer's scoring of the commodity to [0,1] interval, where $R_{\max}$ represents the customer's maximum scoring of commodity. The traditional matrix factorization only uses a simple linear model $R = U^T V$, and the obtained results will be too fitted to the scoring matrix, resulting in the prediction scores deviating too much from the real data, and the final prediction results are distorted. Therefore, the logistic function $g(a) = 1/(1 + e^{-a})$ is used in this paper, so that the customer's scoring of commodity is defined in the range of [0, 1]. The observed conditional probability distribution can be defined ast

$$p\left(R|U, V, \sigma_R^2\right) = \prod_{i=1}^{m}\prod_{j=1}^{n} \mathcal{N}\left[\left(r_{ij}|g\left(U_i^T V_j\right), \sigma_R^2\right)\right]^{I_{ij}^R}, \quad (1)$$

where $\mathcal{N}(x|\mu, \sigma^2)$ indicates that x follows a Gaussian distribution whose mean is μ and variance is σ^2. I_{ij}^R represents

an index function, and if user i has a score of item j, its value is 1; otherwise, it is 0. Suppose U and V obey the spherical Gaussian distribution prior to mean 0:

$$\begin{aligned} p\left(U|\sigma_U^2\right) &= \prod_{i=1}^{m} \mathcal{N}\left(U_i|0,\sigma_U^2 I\right), \\ p\left(V|\sigma_V^2\right) &= \prod_{j=1}^{n} \mathcal{N}\left(V_j|0,\sigma_V^2 I\right). \end{aligned} \tag{2}$$

Then, through Bayesian inference, the posterior probability distribution of U and V could be obtained as follows:

$$\begin{aligned} p\left(U,V|R,\sigma_R^2,\sigma_U^2,\sigma_V^2\right) &\propto p\left(R|U,V,\sigma_R^2\right) p\left(U|\sigma_U^2\right) p\left(V|\sigma_V^2\right) \\ &= \sigma \prod_{i=1}^{m}\prod_{j=1}^{n} \left[\mathcal{N}\left(r_{ij}|g\left(U_i^T V_j\right),\sigma_R^2\right)\right]^{I_{ij}^R} \times \prod_{i=1}^{m} \mathcal{N}\left(U_i|0,\sigma_U^2 I\right) \times \prod_{j=1}^{n} \mathcal{N}\left(V_j|0,\sigma_V^2 I\right). \end{aligned} \tag{3}$$

2.2. Matrix Factorization Recommendation Algorithm Integrating a Social Relationship. In the traditional recommendation algorithm, users are independent of each other, which ignores the users' social relationship. If there is a social relationship between two users, the preferences of users or the choice of items will affect each other. Therefore, it is necessary to integrate social relationships into the recommendation algorithm; thus, recommendation accuracy will be improved greatly.

Suppose that there is only one kind of social relationship between users, and the social relationship can be incorporated into the matrix factorization recommendation algorithm through sharing the user's potential eigenspace, which is the same as that in user scoring matrix. Then, it is analyzed by probability matrix factorization. $C = C_{ik}$ represents an $m \times m$ matrix, which factorizes the social network into user feature matrix $U \in R^{l \times m}$ and social feature matrix $Z \in R^{l \times m}$.

The conditional distribution of observed social relationship can be defined:

$$p\left(C|U,Z,\sigma_C^2\right) = \prod_{i=1}^{m}\prod_{k=1}^{m} \mathcal{N}\left[\left(c_{ik}|g\left(U_i^T Z_k\right),\sigma_C^2\right)\right]^{I_{ik}^C}. \tag{4}$$

Suppose that U and Z follow the spherical Gaussian prior distribution with mean 0:

$$\begin{aligned} p\left(U|\sigma_U^2\right) &= \prod_{i=1}^{m} \mathcal{N}\left(U_i|0,\sigma_U^2 I\right), \\ p\left(Z|\sigma_V^2\right) &= \prod_{j=1}^{n} \mathcal{N}\left(Z_k|0,\sigma_Z^2 I\right). \end{aligned} \tag{5}$$

Then, through simple Bayesian inference, the following results can be obtained:

$$\begin{aligned} p\left(U,Z|C,\sigma_C^2,\sigma_U^2,\sigma_Z^2\right) &\propto p\left(C|U,Z,\sigma_C^2\right) p\left(U|\sigma_U^2\right) p\left(Z|\sigma_Z^2\right) \\ &= \sigma \prod_{i=1}^{m}\prod_{k=1}^{m} \left[\mathcal{N}\left(c_{ik}|g\left(U_i^T Z_k\right),\sigma_C^2\right)\right]^{I_{ik}^C} \times \prod_{i=1}^{m} \mathcal{N}\left(U_i|0,\sigma_U^2 I\right) \times \prod_{k=1}^{m} \mathcal{N}\left(Z_k|0,\sigma_C^2 I\right), \end{aligned} \tag{6}$$

where I_{ik}^C is an indicator function, and if user i has a social relationship with user k, its value is 1; otherwise, it is 0.

The flowchart of matrix factorization recommendation algorithm integrating a social relationship (MFRS1) is shown in Figure 4.

According to the shared user eigenspace, the user's item scoring matrix is closely related to the social relationship matrix, and the posterior distribution of social recommendations can be obtained by logarithm:

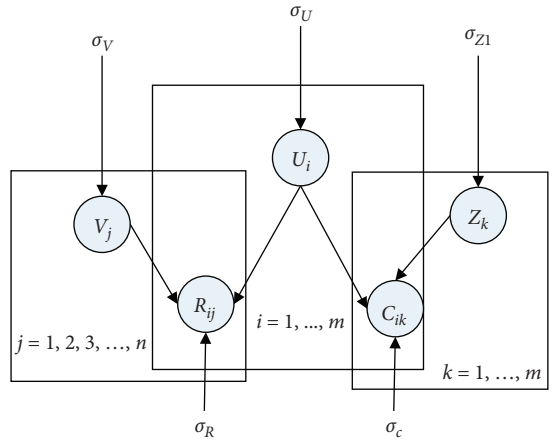

Figure 4: Flowchart of matrix factorization recommendation algorithm integrating a social relationship.

$$\begin{aligned}\ln p\left(U,V,Z|C,R,\sigma_C^2,\sigma_R^2,\sigma_U^2,\sigma_V^2,\sigma_Z^2\right) = &-\frac{1}{2\sigma_R^2}\sum_{i=1}^{m}\sum_{j=1}^{n} I_{ij}^R\left(r_{ij}-g\left(U_i^TV_j\right)\right)^2-\frac{1}{2\sigma_C^2}\sum_{i=1}^{m}\sum_{k=1}^{m} I_{ik}^C\left(c_{ik}^*-g\left(U_i^TZ_k\right)\right)^2\\ &-\frac{1}{2\sigma_U^2}\sum_{i=1}^{m}U_i^TU_i-\frac{1}{2\sigma_V^2}\sum_{j=1}^{n}V_j^TV_j\\ &-\frac{1}{2\sigma_Z^2}\sum_{k=1}^{m}Z_k^TZ_k-\frac{1}{2}\left(\left(\sum_{i=1}^{m}\sum_{j=1}^{n}I_{ij}^R\right)\ln\sigma_R^2+\left(\sum_{i=1}^{m}\sum_{j=1}^{n}I_{ij}^R\right)\ln\sigma_C^2\right)\\ &-\frac{1}{2}\left(ml\ln\sigma_U^2+nl\ln\sigma_V^2+ml\ln\sigma_Z^2\right)+C,\end{aligned} \tag{7}$$

where C is a constant which does not rely on any parameter, and the maximum posterior distribution function should be equal to the minimum objective function, which is as follows:

$$\begin{aligned}\mathcal{L}\left(R,C_1,C_2,U,V,Z_1,Z_2\right) = &\frac{\lambda_C}{2}\sum_{i=1}^{m}\sum_{j=1}^{n}I_{ij}^R\left(r_{ij}-g\left(U_i^TV_j\right)\right)^2+\frac{1-\lambda_C}{2}\sum_{i=1}^{m}\sum_{k=1}^{m}I_{ik}^C\left(C_{ik}^*-g\left(U_i^TZ_k\right)\right)^2\\ &+\frac{\lambda_U}{2}\|U\|_F^2+\frac{\lambda_V}{2}\|V\|_F^2+\frac{\lambda_Z}{2}\|Z\|_F^2,\end{aligned} \tag{8}$$

where $\lambda_C \in [0,1]$ is used to adjust the influence proportion of user scoring matrix and social relationship matrix on recommendation result. When $\lambda_C = 1$, it means that the social relationship between users is not considered, when $\lambda_C = 0$, it means that the user scoring matrix has a proportion of 0, and the rest means that a social relationship is integrated. $\lambda_C = \sigma_R^2/\sigma_C^2$, $\lambda_U = \sigma_R^2/\sigma_U^2$, $\lambda_V = \sigma_R^2/\sigma_V^2$, $\lambda_Z = \sigma_R^2/\sigma_Z^2$, $\|\cdot\|_F^2$ represents regularization.

2.3. Matrix Factorization Recommendation Algorithm Integrating Multiple Social Relationships. In actual social networks, there are often more than one kind of social relationship between users, and each social relationship has a different impact on the recommendation, so introduction of a kind of social relationship would definitely affect recommendation accuracy. Suppose that there are two kinds of social relationships c_1 and c_2 between users, and the flowchart of matrix factorization recommendation algorithm integrating multiple social relationships (MFRS2) is shown in Figure 5.

According to the algorithm, c_1 relationship between users is represented by matrix $C^1 = [C_{ik}^1]_{m\times m}$, and c_2 relationship between users is represented by matrix $C^2 = [C_{ik}^2]_{m\times m}$. If relationship strength of c_1 is β, then relationship strength of c_2 is $1-\beta$, where $\beta \in [0,1]$. Therefore, the objective function for minimizing the introduction of two kinds of social relationships is

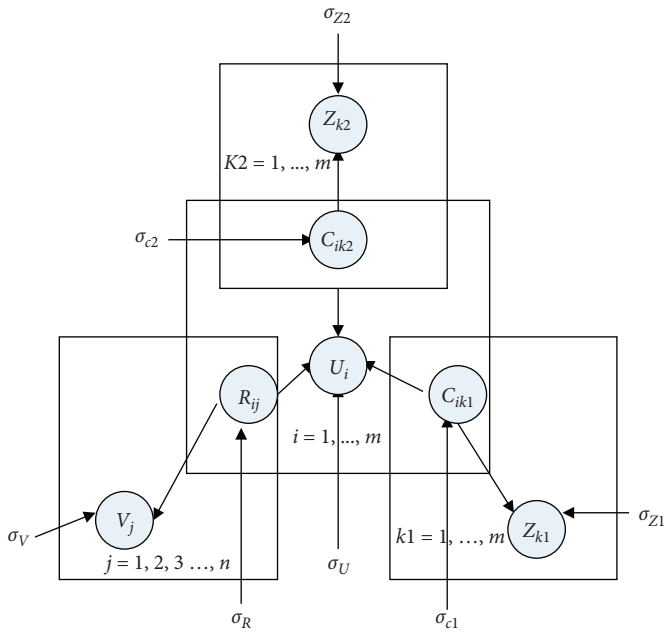

Figure 5: Flowchart of matrix factorization recommendation algorithm integrating multiple social relationships.

$$\begin{aligned}\mathscr{L}\left(R, C_1, C_2, U, V, Z_1, Z_2\right) = {} & \frac{\lambda_C}{2}\sum_{i=1}^{m}\sum_{j=1}^{n} I_{ij}^{R}\left(r_{ij} - g\left(U_i^T V_j\right)\right)^2 \\ & + \frac{\beta\left(1-\lambda_C\right)}{2}\sum_{i=1}^{m}\sum_{k=1}^{m} I_{ik}^{C^1}\left(C_{ik}^{1*} - g\left(U_i^T Z_k^1\right)\right)^2 + \frac{(1-\beta)\left(1-\lambda_C\right)}{2}\sum_{i=1}^{m}\sum_{k=1}^{m} I_{ik}^{C^2}\left(C_{ik}^{2*} - g\left(U_i^T Z_k^2\right)\right)^2 \\ & + \frac{\lambda_U}{2}\|U\|_F^2 + \frac{\lambda_V}{2}\|V\|_F^2 + \frac{\lambda_Z}{2}\|Z\|_F^2.\end{aligned} \tag{9}$$

The gradient descent algorithm can be used to solve the objective function as follows:

$$\begin{aligned}\frac{\partial \mathscr{L}}{\partial U_i} = {} & \lambda_C\sum_{j=1}^{n} I_{ij}^{R} g'\left(U_i^T V_j\right)\left(g\left(U_i^T V_j\right) - r_{ij}\right)V_j + \beta\left(1-\lambda_C\right)\sum_{j=1}^{m} I_{ik}^{C^1} g'\left(U_i^T Z_k^1\right)\left(g\left(U_i^T Z_k^1\right) - C_{ik}^{1*}\right)Z_k^1 \\ & + (1-\beta)\left(1-\lambda_C\right)\sum_{j=1}^{m} I_{ik}^{C^2} g'\left(U_i^T Z_k^2\right)\left(g\left(U_i^T Z_k^2\right) - C_{ik}^{2*}\right)Z_k^2 + \lambda_U U_i, \\ \frac{\partial \mathscr{L}}{\partial V_j} = {} & \sum_{i=1}^{m} I_{ij}^{R} g'\left(U_i^T V_j\right)\left(g\left(U_i^T V_j\right) - r_{ij}\right)U_i + \lambda_V V_j, \\ \frac{\partial \mathscr{L}}{\partial Z_k^1} = {} & \lambda_C\sum_{i=1}^{m} I_{ik}^{C^1} g'\left(U_i^T Z_k^1\right)\left(g\left(U_i^T Z_k^1\right) - C_{ik}^{1*}\right)U_i + \lambda_Z^1 Z_k^1, \\ \frac{\partial \mathscr{L}}{\partial Z_k^2} = {} & \lambda_C\sum_{i=1}^{m} I_{ik}^{C^2} g'\left(U_i^T Z_k^2\right)\left(g\left(U_i^T Z_k^2\right) - C_{ik}^{2*}\right)U_i + \lambda_Z^2 Z_k^2,\end{aligned} \tag{10}$$

where $g'(x) = e^x/(1+e^x)^2$ represents derivative of logistic function $g(x)$. For reducing model complexity, the corresponding parameter setting is $\lambda_U = \lambda_V = \lambda_Z^1 = \lambda_Z^2$.

3. Results and Analysis

3.1. Experimental Data. In this paper, Epinions is used as the experimental dataset, and it is a knowledge-sharing website where customers could review commodities or give integer scorings between one and five. New customers can use these comments or ratings to determine whether the commodity is worth buying. The Epinions dataset includes the customer's trust relationship, customer's scoring for commodities, and comment information of commodities. It includes 49,290 customers, 139,738 commodities, 664,824 comment messages, and 487,181 trust relationships.

In the course of experiment, a five-fold cross-validation method was used to train and verify the proposed recommended algorithm. The Epinions dataset was separated into five equal groups, one group was randomly selected as test set, and the other four groups were acted as training set. Five experiments were conducted to ensure that each test set is tested. The ultimate experimental result was the average of five experiments.

3.2. Evaluation Indicators. In this paper, two identical evaluation indicators are used to measure the accuracy of recommendations, namely, mean absolute error (MAE) and root mean squared error (RMSE) [16]. These two indicators measure accuracy of recommendation algorithm through calculating the error between the prediction score and the actual score. The smaller their value, the higher the recommendation accuracy. The definitions of MAE and RMSE are as follows:

$$\begin{aligned} \text{MAE} &= \frac{1}{\left|E^P\right|} \sum_{(i,j)\in E^P} \left|r_{ij} - r'_{ij}\right|, \\ \text{RMSE} &= \sqrt{\frac{1}{\left|E^P\right|} \sum_{(i,j)\in E^P} \left(r_{ij} - r'_{ij}\right)^2}, \end{aligned} \tag{11}$$

where r_{ij} represents the real scoring of customer i for commodity j, r'_{ij} represents the prediction scoring of customer u_i for commodity j, and E^P represents the test set.

3.3. Experimental Results Analysis. During the experiment, the number of algorithm user features is $K = 5$, the number of iterations is 1000, and $\lambda_U = \lambda_V = 0.001$. The proportion between social relationship matrix and customer scoring matrix can be adjusted by parameter α, and the proportion between the two social relationships can be adjusted by parameter β. The different values of α and β will directly affect the recommendation result. The value of α and β is determined by the method of simulation experiment. $\beta = 1$ means that only one kind of social relationship is introduced, when α takes different values, and the change of MAE value and RMSE value in the dataset is shown in Figures 6 and 7.

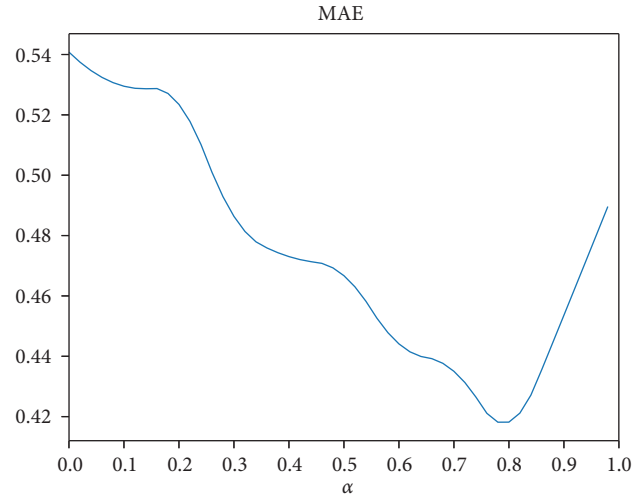

Figure 6: Influence of parameter α for MAE.

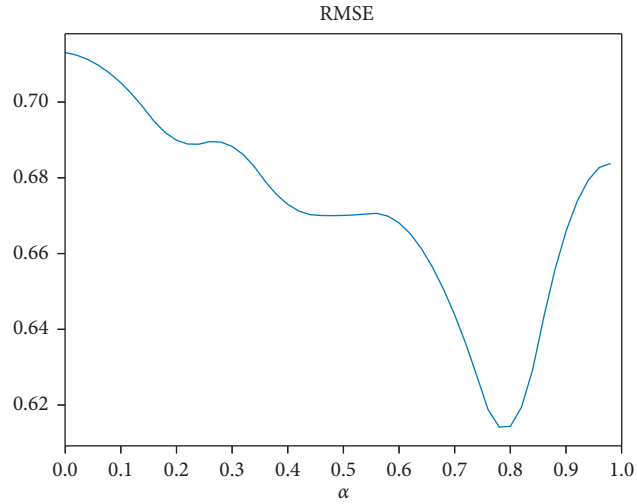

Figure 7: Influence of parameter α for RMSE.

As shown in Figures 6 and 7, in the Epinions dataset, when $\alpha = 0.8$, the values of MAE and RMSE are all the smallest; that is, for one social relationship, when $\alpha = 0.8$, the recommendation accuracy rate is the highest.

O_u and O_v are used to denote the item sets that customers u and v had scored, respectively, the more commodities which customers u and v jointly scored, the more likely they are to have the same interest and influence each other, and the specific definitions are as follows:

$$f_{uv} = \frac{O_u \cap O_v}{O_u \cup O_v}. \tag{12}$$

When $f_{uv} > 0.2$, it means that customers u and v have similar interests. Suppose that the relationship between users satisfying this condition is the c_2 relationship. When α and β take different values, the changes in MAE and RMSE on the Epinions dataset are shown in Figures 8 and 9.

As shown in Figures 8 and 9, in the Epinions dataset, when the parameters $\alpha = 0.3$ and $\beta = 0.4$, the value of MAE

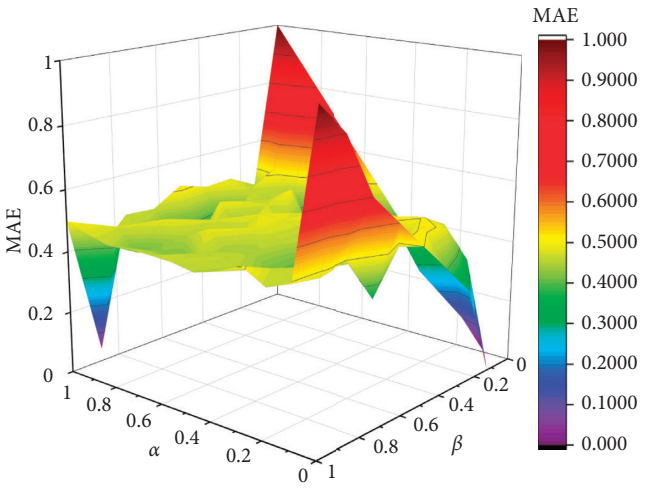

Figure 8: Influence of parameter α and β for MAE.

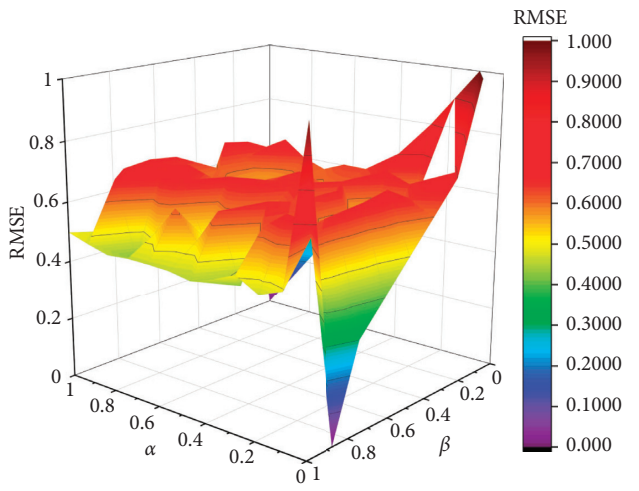

Figure 9: Influence of parameter α and β for RMSE.

is the smallest, that is, the recommended accuracy rate in the proposed algorithm is the highest. Similarly, when $\alpha = 0.7$ and $\beta = 0.5$, the value of RMSE is the smallest, which means that the recommendation accuracy in the proposed algorithm is the highest.

For verifying the performance of MDRS2 algorithm and the impact of various social relationships on the recommendation, we compared MDRS2 algorithm with SocRec algorithm [14], TDSRec algorithm [17], and MDRS1 algorithm on the Epinions dataset. The SocRec algorithm considers the attributes of social relationships between users on the basis of matrix factorization and incorporates a social relationship; the TDSRec algorithm combines the similarity based on user ratings preferences while considering social networks and predicts the values of customer scoring matrix together. The MDRS1 algorithm only considers one kind of social relationship. The MDRS2 algorithm tightly links the user-item scoring matrix and the social relationship matrix through sharing the user's feature space and integrates multiple social relationships into matrix factorization. The experimental statistical result is shown in Table 1.

Table 1: Experiment result comparison of various algorithms.

Evaluation index	SocRec	TDSRec	MDRS1	MDRS2
MAE	0.8932	0.7864	0.4451	0.4394
RMSE	0.9240	0.8679	0.6143	0.5973

As shown in Table 1, in the Epinions dataset, the MAE and RMSE values of the MDRS2 algorithm are smaller than those of other algorithms; that is, the prediction accuracy is higher. It can be seen that the recommendation algorithm that introduces two kinds of social relationships has a higher accuracy rate than other three recommendation algorithms, which indicates that introducing multiple relationships between users would improve recommendation accuracy, and the more relationships between users, the higher the recommendation accuracy.

4. Conclusions

In this paper, through factorizing the user-item scoring matrix, according to multi-subnet composite complex network, a variety of social relationships are integrated into the matrix factorization recommendation algorithm by using the shared user's potential feature space. Using the matrix factorization recommendation algorithm to the user-item dataset after introducing the social relationship, users' preferences for items will be accurately obtained. Through experiments on real datasets, it is proved that the proposed matrix factorization recommendation algorithm, which combines multiple relationships, improves the recommendation accuracy. It means that introducing multiple social relationships can better personalize recommendations for users, and the more relationships introduced, the better the recommendation effect. In future research, the user's indirect relationship and direct relationship can be combined to further study the impact of social relationships on recommendations.

Data Availability

The basic data used in this article are downloaded from the online public dataset: Epinions http://www.trustlet.org/epinions.html.

Conflicts of Interest

The authors declare that there are no conflicts of interest regarding the publication of this paper.

Acknowledgments

This research was funded by the Shandong Provincial Natural Science Foundation, China, grant no. ZR2017MG011, and Humanity and Social Science Youth Foundation of Ministry of Education of China, grant no. 15YJC860001.

References

[1] T. Krpinar, "Optical directional binormal magnetic flows with geometric phase: Heisenberg ferromagnetic model," *International Journal for Light and Electron Optics*, vol. 219, pp. 1–15, 2019.

[2] X. Zhao, Z. Niu, W. Chen, C. Shi, K. Niu, and D. Liu, "A hybrid approach of topic model and matrix factorization based on two-step recommendation framework," *Journal of Intelligent Information Systems*, vol. 44, no. 3, pp. 335–353, 2015.

[3] T. Krpinar, "A new optical Heisenberg ferromagnetic model for optical directional velocity magnetic flows with geometric phase," *Indian Journal of Physics*, vol. 94, pp. 1409–1421, 2019.

[4] F. Xue, X. He, X. Wang, J. Xu, K. Liu, and R. Hong, "Deep item-based collaborative filtering for top-N recommendation," *ACM Transactions on Information Systems*, vol. 37, no. 3, pp. 1–25, 2019.

[5] S. M. Daneshmand, A. Javari, S. E. Abtahi, and M. Jalili, "A time-aware recommender system based on dependency network of items," *The Computer Journal*, vol. 58, no. 9, pp. 1955–1966, 2015.

[6] M. Nilashi, O. B. Ibrahim, and N. Ithnin, "Hybrid recommendation approaches for multi-criteria collaborative filtering," *Expert Systems with Applications*, vol. 41, no. 8, pp. 3879–3900, 2014.

[7] T. Ha and S. Lee, "Item-network-based collaborative filtering: a personalized recommendation method based on a user's item network," *Information Processing & Management*, vol. 53, no. 5, pp. 1171–1184, 2017.

[8] S. Bin, G. Sun, N. Cao et al., "Collaborative filtering recommendation algorithm based on multi-relationship social network," *Computers, Materials & Continua*, vol. 60, no. 2, pp. 659–674, 2019.

[9] J. Z. Sun, D. Parthasarathy, and K. R. Varshney, "Collaborative kalman filtering for dynamic matrix factorization," *IEEE Transactions on Signal Processing*, vol. 62, no. 14, pp. 3499–3509, 2014.

[10] W. Li, J. Qi, Z. Yu, and D. Li, "A social recommendation method based on trust propagation and singular value decomposition," *Journal of Intelligent & Fuzzy Systems*, vol. 32, no. 1, pp. 807–816, 2017.

[11] F. Hao, S. Li, G. Min, H.-C. Kim, S. S. Yau, and L. T. Yang, "An efficient approach to generating location-sensitive recommendations in ad-hoc social network environments," *IEEE Transactions on Services Computing*, vol. 8, no. 3, pp. 520–533, 2015.

[12] J. Chen, S. Feng, and J. Liu, "Topic sense induction from social tags based on non-negative matrix factorization," *Information Sciences*, vol. 280, pp. 16–25, 2014.

[13] L. Lin, H. R. Xie, Y. H. Rao, and F. L. Wang, "Personalized recommendation by matrix co-factorization with tags and time information," *Expert Systems with Applications*, vol. 119, pp. 311–321, 2019.

[14] T. Korpinar, Z. Korpinar, M. Inc, and D. Baleanu, "Geometric phase for timelike spherical normal magnetic charged particles optical ferromagnetic model," *Journal of Taibah University for Science*, vol. 14, no. 1, pp. 742–749, 2020.

[15] G. Sun and S. Bin, "Router-level internet topology evolution model based on multi-subnet composited complex network model," *Journal of Internet Technology*, vol. 18, pp. 1275–1283, 2017.

[16] T. Korpinar, R. C. Demirkol, and Z. Korpinar, "Soliton propagation of electromagnetic field vectors of polarized light ray traveling in a coiled optical fiber in the ordinary space," *International Journal of Geometric Methods in Modern Physics*, vol. 16, pp. 67–81, 2019.

[17] G. Sun and S. Bin, "Construction of learning behavioral engagement model for MOOCs platform based on data analysis," *Educational Sciences-Theory & Practice*, vol. 18, pp. 2206–2216, 2018.

Hindawi
Mathematical Problems in Engineering
Volume 2021, Article ID 6617668, 9 pages
https://doi.org/10.1155/2021/6617668

Research Article

The Impact of the SARS-CoV-2 Epidemic on World Indices: The Entropy Approach

Ayşe Metin Karakaş,[1] **Mine Doğan**,[2] **and Sinan Çalik**[2]

[1]*Department of Statistics, Faculty of Art and Science, Bitlis Eren University, Bitlis, Turkey*
[2]*Department of Statistics, Faculty of Science, Firat University, Elazığ, Turkey*

Correspondence should be addressed to Ayşe Metin Karakaş; aysekarakas5767@gmail.com

Received 10 December 2020; Revised 16 January 2021; Accepted 11 February 2021; Published 26 February 2021

Academic Editor: Mustafa Inc

The coronavirus disease (COVID-19) outbreak started in December 2019 in Wuhan. The virus has spread around the whole world, and it has caused a strong and serious pandemic. Symptoms such as cough, respiratory distress, diarrhea, and fatigue associated with COVID-19 are typical clinical findings. Coronavirus infection has become an important public health concern because of its increasing prevalence, serious complications, and mortality. In light of this information, we examine different entropy methods for world indices (ISE 30, FTSE 100, NIKKEI 225, SP 500, and DAX 30) in the pre-COVID-19 period (02.01.2019–17.11.2019) and the post-COVID-19 period (18.11.2019–23.11.2020) in this article. Besides, we discuss the performances of entropies such as Shannon, Renyi, Tsallis, and approximate entropy (ApEn) in detail and perform the notion of entropy for volatility measure. As a result, we present the numerical results for the data set.

1. Introduction

Entropy is a word that goes back to 1865 when Rudolf Clausius, a German physicist, granted an original noun to irreparable warmth damage termed as equivalent value. The word entropy was chosen for the fact that entropies refer to average component transformative or transformation component in Greek [1]. Tsallis [2] suggests that the concept of entropy should be widened into a notion bearing the statistical status of complicated systems. Then, Rao et al. [3] put forward the cumulative residual entropy, generalized measure of ambiguity, and applied it in reliability and picture arrangement as well as nonadditive measures of entropy. In 2008, Pincus [4] pointed out the use of approximate entropy (ApEn), a model-independent measure of consecutive disorder. Thus, through utilizing a number of varied practices for both empirical data and model-based data, he conceived cross-ApEn, concerning two-variable asynchrony measure that provides a stronger and more omnipresent measure of bivariate correspondence than correlation. In addition, he presented the following containments to various strategies, ensured analytic statements for statistical properties of ApEn, and cross-checked ApEn with nonlinear measures, correlation, and spectral analyses as well as other entropy measures. Later, Ubriaco [5] applied the derivative to a special probability function and obtained the Shannon entropy definition which is based on probability and derivative. The information and its management can be illustrated by entropy. Most information management techniques are based on entropy. The fractional-order derivative and entropy-based binomial distribution yield a series of symmetric functions. Rompolis [6] put forward a varied method to apply the maximum entropy basis for recovering the risk neutral density of forthcoming stock, or any other entity which returns from put prices. In 2015, Sati and Gupta [7] defined a generalized cumulative remaining entropy on the basis of the nonadditive Tsallis entropy. In the same year, Sheraz et al. [8] employed an entropy for volatility markets. Then, Stosic et al. [9] investigated the effect of financial attacks on foreign exchange (FX) markets using the time-dependent block entropy technique and revealed experimental conclusions

which explain that the financial attacks are corporate with an important rise in exchange rate entropy, echoing uncertainty in FX market dynamics. The study in [10] shows every minute of the six years of entropy-dependent usage data between 1999 and 2004 based on time series and volatility, and that the entropy of the fluctuation series is based on the stock market. Khammar and Jahanshahi [11] submitted the weighted condition of this measure and named it "Weighted Cumulative Residual Tsallis Entropy (WCRTE)" and showed that it can specify the value of the survival function and Rayleigh distribution in a unique way. In 2019, Karakas [12] has attained volatility of ethereum and bitcoin, and then, the same author [13] used the world indices such as Istanbul Stock Indices (BIST 30), Brazil Index (Bovespa), Germany Index (DAX 30), Britain Index (FTSE100), South Korea (KOSPİ), Japan Index (NIKKEI 225), United States Index (S&P 500), and China Index (SHANGAI) that have been examined over 8 years between 2010 and 2018, and, as a result, found the entropy notion for volatility measure to draw a comparison. Inc et al. [14] obtained approximate solutions of the nonlinear time-dependent generalized Fitzhugh–Nagumo equation with time-dependent coefficients and Sharma–Tasso–Olver equation subjected to certain initial conditions and showed that this method is efficient and convenient and, thus, it can be applied to a variety of problems. The approximate solutions are compared with the exact solutions. Then, Acay and Inc [15] proposed the temperature dynamics of a building and examined this model which has a crucial place in daily life. In 2020, Houwe et al. [16] investigated analytical solutions for the nonlinear differential-difference equations (DDEs) having fractional-order derivatives and employed the discrete tanh method in computations. As well, Akinlar et al. [17] considered an epidemic disease system by an additive fractional white noise to show that epidemic diseases may be more competently modeled in the fractional-stochastic settings than the ones modeled by deterministic differential equations, generated a new SIRS model and perturbed it to the fractional-stochastic systems, and studied chaotic behavior at disease-free and endemic steady-state points on these systems. After that, Akinlar et al. [18] considered a novel contribution because optimal control formulations, numerical solutions, and stability analysis for the fractional-order Malkus model are studied for the first time in this paper. Later, in the same year, Korpinar et al. [19] analyzed the fractional-stochastic quadratic-cubic nonlinear Schrödinger equation (QC-NLSE) describing the propagation of solitons through optical fibers and employed it to obtain stochastic solutions in the white noise space with Hermite transformation. Besides, Hashemi et al. [20] used the Adams–Bashforth–Moulton scheme (ABMS) to determine the approximate solution of a variable-order fractional three-dimensional chaotic process, demonstrating simulation results. However, Qureshi [21] examined a new time-invariant nonlinear mathematical model in fractional-(noninteger-) order settings that has been proposed under the three most frequently employed strategies of the classical Caputo. Currently, all world stock markets have been affected by the virus. The COVID-19 virus first emerged in China (Wuhan city) spreading around the world. This virus is amongst the deadliest virus known to humans all over, having deadly effect on the health care system of most of the countries. In this study, five world indices (ISE 30, FTSE 100, SP 500, NIKKEI 225, and DAX 30) were used to investigate based on the entropy approach in the pre-COVID-19 period (02.01.2019–17.11.2019) and post-COVID-19 period (18.11.2019–23.11.2020).

2. Materials and Methods

2.1. Shannon Entropy and Renyi Entropy. Shannon entropy states that a measure of the amount of information $_S(p)$ containing a series of events of $p_1, p_2, \ldots, p_N$ should satisfy three requirements:

S should be continuous in p_i

If all p_i are equal probably, then S should be a monotonic increasing function of N

S should be additive

Then, it proves that only S satisfying these three requirements shows

$$S(P) = -\kappa \sum_{i=1}^{N} p_i \ln\ p_i, \tag{1}$$

where κ is a positive constant. This quantity has since become known as the Shannon entropy. In the information theory applications, the asymptotic equipartition property of Shannon is given for $T \subseteq S^n$ $T \subseteq S^n$ with

$$|T| \leq e^{n(S(\rho)+\varepsilon)}, \tag{2}$$

such that illustration n times from P yields a factor of T with probability $>1-\varepsilon$ and $\varepsilon \longrightarrow 0$ as $n \longrightarrow \infty$. Extensions of Shannon's original work have resulted in many alternative measures of information or entropy. For instance, by relaxing the third point of Shannon's requirements, that of additivity, Renyi was able to extend Shannon entropy to a continuous family of entropy measures:

$$S_q(P) = -\frac{1}{1-q} \ln \sum_{i=1}^{N} p_i^q. \tag{3}$$

The Renyi entropy tends to Shannon entropy as $q \longrightarrow 1$. The Renyi entropy is as follows:

The scaling factor is conventional, i.e., it makes S_q nonnegative for all q and ensures $S_q(u_n) = \log n$, where u_n is the uniform distribution on an n-element set.

The main property which the Renyi entropy has in common with Shannon entropy is additivity:

$$S_q(\rho \times r) = S_q(\rho) + S_q(r). \tag{4}$$

For $\beta = 0$, acquire the min-entropy, which is the cardinality of the support of ρ: $S_0(\rho) = \log|\{i \in S|\rho(i)>0\}|$.

For $q = 1$, acquire Shannon entropy:

Table 1: Statistics of world indices in the pre-COVID-19 period (02.01.2019–17.11.2019).

	ISE 30	FTSE 100	NIKKEI 225	SP 500	DAX 30
Mean	1226,0519	7262,6528	21358,17	2896,640	11998,00
Median	1237,215	7274,450	21360,09	2909,190	12034,17
Maximum	1327,420	7686,610	23520,01	3121,750	13289,46
Minimum	1045,03	6692,660	19561,96	2605,500	10416,66
Std. dev.	65,32040	186,4341	873,4083	113,5172	604,7448
Skewness	−0.674607	−0.599872	0.217312	−0.379169	−0.031424
Kurtosis	2.731324	3.472528	3,208747	2.768171	2.689980
Jarque–Bera	17.50623	15.79535	2.208500	5.973792	0.950594
Probability	0.000158	0.000372	0.033145	0.005044	0.006217

Table 2: Statistics of world indices in the post-COVID-19 period (18.11.2019–23.11.2020).

	ISE 30	FTSE 100	NIKKEI 225	SP 500	DAX 30
Mean	1287,1338	6379,9955	22412,79	3165,256	12329,73
Median	1297,285	6123,820	23112,88	3232,250	12822,26
Maximum	1496,790	7674,560	26014,62	3623,000	13789,00
Minimum	1014,100	4993,890	16552,83	2220,500	8441,710
Std. dev.	106,5718	699,3948	1827,824	279,4826	1209,913
Skewness	−0.250346	0.617331	−1.175042	−0.974508	−1.297747
Kurtosis	2.706596	2.110804	3,951717	3,539609	3.795668
Jarque–Bera	3.592315	24.79044	68.84024	43.79541	78.91692
Probability	0.016593	0.000004	0.000000	0.000000	0.000000

Table 3: Different entropy measures of ISE 30, FTSE 100, NIKKEI 225, SP 500, and DAX 30 in the pre-COVID-19 period (02.01.2019–17.11.2019).

	Shannon		Tsallis		Renyi	Approximate entropy
Method	Value	q	Value	r	Value	Value
ISE 30						
ML	5.396743	0	220.0000000	0	5.398163	
MM	5.397149	0.2	92.5761790	0.25	5.397804	0.7846485
Jefferys	5.396744	0.4	40.8280410	0.5	5.397448	
Laplace	5.396745	0.6	19.1544962	1	5.396743	
SG	5.396743	0.8	9.7146361	2	5.395365	
Minimax	5.396749	1	5.3967431	4	5.392732	
CS	5.396743	1.2	3.3008212	8	5.387939	
Shrink	5.39745	1.4	2.2112471	16	5.380020	
		1.6	1.6012332	32	5.368983	
		1.8	1.2333170	64	5.356709	
		2	0.9954624	Infinite	5.319076	
FTSE 100						
ML	5.424631	0	226.0000000	0	5.424950	
MM	5.424699	0.2	94.6256717	0.25	5.424870	0.7947985
Jefferys	5.424631	0.4	41.5280750	0.5	5.424790	
Laplace	5.424631	0.6	19.3935912	1	5.424631	
SG	5.424631	0.8	9.7962946	2	5.424315	
Minimax	5.424631	1	5.4246308	4	5.423694	
CS	5.424631	1.2	3.3103449	8	5.422489	
Shrink	5.424754	1.4	2.2144993	16	5.420221	
		1.6	1.6023437	32	5.416139	
		1.8	1.2336962	64	5.409257	
		2	0.9955919	Infinite	5.368548	
NIKKEI 225						
ML	5.424339	0	226.0000000	0	5.424950	
MM	5.424363	0.2	94.6212737	0.25	5.424798	0.689666
Jefferys	5.424339	0.4	41.5250909	0.5	5.424646	

Table 3: Continued.

	Shannon		Tsallis		Renyi	Approximate entropy
Method	Value	q	Value	r	Value	Value
Laplace	5.424339	0.6	19.3920726	1	5.424339	
SG	5.424339	0.8	9.7956076	2	5.423721	
Minimax	5.42434	1	5.4243394	4	5.422458	
CS	5.424339	1.2	3.3102262	8	5.419834	
Shrink	5.424384	1.4	2.2144524	16	5.414208	
		1.6	1.6023255	32	5.402104	
		1.8	1.2336893	64	5.381751	
		2	0.9955893	Infinite	5.333581	
SP 500						
ML	5.424201	0	226.0000000	0	5.424950	
MM	5.424373	0.2	94.6190516	0.25	5.424762	0.6455126
Jefferys	5.424202	0.4	41.5236068	0.5	5.424575	
Laplace	5.424202	0.6	19.3913293	1	5.424201	
SG	5.424201	0.8	9.7952767	2	5.423462	
Minimax	5.424203	1	5.4242014	4	5.422009	
CS	5.424201	1.2	3.3101709	8	5.419211	
Shrink	5.424507	1.4	2.2144308	16	5.414035	
		1.6	1.6023173	32	5.405173	
		1.8	1.2336862	64	5.391980	
		2	0.9955882	Infinite	5.350668	
DAX 30						
ML	5.42371	0	226.0000000	0	5.424950	
MM	5.423752	0.2	94.6115378	0.25	5.424640	0.5535031
Jefferys	5.42371	0.4	41.5185260	0.5	5.424329	
Laplace	5.42371	0.6	19.3887524	1	5.423710	
SG	5.42371	0.8	9.7941149	2	5.422476	
Minimax	5.423712	1	5.4237103	4	5.420029	
CS	5.42371	1.2	3.3099716	8	5.415223	
Shrink	5.423792	1.4	2.2143522	16	5.406039	
		1.6	1.6022869	32	5.389845	
		1.8	1.2336746	64	5.367814	
		2	0.9955838	Infinite	5.323234	

Table 4: Different entropy measures of ISE 30, FTSE 100, NIKKEI 225, SP 500, and DAX 30 in the post-COVID-19 period (18.11.2019–23.11.2020).

	Shannon		Tsallis		Renyi	Approximate entropy
Method	Value	q	Value	r	Value	Value
ISE 30						
ML	5.557801	0	254.0000000	0	5.541264	
MM	5.558188	0.2	103.9217249	0.25	5.540389	0.605173
Jefferys	5.557804	0.4	44.6150090	0.5	5.539521	
Laplace	5.557806	0.6	20.4188729	1	5.537801	
SG	5.557801	0.8	10.1368950	2	5.534431	
Minimax	5.557813	1	5.5378010	4	5.527964	
CS	5.557801	1.2	3.3479548	8	5.516089	
Shrink	5.558543	1.4	2.2270007	16	5.496175	
		1.6	1.6064999	32	5.468754	

Table 4: Continued.

	Shannon		Tsallis		Renyi	Approximate entropy
Method	Value	q	Value	r	Value	Value
		1.8	1.2350782	64	5.442340	
		2	0.9960515	Infinite	5.390417	
FTSE 100						
ML	5.539317	0	255.0000000	0	5.545177	
MM	5.539395	0.2	104.2128898	0.25	5.543729	0.4216846
Jefferys	5.539318	0.4	44.6980209	0.5	5.542269	
Laplace	5.539319	0.6	20.4418658	1	5.539317	
SG	5.539317	0.8	10.1430007	2	5.533302	
Minimax	5.539326	1	5.5393168	4	5.520987	
CS	5.539317	1.2	3.3482870	8	5.496723	
Shrink	5.539468	1.4	2.2270537	16	5.458418	
		1.6	1.6064983	32	5.421958	
		1.8	1.2350713	64	5.398850	
NIKKEI 225						
ML	5.541764	0	255.000000	0	5.545177	
MM	5.541786	0.2	104.251176	0.25	5.544299	0.4849035
Jefferys	5.541764	0.4	44.723779	0.5	5.543437	
Laplace	5.541764	0.6	20.454859	1	5.541764	
SG	5.541764	0.8	10.148825	2	5.538606	
Minimax	5.541767	1	5.541764	4	5.532970	
CS	5.541764	1.2	3.349274	8	5.523834	
Shrink	5.541811	1.4	2.227440	16	5.510553	
		1.6	1.606647	32	5.490232	
		1.8	1.235127	64	5.457949	
		2	0.996068	Infinite	5.394338	
SP 500						
ML		0	255.0000000	0	5.545177	
MM	5.541305	0.2	104.240513	0.25	5.544141	0.484537
Jefferys	5.541149	0.4	44.7167917	0.5	5.543124	
Laplace	5.54115	0.6	20.4514234	1	5.541148	
SG	5.541148	0.8	10.1473229	2	5.537413	
Minimax	5.541157	1	5.5411479	4	5.530728	
CS	5.541148	1.2	3.3490311	8	5.519871	
Shrink	5.541472	1.4	2.2273475	16	5.504498	
		1.6	1.6066119	32	5.485190	
		1.8	1.2351145	64	5.463312	
		2	0.9960633	Infinite	5.410064	
DAX 30						
ML	5.42371	0	226.0000000	0	5.424950	
MM	5.540173	0.2	104.2217368	0.25	5.543865	0.5196777
Jefferys	5.540133	0.4	44.7046841	0.5	5.542587	
Laplace	5.540133	0.6	20.4455670	1	5.540132	
SG	5.540132	0.8	10.1448044	2	5.535607	
Minimax	5.540138	1	5.5401324	4	5.527909	
CS	5.540132	1.2	3.3486380	8	5.516591	
Shrink	5.540219	1.4	2.2271995	16	5.503120	
		1.6	1.6065573	32	5.489558	
		1.8	1.2350947	64	5.475649	
		2	0.9960562	Infinite	5.432999	

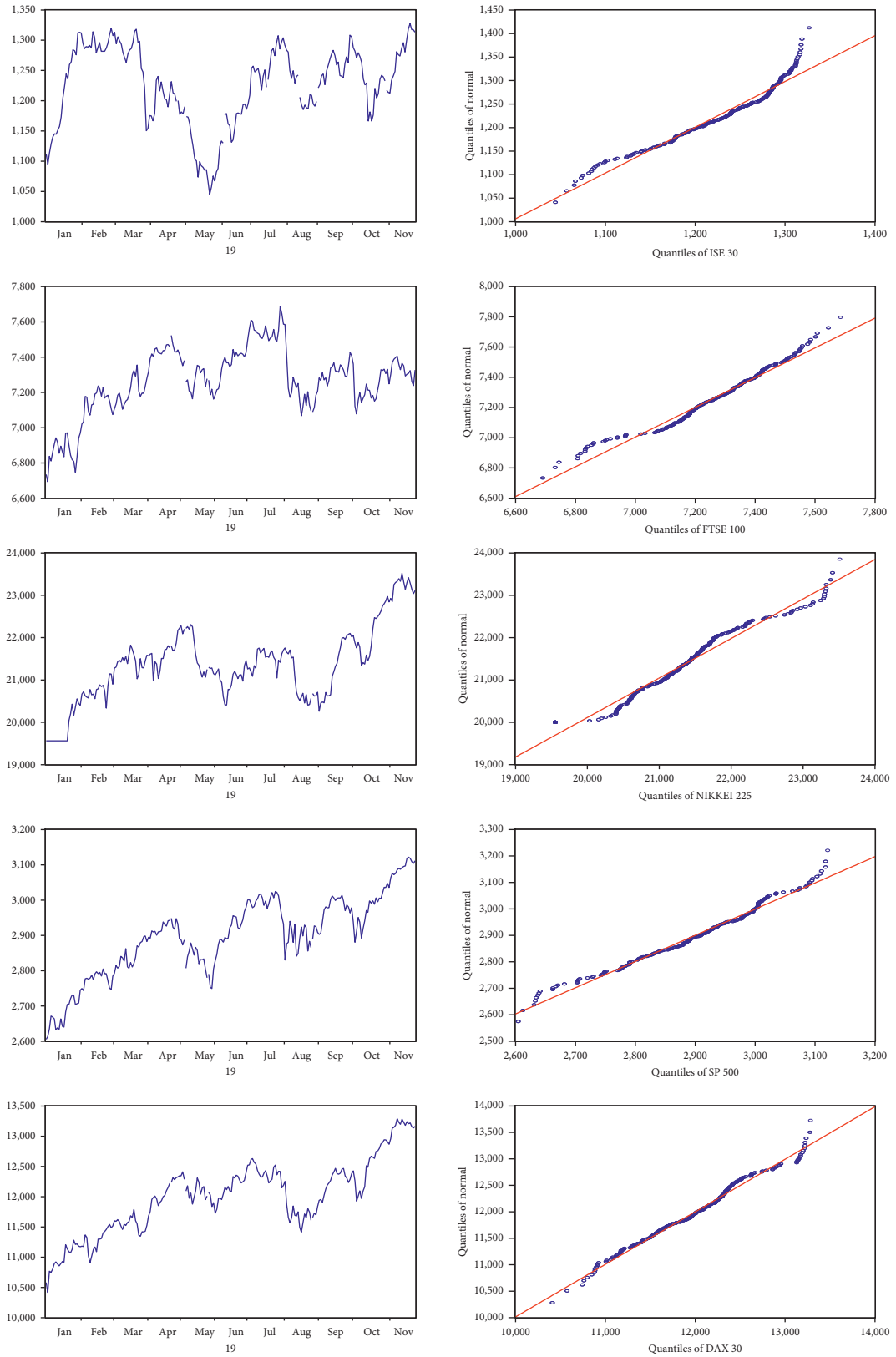

Figure 1: Data of world indices graphs and quantile graphs in the pre-COVID-19 period (02.01.2019–17.11.2019).

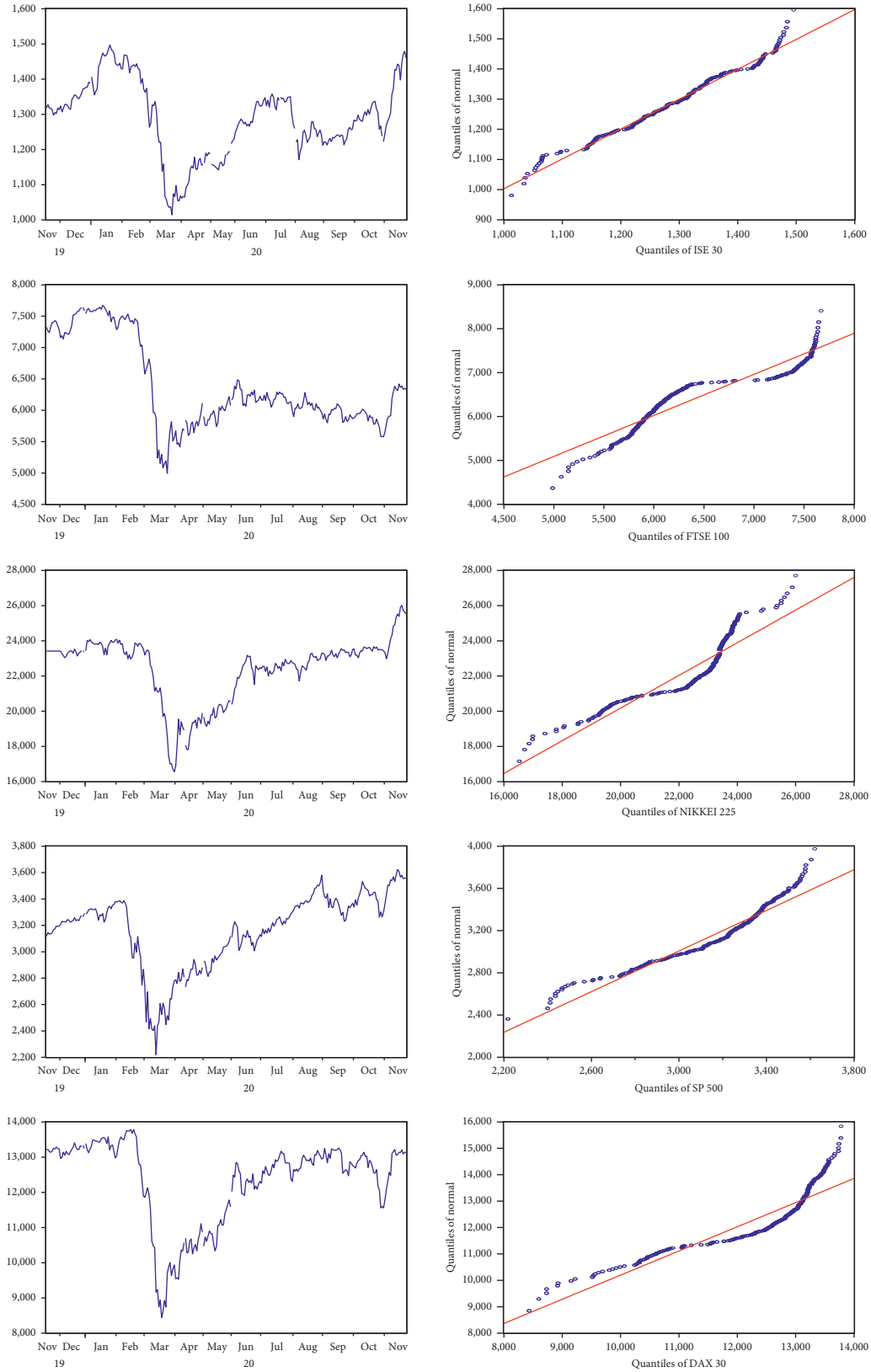

Figure 2: Data of world indices graphs and quantile graphs in the post-COVID-19 period (18.11.2019–23.11.2020).

$$S_1(\rho) = \lim_{q \longrightarrow 1} S_q(\rho),$$

$$\frac{d}{dq}\left(\frac{1}{1-q}\log\left(\sum_i \rho(i)^q\right)\right)_{q=1} = -\sum_i \rho(i)\log\,\rho(i). \tag{5}$$

For $q = \infty$, acquire the min-entropy:

$$S_\infty(\rho) = -\log\max_i \rho(i) = \log\min_i \frac{1}{\rho(i)}. \tag{6}$$

2.2. Tsallis Entropy. For any positive real number α, the entropy of order α of probability measure p on finite set X is defined as

$$S_\alpha(p) = \begin{cases} \dfrac{1}{\alpha-1}\left(1 - \sum_{i\in X} p_i^\alpha\right), & if\,\alpha \neq 1, \\ -\sum_{i\in X} p_i \ln\, p_i, & if\,\alpha = 1. \end{cases} \tag{7}$$

The characterization of the Tsallis entropy is the same as that of the Shannon entropy except that for the Tsallis entropy, the degree of homogeneity under convex linearity condition is α instead of 1.

3. Results

3.1. Data Set. We utilize the world indices of ISE 30, FTSE 100, SP 500, NIKKEI 225, and DAX 30 in the pre-COVID-19 period (02.01.2019–17.11.2019) and post-COVID-19 period (18.11.2019–23.11.2020). Tables 1 and 2 summarize the statistics data of world indices of ISE 30, FTSE 100, SP 500, NIKKEI 225, and DAX 30 before and after the coronavirus pandemic. Tables 1 and 2 indicate varied average values for the data set, and the suitable standard deviations are varied. In Table 2, skewness for data set is negative; in Table 1, except for NIKKEI 225, others are negative. The kurtosis of two data sets is higher than *l*. The Jarque–Bera (JB) test indicates that the normality of distribution for every series is strongly refused at 0.05 level, which means the overall energy terms' index distributions are nonnormal.

3.2. Conclusion: Entropy Approach. We apply the entropy technique for the volatility of world indices such as ISE 30, FTSE 100, SP 500, NIKKEI 225, and DAX 30 before and after the COVID-19 pandemic. For this, we compute Shannon, Tsallis, Renyi, and approximate entropies. In Tables 3 and 4, we initially provide varied forecasters for the Shannon entropy measure in the pre-COVID-19 period (02.01.2019–17.11.2019) and post-COVID-19 period (18.11.2019–23.11.2020). Later, we provide the Tsallis entropy for various values of the parameter and Renyi entropy measures for varied values of the parameter. Finally, we have obtained approximate entropy. When overall potential incidents have a similar probability, the entropy provides maximum value. In our experimental outcomes, volatility indicates variation; this model shows linear and nonlinear dynamics. We obtain from the numerical outcomes that overall entropies are positive, so features of our data series are nonlinear. We find that the world indices of ISE 30, FTSE 100, SP 500, NIKKEI 225, and DAX 30 series have a great value of approximate entropy before and after the coronavirus pandemic. In the data series, when looking at world indices volatility before the coronavirus pandemic in Table 3 and Figure 1, volatility is mostly seen in FTSE 100, followed by ISE 30, NIKKEI 225, SP 500, and DAX 30. Similarly, in Table 4 and Figure 2, when we look at world indices after the coronavirus pandemic, volatility is mostly seen in ISE 30, followed by DAX 30, NIKKEI 225, SP 500, and FTSE 100. It is concluded that before the coronavirus pandemic, FTSE 100 data series is of higher volatility than other data series. Similarly, after the coronavirus pandemic, ISE 30 data series is of higher volatility than other data series. For the Shannon entropy estimators, before the coronavirus pandemic, it is clear that FTSE 100 series have larger values. In a similar way, for the measures of Tsallis and Rényi entropies, if we take attention that q and r are close to 1, then we obtain the Shannon entropy. After the coronavirus pandemic, it is clear that ISE 30 series have larger values.

Data Availability

Data are available from the website www.bloomberght.com.

Conflicts of Interest

The authors declare that they have no conflicts of interest.

Acknowledgments

The authors thank http://www.bloomberght.com for the data set.

References

[1] K. J. Laidler, *Thermodynamics In The World of Physical Chemistry*, pp. 156–240, Oxford University Press, New York, NY, USA, 1995.

[2] C. Tsallis, "Possible generalization of Boltzmann-Gibbs statistics," *Journal of Statistical Physics*, vol. 52, no. 1-2, pp. 479–487, 1988.

[3] M. Rao, Y. Chen, B. C. Vemuri, and F. Wang, "Cumulative residual entropy: a new measure of information," *IEEE Transactions on Information Theory*, vol. 50, no. 6, pp. 1220–1228, 2004.

[4] S. Pincus, "Approximate entropy as an irregularity measure for financial data," *Econometric Reviews*, vol. 27, no. 4-6, pp. 329–362, 2008.

[5] M. R. Ubriaco, "Entropies based on fractional calculus," *Physics Letters A*, vol. 373, no. 30, pp. 2516–2519, 2009.

[6] L. S. Rompolis, "Retrieving risk neutral densities from European option prices based on the principle of maximum entropy," *Journal of Empirical Finance*, vol. 17, no. 5, pp. 918–937, 2010.

[7] M. M. Sati and N. Gupta, "Some characterization results on dynamic cumulative residual Tsallis entropy," *Journal of Probability And Statistics*, vol. 2015, Article ID 694203, 8 pages, 2015.

[8] M. Sheraz, S. Dedu, and V. Preda, "Entropy measures for assessing volatile markets," *Procedia Economics and Finance*, vol. 22, pp. 655–662, 2015.

[9] D. Stosic, D. Stosic, T. Ludermir, W. de Oliveira, and T. Stosic, "Foreign exchange rate entropy evolution during financial crises," *Physica A: Statistical Mechanics And Its Applications*, vol. 449, pp. 233–239, 2016.

[10] L. Ponta and A. Carbone, "Information measure for financial time series: quantifying short-term market heterogeneity," *Physica A: Statistical Mechanics And Its Applications*, vol. 510, pp. 132–144, 2018.

[11] A. H. Khammar and S. M. A. Jahanshahi, "On weighted cumulative residual Tsallis entropy and its dynamic version," *Physica A: Statistical Mechanics And Its Applications*, vol. 491, pp. 678–692, 2018.

[12] A. M. Karakaş, "Entropy approach for volatility of ethereum and bitcoin," *Asian Journal of Business and Management*, vol. 7, no. 1, 2019.

[13] K. A. Metin, "Volatility measurement of the world indices using different entropy methods," *Thermal Science*, vol. 23, no. Suppl. 6, pp. 1849–1861, 2019.

[14] M. İnç, Z. S. Korpinar, M. M. Al Qurashi, and D. Baleanu, "A new method for approximate solutions of some nonlinear equations: residual power series method," *Advances in Mechanical Engineering*, vol. 8, no. 4, Article ID 1687814016644580, 2016.

[15] B. Acay and M. Inc, "Fractional modeling of temperature dynamics of a building with singular kernels," *Chaos Solitons & Fractals*, vol. 142, Article ID 110482, 2020.

[16] A. Houwe, M. Inc, S. Y. Doka, B. Acay, and L. V. C. Hoan, "The discrete tanh method for solving the nonlinear differential-difference equations," *International Journal of Modern Physics B*, vol. 34, no. 19, Article ID 2050177, 2020.

[17] M. A. Akinlar, M. Inc, J. F. Gómez-Aguilar, and B. Boutarfa, "Solutions of a disease model with fractional white noise," *Chaos Solitons & Fractals*, vol. 137, Article ID 109840, 2020.

[18] M. A. Akinlar, F. Tchier, and M. Inc, "Chaos control and solutions of fractional-order Malkus waterwheel model," *Chaos, Solitons & Fractals*, vol. 135, Article ID 109746, 2020.

[19] Z. Korpinar, F. Tchier, M. Inc, F. T. Bousbahi, F. M. Tawfiq, and M. A. Akinlar, "Applicability of time conformable derivative to Wick-fractional-stochastic PDEs," *Alexandria Engineering Journal*, vol. 59, no. 3, pp. 1485–1493, 2020.

[20] M. S. Hashemi, M. Inc, and A. Yusuf, "On three-dimensional variable order time fractional chaotic system with nonsingular kernel," *Chaos, Solitons & Fractals*, vol. 133, Article ID 109628, 2020.

[21] S. Qureshi, A. Yusuf, A. Ali Shaikh, M. Inc, and D. Baleanu, "Mathematical modeling for adsorption process of dye removal nonlinear equation using power law and exponentially decaying kernels," *Chaos: An Interdisciplinary Journal of Nonlinear Science*, vol. 30, no. 4, Article ID 043106, 2020.